

VOLUMES 7-9, 2022

ISSN 2465-7425



NIGERIA JOURNAL OF ENGINEERING AND APPLIED SCIENCES (NJEAS)

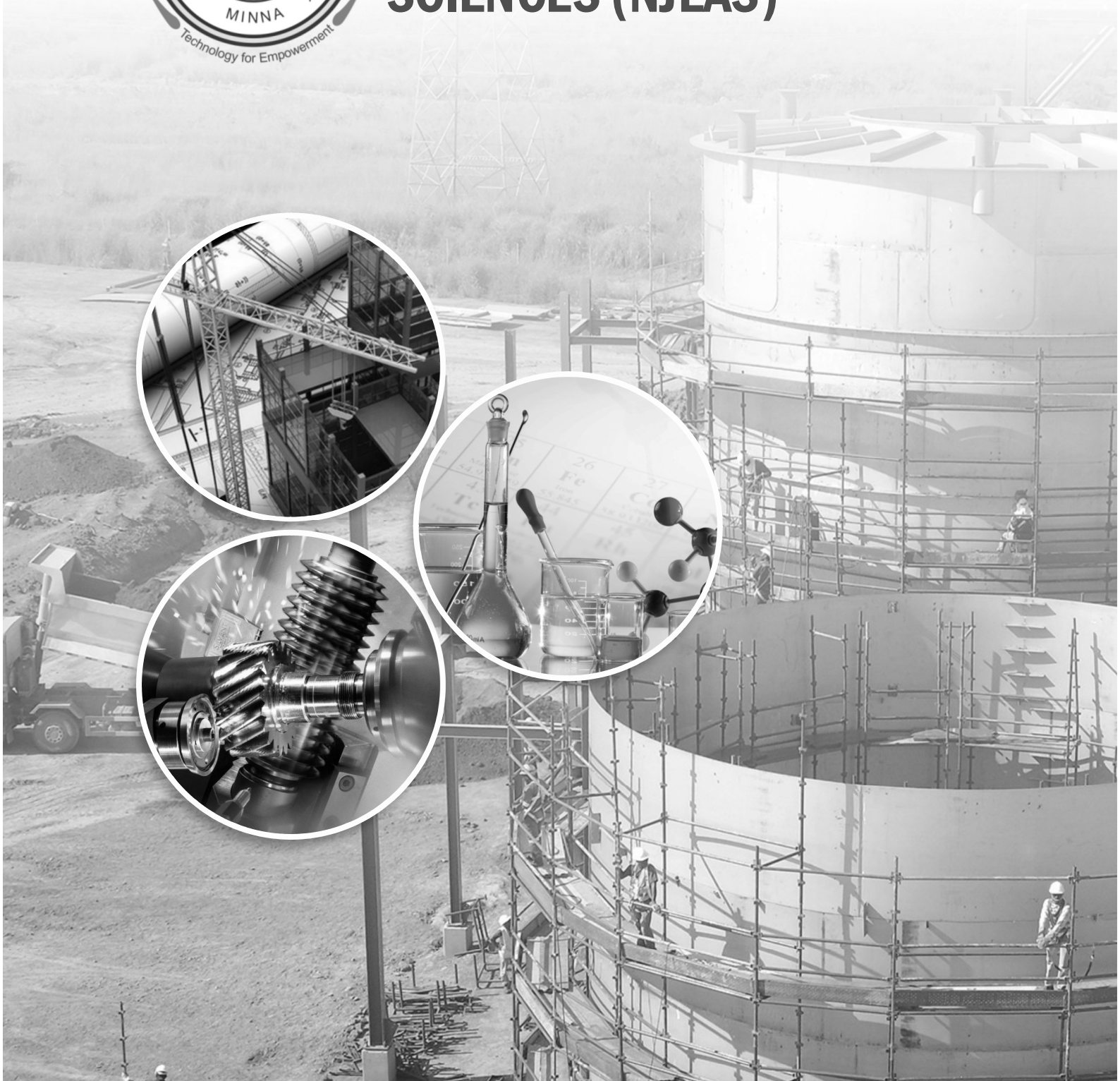


VOLUMES 7-9, 2022

ISSN 2465-7425



NIGERIA JOURNAL OF ENGINEERING AND APPLIED SCIENCES (NJEAS)



NIGERIA JOURNAL OF ENGINEERING AND APPLIED SCIENCES (NJEAS)

Nigeria Journal of Engineering and Applied Sciences – NJEAS (ISSN: 2465-7425) is a publication of the two schools of Engineering: School of Infrastructure, Process Engineering and Technology (SIPET) and School of Electrical Engineering and Technology (SEET) of Federal University of Technology, Minna, Nigeria.

The journal is committed to promoting and publishing original high quality research papers and stresses on academic excellence, knowledge distribution as well as joint scholarly efforts in order to support theoretical, experimental and practical research. Papers for publication are selected through peer review to ensure originality, relevance, and readability.

The subject areas related to this journal include but are not limited to:

1. Chemical, Petroleum and Gas Engineering 2. Civil Engineering 3. Computer Science and Information Technology. 4. Electrical Engineering 5. Electronics & Telecommunication Engineering 6. Mechanical & Mechatronics Engineering and 7. Allied Applied Sciences.

EDITORIAL BOARD MEMBERS

Engr. Prof. A. A. Amadi	Editor-in-Chief
Engr. Prof. O. M. Olaniyi	Managing Editor
Engr. Prof. (Mrs) Z. D. Osunde	Member
Engr. Prof. A. S. Kovo	Member
Engr. Prof. J. O. Okafor	Member
Engr. Prof. A. M. Aibinu	Member
Engr. Prof. M. Abdullahi	Member
Engr. Prof. A. S. Abdulrahman	Member
Engr. Prof. S. A. Lawal	Member
Engr. Dr. P. Adeoye	Member
Engr. Prof. M. Nwohu	Member
Engr. Prof. J. Tsado	Member

Published by:

School of Infrastructure, Process Engineering and Technology, School of Electrical Engineering and Technology and Academic Publishing Centre, Federal University of Technology, Minna, Nigeria.

All Correspondences to:

Editor-In-Chief,
Nigeria Journal of Engineering and Applied Science (NJEAS),
Federal University of Technology, P. M. B. 65, Minna, Nigeria.
E-Mail: njeas@futminna.edu.ng, Website: njeas.futminna.edu.ng

TABLE OF CONTENTS

INTELLIGENT CRIMINAL IDENTIFICATION SYSTEM FOR SEMI-REGULATED ENVIRONMENTS

**Ganiyu, S. O., Akpagher, T. D., Olaniyi, O.M., &Adebayo, S. O.* 1

EXTRACTION OF ADHESIVE FROM GUILL AND PERR (*CISSUS POPULNEA*) FOR PARTICLEBOARD PRODUCTION USING RICE HUSK

**Aboje, A. A., Akor, I. H., Uthman, H., & Bala, A.* 18

INVESTIGATING THE PERFORMANCE OF FULL DEPTH RECLAIMED SURFACE-DRESSED PAVEMENT TREATED WITH CEMENT AND CALCIUM CARBIDE RESIDUE AS ROAD BASE

**Alhassan, M., Alhaji, M. M., & Saidu, A. E.* 35

PACKET DELIVERY RATIO (PDR) OF AN ENHANCED WEIGHT BASED CLUSTER HEAD SELECTION ALGORITHM FOR ROUTING IN VEHICULAR ADHOC NETWORKS (VANETS)

**Jiya, A. G, Usman, A. U and David, M.* 46

MODELLING WATER LOSS IN HYDRAULIC DISTRIBUTION NETWORKS OF SHIRORO WATER DISTRIBUTION SYSTEM MINNA, NIGER STATE.

Tanimu, Y.; Jimoh, O.D. and Adesiji A. R.* 58

HYBRID AUTOREGRESSIVE NEURAL NETWORK (ARNN) MODEL FOR SPECTRUM OCCUPANCY PREDICTION

**Ajiboye, J.A, Adegboye, B.A, Aibinu, A.M, Kolo, J.G, Ajiboye, M.A, Usman, A.U* 68

STRUCTURAL ASSESSMENT OF A LATTICE TOWER IN FEDERAL CAPITAL TERRITORY, ABUJA

Auta S.M., Okunyomi O.O., & Kolo, D.N. 77

COMPARATIVE STUDY ON CO₂ CAPTURE USING ACTIVATED CARBON FROM SUGARCANE BAGASSE AND ZEOLITE (ZSM-5)

*Abdullahi, A., *Alhassan M., Alhassan. B., Audu, O. A., Ayobamiji C. I., Isah, A. G., & Kovo, A, S.* 85

HYDRAULIC CONDUCTIVITY CHARACTERISTICS OF LEACHATE - CONTAMINATED LATERITIC SOIL

Asogwa, E. O., Adie, D. B., Ibrahim, F.B., Amadi, A.A. and Agbonselobho, M.O 95

INTEGRATED MODE SELECTION AND BANDWIDTH ALLOCATION SCHEME FOR INTERFERENCE MITIGATION IN D2D NETWORKS

**Ameh, A. I., Usman, A. U., Mohammed, A. S. & Salihu, B. A.* 101

PHYSICO-CHEMICAL ANALYSIS OF BIO-OIL PRODUCE FROM CO-PYROLYSIS OF *SIDA RHOMBIFOLIA* WITH LOW AND HIGH DENSITY POLYETHYLENE

**Abdullahi, A. M., Garba, M. U., Eterigho E. J., Alhassan, M., Adeniyi. O. D.* 115

A COMPARATIVE ANALYSIS OF GRILLAGE METHOD AND BEAM LINE ANALYSIS OF A REINFORCED CONCRETE WAFFLE BRIDGE DECK

Adamu, H. N.; Abbas B.A.; Abubakar, M.; Yusuf, A.; Kolo, D.N. & Shehu, M. 127

EFFECT OF BINDERS ON THE PROPERTIES OF CONCRETE – A REVIEW	
<i>*Oritola, S. F., Olojede, R. O, Kolo, J. L, Ukog, A. S. and Ekpenyong, D. E</i>	135
APPLICATION AREAS OF OPTICAL WIRELESS COMMUNICATION TECHNOLOGIES IN 5G, 6G AND INTERNET OF THINGS: EXPECTATIONS, DIRECTIONS, AND THREATS	
<i>Abdullahi, B B., Michael, D., Suleiman, Z. and Abraham,. U. U.</i>	146
COMPARATIVE STUDY OF TAMARINDUS INDICA AND ADANSONIA DIGITATA AS COAGULANTS AND DISINFECTANTS FOR WATER TREATMENT	
<i>*Uthman, H.</i>	169
PREDICTING THE FLOW CHARACTERISTICS OF RIVER NIGER USING ARTIFICIAL INTELLIGENCE MODELS	
<i>Gbadebo, O.A., Busari, A. O., Sadiku, S. and Saidu M.</i>	180

INTELLIGENT CRIMINAL IDENTIFICATION SYSTEM FOR SEMI-REGULATED ENVIRONMENTS

*Ganiyu, S. O.¹; Akpagher, T. D.²; Olaniyi, O.M³; &Adebayo, S. O.⁴

¹Department of Computer Science, Kampala International University, Kampala, Uganda

^{1,2}Department of Information Technology, Federal University of Technology Minna, Nigeria

³Department of Computer Engineering, Federal University of Technology Minna, Nigeria

⁴Department of Computer Science, Islamic University in Uganda, Mbale, Uganda

⁴Department of Cyber Security Science, Federal University of Technology Minna, Nigeria

Email: ganiyu.shefiu@kiu.ac.ug, shefiu.ganiyu@futminna.edu.ng

Abstract

Nowadays, algorithms and technologies for criminal identification systems are imperative for the fight against crime in every environment. Thus, closed-circuit television cameras are now being incorporated into physical security mechanisms to identify suspects and criminals at crime scenes. However, crime investigators often spend a great deal of time unravelling the identities of criminals in lengthy video footage, especially in a semi-regulated environment where both known and unknown faces are always present. However, the research that combined a Single Short MultiBox Detector (SSD) and Local Binary Patterns Histograms (LBPH) for criminal identification in a semi-regulated environment is yet to be explored. Hence, this study developed a system that proactively identifies known criminals or documents the presence of non-criminals for reactive investigation by combining SSD with LBPH. To achieve this, SSD was employed to detect faces, while the LBPH algorithm for face recognition. Also, the system sends security alerts via email and short message service once a criminal is identified in the environment. Based on the faces captured by the identification system, SSD and LBPH achieved a precision of 95% and 90% respectively. With this achievement, the system will not only reduce the time taken to identify criminals in a semi-regulated environment, but also will improve the chances of reporting the presence of confirmed criminals.

Keywords: Criminal Identification, Deep learning, Face Detection, Face Identification, LBPH, Semi-regulated Environment.

INTRODUCTION

Apparently, crime is an aspect of societal challenges that has continued to pervade almost all facets of human endeavours. It can be described as an act that leads to offences, which are punishable under applicable laws of the land and the corresponding punishments depends on magnitude of crime, time and location (Oguntunde *et al.*, 2018). Relatedly, crime can be any action that contradicts the criminal (or penal) code of a state. For example, the penal and criminal codes enacted in Nigeria over 50 years ago are still operational in spite of the waves of new digital crimes. Unfortunately, crime rate has continued to increase yearly in many locations (Kakkar & Sharma, 2018).

For example, the number of reported crimes in Nigeria rose from 125,790 in the year 2016 (NBS, 2017) to 134,663 in 2017 (NBS, 2018).

Thus, in order to catchup with present criminal activities, law enforcement agencies are developing or adopting innovative and technology-driven strategies to fight crime, popular among them is the use of biometric identification (Chhoriya, 2019). Simply put, biometric identification is based on the principle that every individual can be identified by a unique and specific set of recognizable and identifiable set of data (Halvi *et al.*, 2017; Malathi & Raj, 2016). For instance, features such as fingerprint, voice and facial recognition can be used to

detect known criminals, spot the entry and exit of individuals.

Ordinarily, security agents are expected to unravel the facial identity of criminals at crime scenes and conduct necessary investigations to aid criminal justice. However, the lack of technology-driven solutions to promptly identify criminals in semi-regulated environments is hampering the smooth operations of security agents. Consequently, the increase in crime rates can be partly attributed to the fact that some criminals who continued to commit crimes in our environments are supposed to be convicted if identified on time. In order to address the problem of criminal facial identification, some research efforts like Abdullah *et al.* (2017), Azeta *et al.* (2015), Chhoriya (2019) Gurav *et al.* (2015), Halvi *et al.* (2017), Kakkar and Sharma (2018), Kumar *et al.* (2018), Sanjay and Priya (2022), Sarkar and Prasad (2022), and Zafar *et al.* (2019) were proposed to assist law enforcement agents in identifying criminals in unregulated and regulated environments through facial recognition systems. However, a thorough review of relevant literature revealed that facial recognition system which combined Single Shot MultiBox Detector (SSD) (Liu *et al.*, 2016) with LBPH to identify criminals in semi-regulated environments is yet to be established (Sarkar & Prasad, 2022; Tela *et al.*, 2022).

In line with the foregoing, this study designed and developed a facial identification system that combined SSD (a variant of deep learning algorithms) with LBPH to assist criminal identification. Specifically, SSD was used for face detection, while LBPH was used to predict the confidence of detected faces. The developed system is a continuation of Ganiyu *et al.* (2020). It could detect, recognise, document and initiate security alerts when criminals or suspects are in semi-regulated environments. In essence, the system has the potential to identify both known and unknown faces to aid security

agencies in criminal investigations. Significantly, this research effort will reduce the time spent searching for criminal faces in video feeds and improves the accuracy of search result. Similarly, it simplifies and provides real-time identification of suspects and criminals in semi-regulated locations by automatically documenting and updating information about known criminals and unknown persons.

The remainder of this paper is organised as follows: section 2 reviews literature that relates to the research, section 3 presents the methodology employed in the design and development of the proposed system, section 4 discusses the implemented facial recognition system and section 5 concludes and recommends future enhancement to the system.

BACKGROUND

The rowdiness and unrestricted movement of people, especially in crowded public places have provided criminals with a plethora of opportunities to perpetrate various crimes (Kumar *et al.*, 2018). These criminals operate in public and private places, loiter around, stalk unsuspecting individuals, and commit crimes due to insufficient or unavailability of physical security measures. Somehow, the modus operandi adopted by criminals will likely depend on restriction to movement within an environment and time amongst others. For example, the styles adopted by malefactors to perpetrate crimes in public places like train station (unregulated environment), will be quite different from those used in secluded locations such as offices within corporate building (regulated environment). Similarly, criminals might reconnoitre different styles in locations that is neither regulated or unregulated, that is, semi-regulated environment like banking halls and customer service centres.

Furthermore, facial recognition is a subset of biometric identification with certain advantages, such as high accuracy, uniqueness and low intrusiveness over other

biometric-based identification methods (Aanchaladevi *et al.*, 2021; Abdullah *et al.*, 2017). Hence, these advantages make it a modest biometric tool for criminal identification and security systems (Tiwari *et al.*, 2015). Also, facial identification systems largely utilise database of saved faces against which comparison is made with captured faces, this comparison could either lead to a match (recognised face) or an unmatched outcome (unrecognised). Therefore, biometric identification systems are simple, convenient and agile means to mitigate criminal activities in any environment (Naik *et al.*, 2019; Singh & Prasad, 2018). Although biometric recognition systems have some limitations, including privacy violations, illuminations, age changing, falsification of faces, face positions, threats to personal rights and data vulnerabilities, these shortcomings were addressed by Karimov *et al.*, (2017). The expected benefits of facial recognition in this study outweigh the limitations.

Mostly, there are two components in a facial identification systems, namely face detection and face recognition (Abdullah *et al.*, 2017). Foremost, face detection is the ability of such systems to distinguish human face from other background images. Next, the recognition component classifies a detected face as that of human, even in the presence of other animal faces that have close facial geometry with human face. Still, the recognition component compares the detected face with already known faces to comprehensively describe the former. Broadly, facial recognition techniques can be categorised into Eigenface, neural network, Fisherface and elastic bunch graph matching (Reddy, 2017). Thus, several statistical and machine learning algorithms could be implemented to separately detect or recognise faces in identification systems (Alskeini *et al.*, 2018; Deebea & Ahmed, 2019; Du *et al.*, 2018; Singh & Prasad, 2018; Zafar *et al.*, 2019). Likewise, several criteria such as the distance of the face from the camera, the angle of the camera relative to the face, wearing of face accessories,

memory usage, recognition rate, and data representation, are commonly used to evaluate the accuracy of these algorithms to ascertain their effectiveness for detecting or recognising human faces (Ahmad *et al.*, 2021; Saini *et al.*, 2014).

Currently, the trend in face identification is progressively transitioning from manual methods to the use of deep learning algorithms (Sarkar & Prasad, 2022; Trigueros *et al.*, 2018). Deep learning is an emerging machine learning concept that is based on Convolutional Neural Network (CNN). It is now being used in various aspect of computing including image processing, particularly for computer vision project with very large dataset (Trigueros *et al.*, 2018). Relatedly, Local Binary Patterns Histograms (LBPH) is among the efficient and simple facial recognition algorithms (Deeba & Ahmed, 2019). It extracts local features from digital images and performs well in recognising both front and side views of human face in different lighting situations (Kakkar & Sharma, 2018), differing facial expressions and poses (Jaturawat & Phankokkruad, 2017; Tela *et al.*, 2022).

Interestingly, some systems and conceptual frameworks have been developed to ease the process of recognising or identifying people through facial identification systems (Azeta *et al.*, 2015; Halvi *et al.*, 2017; Sukhija *et al.*, 2016; Zafar *et al.*, 2019). For example, Ganiyu *et al.*, (2020) proposed an architecture that used deep learning approach for face detection and LBPH algorithm for face recognition, thus creating a hybrid approach to harness the advantages of both LBPH and deep learning approaches for facial identification. Some recent criminal identification systems only find a match for a particular criminal face (Aanchaladevi *et al.*, 2021; Kakkar & Sharma, 2018; Kumar *et al.*, 2020), while others can send threat notifications when faces of documented criminals are detected (Baraka *et al.*, 2021; Kumar *et al.*, 2018).

RELATED WORK

Over the years, facial detection, recognition and identification algorithms have caught the attention of researchers in the field of computer vision. Hence, some research in the domain developed and enhanced the algorithms and their applications to various challenges requiring computer vision, such as crime prevention, control, and analysis. For this reason, Alskeini *et al.* (2018), Deeba and Ahmed (2019), Sukhija *et al.* (2016), Zafar *et al.* (2019) conducted researches on different facial recognition algorithms to demonstrated their suitability and performances. On one hand, Zafar *et al.* (2019) investigated the performance of Bayesian convolution network for facial recognition in surveillance camera. On the other hand, Deeba and Ahmed (2019) proposed an enhancement to LBPH for real-time facial detection. More so, Du *et al.* (2018) and Siregar *et al.*, (2018) applied facial recognition algorithms to embedded system and cloud security respectively. Specifically, Abdullah *et al.* (2017), Azeta *et al.* (2015), Chhoriya (2019), Gurav *et al.* (2015), Kakkar and Sharma (2018), Kumar *et al.* (2018), Naik *et al.* (2019), and Nguyen *et al.* (2018) developed criminal recognition or identification systems using facial detection and recognition algorithms.

Furthermore, Tela *et al.* (2022) used CNN to implement criminal identification system but the system cannot take image directly from CCTV camera in real time. In addition, Aanchaladevi *et al.* (2021), Kumar *et al.* (2020), and Sarkar and Prasad (2022) implemented criminal detection with Haar cascade algorithm. Likewise, Sanjay and Priya (2022) developed a system to improve criminal identification system using CNN and Haar cascade. Similarly, Ahmad *et al.* (2021) implemented a video surveillance system using Haar cascade to identify faces under the following constraints; when accessories cover parts of the face, when a face is positioned at particular angles to the camera, and when the face is far from the camera. According to Sanjay and Priya

(2022) and Shepley (2019), Haar cascade classifier is less efficient than CNN for criminal identification.

In order to underpin the importance of computer vision algorithms to criminal identification, Jaturawat and Phankokkrud (2017), Reddy (2017), Saini *et al.* (2014), Singh and Prasad (2018) and Trigueros *et al.* (2018) conducted extensive reviews and evaluations of several facial recognition algorithms. Recently, Ganiyu *et al.* (2020) reviewed facial recognition algorithms and systems for criminal detection. The authors classified the application domains of existing facial recognition systems into *regulated*, *semi-regulated* and *unregulated* environments. Additionally, the systematic review showed that significant effort had been expended on criminal detections in unregulated and regulated environments, while semi-regulated environment is yet to receive research attention.

Generally, one obvious limitation of existing criminal identification systems is that they rely on a sufficiently populated database of criminals' faces against which comparison were made to recognise and subsequently identify criminals. However, the prepopulated database might not be readily available for identification systems deployed in unregulated or semi-regulated environments. Again, as opined by Trigueros *et al.* (2018), previous research efforts have not explored any hybrid method that comprises deep learning and LBPH for criminal identification, especially in a semi-regulated environment where the dataset of suspected criminals might be limited.

METHODOLOGY

This section presents the tools employed to design and develop the proposed criminal identification system, including use case diagram, system architecture and block diagram. Also, it covers the technique adopted to evaluate the performance of the proposed system.

SYSTEM DESIGN

Primarily, the proposed system will identify criminals in a semi-regulated environment. The system works with three categories of people commonly found in the semi-regulated environment during crime investigations. First, it documents the presence of *known criminals* already tagged due to previous criminal activities. The people in the second category are *known individuals* whose identities are known to the system as non-criminals. The third category belongs to *unknown individuals (strangers)* neither tagged as criminals nor recognised

by the system as non-criminals. In events of crime cases, the people in the third category become prime suspects. Thus, Fig. 1 represents the architecture of the proposed system. It also depicts all the major components within the system and external entities and the interactions among all the system's modules. These components include CCTV cameras, security officers designated in an organisation, the system administrator, external security personnel or law enforcement agents (e.g., police) and facial identification software, which in turn comprises detection and recognition algorithms.

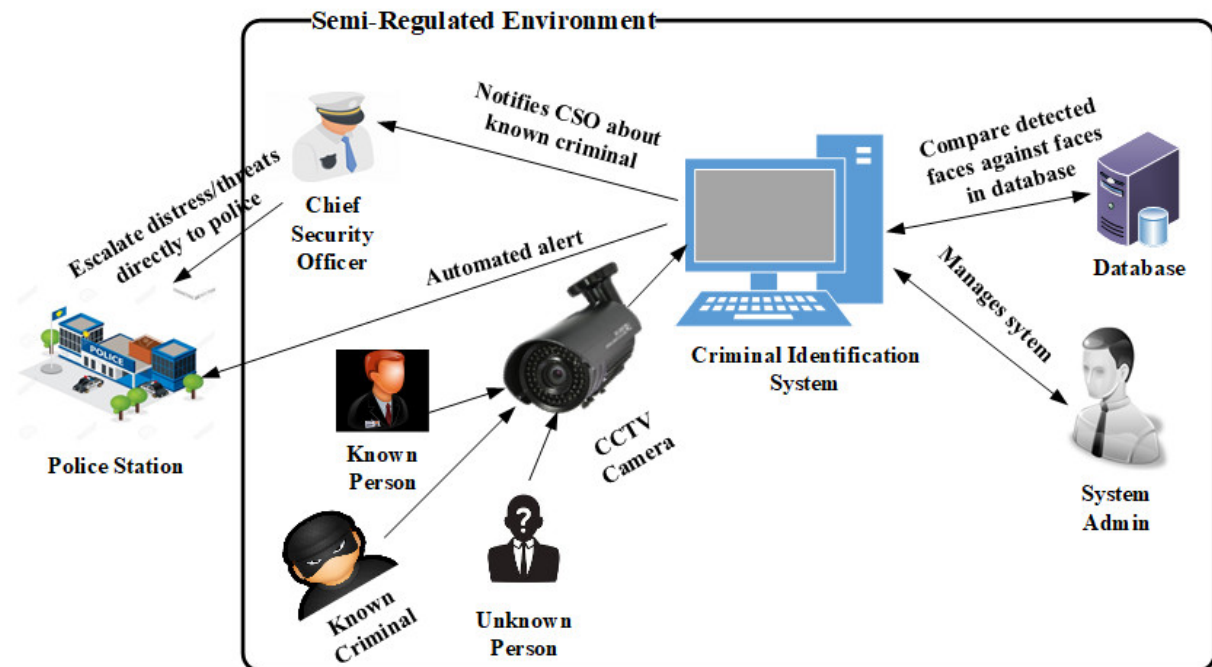


Fig. 1: Architecture of proposed system

Use Case of the Proposed System

The use case diagram captures the basic actions performed by each user in the proposed system, as represented in Fig. 2. As depicted in the figure, the supervisor is in charge of all the activities relating to system maintenance. Thus, the Admin creates security staff who can log into the system to register known individuals and criminals. For security reasons, certain security privileges are restricted for execution by the supervisor to ensure that other security staff

who have access to the system do not perform the function, which can compromise the security of the criminal identification system. For instance, any record deleted by the staff is still viewable by the supervisor or even restored to the system.

As shown in Fig. 2, any individual detected by the CCTV camera could be a known person, criminal or stranger. Once a camera detects a criminal, the Chief Security Officer (CSO) will receive a security notification or alert. In addition, the CSO oversees that particular environment and gives

instructions for immediate actions. Thus, the CSO manages physical security devices and escalates security alerts about criminals or suspects to law enforcement agents duly registered on the system. The threat escalation component sends distress

notifications via Short Message Service (SMS) and Electronic Mail (email) messages to the law enforcement agent for necessary action to complement the internal security posture of an organisation.

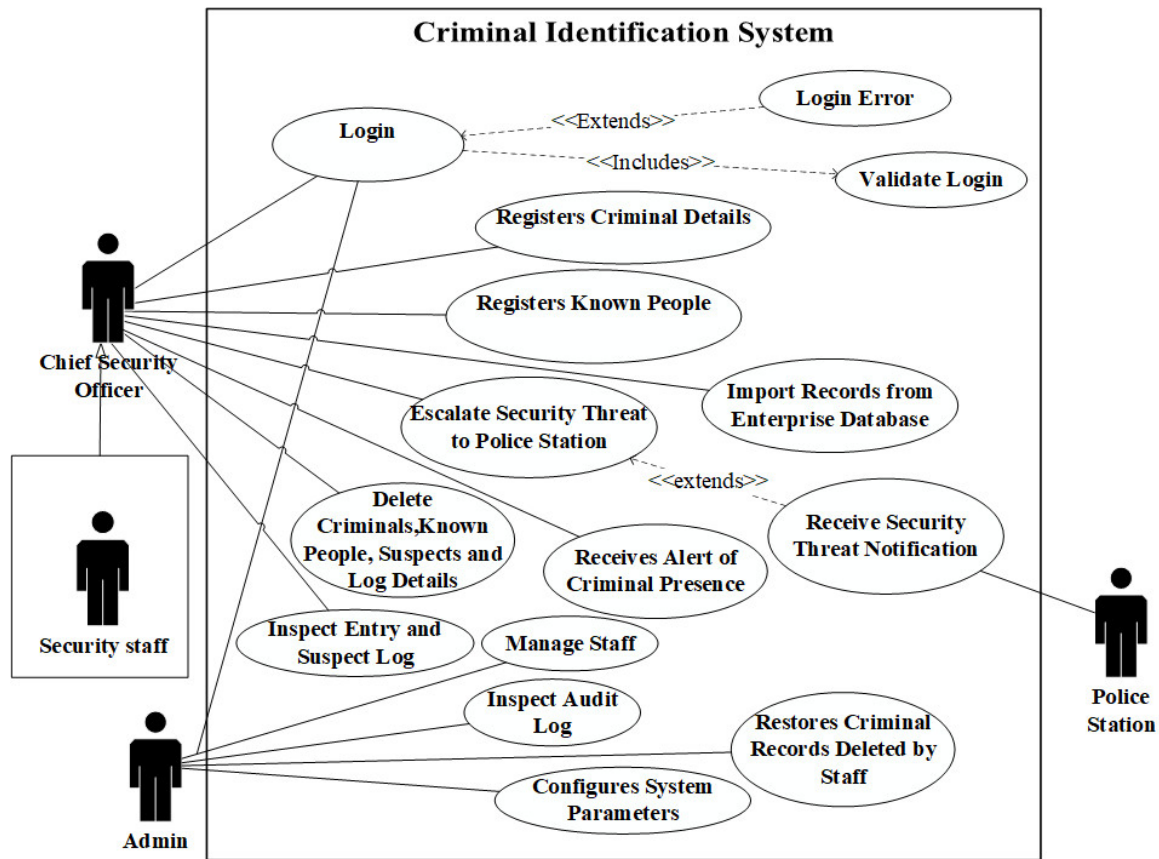


Fig. 2: Use Case Diagram of the Proposed

Flowchart of the Proposed System

In addition, the flowchart presented in Fig. 3 reinforces the design of the proposed system. For this purpose, the entire system is divided into distinct programming tasks and rendered with appropriate flowchart symbols. Primarily, identifying faces involves training the model with the faces of known individuals (registered) in the system. These faces will constitute the training dataset. Afterwards, the recognition module processes the faces captured by the CCTV camera. Once a face is detected, the system predicts its confidence value. If the confidence value is less than the predetermined ideal confidence, the face is recognised as either a known individual or a

criminal. Otherwise, the system categorises the face as an unknown face and saves the detected face along with other information like the date and time of detection.

Block Diagram of the Proposed System

Furthermore, the flow of the proposed system is illustrated by the block diagram presented in Fig. 4. The block diagram provides an overview of relevant modules that ensure the seamless and effective running of the system. As the block diagram reveals, the system receives the video feed from strategically positioned cameras. Next, the deep learning algorithm detects the human faces in the video feed. Subsequently, a face recognition module executes to predict the confidence of the detected face.

Once the confidence value is determined using the LBPH recogniser, the value is compared with the target value (of known faces). Therefore, if the confidence value is less than the target value, then the face is recognised. It follows that a recognised face can either be a criminal or a known (non-criminal) face whose identity already exists in the system. The proposed facial identification system will document the necessary details after a criminal's face is recognised. In addition, the system will send an alert to the CSO of the organisation, and the registered police unit will be alerted. In

the case of an identified non-criminal individual, the time and date are documented appropriately for future reference. However, if the confidence value is greater than the target value, the detected face of the unknown individual is cropped, and documented with the time and date when it was captured. In such case, the system's flow would stop at the recognition phase, because identification cannot be performed without prior information of individuals. Lastly, the admin has access to the facial records of both criminals and known people and can restore deleted records of criminals.

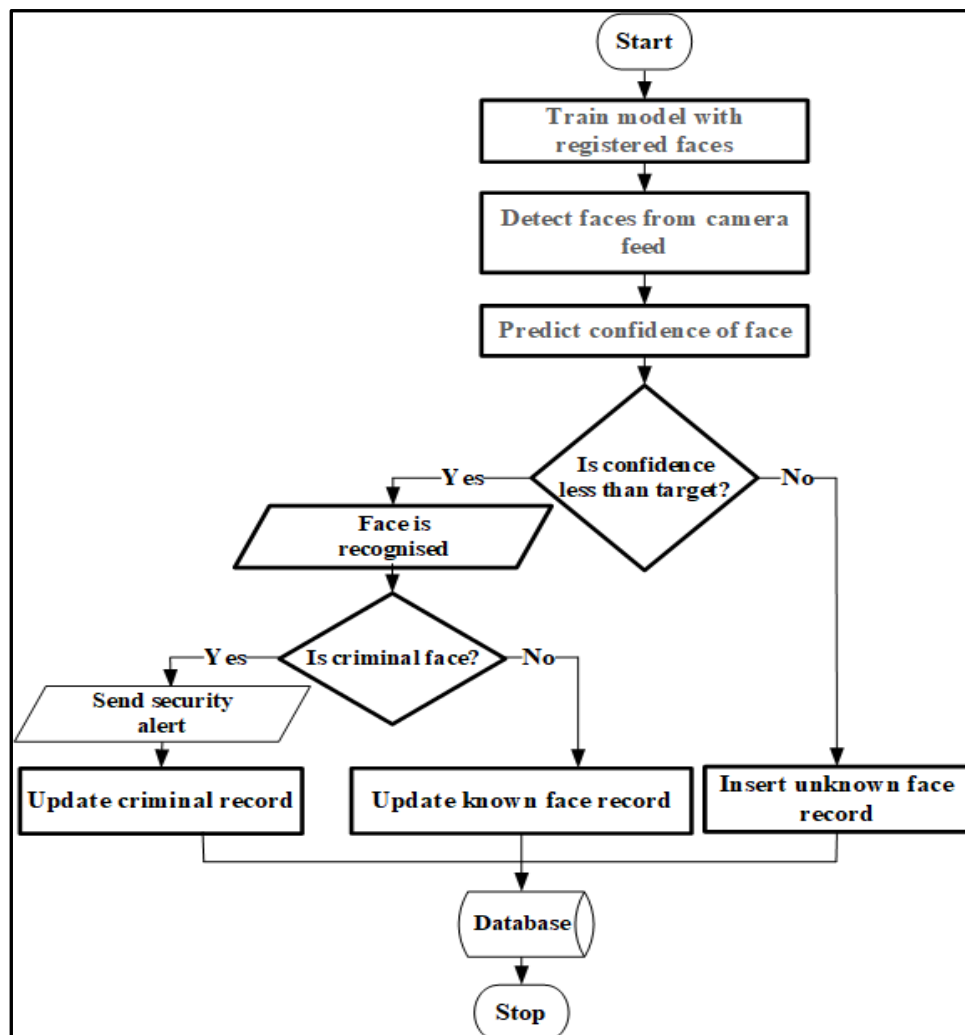


Fig. 3: Flowchart of Criminal Facial Identification System

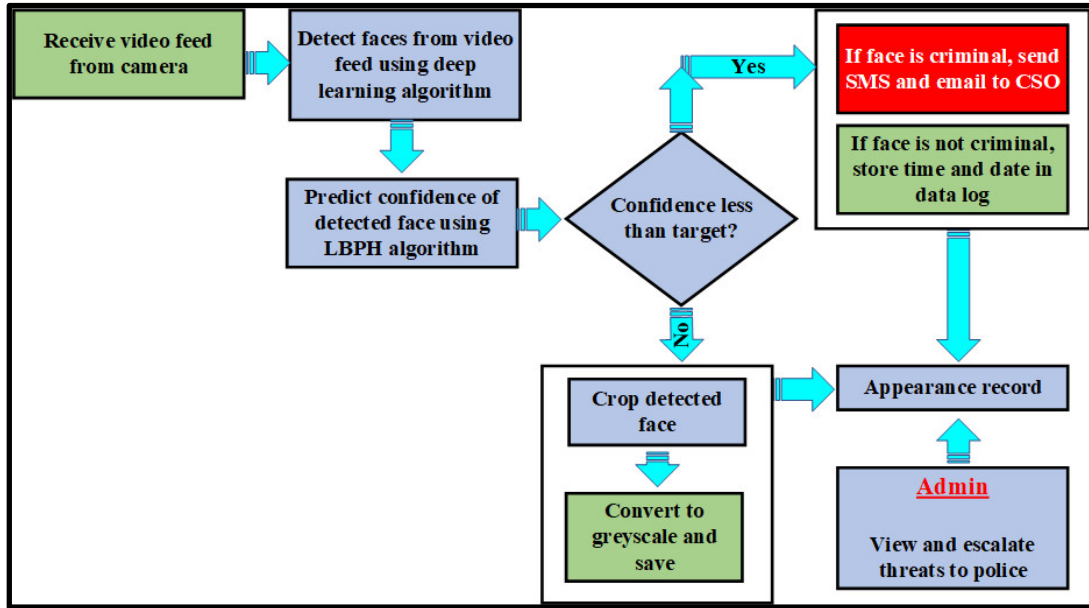


Fig. 4: Block diagram showing important modules (Adapted from Ganiyu *et al.*, (2020))

IMPLEMENTATION OF THE PROPOSED CRIMINAL IDENTIFICATION SYSTEM

The proposed system was implemented as a desktop application using *JavaFX*. Further, *MySQL* was used to store and manage all data for the proposed facial identification system. Also, Application Programming Interfaces (APIs) from *JavaCV*, which is a Java flavour of *OpenCV* was employed for detection and recognition modules. The detection module was implemented using deep learning that consists of two files; a *Prototxt*, which defines the model architecture, and a *Caffe model*, which contains the weights of actual layers. Furthermore, the detection module is built on an SSD framework with a *ResNet*-based network. Particularly, SSD was selected due to its efficiency over other traditional methods for face detection such as LBP and Haar Cascade classifiers (Shepley, 2019).

Subsequently, the recognition of faces was achieved using LBPH facial recognition algorithm. Before adopting LBPH, a comparison between Eigenface, Fisherface and LBPH algorithms was carried out. Interestingly and LBPH gave the best result for face recognition.

PERFORMANCE EVALUATION OF PROPOSED CRIMINAL IDENTIFICATION SYSTEM

This performance evaluation was performed using a confusion matrix presented in Table 1. The matrix comprises measures like a true positive, false positive, false negative and true negative. Also, the performance evaluation involves other performance metrics such as precision, recall, error rates, accuracy and sensitivity. All the performance metrics were utilised to evaluate how well the facial recognition system correctly identified faces already tagged as criminal and non-criminal.

Table 1: Confusion Matrix

		Actual Values	
		Positive	Negative
Predicted Values	Positive	True Positive (TP)	False Negative (FN)
	Negative	False Positive (FP)	True Negative (TN)

The explanation and mathematical realisation of these performance metrics are as follow:

Precision: Otherwise known as reliability, is the fraction of the detected images that are correctly identified. As shown in Equation 1, precision is the total number of correctly recognized images divided by the total images tested,

$$\text{Precision} = \frac{TP}{(FP + TP)} \quad (1)$$

Recall: This is also known as true positive rate and it is the proportion of positive cases that were properly identified as expressed in Equation 2. That is, it is the fraction of relevant images that are successfully detected,

$$\text{Recall} = \frac{TP}{(TP + FN)} \quad (2)$$

Error Rate: This represents quantity of misclassification (misrecognition) over the overall number of validation samples as shown in Equation 3,

$$\text{Error Rate} = \frac{(FP + FN)}{(TP + FP + FN + TN)} \quad (3)$$

Accuracy: Accuracy is defined as “the fraction of quantity of correct classification over the entire number of samples.” This is represented by Equation 4. The number of predictions in classification techniques relies upon the counts of the test records that were properly or incorrectly predicted,

$$\text{Accuracy} = \frac{(TP + TN)}{(TP + FP + FN + TN)} \quad (4)$$

Sensitivity: Sensitivity is otherwise known as true positive rate (TPR) or hit rate. As shown in Equation 5, it is a measure of how well a binary classification test properly

identifies a condition probability of properly labelling members of the target class,

$$\text{Sensitivity} = \frac{TP}{(TP + FN)} \quad (5)$$

RESULTS

Result Presentation

The proposed criminal identification system was implemented and all the modules were tested to ensure their functionality. Similarly, performance evaluation was conducted on the identification system using the performance metrics.

Implemented Criminal Identification System

Generally, all the modules included in the block diagram functioned as designed and implemented. Hence, this section illustrates the core module in the criminal identification system with appropriate screenshots.

Registering Known and Criminal Faces

The process of registering a known individual or criminal by security staff involves saving their basic details such as name, age, gender, and address amongst others. Thus, the registration involved capturing at least 20 images per individual. The face in each image is detected, cropped and then converted to grayscale as illustrated in Fig. 5, with a total of 20 individual faces captured.

Criminal Identification Message for Known Criminal

Normally, the system only documents the time and date for known individuals who can be customer, staff or known person who has not been flagged as a criminal. However, once a known criminal is identified, the system automatically generates and sends alert notifications (email and SMS) to the chief security officer of the organization as shown in Figs. 6(a) and 6(b) respectively.

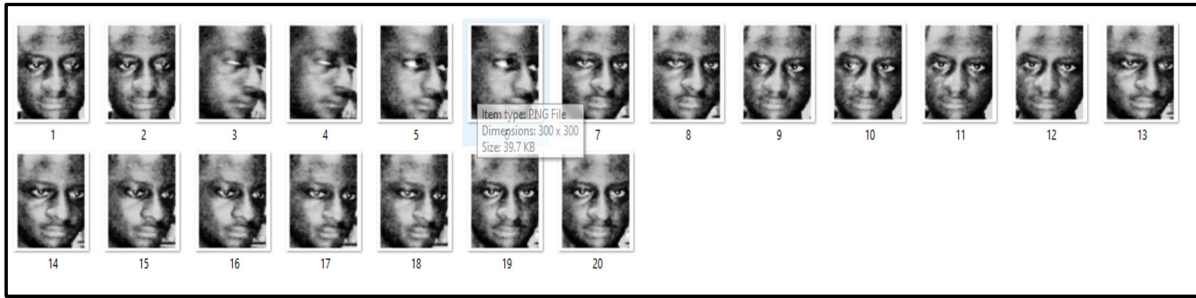


Fig. 5: Grayscale pictures of each individual

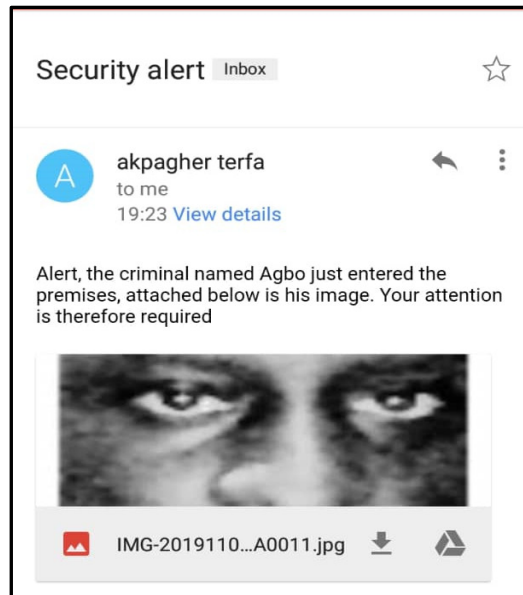


Fig. 6(a): Email notification to chief security officer

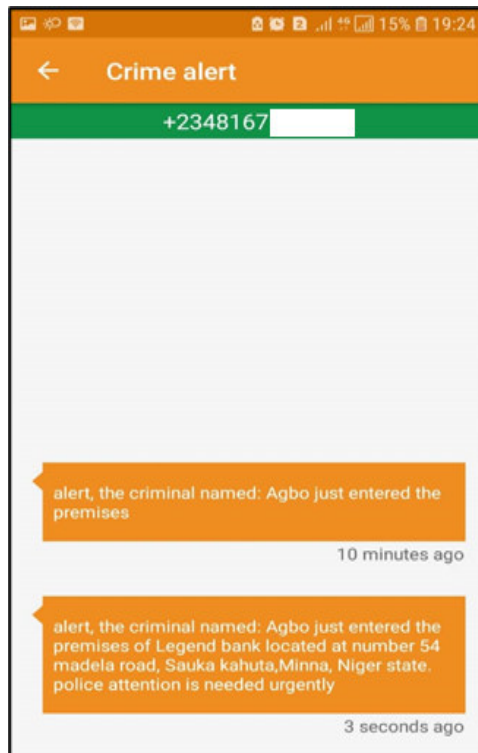


Fig. 6(b): SMS alert to police station

Generating Distress Security Alert

Additionally, any security staff who is currently logged into the system could generate and send distress emails and SMS to the registered law enforcement unit as

shown in Figs. 7 and 6(b) respectively. This functionality is incorporated into the system to address security situations when the CSO has been overpowered or rendered incapacitated by criminals.

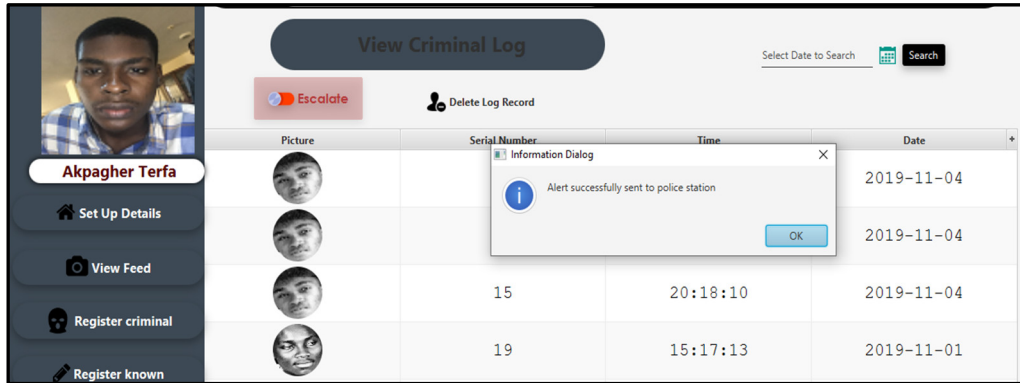


Fig. 7: Distress security alert

Documenting Unknown Faces for Future References

In a situation where the face that is spotted by the system neither matches the registered (known) person nor documented criminal, then the unidentified individual is tagged as a stranger to the semi-regulated environment. Reasonably, the system will automatically and temporarily retag such a stranger as a suspect, if any crime is reported

during the time the stranger is within a semi-regulated environment. Hence, the system stores the face, time and date of each suspect as shown in Fig. 8. Therefore, it will become easier for both the security department of the organisation and the police unit to search for the faces of strangers who are present at crime scenes. Furthermore, this functionality will reduce the time taken to recognise suspects, rather than filtering hours of video footage in the advent of crime occurrence.

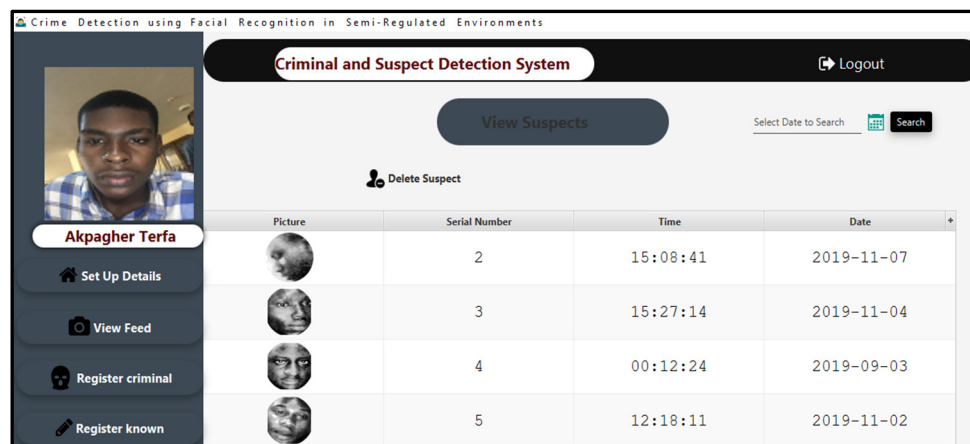


Fig. 8: Record of Unknown (Unidentified) Face

Performance Evaluation of Implemented Criminal Identification System

The detection and recognition modules of the criminal identification system were evaluated using a dataset comprising 20 images per person for 30 persons which were captured by the system. On one hand, deep learning algorithms were adopted due to their efficacy as facial detection algorithms (Sarkar & Prasad, 2022). On the other hand, LBPH, Fisherfaces and Eigenfaces are compared in order to determine the one with the best performance.

Performance Evaluation of Facial Recognition Algorithms

Foremost, a comparison of the three most reported facial recognition algorithms was conducted in order to select the facial recognition algorithm with the best

performance as shown in Table 2. Hence, it revealed that LBPH has the best performance under the five (5) performance metrics that were discussed in section 3.3. For example, Fig. 9 shows performances of the algorithms under precision metric. As observed in the figure, LBPH had the best precisions even when the images were fewer than 10. In the case of Fisherfaces and Eigenfaces, there is no significant difference in their precision rates. Similarly, the precision of LBPH steadily increased with more images. Also, Fisherfaces and Eigenfaces had a steady increase in precision rates, and the three algorithms almost converged to the same precision when images were close to 30. Thus, LBPH learned better than the two other algorithms. The result made LBPH a more suitable facial recognition algorithm in a semi-regulated environment where only a few faces are known to the criminal identification system.

Table 2: Comparison of the three algorithms against dataset of registered faces

Algorithm	Precision	Recall	Error rate	Accuracy	Sensitivity
LBPH	0.90	0.90	0.15	0.84	0.9
Fisherfaces	0.85	0.83	0.23	0.77	0.80
Eigenfaces	0.82	0.80	0.25	0.75	0.80

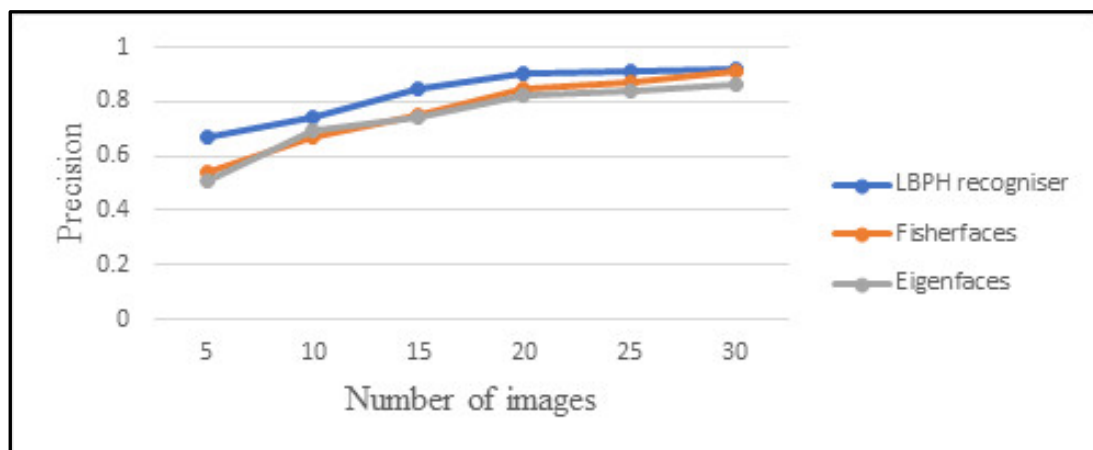


Fig. 9: Graph Precision Performance of Facial Recognition Algorithms

In addition, Fig. 10 shows a graph comparing the speed of processing against number of images per person for LBPH

algorithm. From Fig. 10, it can be seen that the processing time increases with increase in the number of images. Therefore,

the number of images per person in the system was chosen to be 20 since it yielded moderate processing time and produced a high precision value. Significantly, the performance recorded by LBPH on this

dataset points to the fact that this module was effective in recognising the registered faces in the system. Thus, it will contribute to the performance effectiveness of the system at large.

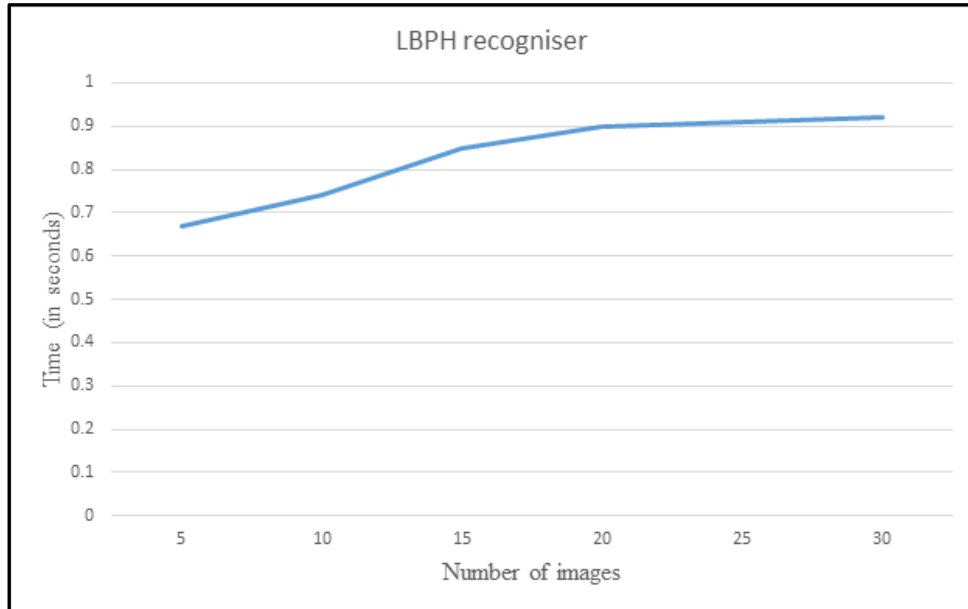


Fig. 10: graph of time against number of images for LBPH recognizer

Performance Evaluation of Face Detection

For the face detection module, the SSD algorithm was adopted and Table 3 is a Confusion matrix that shows the result of its performance evaluation. Again, the algorithm recorded precision and accuracy scores of 0.95 and 0.85 respectively. Going

by the precision and accuracy attained by deep learning of the face detection module and considering the small size of the dataset, it was obvious that the detection of faces by the systems is effective enough to detect faces in video footage. Above all, the performance of the module is expected to even increase for datasets with more facial records.

Table 3: Confusion Matrix for Deep Learning

		Actual Values	
Predicted Values		Positive	Negative
	Positive	19	3
	Negative	1	4

DISCUSSIONS

The proposed system provides security officials with an additional tool to promptly identify known criminals loitering in their environments. It is worth noting that uncovering criminals in semi-regulated

environments can be a difficult task. For illustration, the manual processes involved in pinpointing criminals when both known and unknown faces visit a place, consume time and human effort. The manual methods involve scanning through CCTV live cameras or recorded videos to identify

criminals. In addition, it is a common practice by physical security professionals to stack multiple layers of crime detection and prevention mechanisms. Therefore, it will be easy to integrate this crime prevention mechanism with existing access control measures to strengthen the security architecture of organisations operating in a semi-regulated environment.

Also, the criminal identification system generates alerts to notify security agents when a known criminal appears in an environment of interest. This notification module operates unobtrusively and criminals will not have any clue of impending actions on them. More so, the time taken to process facial data significantly reduces when the dataset increases. This suggests that the LBPH learns faster with the availability of more datasets. Correspondingly, the confusion matrix shows the impressive accuracies and precisions of the SSD and LBPH algorithms. Therefore, the system will flag criminals before they can execute their nefarious intents. The proposed criminal identification system benefits from the strengths of deep learning algorithms, and updating the system with more facial data is possible with backpropagation. Similarly, possessing digitised crime facts improves the storage and backup of information against sabotage and repudiation of crimes.

The operators of the criminal identification system must ensure the safety of facial records and other vital information about individuals. Any unnecessary disclosure or careless handling of records can jeopardise people's privacy. On the contrary, the system inherits the weaknesses of the deep learning algorithms on which it operates for precision and accuracy. For example, the identification system needs more computing resources to train the detection and identification modules as the number of facial records increases in capacity. Although, the cost implications of additional system resources are negligible compared to

the loss that criminals can bring to the assets and organisation's reputation.

CONCLUSION AND RECOMMENDATIONS

Security of lives and properties from criminal elements is essential in public and private places. As part of contributions to academic values, this study designed and developed a criminal identification system for a semi-regulated environment using SSD to detect faces and LBPH for facial recognition. Despite the few facial records commonly found in semi-regulated environments, the security system showed a high degree of accuracy in identifying known criminals' faces. Thus, social settings having few facial datasets could benefit from the system's adoption to maintain detailed information on criminals for future legal reference. Similarly, the proposed system will not only identify criminals, but it can also assist security officers in tracking individuals, thus creating a robust security system that could reduce the time spent by law enforcement agents in crime investigation. A limitation of the security system is that it encroaches on the data privacy of individuals in an environment since it tracks their facial records.

Moving forward, further research is needed to improve the efficacy and performance of the proposed system. Foremost, more research is required to develop more efficient and computationally inexpensive algorithms for handling facial recognition. Additionally, the design of a psychological-oriented module that can predict the likelihood of an unknown individual committing a crime is needed to complement the approach implemented in this study. Again, further research on privacy preservation is desirable to make the proposed system more acceptable in semi-regulated environments. Lastly, there is a need to integrate this system with the national citizen database to identify criminals and document the movement of other individuals in a semi-regulated

environment to foster comprehensive security coverage at the national level.

REFERENCES

- Aanchaladevi, T. S., Shubhangi, G. S., Ashwini, G. S., Mayuri, M. A., & Bankar, A. A. (2021). Criminal Identification by Using Real Time Image Processing. *International Journal of Research in Engineering and Science (IJRES)*, Vol. 9, No. 6, 37–42.
- Abdullah, N. A., Saidi, M. J., Rahman, N. H. A., Wen, C. C., & Hamid, I. R. A. (2017). *Face recognition for criminal identification: An implementation of principal component analysis for face recognition*. October, 020002. <https://doi.org/10.1063/1.5005335>
- Ahmad, A. H., Saon, S., Mahamad, A. K., Darujati, C., Mudjanarko, S. W., Nugroho, S. M. S., & Hariadi, M. (2021). Real Time Face Recognition of Video Surveillance System Using Haar Cascade Classifier. *Indonesian Journal of Electrical Engineering and Computer Science*, Vol. 21, No. 3, 1389–1399. <https://doi.org/10.11591/ijeecs.v21.i3.pp1389-1399>
- Alskeini, N. H., Thanh, K. N., Chandran, V., & Boles, W. (2018). Face recognition: Sparse representation vs. Deep learning. *ACM International Conference Proceeding Series*, 31–37. <https://doi.org/10.1145/3282286.3282291>
- Azeta, A. A., Omoregbe, N. A., Adewumi, A., & Oguntade, D. (2015). Design of a Face Recognition System for Security Control. *International Conference on African Development Issues (CU-ICADI) 2015: Information and Communication Technology Track*, 55–57.
- Baraka, A., Kataliko, S., & Digne, A. (2021). An Intelligent Criminal Detection System: A Case Study of Beni-town. *International Journal of Scientific and Research Publications*, Vol. 11, No. 11, 474–479. <https://doi.org/10.29322/IJSRP.11.11.2021.p11961>
- Chhoriya, P. (2019). *Automated Criminal Identification System using Face Detection and Recognition*, Vol. 06, No. 10, 910–914.
- Deeba, F., & Ahmed, A. (2019). LBPH-based Enhanced Real-Time Face Recognition. *International Journal of Advanced Computer Science and Applications*, Vol. 10, No. 5, 274–280.
- Du, B., Guo, X., & Chen, Y. (2018). Research on Face Recognition System based on Embedded Processor and Deep Neural Network. *ACM International Conference Proceeding Series*, 11–14. <https://doi.org/10.1145/3268866.3268880>
- Ganiyu, S. O., Olaniyi, O. M., Adebayo, O. S., & Daniel, A. T. (2020). Systematic Review of Facial recognition Algorithms and Approaches for Crime Investigations. *International Journal of Information Processing and Communication (IJIPC)*, Vol. 8, No. 1, 55–69.
- Gurav, A., Chevelwalla, A., Desai, S., & Sadhukhan, S. (2015). Criminal Face Recognition System. *International Journal of Engineering Research And*, Vol. V4, No. 03, 47–50. <https://doi.org/10.17577/ijertv4is030165>
- Halvi, S., Ramapur, N., Raja, K. B., & Prasad, S. (2017). Fusion Based Face Recognition System using 1D Transform Domains. *Procedia Computer Science*, 115, 383–390. <https://doi.org/10.1016/j.procs.2017.09.095>
- Jaturawat, P., & Phankokkrud, M. (2017). An evaluation of face recognition algorithms and accuracy based on video in unconstrained factors. *Proceedings - 6th IEEE International Conference on Control System, Computing and Engineering, ICCSCE 2016, November*, 240–244. <https://doi.org/10.1109/ICC>

- Kakkar, P., & Sharma, V. (2018). Criminal Identification System Using Face Detection and Recognition. *International Journal of Advanced Research in Computer and Communication Engineering*, Vol. 7, No. 3, 238–243. <https://doi.org/10.17148/IJARCCCE.2018.7346>
- Karimov, M. M., Ugli, I. S. Z., & Davronova, L. O. K. (2017). Problems in face recognition systems and their solving ways. *2017 International Conference on Information Science and Communications Technologies, ICISCT 2017, 2017-Decem*, 1–4. <https://doi.org/10.1109/ICISCT.2017.8188594>
- Kumar, P., Majeed, A., Pasha, F., & Sujith, A. (2020). Real-time Criminal Identification System Based on Face Recongnition. *Advanced Science Letters*, 26(05), 320–328.
- Kumar, V. D. A., Kumar, V. D. A., Malathi, S., Vengatesan, K., & Ramakrishnan, M. (2018). Facial Recognition System for Suspect Identification Using a Surveillance Camera. *Pattern Recognition and Image Analysis*, Vol. 28, No. 3, 410–420. <https://doi.org/10.1134/S1054661818030136>
- Liu, W., Anguelov, D., Erhan, D., Szegedy, C., Reed, S., Fu, C.-Y., & Berg, A. C. (2016). SSD: Single Shot MultiBox Detector. In *Lecture Notes in Computer Science (including subseries Lecture Notes in Artificial Intelligence and Lecture Notes in Bioinformatics): Vol. 9905 LNCS* (pp. 21–37). https://doi.org/10.1007/978-3-319-46448-0_2
- Malathi, R., & Jeberson Retna Raj, R. (2016). An Integrated Approach of Physical Biometric Authentication System. *Procedia Computer Science*, Vol. 85, No. Cms, 820–826. <https://doi.org/10.1016/j.procs.2016.05.271>
- Naik, A., Bakusala, R., Tiwari, S., Tiwari, T., Bhandari, P., & V, A. (2019). *Criminal identification using facial recognition*. Vol. 5, No. 3, 1936–1940.
- NBS. (2017). *Crime Statistics : Reported Offences by Type and State*.
- NBS. (2018). *Crime Statistics : Reported Offences by Type and State*.
- Nguyen, T., Lakshmanan, B., & Sheng, W. (2018). *A Smart Security System with Face Recognition*. December 2018. <https://doi.org/10.48550/arXiv.1812.09127>
- Oguntunde, P. E., Ojo, O. O., Okagbue, H. I., & Oguntunde, O. A. (2018). Analysis of selected crime data in Nigeria. *Data in Brief*, Vol. 19, 1242–1249. <https://doi.org/10.1016/j.dib.2018.05.143>
- Reddy, K. S. M. (2017). Comparison of Various Face Recognition Algorithms. *International Journal of Advanced Research in Science, Engineering and Technology*, Vol. 4, No. 2, 3357–3361.
- Saini, R., Saini, A., & Agarwal, D. (2014). Analysis of Different Face Recognition Algorithms. *International Journal of Engineering Research & Technology (IJERT)*, Vol. 3. No. 11, 1263–1268.
- Sanjay, T., & Priya, W. D. (2022). Criminal Identification System to Improve Accuracy of Face Recognition using Innovative CNN in Comparison with HAAR Cascade. *Journal of Pharmaceutical Negative Results*, Vol. 13, No. 4, 218–223. <https://doi.org/10.47750/pnr.2022.13.S03.023>
- Sarkar, R. R., & Prasad, G. N. R. (2022). Criminal Detection Using Face Recognition. *International Journal of Advanced Research in Computer and Communication Engineering*, Vol. 11, No. 4, 367–370. <https://doi.org/10.17148/IJARCCCE.2022.11466>
- Shepley, A. J. (2019). *Deep Learning For Face Recognition: A Critical Analysis*. <https://doi.org/10.48550/arXiv.1907.12739>
- Singh, S., & Prasad, S. V. A. V. (2018).

- Techniques and challenges of face recognition: A critical review. *Procedia Computer Science*, 143, 536–543. <https://doi.org/10.1016/j.procs.2018.10.427>
- Siregar, S. T. M., Syahputra, M. F., & Rahmat, R. F. (2018). Human face recognition using eigenface in cloud computing environment. *10th International Conference Numerical Analysis in Engineering*, 308(1). <https://doi.org/10.1088/1757-899X/308/1/012013>
- Sukhija, P., Behal, S., & Singh, P. (2016). Face Recognition System Using Genetic Algorithm. *Procedia Computer Science*, Vol. 85, No. Cms, 410–417. <https://doi.org/10.1016/j.procs.2016.05.183>
- Tela, G., Hiwarale, S., Dhawe, S., & Rathi, D. (2022). CNN Based Criminal Identification. *International Journal of Advanced Research in Science, Communication and Technology (IJARSCT)*, Vol. 2, No. 2, 239–246. <https://doi.org/10.48175/IJARSCT-3645>
- Tiwari, T., Tiwari, T., & Tiwary, S. (2015). Biometrics based user authentication. *Amercian Journal of Engineering Research*, 4(10) Vol. 4, No. 10, 148–159.
- Trigueros, D. S., Meng, L., & Hartnett, M. (2018). *Face Recognition: From Traditional to Deep Learning Methods*. <https://doi.org/10.48550/arXiv.1811.00116>
- Zafar, U., Ghafoor, M., Zia, T., Ahmed, G., Latif, A., Malik, K. R., & Sharif, A. M. (2019). Face recognition with Bayesian convolutional networks for robust surveillance systems. *Eurasip Journal on Image and Video Processing*, Vol. 2019, No. 1. <https://doi.org/10.1186/s13640-019-0406-y>

EXTRACTION OF ADHESIVE FROM GUILL AND PERR (*CISSUS POPULNEA*) FOR PARTICLEBOARD PRODUCTION USING RICE HUSK

*Aboje, A. A.¹; Akor, I. H. ¹; Uthman, H. ¹; & Bala, A.²

¹Chemical Engineering Department, Federal University of Technology, Minna, Nigeria

²Civil Engineering Department, Federal University of Technology, Minna, Nigeria

email: alen248@futminna.edu.ng

Abstract

*Preliminary analysis of the constituent materials of a particleboard shows that by replacement of its major constituent (urea formaldehyde and saw dust) with locally sourced material that has a pozzolanic effect can enable it to become more durable. Rice husk was found to possess some of these composite properties (cellulose, lignin and silica) which can therefore stand as better substitute if properly worked on. The study focuses on the extraction of organic adhesives from the Guill and Perr plant (*Cissus populnea*) for particleboard production using rice husk. The adhesive was extracted using a soxhlet apparatus at different operating conditions (temperature, extraction time and sample dosage) with an optimum temperature of 75 °C, and 40 g sample dosage at 90 minutes for fresh sample using Ethyl acetate as the extraction solvent. Proximate/elemental analysis of the extract shows a viscosity of 0.29 Pa.s, density of 1.25 g/cm³, 42.8 w/w % of carbon, ash content of 3.12 w/w %, protein of 5.56 w/w %, Fat content of 0.68 w/w %, fiber content 1.12 w/w % while an FTIR analysis of the extract shows the presence of carboxylic group at wave number of 1680.64 cm⁻¹. In this study, the method reported by Azumah (2014) from Shanghai Jinnan Import and Export Co. Ltd in line with the manufacturing process of particleboard was viewed under the following stages: Pre-treatment/Chip preparation stage, Drying and sizing stage, Adhesive regulating and applying stage. Others are: simulation and fabrication of Mould Stage, Forming and hot-pressing stage, Cooling and sizing stage and finally Characterisation stage. From the various particleboards produced, the result from the sample tagged J with 1:3 adhesive to rice husk ratio (wt. %) at 70°C within a pressing time of 10 minutes shows the best Modulus of Elasticity (410 N/mm²), Modulus of Rupture (19.04 N/mm²) with an average density of 1013kg/m³ and Scanning Electron Microscopy (SEM) showing the surface morphology and the level of compactedness between the adhesive and the aggregate proportion of rice husk used. This was compared with the conventional boards and it shows similar mechanical properties and met the LD-1 requirement of ANSI A208.1 Standards.*

Keywords: Adhesive, *Cissus Populnea*, Delignification, Particleboard, Rice husk

INTRODUCTION

The desire of mankind to have shelter and furniture requires construction materials; these construction materials can exist in various resources; ranging from stones to timber (Acharya *et al.*, 2011). To satisfy this craving of humanity, the quest for those resources sets in; this led to the use of substances that has the potential of being transformed into shelter and other furniture materials (Topbaşlı, 2013). Due to this change in trend of life patterning furniture

process, the demand for wood became high and led to deforestation (Indah *et al.*, 2018). In the last few decades, successful development and improvement of wood based composites panels (with the economic benefit of producing low cost wooden materials) has been a major alternative to solid wood usage (Mohanty *et al.*, 2015). The demand for composite wood products of various varieties like particleboard, plywood, hardboard, oriented standard board, medium density fiberboard and veneer board has equally increased

significantly throughout the world (Chen *et al.*, 2006, Awopetu *et al.*, 2019). In Modern industrial processes, particleboards are made mainly from selected particles bonded together with a thermosetting resin. Mostly used resins are formaldehyde based, that are usually produced from petrochemical raw materials (Yang *et al.*, 2007). The concept of substituting the fast depleting petrochemical raw material (formaldehyde) which are known to emit carcinogenic gases with other environmental friendly adhesive is always desired (Mohanty *et al.*, 2015). The binding agent in particleboard processing cannot be neglected, as it plays a vital role in its longevity and water permeability. The use of synthetic glue and other chemical bond pose a high cost of production on its processing (Jamaludin *et al.*, 2001, Owofadeju *et al.*, 2016). In this study, the extraction of adhesive from *Cissus populnea* (Okoho Plant) for particleboard production can be attributed to its high availability, low cost of extraction, binding ability, resistance to weathering and eco-friendly makes it a good substitute for phenol-formaldehyde resin and other conventional adhesives used. *Cissus Populnea* adhesive also called Guill and Perr, is a tropical climbing plant usually found in West Africa, particularly in Nigeria (Olutayo *et al.*, 2019). It belongs to the family of Amphilacaceae (Vitaceae). Adhesive, also known as glue, is any compound that adheres or binds particles together when applied to one surface or both surfaces, of two separate items and then resists their separation (Pike, 2013).

MATERIALS AND METHODS

The *Cissus populnea* used in this study were obtained from Inele Ugoh, Olamaboro local government of Kogi State. The rice husks were sourced from Gidan Kwano Village of

Niger State. More so, major reagents used include; Sodium hydroxide (NaOH) pellet - Burgoyne and Co, Hydrochloric acid (HCl) which were both bought from Ochala chemical store in Ankpa Kogi state, Nigeria. Ethyl acetate and distilled water chemistry department faculty of physical sciences Kogi State University Nigeria. All the reagents used are of analytical grade/standard.

A. Methods: Extraction of Adhesive

After getting all the required materials and equipment needed for the extraction of the adhesive, the barks of the fresh *Cissus populnea* stems obtained were scrapped off and chopped into smaller sizes (4-8 cm long) with an average weight of 0.2kg. The chopped sample was delignified by treating with 0.1M NaOH in a 10L plastic bowl at room temperature for 48 hours, after which samples were washed repeatedly with distilled water to neutralize the sample. After the delignification process, the sample was divided into two groups. The first group was oven dried and then pulverized into powdery form and a mesh sieve was used to obtain a particle size of 150 µm. The second group was blended using a laboratory blender to obtain a paste. After each group of the samples had undergone size reduction, the fresh samples were weighed out ranging from 30 g to 50 g respectively and then enclosed in a Muslin cloth. Likewise, the dried samples were also weighed out ranging from 30g to 50g respectively and enclosed with a Muslin cloth. Each of the enclosed

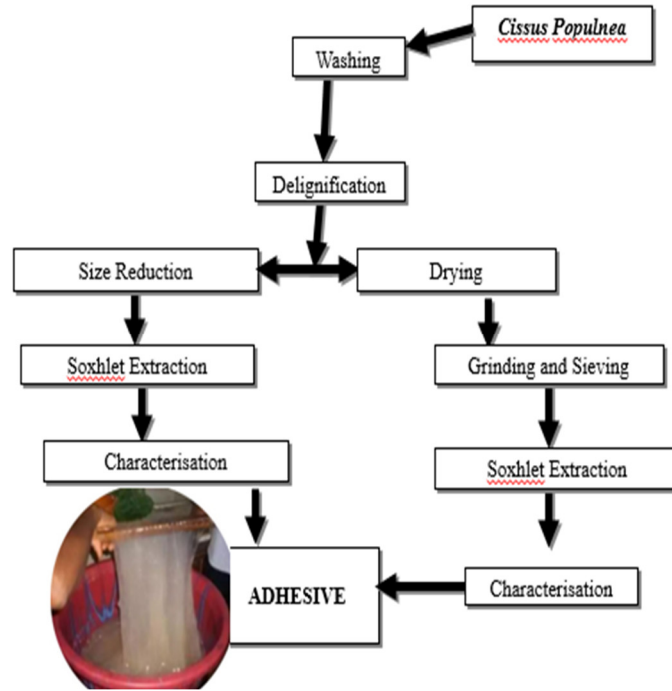


Fig. 1: Extraction process of Adhesive from *Cissus populnea*

samples was placed in the thimble of the soxhlet extractor and the operating conditions were varied, having a temperature range of 65°C to 85°C. More so, the operating time was varied from 30 minutes to 90 minutes respectively. Fig. 1 shows the process and Table 1 shows the variance of variable for response surface model used in the extraction process, comprising of the

lower, middle and upper limit for the extraction. A multiple regression analysis was done using Design Expert software 7.0 to obtain the model to this experimental data in order to get the fitted quadratic response model. A model equation in terms of actual factors including the non – significant terms for percentage yield, Y is given by the truncated second order polynomial equation:

$$Y = 81.88 + 0.6630A + 1.63B + 0.8670C - 0.2512AB - 0.3162AC + 1.42BC - 2.10A^2 + 0.4767B^2 - 7.05C^2 \quad (1)$$

where the extraction temperature is with coded value (A), the extraction time with

coded value (B), and the sample dosage with coded value (C)

Table 1: Variance of variable for response surface model the extraction

Factor	Lower	Middle	Upper
Temperature (°C)	65	75	85
Extraction time (Min)	30	60	90
Amount (wt %)	30	40	50

B. Production of Particleboard

In this study, the method reported by Azumah, (2014) from Shanghai Jinnan Import and Export Co. Ltd in line with the manufacturing process of particleboard was viewed under the following stages (Fig. 2): Pre-treatment/Chip preparation stage, Drying and sizing stage, adhesive regulating and applying stage, Simulation and fabrication of Mould Stage, Forming and hot- pressing stage, Cooling and sizing stage, Analysis/Characterization (quality check). Upon obtaining adequate amount of the rice husk, stones and other materials were handpicked from the samples. Distilled water was used to wash and remove remnants of impurities from the samples.

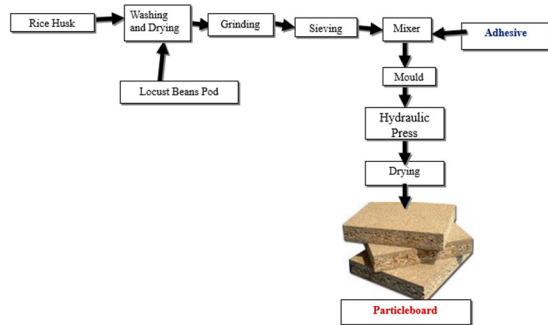


Fig. 2: Particleboard production process

Table 2: Variance of variable for response surface model for particleboard

Factor	lower	centre	Upper
Temperature ($^{\circ}\text{C}$)	60	70	80
Pressing time (Min)	5	10	15
Adhesive to Feed stock Ratio (wt %)	1:3	1:6	1:9

From the prepared mixture of feed stock and adhesive after completion of mould, aggregate proportion of the mixture were properly poured into the mould as relative heat was applied. This was done in accordance with the result obtained from the Response Surface Methodology via composite design expert. This comprises of

After a series of washing, the rice husk was dried. This was carried out using an electrical oven, at 80°C for 8 hours. After the drying comes the sizing stage; when the desirable size was obtained after the crushing, a particle size of $150\mu\text{m}$ was obtained by sieving, Loh *et al.*, (2010) reported similar particle size of rice husk in particleboard production. The American National Standard for Particleboard (ANSI, 2009), classifies particleboard by physical, mechanical and dimensional characteristics as well as adhesive/binder levels. In particleboard production, the ratio of adhesive to feed stock used plays a very important role in meeting up to the regulatory standard. In this research, the ratio for adhesive to feed stock was optimized to know the optimum condition where the best yield will be produced. This was obtained through Response Surface Methodology using the design expert software. Table 2 show the variance of variable for response surface model used in the particle board production.

Rice Husk to Adhesive ratio, taking into consideration the temperature of the pressing and time spent during the pressing respectively. In place of the electric hot-pressing machine, the electrical hot plate was used varying the temperature from 60°C to 80°C , applying pressure from both ends of the mould using bolts and Nuts. The cooling

was done after the forming and hot-pressing stage, to allow the particle board cools off as it dried out. This was done to reduce the heat content of the particleboard. After the cooling process came the sizing of the particle board. This was done by trimming out the extruded edges and area of improper alignment as a result of the compression/pressure applied during the hot-press process. An emery paper was used to remove such areas of default.

C Analysis on Adhesive

In this research several characteristic tests (ash content, moisture content, protein content, lipid content, crude fibre, carbohydrate content, Viscosity, pH) were performed on the adhesive extracted in accordance with Association of Official Analytical Chemistry method (AOAC, 1990) on the performance of an adhesive. More so, instrumental analysis like Fourier transforms infrared (FTIR) was carried out to know the presences of functional groups in the samples at respective wave number using the Infrared Spectrophotometer.

D Analysis on Particleboard

In this research, several characteristic tests were performed on the particleboard produced in accordance with the German Institute for Standardization of particleboard (DIN EN 312, 2010), which requires three main standard tests. These standard tests carried out on the produced particleboards are: Modulus of Elasticity (MOE), Modulus of Rupture (MOR) and the swelling in thickness test. These tests were necessary to ascertain if the panels satisfy the minimum required values of MOR, and swelling in thickness due to moisture absorption. The DIN EN 312 particleboard requirement is equivalent to the American National Standard A208.12009 (CPA, 2009) for wood particleboard classes M-2 and M-3 (Li *et al.*,

2010). Modulus of rupture (MOR) is a measure of the ability of a sample to resist a transverse (bending) force perpendicular to its longitudinal axis. The bending strength of each test piece was calculated from the formula show below.

$$\text{MOR} = \frac{3 f_{\max} L_1}{2bt^2} \quad (2)$$

where: f_{\max} is the maximum load, L_1 is the distance between the centers of the supports, in millimeters, b is the width of the test piece in millimeters, and t is the thickness of the test piece in millimeters. In accordance with DIN EN 312, Internal Bond Strength of a sample is the ability of the material to withstand internal stress within the sample in relation to its adhesive bond. Internal Bond Strength of a sample generally correlates with the density in the panel core. This was investigated by using Instron machine to compress the sample to determine the IB strength. The MOE of a material show the extent to which a material can be stretched before yielding or breaking. In accordance with DIN EN 312, this was done using the Instron machine. The modules of elasticity of each test piece were calculated from the formula below:

$$\text{MOE} = \frac{f_{\max} L_1 \cdot 3}{4bdt^3} \quad (3)$$

where d is the deformation occurring against the load. The water absorption test was conducted to determine the rate of water penetration into the sample which will in turn result in physical change in samples dimension. In accordance with the DIN EN 312, the weight of each sample were carefully measured out after which, they were submerged in the distilled water after taking their measurements at room temperature for 12 hours to determine long term water resistance properties,

respectively. The samples were taken out and surfaces were dried using a clean dry cloth after going through an immersion process. They were weighed again for every 4 hours until a constant weight was obtained. Water absorption at time (t) was calculated as follows:

RESULTS AND DISCUSSION

A. Analysis on the Feed Stock

The proximate compositions of the feed stock (rice husk) is presented in Table 3. The Ash contents and Moisture contents of the sample were 26.18 and 4.55 % w/w respectively. These values compare favorably with those reported by Cuthbert (2014), although it is slightly less than the range, 26.20 % as reported by Cuthbert (2014). It is also slightly greater than the 18.5 % reported by Anbu et al. (2009)

$$W.A(t) = \frac{(W_f(t) - W_0)}{W_0} \times 100 \quad (4)$$

where: $W.A(t)$ is the water absorption (%) at time t , W_0 is the initial weight, $W_f(t)$ is the weight of the samples at a given immersion time, t . The surface morphology of the samples was observed using SEM machine, this was carried out to check the surface morphology of the samples. Moderate resolution scanning electron microscope (SEM) of JEOL JSM – 630 models was used to study the morphology of the samples. More so, other physical and mechanical tests were carried out including: Moisture content test, Particleboard density, Water absorption test. This was done in accordance to ANSI A208.1-2009, an American Standard of Testing and Methods (ASTM) which were compared with the minimum required for particleboard production by the norm of these Standards Institute. Particle board Morphology Characterization using SEM was also carried out on the sample to analyze the sample surface morphology and compatibility.

Table 3: Proximate Analysis of rice husk

Composition	Experimental % Composition	Anbu <i>et al.</i> (2009) % Composition	Cuthbert, (2014) % Composition
Ash	26.18	18.15	26.20
Moisture	4.55	10.40	8.80
Volatile Matter	52.38	54.10	59.20
Fixed Carbon	8.04	10.35	14.60

B. Extraction Yield of Adhesive

After the delignification and the extraction of Adhesive from *Cissus populnea* plant, the percentage yield from both the dried and the fresh samples was calculated as shown in Table 4 using ethyl acetate as the extraction solvent. The Model F-value of 13.59 as seen in Table 5 implies the model is significant. There is only a 0.52% chance that an F-value

this large could occur due to noise. P-values less than 0.0500 indicate model terms are significant. In this case B, BC, C² are significant model terms. Values greater than 0.1000 indicate the model terms are not significant. If there are many insignificant model terms (not counting those required to support hierarchy), model reduction may

improve the model. From Table 5, the optimum yield from the fresh sample was obtained at the sample dosage of 40g (highest point) and 50g (lowest point).

Likewise, the optimum yield from the dried sample were obtained at the sample dosage of 40g (highest point) and 50g (lowest point) respectively.

Table 4: Extraction Response using Ethyl Acetate

Std	Run	Temperature (°C)	Time (Minutes)	Amount (g)	Fresh Sample (Wt. %)	Dried Sample (Wt. %)
6	1	85.00	30.00	50.00	70.80	60.00
5	2	65.00	30.00	50.00	70.40	65.20
13	3	75.00	60.00	30.00	72.00	71.33
4	4	85.00	90.00	30.00	73.33	70.00
12	5	75.00	90.00	40.00	84.15	72.00
7	6	65.00	90.00	50.00	76.40	66.80
2	7	85.00	30.00	30.00	74.00	70.00
3	8	65.00	90.00	30.00	72.67	66.67
8	9	85.00	90.00	50.00	76.80	68.40
11	10	75.00	30.00	40.00	80.50	67.50
15	11	75.00	60.00	40.00	82.00	68.50
9	12	65.00	60.00	40.00	78.50	66.50
1	13	65.00	30.00	30.00	71.33	67.33
14	14	75.00	60.00	50.00	77.60	67.20
10	15	85.00	60.00	40.00	81.00	65.00

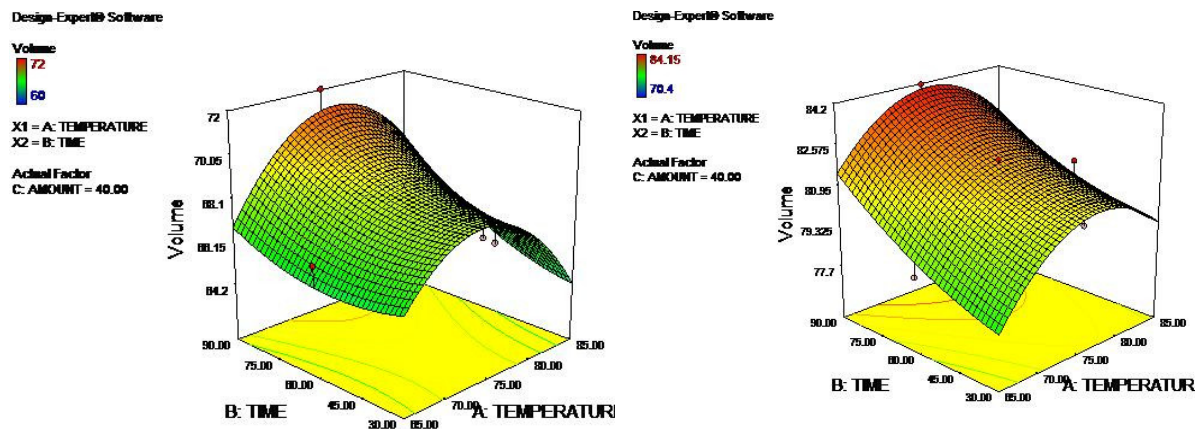
These results obtained can be attributed to the effects of the process variables, such as; Temperature and extraction time. Fig. 3 shows the effect of process variables on the extraction yield using Response surface methodology. From the result, it can be seen that the maximum yield of 84% was obtained at 75°C with 40g sample dosage at 90mins for fresh sample using Ethyl acetate

as the extraction solvent. While the minimum yield of 60% was obtained at 85°C with 50g sample dosage at 30mins from dried sample using Ethyl acetate as extraction solvent. This shows that fresh samples give higher yield of extract than the dried samples and shows a good extraction process variable to use in the extraction technique.

Table 5: Analysis of Variance for the Response Surface Model

Source	Sum of Squares	Df	Mean Square	f-Value	p-Value	
Model	264.74	9	29.42	13.59	0.0052	significant
A-Temperature	4.40	1	4.40	2.03	0.2134	
B-Time	26.63	1	26.63	12.31	0.0171	
C-Amount	7.52	1	7.52	3.47	0.1214	
AB	0.5050	1	0.5050	0.2333	0.6495	
AC	0.8001	1	0.8001	0.3697	0.5697	
BC	16.05	1	16.05	7.41	0.0416	
A ²	11.32	1	11.32	5.23	0.0709	
B ²	0.5843	1	0.5843	0.2700	0.6255	
C ²	127.75	1	127.75	59.02	0.0006	
Residual	10.82	5	2.16			
Cor Total	275.56	14				

$$SD = 0.47 \quad R^2 = 0.997 \quad Adj R^2 = 0.9800 \quad Pred R^2 = 0.892$$

**Fig. 3:** Response using Ethyl acetate for dried and fresh sample

C. Analysis on Adhesive

Proximate analysis on the Adhesive shows how effective the extraction process was. This can be seen in Table 6. From the result obtained, the Ash, Moisture, Protein, Fat, Fibre and carbohydrate content of the adhesive were: 3.12 %, 12.74 %, 5.56%,

0.68 %, 1.12% and 76.78 % w/w respectively. Hanninen *et al.* (2020) have shown that the bonding strength decreases when the moisture content is increased above 20%. The carbohydrate content of the adhesive is slightly less than the values reported by Olutayo *et al.* (2019) and Oyedemi (2012), ranging from 82.31-

87.81% w/w. The ash content of the adhesive was slightly higher than that of Oyedemi, (2012) but lower than the value reported by Olutayo et al., (2019). The FTIR spectrum of the extract is shown in Fig. 4. The finger print region of the spectrum consists of characteristic peaks between 800 and 3400 per cm; these peaks are attributed to the C-N stretching, the C-O bond stretching, the OH stretching, N-H bond stretching and C-H bond stretching respectively, as reported by Azeez and Onukwuli (2019) in their study. The pH values of the adhesive as recorded Table 7, is 6.5. This pH values as compared with the other adhesive that have been reported in literature is within the range. Iwe *et al.*

(2004) reported Cissus extracted with the aid of edible starch has a pH value of 6.49 while the pH of the polyamine – adhesives formulated with mucuna and African yam bean were 6.3 and 5.5 respectively Owofadeju and Alawode (2016). pH is critical for determining the product shelf life from the view point of microbiological degradation of sensitive ingredients. Preservation of Cissus extract could be by acidification and mild heating (Iwe *et al.*, 2004). The differences in the pH could be due to solute hydration, physicochemical environment and thermodynamic properties of the system.

Table 6: Proximate Analysis of Adhesive

Composition	Experimental % Composition	Achikanu and Ani (2020) % Composition
Ash	3.12	4.61
Moisture	12.74	2.67
Protein	5.56	1.49
Fat content	0.68	13.07
Fiber Content	1.12	22.13
Carbohydrate content	76.78	56.04

Table 7: Physiochemical Analysis of Adhesive

Composition	Unit	Experimental Value	Iwe <i>et al.</i> (2004)	Oyedemi, (2012)
pH	-	6.5	6.4	6.8
Specific Gravity	-	1.25	1.25	-
Viscosity	Pa.s	0.294	0.24	0.26
Density	g/cm ³	1.25	1.25	-

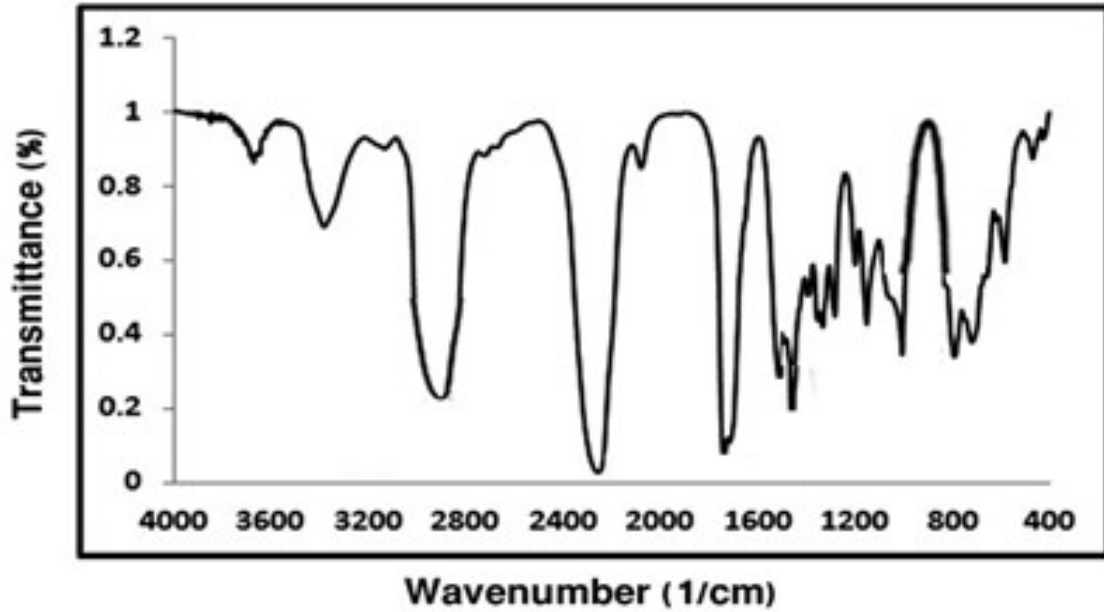


Fig. 4: FT-IR Spectrum of *Cissus Populnea* Adhesive

D. Analysis on Particleboard

From the particleboard produced, it was observed that some of the products were found to be inappropriate (twisted, Cracked and bent) while others appeared appropriate. This is as a result of the different mixing ratio, temperature applied and pressing time applied. From the result (Table 8), product with high dosage of Locust Beans Pod tends to twist more at high temperature compared to others. More so, the highest number of cracked products was observed from the 50-50% mixing at low adhesive ratio.

Appropriate and moderate products were obtained at high adhesive ratio, low temperature, high rice husk to locust beans Pod dosage and moderate pressing time. From the result, it can be seen that the adhesive ratio plays a very important role in the resistance to stress property of the particleboard. Compared with literature, Azumah (2014) recorded its highest bending mean stress at a high adhesive ratio. More so, the effect of the pressing temperature can also be seen as higher temperature weakens the adhesive bonding capacity thus reducing its bending stress. The water content of each

Table 8: Produced particleboard with varying process parameters.

Rice Husk (wt. %)	Locust Beans Pod (wt. %)	Gum to Feed stock Ratio (wt. %)	Pressing Temperature (⁰C)	Pressing Time (Min.)	Product Tag
25	75	6	70	10	A
50	50	9	60	15	B
75	25	3	80	5	C
100	0	6	70	10	D
50	50	6	70	10	E
75	25	9	60	5	F
100	0	3	80	15	G
100	0	9	60	10	H
50	50	9	80	5	I
75	25	3	70	10	J
50	50	6	60	15	K
75	25	9	80	5	L
50	50	3	70	5	M
75	25	6	60	15	N
100	0	9	80	5	O
75	25	3	60	10	P
25	75	9	70	5	Q
50	50	3	60	15	R
75	25	6	80	5	S
100	0	9	70	10	T

of the samples was determined using the equation reported by Huang & Li (2016). Tests were carried out to determine the moisture content, Modulus of Elasticity (MOE), water absorption, swelling in thickness, Modulus of rupture (MOR) and density of the particle board produced. The results of the test are presented in Table 9. The results for the moisture content, swelling in thickness, MOR and MOE are also presented in the form of histograms in Figs. 5 - 8 for better comparison. It was

observed that the Particleboard with the highest amount of Moisture content was obtained from the particleboard containing high quantity of rice husk to adhesive ratio at low temperature and pressing time. While the lowest Moisture content was obtained from particleboards that contain higher amount of Adhesive to rice husk ratio at high temperature and pressing time. Hence, this shows that production temperature affects the moisture content of a sample. The higher

Table 9: Mechanical and Physical Properties of Produced Particleboard

Product Tag	Moisture content (wt. %)	MOE (N/mm²)	Water Absorption (%)	Swelling in thickness (%)	MOR (N/mm²)	Density (Kg/m³)
A	2.38	230	4.65	3.33	10.67	1147
B	5.26	191	10.00	6.67	8.86	1067
C	8.33	333	12.82	13.33	15.47	1040
D	11.76	272	13.16	16.67	12.62	1013
E	5.41	210	10.26	10.00	9.73	1040
F	8.57	320	10.53	6.67	14.83	1013
G	8.82	233	13.51	13.20	10.79	987
H	12.50	360	13.89	17.27	16.71	960
I	8.11	250	7.50	7.33	11.62	1067
J	8.57	410	10.53	12.93	19.04	1013
K	5.26	206	7.50	5.73	9.55	1067
L	8.82	344	13.51	12.20	15.95	987
M	5.41	176	10.26	7.27	8.16	1040
N	5.56	409	10.53	12.00	18.99	1013
O	8.82	304	16.22	19.67	14.09	987
P	8.33	360	7.69	12.67	16.68	1040
Q	2.38	230	7.14	4.00	10.67	1120
R	5.26	191	7.50	6.67	8.86	1067
S	8.33	333	10.53	10.40	15.47	1013
T	11.76	272	13.89	17.33	12.62	960

the temperature the lower the moisture content of the sample, while the lower the temperature the higher the moisture content recorded. More so, it shows that rice husk is more hydrophilic than the adhesive. This is attributed to the fact that the absorption capacity of water is higher than that of the adhesive owing to the fact that carbon-hydrogen ratio is dominant (starch). This result is similar to that reported by Azumah (2014). From the standard equation for calculating the density (ρ) of a material as a ratio of its mass to the volume occupied, the

density was evaluated from its uniform volume (75cm³) and varying masses ranging from 72-86g respectively. It was observed that sample Q had the highest density at 1120 Kg/m³, which was obtained from the particleboard containing highest quantity of rice husk to adhesive ratio. The Modulus of elasticity (MOE) is an evaluation of the flexibility characteristics of a sample. In this paper, the optimum MOE was achieved with sample J, which also recorded the highest MOR. This shows that modulus of rupture (MOR) and MOE are somehow linked with

respect to the mechanical property of the material. Also, the result of the Termite resistivity test (TRT) showed that the best result was obtained with samples that have high adhesive dosage and it decreased with reduction of the adhesive. Fig. 9 shows samples of the produced particle board. The surface morphology of the sample was observed using SEM machine. From Fig. 10 we can deduce the binding interaction

between the adhesive and the feed stock. The binding capacity of an adhesive used in particleboard production contributes to mechanical properties and also water permeability of the product. From the result, an average distribution of the adhesive is seen and region around the right corner of the result shows lower distribution of adhesive as compared to other region.

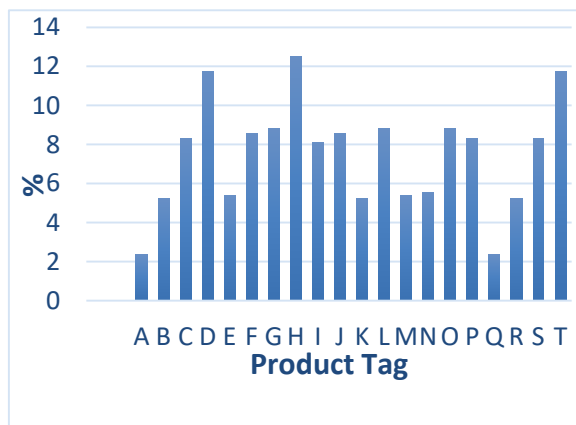


Fig. 5: Moisture content (wt.%)

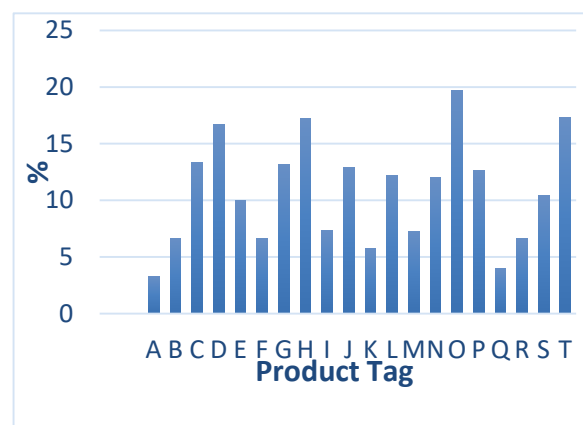


Fig. 6: Swelling in thickness (%)

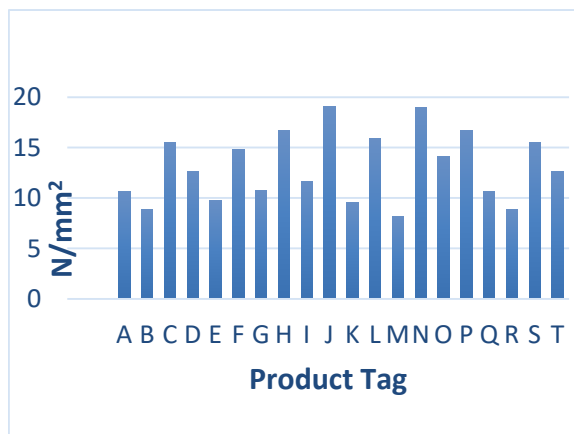


Fig. 7: MOR (N/mm²)

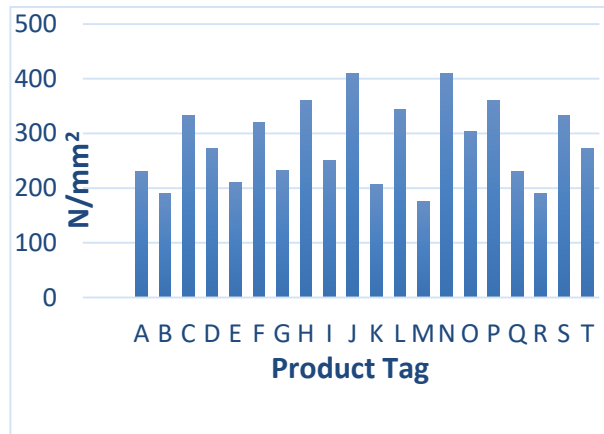


Fig. 8: MOE (N/mm²)



Fig. 9: Samples of produced Particleboard

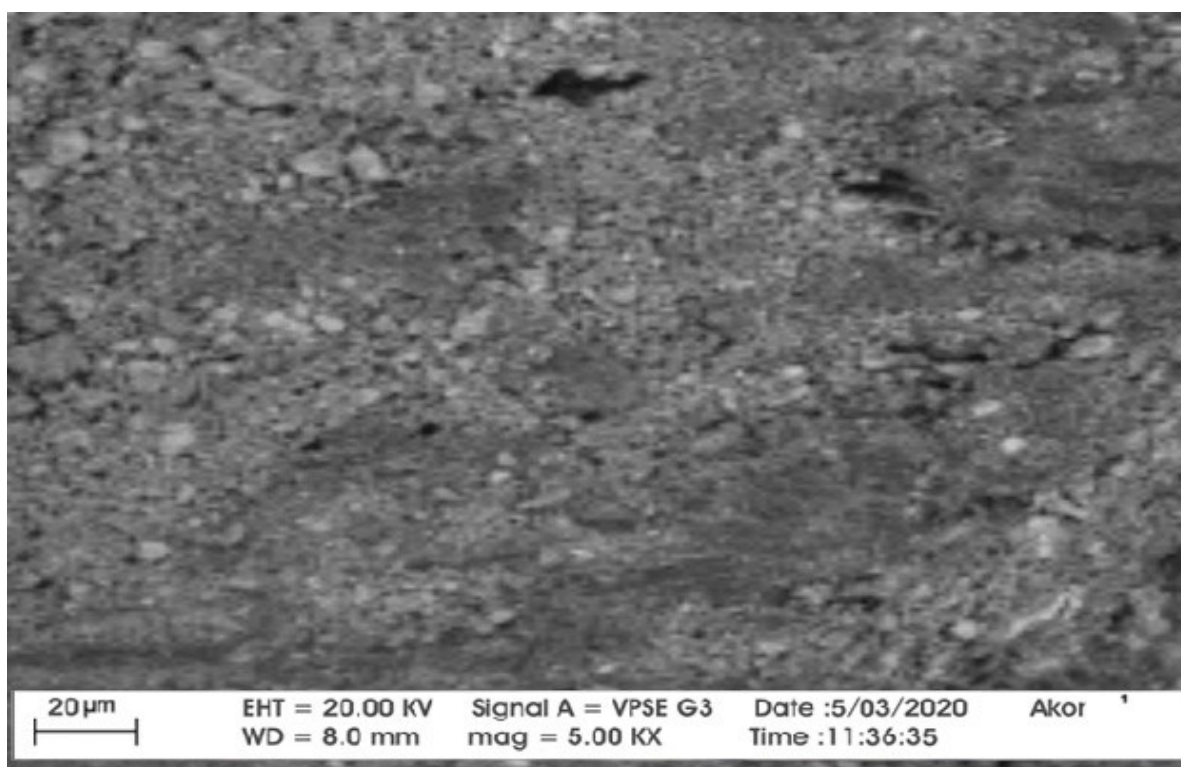


Fig. 10: SEM morphology of Particleboard

CONCLUSION

In the study, the following conclusions were drawn: The Adhesive was successfully extracted from *Cissus populnea* plant studying the effect of process parameters via RSM and the optimum yield (84%) was obtained at 75°C with 40g sample dosage at 90mins for fresh sample, while the lowest yield (60%) was obtained at 85°C with 50g

sample dosage at 30mins from dried sample using Ethyl acetate as extraction solvent respectively. Comparative study on the yield of the Adhesive obtained from different Samples (fresh and dried) shows higher percentage of adhesive in fresh sample to dried sample. The analysis of the sample using Fourier Transform Infrared Spectroscopy (FT-IR) shows the presence of carboxylic group in the substance at similar

stretching with literature. The result of the analysis of the particleboard indicated that sample J has the best MOE of 410 N/mm², MOR of 19.04 N/mm², with an average density of 1013kg/m³ respectively. Hence, the particleboard produced shows similar mechanical and physiochemical properties with the conventional boards and its mechanical properties met the LD-1 requirement of ANSI A208.1 Standards.

ACKNOWLEDGEMENT

The authors would like to acknowledge support from Mr. Bulus B. Musa of Water Resources, Aquaculture and Fisheries Technology Department Federal University of technology Minna for his Laboratory guidance and Mr. Clement O. of Shestco chemical Advance laboratory Sheda Abuja, for the technical assistance they rendered during the analysis. The authors also express their sincere gratitude to the Department of Chemical Engineering, Federal University of technology Minna for the technological know-how and to Mr. Ochala A. of Chemistry Department Kogi State University Nigeria, for the technical support and laboratory assistance rendered.

REFERENCES

- Achikanu, C. and Ani, O. N. (2020). Nutritional and Phytochemical Content of *Cissus populnea* (Okoho) Stem Bark. Biology. DOI:10.9734/ajrb/2020/v7i330139 Corpus ID: 225292804.
- Awopetu, O. O. and Hassan, B. B. (2019). Production and Characterization of Particleboards from Common Agrowastes in Nigeria. *International Journal of Innovative Science and Research Technology*, 4(1).
- Azeez, T.O.; Onukwuli, O. D. and Chukwudi, M. M. (2018). Mechanical properties of lignocellulosic fibers (saw dust, rice husk and okpa seed husk) reinforced waste and virgin polyethylene. *Pakistan Journal of Scientific and Industrial Research* 61A(1):28 - 33.
- Acharya, S. K.; Mishra, P., & Mehar, S. K. (2011). Effect of surface treatment on the mechanical properties of bagasse fiber reinforced polymer composite. *BioResources*, 6(3), 3155–3165.
- Anbu, C. J.; Dato, Y. B. & Nordin, B. Y. (2009). Particleboards from Rice Husk. A Brief Introduction to Renewable Materials of Construction.
- ANSI. (2009). American National Standards Institute, A208.1-2009, Composite Panel Association, 19465 Deerfield Avenue, Suite 306, Leesburg, VA 20176, USA.
- AOAC. (1990). Association of Official Analytical Chemistry. Official Methods of AOAC International, 14th Edition, Gaithersberg, MD, USA.
- Azumah, O. K. (2014). Production of Particleboard Using Sawdust and Plastic Waste. Kwame Nkrumah University of Science and Technology College of Agriculture and Natural Resources Faculty of Renewable Natural Resources, Department of Wood Science and Technology.
- Chen, H. C.; Chen, T. Y. & Hsu, C. H. (2006). Effects of wood particle size and mixing ratios of HDPE on the properties of the composites. *Holz Roh Werkst*, 64, 172–177.
- Cuthbert, M. F. (2014). Analysis of energy characteristics of rice and coffee husks

- blends. International Scholarly Research Notices.
- DIN EN 312. (2010). German Institute for Standardization. Particleboards and fibreboards Specifications.
- Hanninen, T.; Rautkari, L.; Hautamaki, L., & Altgen, M. (2020). The effect of diammonium phosphate and sodium silicate on the adhesion and fire properties of birch veneer. *Holzforschung*, 74(4), 372–381.
- Huang, J., & Li, K. (2016). Development and characterization of a formaldehyde-free adhesive from lupine flour, glycerol, and a novel curing agent for particleboard (PB) production. *Holzforschung*, 70(10), 927–935.
- Indah, R.; Nurfika, R.; Karim, A. & Musrizal, M. (2018). Modifying Of Particle Boards From Rice Husk and Pinus Merkusii Sawdust And Using Soybean Waste Waters Based Adhesive. 2nd International Conference on Science (ICOS), Makassar, Indonesia, 279.
- Iwe, M. O.; Obaje, P. O., & Akpapunam, M. A. (2004). Physicochemical Properties of Cissus Gum Powder extracted with the aid of Edible Starches. *Plant Foods for Human Nutrition*, 59, 161–168.
- Jamaludin, K.; Jalil, H. A.; Jalaludin, H.; Zaidon, A. A.; Latif, M. M., & Nor, M. Y. (2001). Properties of Particleboard Manufactured from Commonly Utilized Malaysian Bamboo. *Pertanika J. Trop. Agric. Sci*, 24(2), 151–157.
- Li, X.; Cai, Z.; Winandy, J. E., & Basta, A. H. (2010). Selected properties of particleboard panels manufactured from rice straws of different geometries. *Bioresource Technology*, 101(12), 4662–4666.
- Loh, Y. W.; H'ng, P. S.; Lee, S. H.; Lum, W. C. & Tan, C. K. (2010). Properties of Particleboard Produced from Admixture of Rubberwood and Mahang Species. *Asian Journal of Applied Sciences*, 3, 310–316.
- Mohanty, B. N.; Sujatha, D. & Uday, D. N. (2015). Bamboo Composite material: Game - changer for developing economies. 10th World Bamboo Congress, Korea 2015.
- Olutayo, A. A.; Mbang, N. F.; Michael, A. O., & Tolulope, O. A. (2019). Evaluation of Cissus populnea gum as a directly compressible matrix system for tramadol hydrochloride extended-release tablet. Department of Pharmaceutics and Pharmaceutical Technology, Olabisi Onabanjo University, Ago Iwoye, Nigeria.
- Owofadeju, F. K. & Alawode, A. O. (2016). Evaluation of Vetiver (*Vetiveria nigriflora*) plant extract as eco-friendly wood preservative. *Arid Zone Journal of Engineering, Technology and Environment*, 12, 49–57.
- Oyedemi, T. I. (2012). Characterization of Fuel Briquettes from Gmelina Arborea (Roxb) Sawdust and Maize Cob Particles Using Cissus Populnea Gum as Binder. Department of Agricultural and Environmental Engineering, University of Ibadan, Nigeria.
- Pike, R. (2013). Adhesive. *Encyclopædia Britannica Online*. Encyclopædia Britannica Inc. Retrieved 9 April, 2021.
- Topbaşlı, B. (2013). The examination of mechanical and physical properties of particleboard produced from waste

banana peel. Institute of Science,
Süleyman Demirel University, Isparta,
Turkey.

Yang, T. H.; Lin, C. J.; wang, S. Y. & Tsai,
M. J. (2007). Characteristics of

particleboard made from recycled
wood-waste chips impregnated with
phenol formaldehyde resin. *Building
and Environment*, 42(1), 189–195.

INVESTIGATING THE PERFORMANCE OF FULL DEPTH RECLAIMED SURFACE-DRESSED PAVEMENT TREATED WITH CEMENT AND CALCIUM CARBIDE RESIDUE AS ROAD BASE

*Alhassan, M.¹; Alhaji, M. M.²; & Saidu, A. E.³

^{1,2}Civil Engineering Department, Federal University of Technology, Minna, Nigeria

³Niger State Ministry of Works and Infrastructural Development

*alhassankuta@futminna.edu.ng (Corresponding author)

Abstract

Investigation of performance of Full Depth Reclaimed Surface-dressed Pavement (FDRSP), treated with cement and Calcium Carbide Residue (CCR) as road base was undertaken. Wearing and base courses of a surface-dressed road was scarified and mixed to form the FDRSP, which was found to consist of 28.7 % Reclaimed Surface-dressed Pavement (RSP) and 71.3% soil from the natural base course. Laboratory tests were carried out to determine the most optimal of FDRSP/cement/CCR that will give a California Bearing Ratio (CBR) value of 150%, required for heavy traffic roads. The results showed that the original base course material of the road classified under A-2-5, but when mixed with Reclaimed Surface-dressed Pavement (RSP), the resulting material (FDRSP) classified under A-2-4 according to AASHTO soil classification system. 2% cement and 4% CCR, added to the FDRSP, satisfied the 150% CBR required for heavy traffic roads. From laboratory and field test results of the FDRSP/cement/CCR composites, soaking did not have adverse effect on the strength.

Keywords: Calcium carbide residue, California Bearing Ratio, Density, Reclaimed surface-dressed pavement, Stabilization, Road base.

INTRODUCTION

The rate of depletion of deposits of natural resources has become a global concern. This has prompted the concept of ‘use and reuse’ of these resources, which is an aspect of the globally known concept of ‘Sustainable Development Goals’. Some of the deposits under this threat are those of lateritic soils. Good lateritic soil deposits were initially thought to be inexhaustible, but the current situation (especially in Minna, the capital city of Niger state and environs) have shown otherwise. Lateritic soil has been extensively used as sub-grade, sub-base and base courses for low to medium trafficked roads in Nigeria (Amu *et al.* 2010) and some other countries, where their deposit exists (Alhaji *et al.*, 2019). Some of these soils performed well when used as sub-base and base course materials for roads, while others have been observed to fall short of the specifications for them to be used as such (Aginam *et al.*, 2014; Oghenero *et al.*, 2014 and Alhaji *et al.*,

2014). In the later situation, the engineering properties of such soils are improved (Alhassan and Alhaji, 2007; Mu’azu, 2007; Osinubi *et al.*, 2007; Alhassan, 2008a; Alhassan, 2008b; Osinubi and Mustapha, 2009; Eberemu *et al.*, 2012; Sultan and Guo, 2016; Horpibulsuk *et al.*, 2017; Alhaji and Alhassan, 2018, Suleiman *et al.*, 2020 and Kanko *et al.*, 2020) to make them fit for the intended use.

In most cases, lateritic soil materials that were initially found to be good for use as road bases become deteriorated with age while in service or during routine maintenance/reconstruction work. In such instances, and considering the current global trend, such materials are now being recycled and reused, thanks to utilisation of recycling/improvement techniques, using locally available and cheap additives. An example of these recycling/improvement techniques is the use of reclaimed pavement surface materials (eg Reclaimed Asphalt Pavement - RAP). In recent past, studies

have been carried out on the possibility of using RAP for road pavement structures.

Mohammad *et al.* (2003) investigated the potential use of foamed asphalt treated RAP as a base course material instead of crushed limestone base and concluded that the foam asphalt showed higher in-situ stiffness than limestone base. In an attempt to reuse aged asphalt surface, Gregory and Halsted (2007), used Full Depth Reclamation (FDR) of RAP and the existing base and sub-base materials, mixed with small amount of cement to form new road base material that was considered excellent.

Edeh *et al.* (2012) investigated the possibility of using reclaimed asphalt pavement-lime stabilized clay as a highway pavement material, and obtained an unsoaked CBR of 36.56% and a 24hours soaked CBR of 34.23%, concluding that the material could be used for sub-grade and sub-base courses. A study aimed at increasing strength and reducing creep of RAP, by adding high quality aggregate and/or adding chemical stabilizer was carried out by Bleakley and Cosentino (2013), using Limerock Bearing Ratio (LBR) and creep tests to evaluate the strength and creep of the mixture respectively. Ochepo (2014) stabilized deficient lateritic soil using RAP and Sugarcane Bagasse Ash (SCBA) for pavement construction, and observed that the soil, stabilized with 6 and 8% SCBA gave a CBR value that was sufficient for the mixture to be used as subgrade and sub-base courses for road, while that treated with 10% SCBA gave CBR value that was sufficient for the mixture to be used as base course material.

Alhaji *et al.* (2014) worked on possible stabilization of A-6 lateritic soil using RAP without any chemical admixture, and reported minimal increase in Unconfined Compressive Strength (UCS) from 346kN/m² for the natural soil to 384 kN/m² at 40% soil mixed with 60% RAP, while the CBR increased marginally from 45.1% for natural soil to 48.6% at 40:60 mixtures.

Alhaji and Alhassan (2018) also investigated the effect of RAP stabilization on the microstructure and strength of Black Cotton Soil (BCS), and reported optimal UCS value of 947kN/m² at optimal mixture of 30% RAP-70% BCS, representing 54.5% increase, maximum modulus of elasticity (E) of 42.52MPa at same mix ratio, representing 75.5% increase, reduction in free swelling of the compacted mixtures from 16.08% at 0% RAP to 0% at 80%, with 9.99% at optimal mixture of 30% RAP content, translating to 37.9% reduction in free swelling.

Mishra (2015) studied the use of RAP material in flexible pavements in which typical values of unit weight, natural moisture content, asphalt content, compaction densities and CBR values were reported, with the author concluding that 30% replacement of natural aggregate with RAP can successfully be used in base course. The use of geopolymer materials to stabilize RAP for road base courses was carried out by Avirneni *et al.* (2016), with the authors observing that Fly-Ash (FA) stabilization alone could not impact sufficient strength on the RAP-FA mixtures. They therefore concluded that 7 days UCS of the compacted RAP-FA blend at OMC met the strength requirement for base course specified by national road authority.

Alhaji and Alhassan (2018) worked on the microstructure and strength of RAP stabilized clay for road structure, with the result indicating CBR increased from 11% at 0% RAP-100% clay to 35% at 30% RAP-70% clay, after which the values reduced to 5% at 100% RAP- 0% clay. Suebsuk *et al.* (2014) studied effect of RAP on compaction characteristics and UCS of cement-treated soil–RAP mixtures, adopting porosity as a state parameter for assessing strength of the mixtures, with the results showing that as RAP content increases, OMC tended to decrease to an optimum soil-RAP ratio of 50/50. The asphalt fixation point was recorded to be at an asphalt content of 3.5% (50/50 soil-RAP ratio).

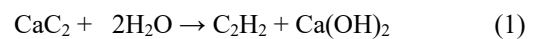
Kamel *et al.* (2016) evaluated the suitability of soil-RAP mixture for use as sub-bases, and from an extraction test observed the bitumen content of RAP to be 5.09% and maximum CBR to be 61.2% in a 50% soil-50% RAP mixture. Abukhettala (2016) also investigated the possibility of using RAP for road pavement structure. Rupnow *et al.* (2015) conducted a case study on the stabilization of a RAP-soil mixture with class C fly ash for use as a sub-grade., using Dynamic Cone Penetration (DCP) test to evaluate the strength gain in the field.

From the above review, it is evident that a lot have been done on the possibility of using RAP, either alone or mixed with additives, as road pavement structures. Study on the possibility of using Reclaimed Surface-dressed Pavement (RSP) material or Full Depth Reclaimed Surface-dressed Pavement (FDRSP) material, either alone or with additives have not received much attention in the literature. FDRSP material is obtained when surface-dressed layer together with the base course of a surface-dressed road are removed for reuse. This study is therefore aimed at investigating the possibility of using this FDRSP material together with cement and Calcium Carbide Residue (CCR) as road base.

Surface dressing is usually designed for light traffic roads, although it can be used on all types of roads. Reclaimed Surface-dressed Pavement (RSP) material is aged chippings embedded in bitumen, removed from road surfaces during maintenance or rehabilitation works on roads. These materials are usually carted away from site as waste. Physically, RSP also contains crushed gravel which can be used in mechanical stabilization. Due to high specific gravity of gravel compared to laterite, the combination of the two will result to increase in Maximum Dry Density (MDD) of the laterite gravel mixtures, improving the engineering properties of deficient soils. Incorporating cement and other additives to, especially Full Depth Reclaimed Surface-dressed Pavement

(FDRSP) could further enhance attainment of desired properties of road bases.

Cement is a well-known conventional soil stabilization additive because of its cementitious property (Suebsuk *et al.*, 2014; Alhassan and Alhaji, 2007; Osinubi and Mustapha, 2009; Alhaji *et al.*, 2019; Alhaji *et al.*, 2020). CCR is a by-product from acetylene gas production, which is used around the world for welding, lighting and metal cutting. CCR is obtained from a reaction between calcium carbide and water to form acetylene gas and calcium hydroxide in a slurry form, which mainly consists of calcium hydroxide Ca(OH)_2 along with silicon dioxide SiO_2 , CaCO_3 and other metal oxides (Eqn. 1). The presence of natural pozzolanic materials in clayey soil, makes calcium hydroxide $[\text{Ca(OH)}_2]$ a rich material that can be used to produce high strength geo-material (Gurugubelli *et al.*, 2017). For environmental and economic impact, such waste materials can be utilized collectively with natural pozzolanic material in clay to form cementitious material. Calcium carbide residue production is described in the following reaction equation:



From the Equation (1), Kumrawat and Ahirwar (2014) stated that 64g of calcium carbide (CaC_2) will produce 26g of acetylene gas (C_2H_2) and 74g of Calcium carbide residue (CCR) as Ca(OH)_2 . Jaturapitakkul and Roongreung (2003) and Horpibulsuk *et al.* (2014) used CCR, blended with pozzolanic materials such as fly ash and Rice Husk Ash as an alternative to Ordinary Portland cement, to form cementing agent for manufacturing concrete and masonry units. Latifi, *et al.* (2018), Suleiman *et al.* (2020) and Kanko *et al.* (2020), stabilised deficient soils with CCR, and reported decrease in MDD with increase in dosage of the CCR, while OMC was observed to increase with increase in CCR. A similar trend of MDD and OMC with increase in CCR was earlier reported by Du *et al.* (2011).

MATERIALS AND METHODS

Materials

The materials used in this study were Full Depth Reclaimed Surface-dressed Pavement (FDRSP), Portland cement and Carbide Residue (CCR).

Full Depth Reclaimed Surface-Dressed Pavement

The full depth reclaimed surface-dressed pavement used in the study was obtained by mechanically scarifying a surface dressed road. This material was obtained from Morris road, Minna, Niger State, Nigeria. The road was constructed to serve as entrance access to Morris Fertilizer Company, but has since gone bad, due to the heavy trucks plying the road and lack of routine maintenance. As of the time of this study, the road was being rehabilitated. Because of the relative difficulty in obtaining only Reclaimed Surface-dressed Pavement (RSP) material as compared to RAP, Full Depth Reclamation (FDR) method was employed. This is because asphalt pavement surface have defined separation from the road base, while surface-dressed pavement have no such because of the embedment of chippings, over time, into the bitumen/road base layers, resulting from vehicular loads. The resulting Full Depth Reclaimed Surface-dressed Pavement (FDRSP) was found to consist 28.7 % Reclaimed Surface-dressed (RSP) material and 71.3% soil from the base course.

Cement

The Portland cement (Dangote brand) used for the study was procured from a cement vendor at Minna building materials market. The cement was properly stored under dry condition.

Calcium Carbide Residue

The Calcium Carbide Residue (CCR) used in the study was obtained from panel beaters in Minna. The collected CCR was air dried and

milled to fine particles passing through BS sieve No. 200 (75 μ m) before use.

Test Location

The laboratory aspect of this study was carried out in Civil Engineering Laboratory of Federal University of Technology, Minna, Niger State, Nigeria, while the field (in-situ) test was carried out on an access road to Morris Fertilizer Company, Minna, Nigeria.

METHODOLOGY

Laboratory tests

The materials were manually mixed to allow for uniformity in the samples. Samples were taken from each of the stockpiled materials and carried to Civil Engineering laboratory for tests, which includes particle size analysis, Atterberg limits, compaction test and California Bearing Ratio tests. These tests were carried out in accordance with BS 1377 (1990) and BS 1924 (1990) for unstabilised and stabilized materials respectively. Considering the nature of the resulting composite material, and in an attempt to use less energy during field densification, West African Standard (WAS) compaction, as described in Nigeria General Specification (1997) was employed. CBR tests, at Optimum Moisture Content (OMC) were carried out on the FDRSP mixed with 0, 2, 4, and 6% cement and CCR, by dry weight of the FDRSP. Unsoaked and 24hour soaked CBR tests were carried out on the compacted mixtures after 7 days curing. Based on the nature of the traffic being experienced by the road (Fig. 1), unsoaked CBR value of 150% (Overseas Road Note 31, 1993) for heavy traffic roads was used to select the optimal percentage combination of FDRSP/additives that will be used for the field test. Based on this, 2% cement/4% CCR was chosen, together with that containing 0% additive and 2% cement, so as to provide basis for comparison.



Fig. 1: Nature of traffic on the road

Field Tests

The field tests were carried out on a section of the road. Adopting the test method used by Alhaji *et al*, (2019), the width of the test section of the road was 7.5m, while the length was 15.0m. The test section of the road was mechanically scarified to depth of 30cm using ripper (Fig. 2), with lumps of the soil-RSP mixture properly pulverized, in preparation for addition of cement and CCR. The 15.0m length of the test section was divided into three sections of 5.0m each. To effectively study the effect of these additives on the reclaimed pavement, the first test section consisted of the reclaimed pavement (FDRSP) only, the second section consisted of the reclaimed pavement (FDRSP) + 2% cement, while the third section consisted of reclaimed pavement (FDRSP) + 2% cement + 4% CCR. Fig. 3 shows a sketch of test sections of the road and the test points.

The test section of the road was cleared and cleaned of any possible organic matters or other impurities, before the mechanical scarification and crumbling of the lumps

were carried out. The test sections were then demarcated using pegs, into three sections of 5m length each. On the second and third sections, the additives were added and properly mixed, making sure that each of the sections was consisted of only the additives intended. After adding and properly mixing the FDRSP-cement and FDRSP-cement-CCR mixtures at the respective sections, compaction was carried out using sheep-foot (Fig. 4) and smooth drum vibrating rollers. During the compaction, in-situ density determination using sand replacement method (Fig. 5) was carried out intermittently to determine the maximum in-situ density, which eventually became constant with further compaction. Average of three in-situ density tests were performed after 1, 7, 28, 60 and 90 days of compaction. Dynamic Cone Penetration (DCP) tests (Fig. 6) were also conducted at three positions on each of the three sections, after 1, 7, 14, 28, 60 and 90 days of compaction. Data from the DCP test were used to compute CBR of the road base, with the aid of an empirical relationship developed by TRL (2014).



Fig. 2: Scarification of the test sections using ripper

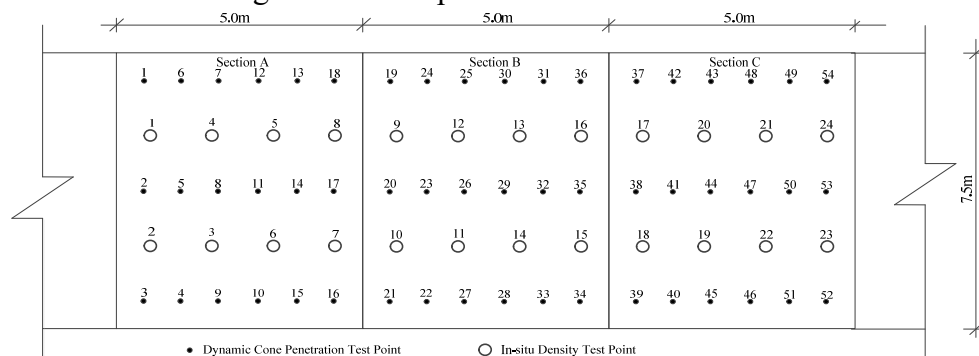


Fig. 3: Schematic diagram of the test section of the road showing the test points



Fig. 4: Compaction of the test sections using sheep-foot roller



Fig. 5: Determination of in-situ density of the test sections



Fig. 6: Dynamic cone penetration test to estimate CBR of the test sections

RESULTS AND DISCUSSION

Laboratory Results

Results of index properties of the initial base soil and FDRSP are presented on Table 1. From the table the initial base course material of the road classified under A-2-5 and SC according to American Association of State Highway and Transportation Officials (AASHTO) and Unified Soil

Classification System (USCS) respectively. On the other hand, FDRSP classified under A-2-4 and GC, according to AASHTO and USCS respectively. This indicates that the surface-dressed material improved both grading and consistency of the original base course material, by changing it from clayey sand (SC) to clayey gravel (GC) and reducing the PI from 9.26 to 6.49%. This improvement is evident in the MDD and OMC of the resulting FDRSP. The plasticity characteristics of the mixtures have been provided in previous study by Saidu (2021).

Variation of Compaction

Characteristics of the FDRSP Material with Dosage of the Additives

Variations of compaction characteristics (MDD and OMC) of the FDRSP with varied dosage of the additives are presented on Figs. 7 and 8 respectively. The result indicates gradual increase in MDD of the FDRSP material with increase in cement content. This is expected, as cement with higher specific gravity and fineness fills the voids in the FDRSP, resulting to a more compact and dense material. At constant cement content, the MDD of the mixtures was observed to decrease with increase in CCR. The decrease in MDD with increase in CCR is as a result of the lower specific gravity (2.21) being contributed to the mixture by the CCR.

Table 1: Geotechnical properties of Initial base material and FDRSP

Property	Existing base	FDRSP
Fraction passing BS	26.6	14.7
No 200 sieve (%)		
Liquid limit (%)	57.84	40.10
Plastic limit (%)	48.58	33.49
Plasticity index (%)	9.26	6.49
USCS	SC	GC
AASHTO classification	A-2-5	A-2-4
MDD (g/cm ³)	1.92	2.20
OMC (%)	17.0	10.0
Unsoaked CBR (%)	75	111
Soaked CBR (%)	37	78

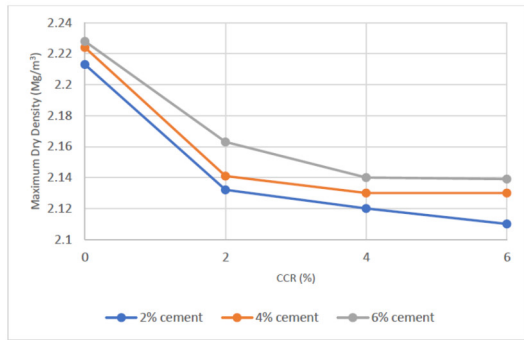


Fig. 7: Variations of maximum dry density with dosage of the additives

Reference to OMC (Table 1) of the untreated FDRSP, initial decreased in the value was observed on addition of 2% cement, but with subsequent increase in the cement content, the OMC gradually increased. The initial decrease in OMC with first dosage of cement is attributed to the consistency of the fines in the FDRSP, as cement modifies the consistency. The subsequent increase in OMC observed, with increase in cement content is attributed to hydration reaction of the cement and subsequent reaction of the CCR, which require water to proceed. This observed trends in variation of MDD and OMC with increase in CCR is similar to those reported by Latifi *et al.* (2018) and Du *et al.* (2011).

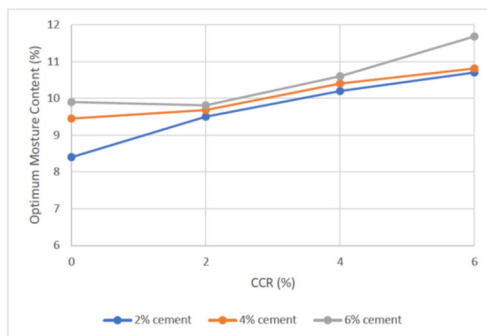


Fig. 8: Variations of optimum moisture content with dosage of the additives

Effect of the additives on CBR of the mixtures

Variation of laboratory soaked and unsoaked CBR of the FDRSP with changes in dosage of the additives are presented on Table 2. From the table, it is observed that both soaked and unsoaked CBR value of the FDRSP increased with increase in cement content. This is expected, as more cement means more binding material in the mixture. On the other hand, at constant percentage of cement, CBR values of the mixtures increased to their maximum values at 4% CCR, after which the values decreased at 6% CCR. Observation of the soaked and unsoaked CBR values indicated that the mixtures still maintained comparatively high strength even after 24 hours soaking. This is attributed to the hardened mass that resulted from the cementitious compounds from cement and the subsequent CCR reactions, and the waterproofing properties of the bitumen present in the FDRSP. Similar trend of soaked CBR values was reported by Edeh *et al.* (2012) for clay-RAP-lime composite. Based on the unsoaked minimum CBR value of 150% for base course of heavy traffic roads, the optimal percentage combination for stabilization of the FDRSP with cement and CCR for use as base course material, for heavy traffic roads will be 2% cement and 4% CCR. This is the combination with with least cement content that gave the required strength. Therefore, the performance of this mixture was studied on the field.

Table 2: Variation of laboratory CBR of the FDRSP with changes in dosage of the additives

Cement [%]	CBR (%)							
	Unsoaked	Soaked	Unsoaked	Soaked	Unsoaked	Soaked	Unsoaked	Soaked
	0% CCR		2% CCR		4% CCR		6% CCR	
2	123	111	136	124	159	147	107	91
4	165	151	192	176	270	248	175	155
6	231	213	296	266	320	285	281	241

FIELD RESULTS

Field densities

During compaction, the test was routinely conducted on the three sections of the road until three consecutive trials gave consistent results. This was repeated after 1, 7, 14, 28, 60, and 90 days. Summary of the results are presented on (Table 3). From the table, it is observed that the dry densities of the three sections changes throughout the 90 days of the study. The rate of increase in the densities was more pronounced in section B, section A has recorded the least rate of increase in the densities. In all the sections, more than 95% of the laboratory densities were achieved after 14 days, while more than 100% was achieved after 28 days, as compared to about 90% that was achieved before exposure of the test sections of the road to traffic. Alhaji *et al.* (2019) recorded 99.8 and 98.8% for lateritic soil/RAP/cement and lateritic soil/RAP mixtures respectively, after 60 days. The relatively early attainment of laboratory density is attributed to the nature traffic the road was exposed to, after the compaction.

Table 3: Summary of the field densities for the three sections of the road

Test Section	Density (Mg/m ³) After					
	1 day	7 days	14 days	28 days	60 days	90 days
A	2.1	2.19	2.19	2.21	2.21	2.22
	80	4	8	0	5	3
B	2.1	2.21	2.23	2.25	2.26	2.26
	91	1	4	8	1	2
C	2.0	2.10	2.11	2.12	2.12	2.13
	80	8	8	0	3	0

Field CBR

The field CBR of the compacted surfaces was determined using the Dynamic Cone Penetration (DCP) test data with the help of the empirical relation, developed by Transport Research Laboratory-TRL (2014).

$$\log(CBR) = 2.48 - 1.057(PI) \quad (1)$$

Where PI, is the penetration index

Variation of CBR with days of exposure to traffic is presented on Fig. 9.

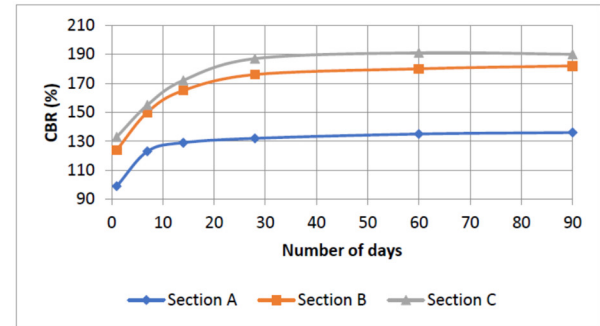


Fig. 9: Variation of In-Situ CBR values with number of days

From the fig. 9, it is observed that the CBR of section A is generally less than those of sections B and C. The relatively higher strength (CBR), recorded from these sections in comparison to section A, is as a result of the cementation, resulting from reactions of the additives (cement and CCR). At 7 days after compaction, the CBR values of sections A and B were generally more than 100% of the laboratory CBR, while that of section C was 98%. This tremendous increase in CBR values of the test sections is as a result of the combined effect of stabilisation reaction and the nature of traffic the road is exposed to. This road, being access road to entrance to Morris Fertilizer Company, Minna, is plied by heavy and articulate vehicles, transporting raw materials and products, in and out of the company. After 14 days, only marginal increase in CBR was noticed in section A, which could be attributed to the marginal increase in density of the section. Sections B and C recorded relatively noticeable increase in CBR up to 28 days, after which the increase became marginal to 90 days.

CONCLUSION

The following conclusions were drawn from the study:

- The initial lateritic soil that constituted the base course of the road classified under A-2-5. When this soil was mixed with RSP, the resulting material (FDRSP) classified under

A-2-4 according to AASHTO soil classification system.

ii. Field CBR results of the compacted FDRSP/2% cement/4% CCR used in sections C, after 14 days of exposure to traffic was 172%, which was higher than the laboratory 159%.

iv. The field CBR result of the FDRSP used in section A, after 7 days was 129% as against the 111% laboratory value.

v. Due to the cementitious properties imparted to the composite mixtures, soaking did not have adverse effect on strength.

vi. From the study FDRSP treated with 2 and 4% cement and CCR respectively can be used as base course for heavy traffic roads.

REFERENCES

- Abukhattala, M. (2016). Use of Recycled Materials in Road Construction, *Proceedings of the 2nd International Conference on Civil, Structural and Transportation Engineering*, Ottawa, Canada, 138-1 – 138-8.
- Aginam, C. H., Chidolue, C. A. and Nwakaire, C., (2014). Geotechnical Properties of Lateritic Soils from Northern Zone of Anambra State, Nigeria. *International Journal of Engineering Research and Development*, 10(12), 23–29.
- Alhaji, M. M., Alhassan, M., Adejumo T. W. and A. I. Dogo (2020). Microstructural Investigation and Strength Properties of Clay Stabilized with Cement, Rice Husk Ash and Promoter. *Jurnal Teknologi, UTM, Malaysia*, 8 (5), 11-22.
- Alhaji, M. M., Alhassan, M., Adejumo, T. W. and Umar, A. T. (2019). Laboratory and Field Evaluation of A-6 Lateritic Soil Treated with Reclaimed asphalt pavement and Ordinary Portland Cement. *International Journal of GEOMATE*, Vol. 17(63), 360–370.
- Alhaji, M. M., and Alhassan M. (2018). Effect of Reclaimed Asphalt Pavement Stabilization on the Microstructure and Strength of Black Cotton Soil. *International Journal of Technology*, 9(4), 727–736.
- Alhaji, M. M., Jibrin, R. Etsuwor, N. M. and Alhassan, M. (2014). Stabilization of A-6 Lateritic Soil using Cold Reclaimed Asphalt Pavement, *International Journal of Engineering and Technology, Center for Professional Research*, UK, Vol. 4(1), 52–57.
- Alhassan, M. (2008a). Potentials of Rice Husk Ash for Soil Stabilization. *Assumption University (AU) Journal of Technology, Bangkok, Thailand*, 11(4), 246-250.
- Alhassan, M. (2008b). Permeability of Lateritic Soil Treated with Lime and Rice Husk Ash. *Assumption University (AU) Journal of Technology, Bangkok, Thailand*, 12(2), 115–120.
- Alhassan, M. and Alhaji, M. M. (2007). Effect of Rice Husk Ash on Cement Stabilized Laterite. *Leonardo Electronic Journal of Practices and Technologies, Romania*, 6(11), 47–58.
- Amu, O. O., Owokade, O.S., Shitan, O.I., (2010). The Geotechnical Properties of Lateritic Soil for Road Works. *International Journal of Engineering and Technology*. 3(2).87-94.
- Avirneni, D., Peddinti P. R. T., and Saride S. (2016). Durability and Long Time Performance of Geopolymer Stabilized RAP Base Courses. *Construction and Building Materials*, 122, 198-209.
- Bleakley, A. M., and Cosentino P. J. (2013). Improving the Properties of Reclaimed Asphalt Pavement for Roadway Base, Application through Blending and Chemical Stabilization. *Annual Meeting of Transport Research Board*, 20-28.

- BS 1377 (1990). *Methods of Testing Soils for Civil Engineering Purposes*, British Standards Institute, London.
- BS 1924 (1990). *Methods of testing for stabilized soils*, British Standards Institute, London.
- Du, Y. J., Zhang, Y. Y. and Liu, S. Y. (2011). Investigation of Strength and California Bearing Ratio Properties of Natural Soils Treated by Calcium Carbide Residue, *Geo-Frontiers, ASCE 2011*, 1237-1244.
- Eberemu, A. O., Amadi, A. A. and Lawal, M. (2012). The Geotechnical Properties of Black Cotton Soil Treated with Glass Cullet, *Nigeria Journal of Engineering*, 2, 23–30.
- Edeh, J. E., Eberemu, A. O., Abah, A.B. (2012). Reclaimed Asphalt Pavements-lime Stabilization of Clay as Highway Pavement Materials. *Journal of Sustainable Development and Environmental Protection*, 2(3), 62–75.
- Gregory, E., and Halsted P. E. (2007). Using cement to reclaim asphalt pavement. *Annual Conference of the Transportation Association of Canada*, Saskatoon, Saskatchewan, 1-20.
- Gurugubelli, S., Prasad, D. S. V., and Eswararao, B. (2017). A Laboratory Study on the Strength Improve of Expansive Soil treated with Calcium Carbide Residue and Fly Ash. *International Journal of Innovative Research in Technology*, 3(12), 120 - 125.
- Horpibulsuk S., Hoy M., Witchayaphong P., Rachan R., Aruliajah A., (2017). Recycled Asphalt Pavement – Fly ash Geopolymer as a Sustainable Stabilized Pavement Material. *INCITE Conference in Material Science and Engineering*, 273, 1–11.
- Horpibulsuk, S., V. Munsrakes, Udomchai, A., Chinkulkijniwat, A. and Arulrajah, A. (2014). Strength of Sustainable Non-bearing Masonry Units Manufactured from Calcium Carbide Residue and Fly Ash. *Construction and Building Materials*, 71, 210–215.
- Jaturapitakkul, C., and B. Roongreung (2003). Cementing Material from Calcium Carbide Residue-rice Husk Ash. *Journal of Materials in Civil Engineering*, 15(5), 470–475.
- Kamel, M. A., Al-Bustami, N. M., Al-Sulami, B. T. (2016). Evaluation of the Suitability of Recycled Asphalt Pavement (RAP) for Subbases. *International Journal of Emerging Technology and Advanced Engineering*, 6(5), 212–215.
- Kanko, I. M., Alhassan, M. and Alhaji, M. M. (2020). Improvement of Deficient Laterite Soil using Cement and Calcium Carbide Residue, *Proceeding of 2nd International Civil Engineering Conference, Department of Civil Engineering, Federal University of Technology, Minna, Nigeria*, 218-225.
- Kumrawat, N., and Ahirwar, S.K. (2014). Experimental Study and Analysis of Black Cotton Soil with CCR and BA. *International Journal of Engineering Sciences & Management*, 4(3), 46 –53.
- Latifi, N., Vahedifard, F., Ghazanfari, E. and Safuan, A. A. R. (2018). Sustainable Usage of Calcium Carbide Residue for Stabilization of Clays, *Journal of Materials in Civil Engineering*, 30(6), 04018099-1 - 04018099-10.
- Mishra, B. (2015). A Study on Use of Reclaimed Asphalt Pavement (RAP) Materials in Flexible Pavements, *International Journal of Innovative Research in Science, Engineering and Technology*, 4(12), 12170-12177, 2015.
- Mohammad, L. N., Abu-Farsakh, M. Y., Wu, Z., and Abadie, C. (2003). Louisiana Experience with Foamed Recycled Asphalt Pavement Base

- Materials, 82nd Transport Research Board Annual Meeting, 1-19.
- Mu'azu, M. A. (2007). Evaluation of Plasticity and Particle Size Distribution Characteristics of Bagasse Ash on Cement Treated Lateritic Soil, *Leonardo Journal of Sciences*, Issue 10, January-June, 137–152.
- Nigerian General Specification for Roads and Bridge Works (1997). *Federal Republic of Nigeria Highway Manual*, Federal Ministry of works, Lagos, Nigeria.
- Ochepo, J. (2014). Stabilization of Lateritic Soil Using Reclaimed Asphalt Pavement and Sugarcane Bagasse Ash, for Pavement Construction. *Journal of Engineering Research*, 2(4), 1-13.
- Oghenero, A. E., Okey, A. T., Brume, O., Okunuwadije, S. E. and Jerry, O. (2014). Classification and Compaction Characteristics of Lateritic Soils of Warri, Delta State, Nigeria, *Advances in Applied Sciences Research*, 5(3), 451–457.
- Osinubi, K. J and Mustapha, A. M. (2009). Optimal use of Bagasse Ash on Cement Stabilized Laterite. *NSE Technical Transactions*, 44(1), 1–16.
- Osinubi, K. J., Bafyau, V. and Eberemu, A. O. (2007). Bagasse ash stabilization of lateritic soil”, *Proc. of the First Inter. Conf. on Environ. Res., Techn. and Policy “ERTEP 2007” under the auspices of International Society of Environmental Geotechnology*, Accra, Ghana, 16 -19 July, Category E: State-of-the-Art Technologies for Environmental Performance and Protection, 1 – 17.
- Overseas Road Note 31 (1993). A guide to the structural design of bitumen surfaced roads in tropical and sub-tropical countries. Overseas Centre, Transport and Road Research Laboratory, Crowthorne, Berkshire, United Kingdom.
- Rupnow, T. D., Franklin, B., White, D. J., (2015). Class C Fly Ash Stabilization of Recycled Asphalt Pavement and Soil: A Case Study, In: *World of Coal Ash (WOCA) Conference*, Nashville, 5–7 May, TN, 1–19.
- Saidu, A. E. (2021). *Performance Evaluation of Full Depth Reclaimed Surface-dressed Pavement Treated with Cement and Calcium Carbide Residue as Road Base*. MEng thesis, Department of Civil Engineering, Federal University of Technology, Minna, Nigeria.
- Suebsuk, J., Suksan, A., Horpibulsuk, S., (2014). Strength Assessment of Cement Treated Soil-Reclaimed Asphalt Pavement (RAP) Mixture. *International Journal of GEOMATE*, 6(2), 878–884.
- Suleiman, M., Alhassan M. and Alhaji, M. M. (2020). Stabilisation of Tropical Black Clay using Calcium Carbide Residue and Coconut Shell Ash. *Proceeding of 18th International Conference and Annual General Meeting of Nigerian Institution of Civil Engineers*, 123 – 135.
- Sultan, S. A. and Guo, Z. (2016). Evaluating the Performance of Sustainable Perpetual Pavements Using Recycled Asphalt Pavement in China. *International Journal of Transportation Science and Technology*, 5, 200–209.
- TRL (2014). Transportation: Past, Present and Future Conference, *Transportation Association of Canada*, Montreal, Quebec, 2014, 1-13.

PACKET DELIVERY RATIO (PDR) OF AN ENHANCED WEIGHT BASED CLUSTER HEAD SELECTION ALGORITHM FOR ROUTING IN VEHICULAR ADHOC NETWORKS (VANETs)

*Jiya, A. G, Usman, A. U and David, M.

Department of Telecommunication Engineering, Federal University of Technology, Minna, Niger State. E-mail: jiya.pg915206@st.futminna.edu.ng

Abstract

Packet delivery ratio is the ratio of packet sent to packet received. It is one of the most important reasons why clusters are formed in the first place. In weight-based cluster head selection algorithm, the cluster head is selected based on the aggregate weights of the vehicles. Because of frequent topology changes in VANETs routing is a serious problem. In this work, an enhanced cluster head selection algorithm for routing has been proposed in which cluster head is selected based on aggregate weights of the vehicle. The algorithm was simulated on MATLAB for 40, 50, 60 and 70 nodes with a 0%, 11.4%, 26% and 28% improvement respectively in terms of packet delivery ratio (PDR) compared to the existing weight-based cluster head selection scheme. In evaluating the algorithm for 40, 50, 60 and 70 nodes, the average packet delivery ratio as sensor radius increased was 0.62, 0.57, 0.63 and 0.61 respectively.

Keywords: clustering, VANETs, weight, cluster head, v2i, v2v.

INTRODUCTION

Vehicular adhoc networks (VANETs) remains one of the disruptive technologies of the fourth industrial revolution. Vanets are a type of Mobile Adhoc Networks (MANETs) (Bhatia *et al.*, 2020), which are networks that are not permanently tied to existing infrastructure but are constituted by nodes forwarding packets among themselves (Karthikeyana & Usha, 2021). This makes it easy for small devices to communicate at close range (Grace *et al.*, 2020; Guo *et al.*, 2020). One of the fastest-growing research areas in the field of communication engineering is adhoc networks. Adhoc networks are temporary networks, they do not require a central entity coordinating them; instead, the communicating nodes are able to use tailored techniques to control communication among themselves. Vehicular adhoc networks (VANETs) are a category of mobile adhoc networks (MANETs), and are typically nodes on wheels, with mobility (Manoj and Charanjeet, 2019). Vehicular

communications have emerged as an important application of wireless technology. Vehicular communication networks are an interconnection of vehicles to achieve autonomous driving. Vehicular Adhoc Networks (VANETs) could be Vehicle-to-Vehicle (V2V), Vehicle-to-Infrastructure (V2I), Vehicle-to-Network (V2N), Vehicle-to-Devices (V2D) and generally, Vehicle-to-Everything (V2X) (Grace *et al.*, 2020).

In recent times, a trend in hybrid connectivity is fast emerging as seen in vehicle-to-vehicle-to-infrastructure (V2V2I) (Fuqiang and Lianhai, 2010). This implies that vehicles are not only communicating among themselves, or communicating with cellular towers but they communicate among themselves and with network infrastructure also referred to as road side unit (RSU) (Aljeri and Boukerche, 2017). Communication with network infrastructure allows vehicular clients access remote services (Emara *et al.* 2018; Huanget

al., 2020). Considering the limited capabilities of vehicles in terms of storage and processing, it is imperative that VANETS should be equipped with higher storage and processing capabilities. Alternatively, provisions are being made for storage and computation at the edge of the infrastructure (Wanget *al.*, 2018; Wang *et al.*, 2020; Zhouet *al.*, 2018). Fig. 1 shows the inter-vehicular communication and a vehicle to infrastructure connection. Inter-vehicular communication is made possible via direct short-range communication (DSRC), while V2I communication is made possible by wireless access in vehicular environment (WAVE) which consists of 802.11p protocol among several other protocols. (Nkoko & Kogeda, 2013; Zhou *et al.*, 2018)

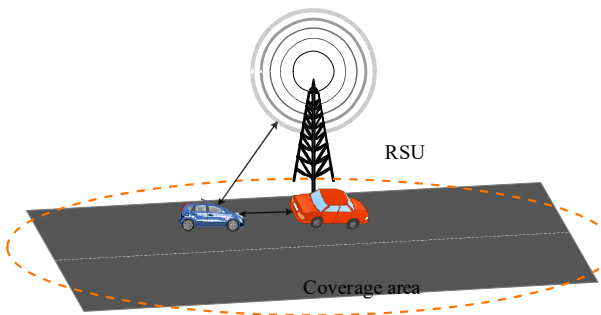


Fig. 1: Vehicle to Vehicle to Infrastructure Communication

Communication is possible in V2V networks using sensors. The Onboard Unit (OBU) is a network of sensors which are always in constant communication with other sensor nodes (Raza *et al.*, 2019; Storck and Duarte-Figueiredo, 2019). The VANETs perform such functions as vehicle diagnostics services, location information reporting, and communication with other vehicles and infrastructure, provision of safety information and monitoring for road users, information and entertainment (infotainment), traffic management and internet connectivity. Busari *et al.* (2019) proposed a generalized hybrid beam forming

technique for connectivity in vehicular communication using massive Multiple Input Multiple Output (MIMO). A new parameter known as sub-array spacing was introduced. Varying this parameter, brings about different sub-array configuration and by extension, variations in system performance.

Clustering algorithms in VANETs group vehicles in each spatial location based on certain properties such as speed, direction of travel and lane identification (id). Clusters are managed by cluster heads, other vehicles within the vicinity of the cluster head assumes the status of cluster members. Packet transmission and reception from or to any member is done through cluster heads. The cluster head therefore serves as routers as in traditional computer networks. The cluster head forwards packets to RSUs within the vicinity of the cluster. A vehicle that must be chosen as cluster head must meet certain criteria. Several protocols are available in literature and major emphasis of these protocols is optimal cluster head selection which will reduce packet delay, maximize throughput and also reduce packet loss. Several challenges have been witnessed in the area of vehicular communications. One of such is cluster head selection in cluster-based communication (Duan *et al.*; 2016, Ren *et al.*; 2021).

Clustering has emerged as a means of disseminating information, in clustering in vehicular communications, vehicles are either cluster heads (CH) or cluster members. cluster heads are chosen on the basis of balanced parameters and enhanced functionality (Grace *et al.*, 2020; Waleed *et al.*, 2020), such parameters include speed, direction of travel, driver behaviour, inter-nodal distance and communication range. It is desired that a cluster have good stability,

high efficiency, and reduced frequency of cluster head selection. Without loss of generality, cluster heads must have good ranking to be chosen as cluster heads. Cluster heads are required to coordinate inter cluster and intra cluster communication.

The IEEE 802.11p standard is a proposed standard which is meant to enable Wireless Access in Vehicular Environment (WAVE). The standard specifies operation in the 5.9 GHz frequency band. WAVE is composed of IEEE 802.11p and IEEE 1609.x. The IEEE 802.11p controls the physical layer and the medium access layer (PHY/MAC) while the IEEE 1609.x provides specifications for the control of upper layers. In the 1609.x family, IEEE 1609.3 specifies standards for transport and network layers. The 1609.4 documents specify standards for multi – channel operation. It is widely accepted in literature that in multi – channel operation, a WAVE system makes use of a single common control channel (CCH) and a number of service channels (SCHs) (Hu & Lee, 2022).

One of the major challenges of clustered communication in vanets is routing (Manoj & Charanjeet, 2019). Because of the frequent topology changes in VANETs, clustering is important because it helps to segment the network thereby reducing packet loss due to collision. This makes it important that efficient routing techniques be developed to cater for the rapid changes observed. The enhanced weight-based cluster head selection algorithm is a technique which selects cluster heads based on suitability index which is determined by the aggregate weight of all vehicles within the cluster. The algorithm also employs dynamic cluster sizing in improving packet delivery ratio when packets are routed from

cluster heads to cluster members, since as vehicular traffic rises from low to moderate, network performance indicators such as packet delivery ratio is also affected. With this kind of algorithm, the network remains in optimum state even as vehicular traffic increases.

RESEARCH QUESTIONS

This work seeks to answer the following research questions.

1. How can weight-based cluster head selection techniques be improved to accommodate frequent topology changes?
2. What is the sensor radius within which packet delivery ratio does not deteriorate?
3. What should be done to keep packet delivery ratio from deteriorating as traffic volume increases?

REVIEW OF RELATED WORKS

The concept of packet delivery of cluster heads is gaining more attention in VANETs. The purpose of clustering is to segment communicating nodes according to certain features. Clustering in VANETs is quite complex due to frequent topology changes, hence several factors have to be considered when clustering in VANETs. Cluster stability besides cluster head selection becomes a thing of interest as well. Cluster stability is dependent on certain constraints and it is when stable clusters are formed that efficient routing can be achieved (Yassine & Salah, 2019).

In the work of Waleed *et al.*, (2020), an optimized node clustering algorithm in vanets was developed by using meta-heuristic algorithms. This algorithm used parameters such as node's direction, communication link capacity, network area,

node density and transmission range. The algorithm is based on the grasshopper optimization algorithm (GOA) and mathematically modeled the swarming behaviour of grasshoppers. However, this algorithm is more suitable in high traffic areas. Ghassan, (2021) proposed an intelligent cluster optimization algorithm based on whale optimization algorithm for vanets. In this framework, an intelligent clustering approach was used to optimize the routing of packets in the vanets. The algorithm mimicked the behaviour of whales. This algorithm is however complex and several analyses are required to compute the performance metrics. Nivedita and Soumitra (2014), Ftaimi and Mazri (2020), surveyed the various cluster head selection techniques based on fuzzy logic, neural network and genetic algorithm. This work did not consider other algorithms apart from machine learning techniques. Cluster head selection routing algorithms should be implemented even without machine learning techniques. In Karthikeyana and Usha (2021), an adaptive clustering algorithm for stable communication in vanet was proposed. This algorithm combined weight based and neuro-fuzzy prediction by developing a static zone-based clustering and a k time zone base clustering, static time zones does not take to cognizance the frequent topology changes in VANETs. The scheme of Xiaoyu *et al.*, (2016) introduced a software defined networking (SDN) programmable network structure as an enabling platform to apply intelligence and control in 5G-vanet HetNet. The SDN controller has a global view of the HetNet so as to be able to execute clustering only when needed. The dual cluster design also guarantees seamless end-user data access

especially when there is cluster head service disruption.

Mohammed *et al.* (2017) proposed a center-based stable evolving clustering algorithm with grid partitioning and extended mobility features for VANETs. This article proposes a Vehicle-to-Infrastructure (V2I) based clustering framework in vanet using a modified evolving clustering algorithm with adoption of the concept of the grid in vanet clustering for the first time. It has developed a novel traffic generator that includes in addition to driving behaviour, a novel lane changes probabilistic model. It proposes grid partitioning for the road environment before doing clustering, which makes it suitable for high density highways. It also proposes an extended mobility feature that combines in addition to relative position and velocity of vehicles, a relative acceleration which makes the clustering more dynamically aware of higher moments when mobility variables can be added. The algorithm is more suitable for cases where mobility is low and traffic density is high, it is not suitable for high mobility road traffic, this is because it employs grid partitioning.

Grace *et al.* (2020) proposed a vanet clustering based on weighted trusted cluster head selection, this proposed technique proposed a new clustering protocol with a unique cluster head selection process while still retaining the features of vanet clustering. The cluster head selection in this protocol is based on the weighted formula. The algorithm does not allow for dynamic cluster adjustment hence, packet delivery ratio deteriorates with increase in vehicles in a linear fashion.

In Sharma *et al.*, (2022) a weight-based based clustering technique was proposed by

using a rhombus shaped network with an average speed and degree of suitability of each vehicle to determine the cluster head among a group of vehicles. The work used a transmission range of 150 – 200 meters for vehicles to be in a cluster. This work like that of Tambuwal *et al.*, (2019) and Iskandarani, (2022), opined that the speed of vehicles is assumed to have a normal distribution. Iskandarani, (2022) further compared aodv to dsr routing protocols in clustered communication. It is however interesting to ascertain the behaviour of cluster head routing with varying node density. This will help in understand the tolerance that can be associated with cluster based communication in vanets.

According to Tambuwal *et al.*, (2019), in “Enhanced weight-based clustering algorithm to provide reliable delivery for VANET safety applications”, the weight associated to each parameter is based on its importance and relevance in the vehicles’ mobility. The work also did not only carry out cluster head selection, it went ahead to select a backup cluster head which assumes the position of the cluster head in the event of link failure or incumbent cluster head exiting the cluster. The problem with this is that there needs to be a new selection process if this happens to cluster head and the back-up cluster head. A mechanism by which every vehicle is indexed based on its weighted value and can assume leadership in the event of cluster head and back up failure is more scalable as it will reduce the overhead involved in frequent cluster head selection.

In the work of Bijalwan *et al.*, (2022), A Self-Adaptable Angular Based K-Medoid Clustering Scheme (SAACS) for Dynamic VANETs was proposed. This work seeks to reduce the overhead incurred during

clustering by estimating the road length and transmission range. This action also reduced network delay. The cluster head is selected based novel performance metrics called cosine-based node uncoupling frequency that is used to find the most suitable node irrespective of their current network statistics. The scheme uses similarity value to determine the suitability of a vehicle to be in a cluster. The parameters of interest in the scheme are direction, relative speed and proximity. The scheme also chose the vehicle with the highest wait as the cluster however, in the event of link failure of the cluster head, the cluster member closest to the centroid is chosen as cluster member. This does not take cognizance of the weight. Another drawback of this scheme is that re-clustering process is initiated in the case of unstable clustering thus incurring another overhead. Alternate solutions to unstable clustering should be sought without placing much constraints on the network resources. Similarly, Saleem *et al.*; (2021) proposed a deep-learning based dynamic stable cluster head selection in vanets. This scheme also used a weighted formula to determine the cluster head based on four parameters namely, benefit factor, community neighborhood, eccentricity, and trust, the stability of the cluster head depends on the vehicle’s speed, distance, velocity, and change in acceleration. Kalman filter was used to determine the accurate location of any given vehicle at any time. The major issue with this work is the computational complexity of the various machine learning models required to arrive at a stable cluster head.

Several machine learning and AI models have been used in this sphere of research. Machine learning models remains

predominant within the research arena. The proposed algorithm therefore carries out weight-based cluster head selection algorithm by using K-means clustering algorithm and:

- i. factoring in the dynamic cluster resizing of the network as vehicles continues to increase in a low to medium vehicular network for the purpose of retaining good packet delivery ratio as vehicular traffic increases.
- ii. Indexing the vehicles so that the next vehicle with the highest weight assumes the leadership of the cluster.

METHODOLOGY AND NETWORK MODEL

The clustered network is built on a bidirectional road with a moderate traffic where vehicles share broadcast messages with vehicles in their clusters and communicate with other clusters through the cluster head which is chosen based on certain parameters. Vehicles within the same cluster are referred to as neighbours and their neighbourliness is governed by the condition:

$$\sum_{j=1}^k d(i, j, k) \leq R_{max} \quad (1) \text{ (Sharma et al., 2022).}$$

where i, j and k coordinates of the vehicle.

The following assumptions are made:

1. The vehicles are equipped with GPS which enables them to know their location relative to their trajectory.
2. The traffic density is moderate. The average velocity of the cluster is dependent on the specification of the group of vehicles.
3. The vehicles are equipped with 802.11p interface for direct short range communication, Vehicle-to-Vehicle (V2V) and wireless interface for (V2I) communication.

4. The first vehicle to send hello messages is chosen as the cluster center. The cluster center is the vehicle around which the cluster is created.

The vehicles are clustered based on their velocities using K-means clustering. Vehicles with velocities within the vicinity of the mean velocity can constitute a cluster. The cluster boundary is specified by the distance of other vehicles from the cluster center.

The vehicles that come together to form a cluster send hello messages to vehicles within its transmission range R_{max} . Vehicles within that range that reply to the hello messages sent and do not belong to any cluster, begin cluster formation by k-means clustering while those belonging to a cluster will ignore the hello message received. The flowchart for this work is presented in Fig. 2.

When the cluster head is selected, a simple flooding technique is then used in broadcast protocols to send packets to all the vehicles within a cluster.

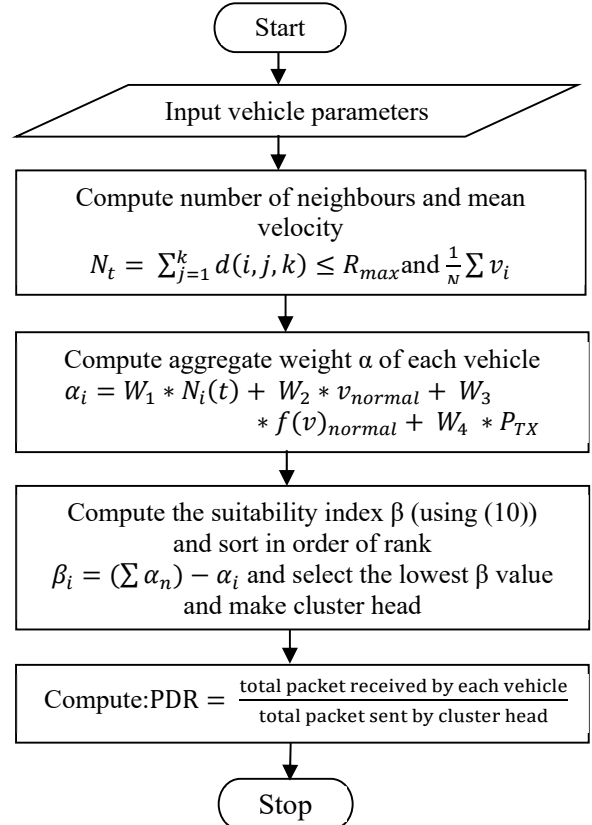


Fig. 2: Flowchart for the proposed work.

CLUSTERING PROCEDURE

- i. Initialize speed, direction, transmission power, and position
- ii. Check for available clusters from hello messages received
- iii. If there are more than one clusters,
- iv. {
- v. choose most suitable cluster and join
- vi. }
- vii. Else,
- viii. Initiate cluster formation
- ix. Compare speed of vehicles within range
- x. Compute average speed and pdf
- xi. Cluster vehicles by k-means clustering
- xii. Begin cluster head selection
- xiii. compute weight
- xiv. compute suitability index
- xv. Select cluster head
- xvi. Send broadcasts
- xvii. Perform analysis
- xviii. End

CLUSTER HEAD SELECTION PARAMETERS

Mean Speed

In this work, the speed of the vehicles is assumed to have a Gauss/Random distribution as widely stated in literature. This is because vehicles on a lane only have low, moderate, and high speed. The probability density function (pdf) is expressed as:

$$f(v) = \frac{1}{\sigma\sqrt{2\pi}} e^{\left[-\frac{1}{2}\left(\frac{(x_v - \mu_v)^2}{\sigma^2}\right)\right]} \quad \sigma > 0 \quad (2)$$

where μ , σ , x_v and μ_v are the mean, standard deviation, velocity of vehicle x and mean velocity respectively while $\frac{1}{\sigma\sqrt{2\pi}}$ is a constant factor that makes the area under the normal distribution curve equal to 1.

$$\frac{D_{a,b}}{R_{max}} = \sqrt{\frac{(X_b - X_a)^2 + (Y_b - Y_a)^2}{R_{max}^2}} \leq 1 \quad \text{(Sharma et al., 2022)} \quad (3)$$

The mean velocity $\mu_v = \frac{1}{N} \sum_{j=1}^m v_i$ or

$$\mu_v = \sum_{j=1}^m \frac{\Delta d}{\Delta t}$$

And the normalized velocity is expressed as:

$$v_n = \frac{x_v - \mu_v}{\sigma} \quad (4)$$

Mean Distance

By using the Euclidean distance, the mean distance between the nodes say a and b is given by:

$$\mu_d = \frac{\sum_{j=1}^m D_{a,b}}{N(t)} \quad (5)$$

$$d_{normal} = \frac{x_p - \mu_d}{\sigma_d} \quad (6)$$

where x_p , μ_d and σ_d are position of vehicle x , mean standard deviation of the distance.

Weight Computation

The suitability value of a vehicle is computed based on the weighted value assigned to each of the parameters discussed. Each node computes its mean distance μ_d using (5). The values W_1 , W_2 , W_3 and W_4 are chosen based on how critical the parameters are in the network. Hence higher weights are assigned to number of neighbours and transmission power.

The aggregate weight of each vehicle is computed as follows:

$$\alpha_i = W_1 * N_i(t) + W_2 * v_{normal} + W_3 * f(v)_{normal} + W_4 * P_{TX} \quad (7)$$

Subject to:

$$W_1 + W_2 + W_3 + W_4 = 1 \quad (8)$$

where: $W_1=0.3$, $W_2=0.2$, $W_3=0.2$, $W_4=0.3$

and W_1 , W_2 , W_3 and W_4 are the weights associated with each parameter.

P_{TX} = transmission power of the vehicle

α_i = the weight of each vehicle i

To be able to form a table of suitability value in ranking order, a vehicle computes its rank on the table by the (10)

$$\beta_i = (\sum \alpha_n) - \alpha_i \quad (9)$$

β_i = suitability index of vehicle i

The smaller the value of β , the better the position of the vehicle in the ranking. Vehicles with smaller suitability values have good chances of appearing at the top of the table while vehicles with high suitability values do not have a good chance of appearing at the top of the suitability value table.

Packet Delivery Ratio

The packet delivery ratio (PDR) is the ratio of total packet received by each node to the total number of packets sent by the cluster head. It is expressed as:

$$\text{PDR} = \frac{\text{total packet received}}{\text{total packet sent}}$$

(10) (Sharma *et al.*, 2022)

Table 1: Simulation Parametrs

Parameter	Value
Number of Lanes	2
Length of Road	4km
Packet Size	500 bytes
Number of Vehicles	40, 50, 60, 70
Sensor Radius (m)	0, 50, 100, 150, 200, 250, 300, 350
Cluster Size	Variable
Number of Clusters	Variable

SIMULATION AND RESULTS

The simulation was carried on MATLAB. To validate this algorithm, the enhanced weight-based clustering algorithm was benchmarked with the existing weight based cluster head selection algorithm in terms of their packet delivery ratios for 40, 50, 60 and 70 nodes. This is because this work is simulated for a moderate traffic size as can be seen from the assumptions. Fig. 3 shows that there is no difference in performance (0%) in terms of packet delivery ratio (PDR) for 40 nodes. This suggests that at lower number of nodes, cluster head selection techniques will behave averagely the same, this can be attributed to the clear line of sight and

reduced travel distance of packets within the cluster. The pdr is uniform with low sensor radius between 50-100 meters, it however begins to experience packet drop between 100 to 200 meters justifying the Sharma *et al.*, (2022) position of having a transmission range between 150 – 200 meters. Beyond 200 meters, the relationship between pdr and sensor radius becomes non-linear. It is hence technically correct to limit the transmission radius of vehicles to 150-200 meters.

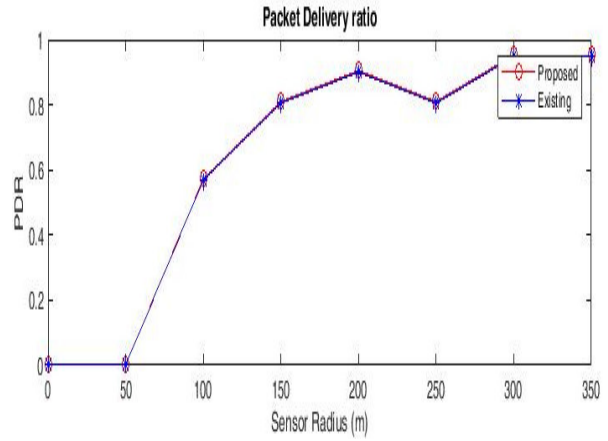


Fig. 3 Packet delivery ratio for 40 nodes

From Fig. 4 as the number of nodes increase, there is a dynamic adjustment in cluster size. This keeps the packet delivery ratio from falling off with respect to sensor radius. Hence packet delivery ratio will improve despite the increase in nodes. It is however observed that packet delivery ratio decreases as the number of nodes increase as seen in Figs. 3 and 4. As the sensor radius increases for all number of nodes, there are different sensor radius beyond which the packet delivery ratio flattens and fails to improve. Hence in comparison with the existing scheme, there is an 11.4 percent improvement in the packet delivery ratio as observed in figure 3. Number of nodes and sensor radius is linear, and changes occur at 100 meters, 150 meters, 200 and 250 meters because of the cluster re-sizing as against re-clustering as proposed in Bijalwan *et al.*, (2022). This eliminates time wasted in re-clustering when clusters become unstable. It thus emphasizes the general opinion of this

work that smaller clusters will help in keeping packet delivery ratio high.

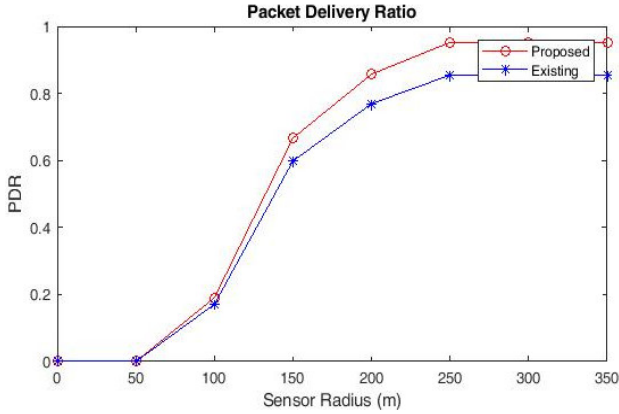


Fig. 4 Packet delivery ratio for 50 nodes

As the number of the number of nodes continues to increase, the proposed algorithm continues to outperform the fixed cluster head selection technique. For 60 nodes, 26% improvement was observed, and this is caused by the dynamic adjustment that comes with increase in nodes in this algorithm. However, beyond 200m, the packet delivery ratio becomes constant as observed in Fig. 5. It is observed that the linearity of pdr with sensor radius has improved in the proposed technique compared to the existing and the percentage difference has increased further justifying that at higher nodes, only smaller cluster sizes will keep pdr. Although it is clear that for this number of nodes, this technique becomes non-linear at 155 meters as against the 150 meters of the existing technique.

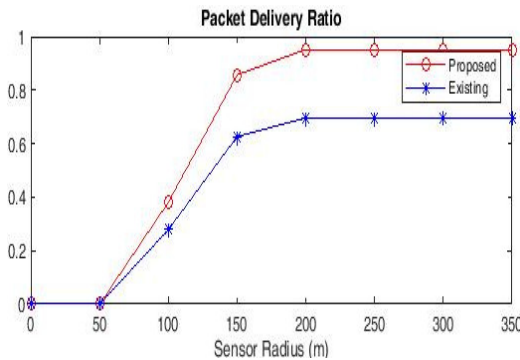


Fig. 5 packet delivery ratio for 60 nodes

In Fig. 6 it is further observed that for the moderate traffic which is being considered, given the sensor radius from 0 to 350 meters, packet delivery ratio begins to rise from below

50m, this is because the vehicles are closer within the clusters, however, there was approximately 0% difference between the proposed scheme and the existing scheme and this means that both algorithms are alike at lower sensor radius in terms of packet delivery ratio and this suggests that small sensor radius has higher packet delivery ratio. Overall, there was a 28.5% improvement at 70 nodes. Having too many nodes implies having many clusters. When this happens, packet delivery ratio is hugely affected as seen in the Fig. 5

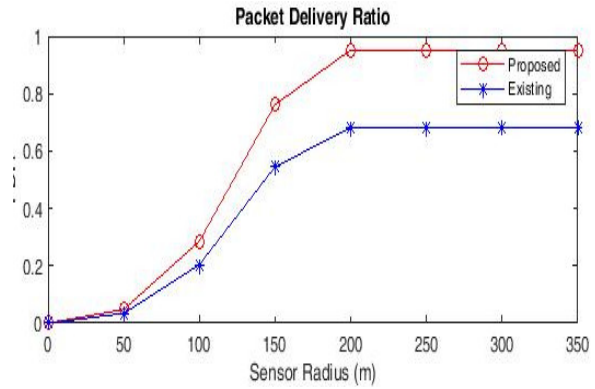


Fig. 6 packet delivery ratio for 70 nodes

The enhanced weight-based cluster head selection algorithm was evaluated alone for 40, 50, 60 and 70 nodes as shown in Fig. 7. It is observed that the average packet delivery ratio for 40, 50, 60 and 70 nodes are 0.62, 0.57, 0.63 and 0.61 respectively, this once again validates the fact that packet delivery ratio improves with dynamic cluster adjustment. It is observed here that at 70 nodes, packet delivery ratio is higher than that of 50 nodes. At 60, the cluster sizes become reduced leading to the formation of smaller but more number of clusters. The reduced cluster sizes then cause pdr to improve for 60 nodes but at 70 nodes the pdr drops to 0.61 making this scheme suitable for small traffic volume. Higher traffic volume will require more modifications.

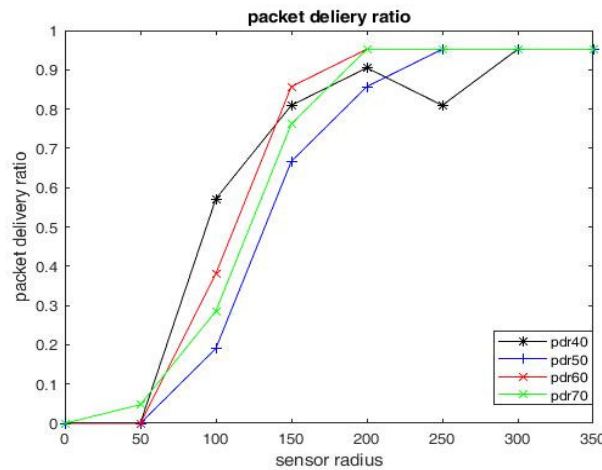


Fig. 7 comparison of packet delivery ratio for different number of nodes at different sensor radius

CONCLUSION/LIMITATION

In this paper, the authors have been able to analyze packet delivery ratio by using the enhanced weight-based cluster head selection algorithm, we also have been able to demonstrate that the proposed algorithm is a significant improvement against the existing weight-based cluster head selection technique. Dynamic cluster head selection helps in resizing clusters to keep packet delivery ratio from deteriorating beyond acceptable limits. This produced an average packet delivery ratio of 0.62, 0.57, 0.63 and 0.61 for 40, 50, 60 and 70 nodes respectively. This algorithm needs to be improved upon if it must serve for vehicles at higher velocities. In future works, we shall analyze cluster head selection delay and end to end delay in enhanced weight-based clustering algorithm. This work is constrained to moderate traffic size of 40, 50, 60 and 70 nodes making this model is most suitable for low to medium traffic because it assumes a normal distribution.

REFERENCES

- Aljeri, N., & Boukerche, A. (2017). Performance evaluation of movement prediction techniques for vehicular networks. Paper presented at the 2017 IEEE International Conference on Communications (ICC).
- Tambawal A. B, Noor M. R, Salleh R, Chembe C, Oche M (2019). Enhanced weight-based clustering algorithm to provide reliable delivery for VANET safety applications. PLoS One. 4;14(4):e0214664. doi: 10.1371/journal.pone.0214664. PMID: 30946766; PMCID: PMC6448915.
- Bhatia, T. K., Ramachandran, R. K., Robin, D., & Lei, P. (2020). *A review of simulators used for VANETs: The case-study of vehicular mobility generators*. Paper presented at the International Conference on Signal Processing and Integrated Networks (SPIN), Noida, India. <https://ieeexplore.ieee.org/abstract/document/9070933>
- Bijalwan, A.; Purohit, K.C.; Malik, P.; Mittal, M. A (2022) Self-Adaptable Angular Based K-Medoid Clustering Scheme (SAACS) for Dynamic VANETs. *Electronics* **2022**, *11*, 3071. <https://doi.org/10.3390/electronics11193071>
- Busari S. A, Huq K.M.S., Mumtaz S, Rodriguez J. Fang Yi., Sicker D. C., Al-Rubaye S. Tsourdos A. (2019). Generalized Hybrid Beamforming for Vehicular Connectivity Using THz Massive MIMO. *IEEE Transactions on Vehicular Technology*, 68, 8372 - 8383.
- Duan X, Wang, Y. Liu Y, & Zheng K. (2016). SDN Enabled Dual Cluster

- Head Selection and Adaptive Clustering in 5G-VANET. 2016 *IEEE 84th Vehicular Technology Conference (VTC-Fall)*, 18 – 21 September, 2016. Montreal, Canada, pp1-5, doi:10.1109/VTCFall.2016.7881214
- Emara, M., Filippou, M. C., & Sabella, D. (2018). *MEC-assisted end-to-end latency evaluations for C-V2X communications*. Paper presented at the 2018 European Conference on Networks and Communications (EuCNC), Ljubljana, Slovenia. pp1-9, doi:10.1109/EuCNC.2018.8442825
- Ftaimi, S., & Mazri, T. (2020). *A comparative study of Machine learning algorithms for VANET networks*. Paper presented at the Proceedings of the 3rd International Conference on Networking, Information Systems & Security, Marrakech Morocco. Article No. 10, pp 1-8. <https://doi.org/10.1145/3386723.3387829>
- Fuqiang, L., & Lianhai, S. (2010). Heterogeneous vehicular communication architecture and key technologies. *ZTE Communications*, 8(4), 39-44.
- Ghassan H. & Anwar S. (2021). An intelligent cluster optimization algorithm based on whale optimization algorithm for VANETs (WOACNET). *PLoS ONE*, 16(4). doi:. <https://doi.org/10.1371/journal.pone.0250271>
- Grace, K., Constandinos, X. M., George, M., Jordi, M. B., Hoda, M., & Evangelos, P. (2020). VANET Clustering Based on Weighted Trusted Cluster Head Selection. *IEEE Xplore*.
- Guo, J., Luo, W., Song, B., Yu, F. R., & Du, X. (2020). Intelligence-Sharing Vehicular Networks with Mobile Edge Computing and Spatiotemporal Knowledge Transfer. *IEEE Network*, 34(4), 256 - 262. doi: 10.1109/MNET.001.1900512
- Hu, H., & Lee, M. J. (2022). Graph Neural Network-based Clustering Enhancement in VANET for Cooperative Driving. In *2022 International Conference on Artificial Intelligence in Information and Communication (ICAIIIC)* (pp. 162-167). IEEE.
- Huang, C.-M., Lin, S.-Y., & Wu, Z.-Y. (2020). The k-hop-limited V2V2I VANET data offloading using the Mobile Edge Computing (MEC) mechanism. *Vehicular Communications*, 26, 1 - 12. doi: 10.1016/j.vehcom.2020.100268
- Iskandarani M. Z (2022). Dynamic Vehicular Communication using Gaussian Interpolation of Cluster Head Selection (GI-CHS) **International Journal of Advanced Computer Science and Applications; West yorkshire** Vol. 13, Iss. 2, (2022). D OI: .14569/ IJACSA.2022.0130257 **pp 489-494**
- Karthikeyana, H., & Usha, G. (2021). Adaptive Clustering Algorithm for Stable Communication in Vanet. *Turkish Journal of Computer and Mathematics Education*, 12(9), 1778- 1785.
- Manoj, S., & Charanjeet, S. (2019). Comparative Study of Cluster Head Selection Techniques in VANET under traffic conditions. *Journal of Emerging Technologies and Innovative Research (JETIR)*, 6(2), 66 - 78.
- Mohammed, S. T., Aslinda, H., Thamer, A., Zuraida, A. A., Ali, A.-J. M., Ali, J. I., & Nihad, I. (2017). A Center-based Stable Evolving Clustering Algorithm with Grid Partitioning and Extended Mobility Features for VANETs. *IEEE Access*. doi:10.1109/ACCESS.2020.3020510
- Nivedita, B. N., & Soumitra, S. D. (2014). A Survey on Cluster Head Selection

- Techniques. *Multidisciplinary Journal of Research in Engineering and Technology*, 1(1), 5.
- Saleem M. A, Shijie Z, Sarwar M. U, Ahmad T, Maqbool A, Shivachi C. S, Tariq M. (2021) "Deep Learning-Based Dynamic Stable Cluster Head Selection in VANET", *Journal of Advanced Transportation*, vol. 2021, Article ID 9936299, 21 pages, 2021. <https://doi.org/10.1155/2021/9936299>
- Nkoko S. S, & Kogeda, O. P. (2013) *A Cross-Layer Based Enhanced Handover Scheme Design in Vehicular Ad Hoc Networks*. Paper presented at the World Congress on Engineering and Computer Science San Francisco, USA.. Vol. 2
- Raza, S., Wang, S., Ahmed, M., & Anwar, M. R. (2019). A survey on vehicular edge computing: architecture, applications, technical issues, and future directions. *Journal of Wireless Communications and Mobile Computing*, 2019, 1 - 20. doi:doi.org/10.1155/2019/3159762
- Ren, M., Zhang, J., Khoukhi, L. et al. A review of clustering algorithms in VANETs. *Ann. Telecommun.* 76, 581–603 (2021). <https://doi.org/10.1007/s12243-020-00831-x>
- Sharma M, Kumar P, and Tomar R. S (2022). , "Weight-Based Clustering Algorithm for Military Vehicles Communication in VANET," in *SAIEE Africa Research Journal*, vol. 114, no. 1, pp. 25-34, March 2022 doi: 10.23919/SAIEE.2023.9962790.
- Storck, C. R., & Duarte-Figueiredo, F. (2019). A 5G V2X ecosystem providing internet of vehicles. *Sensors*, 19(3), 550. <https://doi.org/10.3390/s19030550>.
- Waleed A, Muhammad, F. K., Farhan Aadil, Muazzam Maqsood, Staish Ashraf , Yunyoung Nam, Seungmin Rho. (2020). Optimized Node Clustering in VANETs by Using Meta-Heuristic Algorithms. *Electronics*, 9, 394. doi:10.3390
- Wang, S., Chou, W., Wong, K.-S., Zhou, A., & Leung, V. C. (2018). Service Migration in Mobile Edge Computing. *Journal of Wireless Communications and Mobile Computing*, 2018, 1 - 2. doi:doi.org/10.1155/2018/3823721
- Wang, Y., Lang, P., Tian, D., Zhou, J., Duan, X., Cao, Y., & Zhao, D. (2020). A game-based computation offloading method in vehicular multi-access edge computing networks. *IEEE Internet of Things Journal*, 7(6), 4987 -4996. doi:10.1109/IIOT.2020.2972061
- Xiaoyu, D., Xianbin, W., Yanan, L., & Kan, Z. (2016). SDN Enabled Dual Cluster Head Selection and Adaptive Clustering in 5G-VANET. *IEEE*.
- Yassine, H., & Salah, M. (2019), *VANET Cross-Layer Routing*. Paper presented at the 2019 International Conference of Computer Science and Renewable Energies (ICCSRE), 22-24 July 2019, pp 1-2. Agadir, Morocco. Doi: 10.1109/ICCSRE.2019.8807634.
- Zhou, Z., Liu, P., Chang, Z., Xu, C., & Zhang, Y. (2018) *Energy-efficient workload offloading and power control in vehicular edge computing*. Paper presented at the 2018 IEEE Wireless Communications and Networking Conference Workshops (WCNCW), Barcelona, Spain. (15-18 April). Pp 191-196, doi:10.1109/WCNCW.2018.8368975.

MODELLING WATER LOSS IN HYDRAULIC DISTRIBUTION NETWORKS OF SHIRORO WATER DISTRIBUTION SYSTEM MINNA, NIGER STATE.

Tanimu, Y.*; Jimoh, O.D. and Adesiji A. R.

Civil Engineering Department, Federal University of Technology, Minna.

*Corresponding Author: tanimuyaba@gmail.com

Abstract

Minna, Niger State capital has been facing severe water supply scarcity in recent time, this scarcity has been further complicated with high water losses and non-revenue water in spite of government's allocation to the water sector in the state. Hence, there is need for new and modern approaches which will involve increased automation and proper monitoring of leakages and water loss. In this paper, the hydraulic machine, EPANET was used for the hydraulic modelling of the water loss in the networks of Shiroro District Metered Area, DMA. Leaks were collected and measured from 37 nodes in the network which were prone to leakages. 24 hours Extended Period Simulation, EPS, was carried out by varying emitter coefficient from 0.1, 0.15, 0.2 and 0.3 respectively. The water loss or discharge, Q_{leaks} generated from the model using discharge coefficient of 0.2 and the values of observed leaks Q from site were compared statistically using Nash-Sutcliffe efficiency model to check the performance of the model. The performance of the model suggested that using the emitter coefficient of 0.2 can model the water loss in Shiroro Water Distribution system because of high correlation between the simulated and the observed discharges.

Keywords: Shiroro Water Distribution System, Non-Revenue Water, EPANET, Emitter Coefficient

INTRODUCTION

Water distribution systems are primary means of safe drinking water supply to the system. Water produced and delivered to the distribution system is intended for the customers or users. However, a significant amount of water is lost in the system before it gets to its intended users as leak which is termed a physical component of Non-Revenue Water, NRW. The occurrence of leaks depends on the factors like materials, composition, age, pressure and joining. Due to complexity of the distribution system, it may be difficult for the utility personnel to identify and fix all the leaks. Current statistical surveys indicated that NRW in developing countries is around 45 to 50% (Putri *et al.*, 2021) which represents half of the total system input volume. A high level of apparent losses reduces the principal revenue stream to the utility. Zabidi *et al.* (2020) reported that losses in water distribution system in some urban areas in

Nigeria is as high as 50%. High levels of water losses are indicative of poor governance and poor physical condition of the Water Distribution System, WDS, (Kamrani *et al.*, 2020). The amount of water loss in water distribution systems varies widely from one system to another, from as low as 3–7 % in the well-maintained systems of developed countries to as high as 50 % of distribution input volume in less maintained system in developing countries respectively (Chan *et al.*, 2018).

Many water distribution systems in developing countries are operated under intermittent conditions (Simukonda *et al.*, 2018). As a result, water supply efficiency in these countries is compromised. Losses from leaks that are discovered and repaired should be measured to determine the rate of loss and the total volume lost during the life of the leak. Other methods of leak detection are suggested (from Leak Detection Productivity) by Douglas (AWWA California Nevada section, 1992).

1. Use a container of known volume.
2. Use a hose and a meter.
3. Calculate losses using modified orifice and friction formula.

An effective leakage management strategy should take into account the pressure dynamics of a water distribution network. This is because pressure plays a pivotal role in enhancing the magnitude of water leakage and because there is a physical relationship between leakage flow rate and pressure (Zhou *et al.*, 2018). Thus, the pressure exerted by either gravity or by water pumps results in a corresponding change in leakage rate (Kan *et al.*, 2022). The frequency of new pipe bursts is also a function of pressure such that the higher or lower the pressure, the higher or lower the leakage (Berardi and Giustolisi 2021). According to Nasrollahi *et al.* (2021), pressure level and pressure cycling strongly influence burst frequency. Some of the most important ways of managing pressure is by either using pressure reducing valves, PRVs (manual or automatic) or by using variable speed pump controllers. Under normal circumstances a PRV is used to maintain a fixed downstream pressure regardless of the upstream pressure dynamics. The leakage from water distribution systems has been shown to be directly proportional to the square root of the distribution system pressure (García-Ávila *et al.*, 2019). Past studies have shown that the rate of increase of bursts is more than linearly proportional to pressure (Xu *et al.*, 2020; Berardi and Giustolisi, 2021; Mathye *et al.*, 2022). Indeed, it has even been suggested that there could be a cubic relationship, i.e. burst frequency proportional to pressure cubed as reported by Farley and Trow (2003) and Wéber *et al.* (2020).

The objective of this study is to model water loss in the distribution network of Shiroro District Metered Area, Minna, Niger State and to investigate sustainability in terms of equity in the distribution of pipe-borne water in Minna metropolis as regular maintenance of infrastructure also helps to maintain water

efficiency levels and is more cost-effective than rehabilitation (Libey *et al.*, 2020). Simulation software used in the study area is EPANET. The method used in EPANET to solve the flow continuity and headloss equations that characterize the hydraulic state of the pipe network at a given point in time can be termed a hybrid node-loop approach. Assume we have a pipe network with N junction nodes and NF fixed grade nodes (tanks and reservoirs). Let the flow-headloss relation in a pipe between nodes i and j be given as:

$$H_i - H_j = h_{ij} = rQ_{ij}^n + mQ_{ij}^2 \quad (1)$$

where H = nodal head, h = headloss, r = resistance coefficient, Q = flow rate, n = flow exponent, and m = minor loss coefficient. The value of the resistance coefficient will depend on which friction headloss formula is being used. EPANET contains a state-of-the-art hydraulic analysis engine that include the following capabilities:

- Places no limit on the sizes of network that can be analysed
- Computes friction head loss using the Hazen-Williams, Darcy Weisbach, or Chezy-Manning formulas
- Includes minor head loss for bends, fittings
- Models constant or variable speed pumps
- Computes pumping energy and cost
- Models various types of valves including shutoff, check, pressure regulating, and flow control valves
- Allow storage tank to have any shape (i.e., diameter can vary with height)
- Consider multiple demand categories at nodes, each with its own pattern of time variation
- Model pressure-dependent flow issuing from emitters (sprinkler head)
- Can base system operation on both simple tank level or timer controls and on complex rule-based controls. One

of the challenges of EPANET is it takes a long time to learn.

From an energy standpoint its capacity is limited to the point at which, in certain circumstances it can supply erroneous results.

METHODOLOGY

Study Area

The study area is Distribution Network System of Shiroro District Metered Area, Minna, Niger State which is located within Latitude 9.59467° , Longitude 6.55427° and 9.59389° , 6.56032° with the total area covered by the distribution network as 1.9Sq km (Fig. 1). The flow chart methodology is depicted in Fig. 2

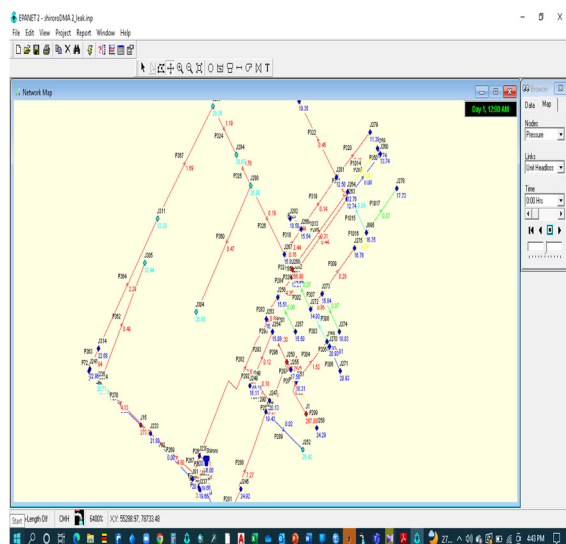


Fig. 1: Shiroro DMA showing the selected nodes for analysis

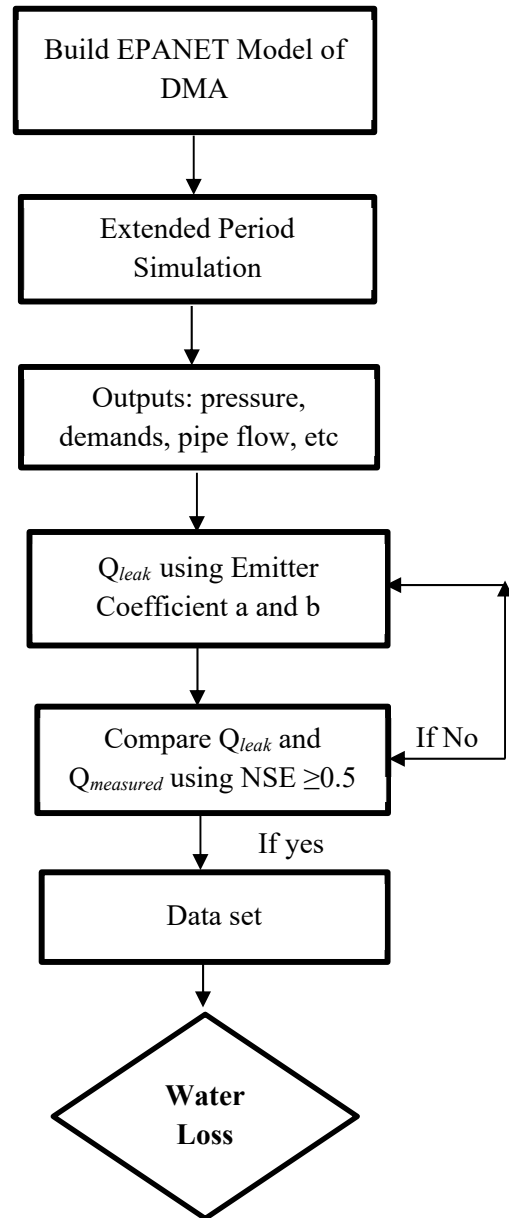


Fig. 2: Flow Chart Methodology

Water Distribution Network Simulation

The hydraulic machine, EPANET was used for the hydraulic modelling of the networks. Other supporting analytical tools for data collection to accomplish this assignment EPANET modelling include: ArcGIS, AutoCAD, EpaCAD, Google Earth Pro and TCX converter. Shape files of digitized maps of transmission and distribution mains, reservoirs, tanks and valves were loaded to AutoCAD and converted to metafiles. The

metafiles were used as backdrop in EPANET. The shape files were as well converted to Keyhole Markup Language, KML and superimposed in google earth to obtain nodal elevation values. Networks were then modelled.

Table 1: Velocity and Unit Headloss of the Network

Network Table - Links at 0:00 Hrs			
	Flow m³/h	Velocity m/s	Unit Headloss m/km
Pipe P91	29.24	0.02	0
Pipe P92	16.1	0.01	0
Pipe P256	-81.51	0.57	1.67
Pipe P257	12.24	0.02	0
Pipe P258	3.62	0.01	0
Pipe P261	-33.1	0.52	2.26
Pipe P262	-77.65	1.22	10.98
Pipe P263	-40.69	0.64	3.32
Pipe P264	-3.86	0.06	0.04
Pipe	6.85	0.11	0.12

Table 2: Elevation and Pressure Values of the Network

Network Table - Nodes at 8:00 Hrs				
Node ID	Elevation	Demand	Head	Pressure
	m	m³/h	m	m
Junc J91	253	3.86	271.3	18.3
Junc J92	254	3.86	271.3	17.3
Junc J228	254	3.86	271.43	17.43
Junc J229	254	3.86	271.35	17.35
Junc J230	254	3.86	271.25	17.25
Junc J231	254	3.86	271.28	17.28
Junc J232	254	3.86	271.25	17.25
Junc J233	250	3.86	269.52	19.52
Junc J234	247	3.62	271.3	24.3
Junc J235	247	3.62	271.3	24.3
Junc J237	254	3.86	271.25	17.25
Junc J238	253	3.86	271.28	18.28
Junc J240	247	3.86	267.67	20.67
Junc J241	247	3.86	267.64	20.64

Leak Identification and Measurement at Nodes Rule Based Leakage identification:

Section of the DMA with old pipes, smaller diameter, Longer lengths of link, more service connections and sections of the network with residual chlorine lower than 0.1mg/l were identified as leak points with high probability. In obtaining the parameters of leakages for analysis in NSE, water samples were taken from different points in the DMA and analyzed using pocket colorimeter DR300 and the reagents DPD. Samples with values of less than 0.1ppm or mg/l were selected for leak modelling. EPANET output is indicated in Fig. 1.and Tables 1 and 2.

Data Observation and Parameter Calibration Steps:

Step 1: The leaks on the 37 nodal demand points were physically measured using calibrated plastic containers, hoses, GPS, stop watch and flow meters.

Step 2: $Q = a * P^b$ (2)

was applied to nodes in the loop or DMA to estimate the leak, Rossman, (2000) and Burrows *et al.* (2003).

Where

Q =Leakage,

a = leakage coefficient and

b = leakage exponent

Rule Based Leakage Identification

To obtain Q_{leak} , nodes with the following conditions were considered to evaluate “a”

- 1 Nodes with values with residual chlorine less than 0.1mg
- 2 Nodes between aged Pipes
- 3 Nodes between longer length of Pipes >50m
- 4 Nodes with pipes having more service connections.

0.5 was used as leak exponent as default in EPANET for pipes. Leak coefficients of 0.1, 0.15, 0.2 and 0.3 were varied in the emitter for the purpose of calibration and Q_{leak} were generated for each of the leak coefficients. These ranges of numbers are often provided by the manufacturers.

Step 3: Model run was done by logging data obtained through physical measurement of leakages using EPANET. The pressure head at each node was known after Extended Period Simulation of 24 hours

Step 4: The observed and the model values of the leaks were statistically compared using Nash-Sutcliffe Efficiency to indicate how well the plot of the observed and modelled data fits the 1:1-line $NSE = 1$ which corresponds to a perfect match of the modelled to the observed data.

Step5: Decision taken based on the NASH coefficients values of 0.2 which correlate with the observed values

MODEL CALIBRATION

Nash–Sutcliffe model efficiency coefficient was used in assessing the predictive power

of hydrological models, and it is defined as

$$E = 1 - \{ \sum_{t=1}^T (Q_o^t - Q_m^t)^2 / \sum_{t=1}^T (Q_o^t - \bar{Q})^2 \} \quad (3)$$

Where;

Q_o = mean of observed discharges, and

Q_m = modelled discharge and

Q_o^t = observed discharge at time t .

Nash–Sutcliffe efficiency ranges from infinity to 1. The value of efficiency of 1 (when $E = 1$) means there is a perfect match of modeled discharge relative to the observed data. Therefore, the closer the model efficiency is to 1, the more accurate the model is (Karthikeyan *et al.* 2013). And according to Dongquan *et al.* (2009), a Nash-Sutcliffe simulation efficiency, E_{NS} greater than 0.5 indicates acceptable model performance for model simulation.

RESULTS AND DISCUSSION

Modelled and Observed Data Test in NASH Sutcliffe Coefficient Model

Analyses at 8 hours

The application of the leak coefficients of 0.1, 0.15, 0.2 and 0.3 in the emitter equation at 8 hour, showed the result of the observed and modelled data from NASH Sutcliffe Efficiency Coefficients as -4.552, 0.092, 0.73 and 0.187, respectively. These values deviated from the required standards of perfect or nearly perfect match except at 0.2 which gives a nearly perfect match. Figs. 3, 4, 5, and 6 depicts these NASH coefficients.

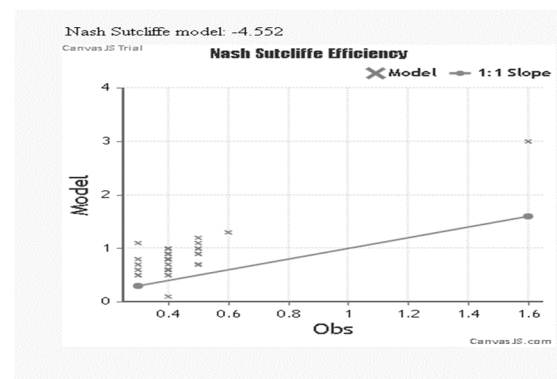


Fig. 3: NASH Coefficient with leak coefficient = 0.1

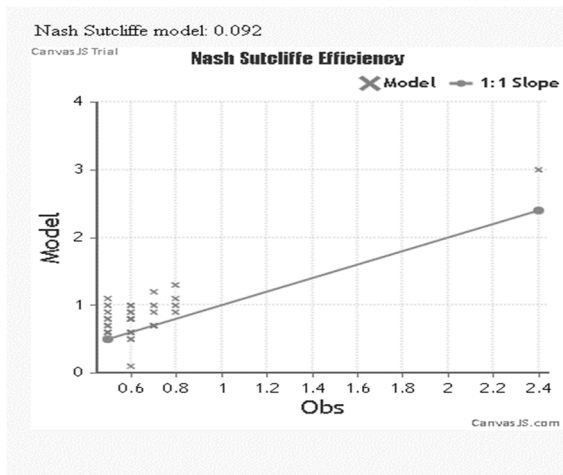


Fig. 4: NASH Coefficient with leak coefficient = 0.15

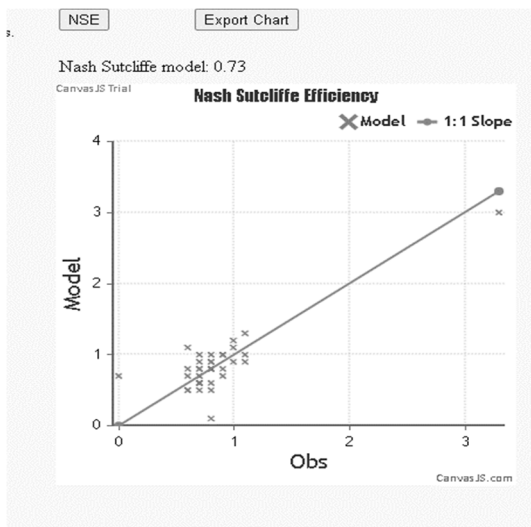


Fig. 5: NASH Coefficient with leak coefficient = 0.2

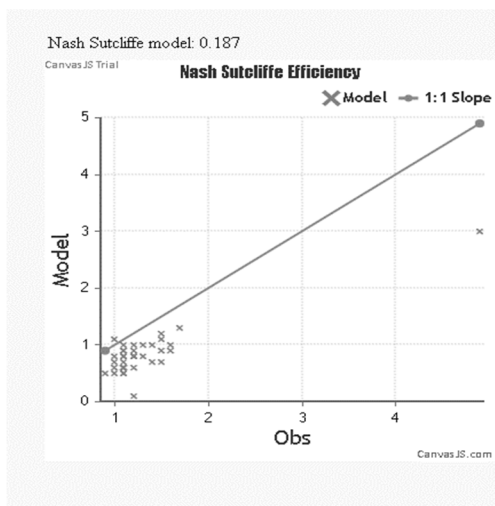


Fig. 6: NASH Coefficient with leak coefficient = 0.3

Analyses at 9 hour

With the leak coefficients of 0.1, 0.15, 0.2 and 0.3 in the emitter equation at 9hr, the observed and modelled data loaded in the NASH-Sutcliffe Model provided the NASH Sutcliffe Efficiency Coefficients of -3.777, 0.143, 0.68 and -0.07 respectively. These values deviated from the required standards of perfect or nearly perfect match but at 0.2 which gives a near perfect match. Figs. 7, 8, 9, and 10 depicts these NASH coefficients.

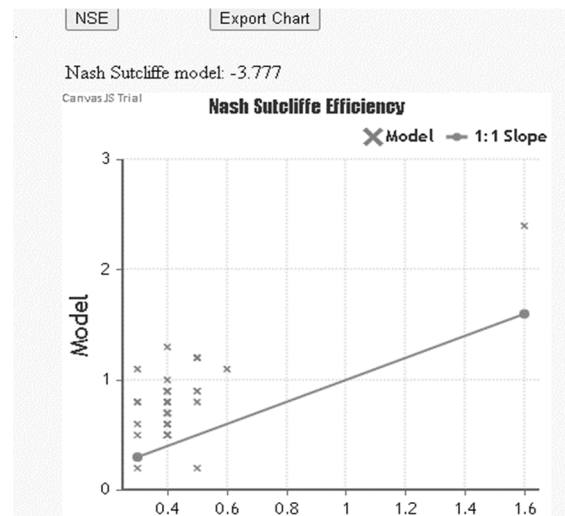


Fig. 7: NASH Coefficient with leak coefficient = 0.1

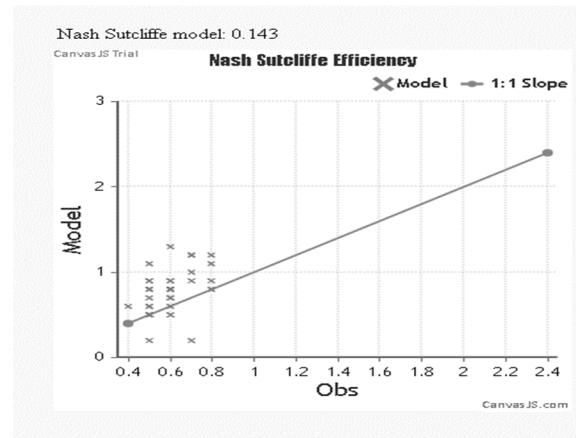


Fig. 8: NASH Coefficient with leak coefficient = 0.15

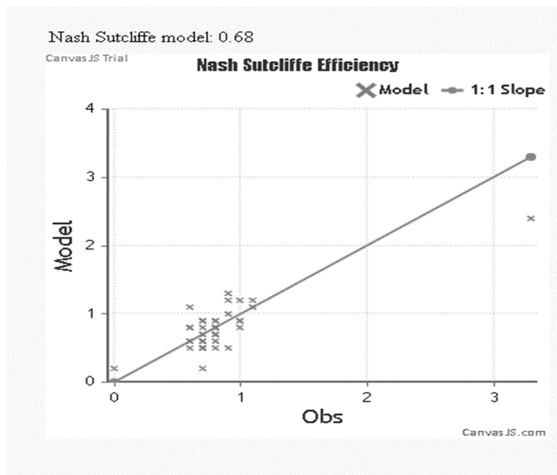


Fig. 9: NASH Coefficient with leak coefficient = 0.2

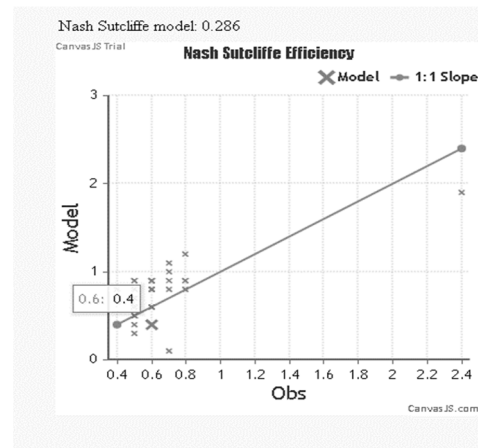


Fig. 12: NASH Coefficient with leak coefficient = 0.15

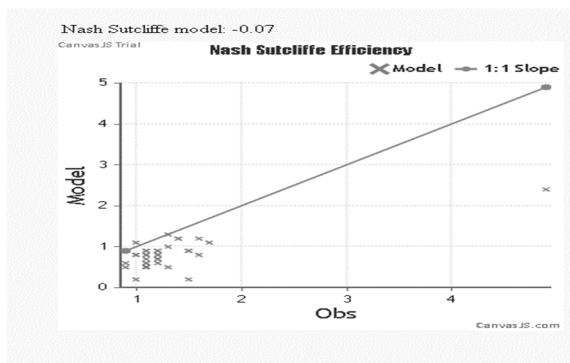


Fig. 10: NASH Coefficient with leak coefficient = 0.3

Analyses at 10 hour

With the leak coefficients of 0.1, 0.15, 0.2 and 0.3 used in the emitter equation at 10hr, observed and modelled data loaded in the NASH provided the Nash Sutcliffe Efficiency Coefficients of -2.573, 0.286, 0.582 and -0.288 respectively. These values deviated from the required standards of perfect or nearly perfect match except at 0.2 which meets the required standard. Figs. 11, 12, 13, and 14 depicts these NASH coefficients.

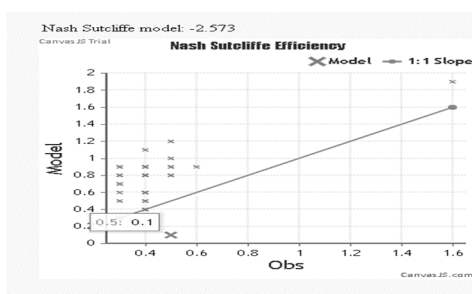


Fig. 11: NASH Coefficient with leak coefficient = 0.1

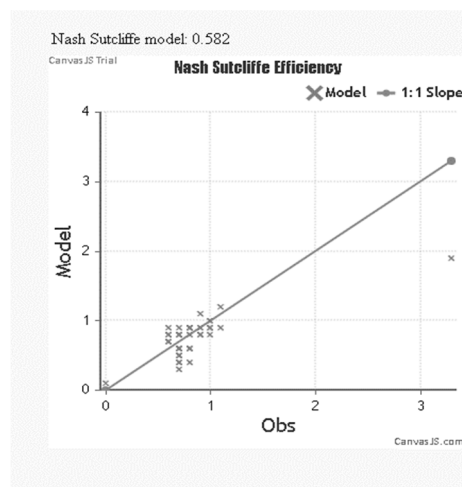


Fig. 13: NASH Coefficient with leak coefficient = 0.2

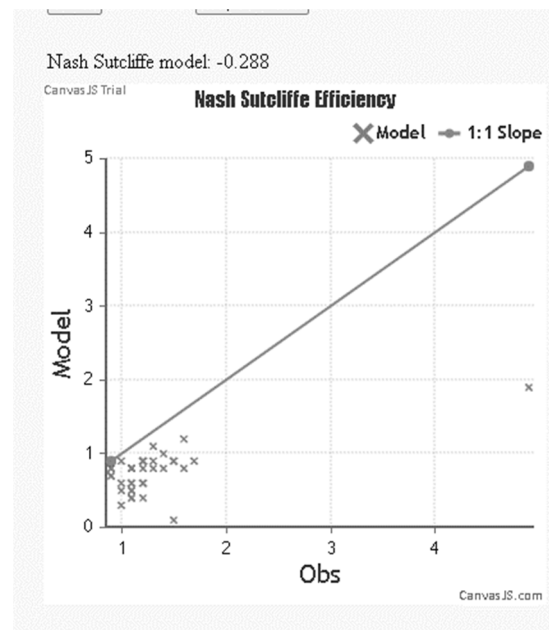


Fig. 14: NASH Coefficient with leak coefficient = 0.3

Analyses at 11 hours

With the leak coefficients of 0.1, 0.15, 0.2 and 0.3 in the emitter equation at 11hour, observed and modelled data loaded in the NASH provided the NASH Sutcliffe Efficiency Coefficients of -0.689, 0.256, 0.516 and -0.826 respectively. These values deviated from the required standards of perfect or nearly perfect match at except at 0.2 which shows nearly perfect match. Figs. 15, 16, 17, and 18 depicts these NASH coefficients.

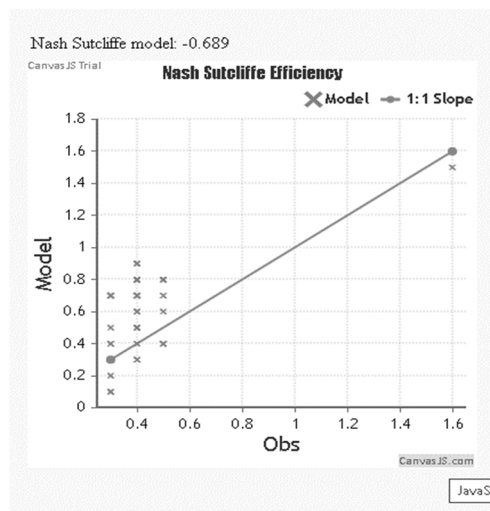


Fig. 15: NASH Coefficient with leak coefficient = 0.1

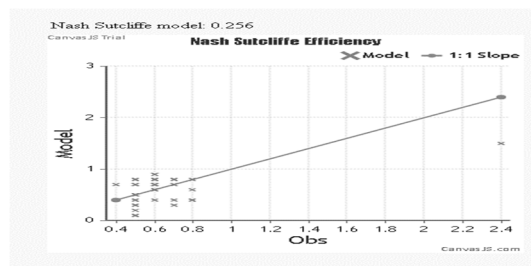


Fig. 16: NASH Coefficient with leak coefficient = 0.15

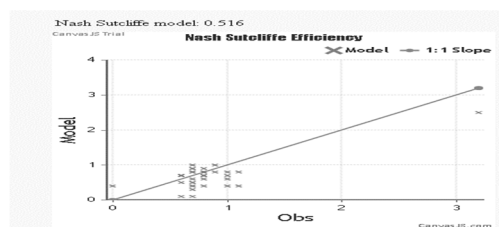


Fig. 17: NASH Coefficient with leak coefficient = 0.2

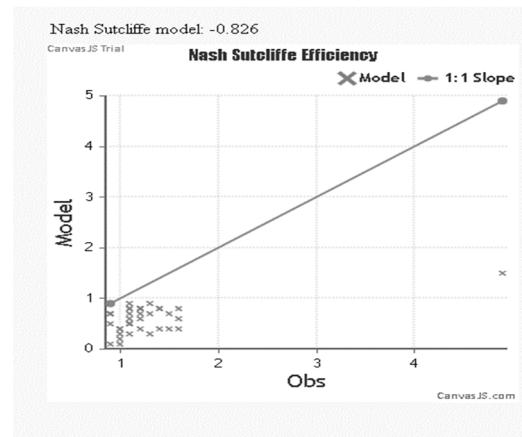


Fig. 18: NASH Coefficient with leak coefficient = 0.3

The performance of the model has suggested that using the emitter coefficient of 0.2 can model the study area because of high correlation between the observed and model data. Table 3 shows the model performance in NSE with varied emitter coefficients and at different trial hours of 8 to 11 hours

Table 3: Summary of the Model Performance in NSE

Hour	A			
	0.1	0.15	0.2	0.3
8	-4.552	0.092	0.73	0.187
9	-3.777	0.143	0.68	-0.07
10	-2.573	0.286	0.582	-0.288
11	-0.689	0.256	0.516	-0.826

Summary of the modelled and measured leaks is shown in Table 4. This is as a result of using the leak coefficient 0.2 in the emitter equation. The coefficient, 0.2 used in the emitter equation yielded the Simulated Q_{leak} while the physical measurement yielded Observed Q_{leak} for the nodes in the distribution networks.

Table 4: Simulated and Observed Leaks as obtained at nodes

Node	Pressure (m)	Simu Q_{leak} (m^3/h)	Obs Q_{leak} (m^3/h)
249	16.08	0.8	1
242	24.16	1	0.7
252	13.88	0.7	0.8
253	12.83	0.7	0.6
250	15.32	0.8	0.1
252	13.28	0.7	0.9
252	13.27	0.7	1
243	22.06	0.9	1
254	10.53	0.6	0.5
253	11.53	0.7	0.6
252	12.79	0.7	0.6
252	12.72	0.7	0.8
254	10.53	0.6	1.1
254	10.55	0.6	0.8
251	13.33	0.7	0.6
251	13.67	0.7	0.6
0	264.68	3.3	3
248	16.72	0.8	0.8
246	18.71	0.9	1

The study has shown 17.15% of loss in the network the total loss from all nodes in 4 hours is 338.4m³ from the nodes under investigation and the District Metered Area, DMA System Input Volume, SIV is 2235m³

CONCLUSIONS

Modelling Water Loss in Shiroro Distribution System in Minna, Niger State has been carried out. Emitter equation was used as the basis in the modelling where leak coefficients were varied to arrive at appropriate leak coefficient. It was established that the use of emitter coefficient of 0.2 can be efficiently used to model Shiroro water distribution system. The coefficient of 0.1 0.15 and 0.3 deviated widely from the required model value. of 0.5 to 1. The physical loss recorded in the study area was 17.15% as against 40.1% presumably used by the Utility (Niger State Water and Sewage Corporation). The values of simulated and observed leaks were correlated in NSE. Use of emitter coefficient

of 0.2 can be efficiently used to model the study area. The coefficient of 0.1 0.1 and 0.3 deviated widely from the required model value. It is necessary that concerned administrators are guided by the simulation results showing pipe-borne water pressure and flow rate and velocities within the network. In the same vein, pressure break tanks or Pressure Reducing Valves, (PRVs) should be installed on the revealed high-pressure lines. This is to check damage of pipes from extreme pressures. There is need to establish and strengthen active and passive leakage monitoring mechanism in the Utility.

REFERENCES

- Berardi, L., & Giustolisi, O. (2021). Calibration of design models for leakage management of water distribution networks. *Water Resources Management*, 35(8), 2537-2551.
- Burrows, R., Mulreid, G. & Hayuti, M. (2003). Introduction of a fully dynamic representation of leakage into network modelling studies using EPANET. In: Maksimovic C, Butler D, Memon A (eds) Proceedings of the international conference on advances in water supply management. Swets & Zeitlinger, Lisses, 109–118
- Chan, T. K., Chin, C. S., & Zhong, X. (2018). Review of current technologies and proposed intelligent methodologies for water distributed network leakage detection. *IEEE Access*, 6, 78846-78867.
- Dong-quan, Z. O., Hao-zheng, W. G., Jining, C. N. & Hao-chang, W. G. (2009). Parameters uncertainty analysis of urban rainfall-runoff simulation, 20(1), 45-51.
- Farley, M., & Trow, S. (2003). *Losses in water distribution networks*. IWA publishing, London, UK

- García-Ávila, F., Aviles-Anazco, A., Ordóñez-Jara, J., Guanuchi-Quezada, C., del Pino, L. F., & Ramos-Fernández, L. (2019). Pressure management for leakage reduction using pressure reducing valves. Case study in an Andean city. *Alexandria Engineering Journal*, 58(4), 1313-1326.
- Kamrani, K., Roozbahani, A., & Shahdany, S. M. H. (2020). Using Bayesian networks to evaluate how agricultural water distribution systems handle the water-food-energy nexus. *Agricultural Water Management*, 239, 106265.
- Kan, K., Xu, Z., Chen, H., Xu, H., Zheng, Y., Zhou, D., ... & Maxime, B. (2022). Energy loss mechanisms of transition from pump mode to turbine mode of an axial-flow pump under bidirectional conditions. *Energy*, 257, 124630.
- Karthikeyan, L., Kumar, D. N., Graillot, D. & Gaur, S. (2013). Prediction of ground water levels in the uplands of a tropical coastal riparian wetland using artificial neural networks. *Water resources management*, 27(3), 871-883.
- Libey, A., Adank, M., & Thomas, E. (2020). Who pays for water? Comparing life cycle costs of water services among several low, medium and high-income utilities. *World Development*, 136, 105155.
- Mathye, R. P., Scholz, M., & Nyende-Byakika, S. (2022). Optimal Pressure Management in Water Distribution Systems: Efficiency Indexes for Volumetric Cost Performance, Consumption and Linear Leakage Measurements. *Water*, 14(5), 805.
- Nasrollahi, H., Safaei Boroujeni, R., Shirmohammadi, R., Najafi Nobar, S., Aslani, A., Amidpour, M., & Petrakopoulou, F. (2021). Optimization of Water Pressure of a Distribution Network within the Water-Energy Nexus. *Applied Sciences*, 11(18), 8371.
- Putri, B. N., Ahmad, I., & Abdullah, N. (2021). Water Distribution and Non-Revenue Water Management Scenario in Asian countries: Malaysian Perspective. *Journal of Advanced Research in Applied Sciences and Engineering Technology*, 25(1), 94-105.
- Rossman, L. A. (2000). EPANET 2 User Manual. Water Supply and Water Resources Division National Risk Management Research Laboratory, Cincinnati, OH, EPA/600/R-00/057.
- Simukonda, K., Farmani, R., & Butler, D. (2018). Intermittent water supply systems: causal factors, problems and solution options. *Urban Water Journal*, 15(5), 488-500.
- Wéber, R., Huzsvár, T., & Hős, C. (2020). Vulnerability analysis of water distribution networks to accidental pipe burst. *Water Research*, 184, 116178.
- Xu, W., Zhou, X., Xin, K., Boxall, J., Yan, H., & Tao, T. (2020). Disturbance extraction for burst detection in water distribution networks using pressure measurements. *Water Resources Research*, 56(5), e2019WR025526.
- Zabidi, H. A., Goh, H. W., Chang, C. K., Chan, N. W., & Zakaria, N. A. (2020). A review of roof and pond rainwater harvesting systems for water security: The design, performance and way forward. *Water*, 12(11), 3163.
- Zhou, S., O'Neill, Z., & O'Neill, C. (2018). A review of leakage detection methods for district heating networks. *Applied Thermal Engineering*, 137, 567-574.

HYBRID AUTOREGRESSIVE NEURAL NETWORK (ARNN) MODEL FOR SPECTRUM OCCUPANCY PREDICTION

***Ajiboye, J.A¹, Adegboye, B.A², Aibinu, A.M³, Kolo, J.G⁴, Ajiboye, M.A⁵, Usman, A.U⁶**
^{1,2,4}Department of Electrical and Electronics Engineering, Federal University of Technology, Minna, Nigeria. ³Department of Mechatronics Engineering, Federal University of Technology, Minna, Nigeria. ⁵Abuja Electricity Distribution Company (AEDC), ICT Department, Niger Regional Office, Minna, Nigeria. ⁶Department of Telecommunication Engineering, Federal University of Technology, Minna, Nigeria. *Email: ajiboye2003@yahoo.com

Abstract

A secondary spectrum user cannot transmit in a channel before sensing and knowing the spectrum occupancy state as this may cause interference. This poses a major challenge because these operations ought to be performed in each time slot and thereby causing a substantial delay before the user gains access to the spectrum, leading to inefficient utilization. Therefore, a channel predictive system will mitigate this problem. In this work, an ensemble machine learning model for spectrum occupancy prediction was developed. The developed model was trained using a sample of Power Spectrum Density (PSD) data collected from the field for a period of twenty four hours within a frequency range of 30-300 MHz. The frequency range was grouped into sub bands. Based on the training data and the corresponding output data, the neural network model trains itself to come up with the best weights which can generally be used by the AR model for unseen data. After computing the weights, the performance was first tested on the entire training data, on the validation dataset and on the test dataset. Prediction results revealed an overall accuracy of 98.32% with band 4 (74.85-87.45 MHz) having the highest accuracy of 99.01% and the lowest accuracy of 89.39% in band 2 (47.05-68 MHz).

Keywords: Cognitive Radio, Frequency Modulation, Primary Users, Power Spectrum Density, Secondary Users, Very High Frequency.

INTRODUCTION

The demand for wireless equipment is high. Similarly, the usage of data and multimedia applications has resulted in a massive increase in demand for faster data rates. This has resulted in a greater need for radio spectrum (Oluwafemi *et al.*, 2021). The radio spectrum is the wheel on which wireless communication systems are driven. The demand for radio spectrum can be observed in the auctions that have been conducted in nations where large sums have been paid for spectrum licenses (Kyeremateng-Boateng *et al.*, 2020; Mishra *et al.*, 2012; Doerr *et al.*, 2008; Dame, 2001). Due to the restricted natural frequency usage, there is a spectrum deficit. Because the entire radio spectrum has been assigned to various wireless services, some newly emerging wireless technologies are unable to

operate (Gupta and Jha, 2015). The spectrum's opportunity cost rises as a result. Because of inefficient static spectrum distribution policies, spectrum scarcity is not real but artificial (Peha, 2009).

Early spectrum survey in the United States of America (USA) found a shocking result of spectrum underutilization, corroborating the assertion of inefficient spectrum management (McHenry *et al.*, 2006). According to the study, a considerable amount of the available spectrum is unused. Due to time, frequency, and geographic location, 15 percent to 85 percent of the allocated spectrum remains inactive (Seflek and Yaldiz 2019; Akyildiz *et al.*, 2006). These studies reveal that the existing spectrum allocation mechanism is faulty and incapable of meeting the increased demand for spectrum for future cellular services. The present system of spectrum management is

very rigid, with major licensed users having entire or absolute control over the radio frequency spectrum (Matheson and Morris, 2012).

Ensemble modeling is a machine learning technique in which two or more different models are used to predict a result, either by employing a variety of modeling techniques or using a variety of training data sets in which the ensemble model integrates several base model's predictions to obtain a final forecast for unknown data. The basic goal of using ensemble models is to reduce the generalization error of predictions. When using the ensemble approach, as long as the basic models are diverse and independent, the model's prediction error reduces (Re and Valentini, 2012). The integration of different

models can be an effective approach of increasing their predictive accuracy, according to both theoretical and empirical studies, especially when the models in the ensemble are somewhat distinct.

RELATED WORKS

Table 1 provides a list of previously conducted spectrum studies including the studies conducted at the Radio Spectrum Engineering Laboratory of Georgia Institute of Technology (GIT), the Institute of Telecommunication Sciences (ITS) in USA, the Mobile Portable Radio Group (MPRG) at Virginia Tech and the Shared Spectrum Company in Virginia, USA (Petrin and Steffes, 2005; Petrin and Steffes, 2004a; Hoffman and Matheson, 2005).

Table 1: Previously Conducted Spectrum Surveys

Name	Frequencies	Purpose of Survey
ITS	LMR Bands	Improve usage of LMR bands, prediction of usage
MPRG	30-300 MHz	Assess feasibility of DSA
SS Co.	54-3000 MHz	Quantify Spectrum Occupancy
GIT	0.4-7.2 GHz	Determine spectrum occupancy, interference to radiometric services

The spectrum data can be used to extract patterns of transmission activity, as well as for interference analysis (Petrin and Steffes, 2004b). A thorough understanding of the spectrum behavior and interference issues can be helpful in devising solutions to maximize the spectrum utilization and assist in the design of secondary spectrum access technologies (Petrin and Steffes, 2004b; Hoffman and Matheson, 2005).

These studies were performed to determine how the spectrum utilization can be improved and to provide a basis for prediction of the future usage of these bands. The amount of unused spectrum can be quantified in order to assess the feasibility of broadband communication through cognitive radio operation in spectrum white

spaces (Ellingson, 2005). The spectrum utilization can be quantified using a metric, called spectrum occupancy, which is defined as the probability that a signal is detected above a certain threshold power level.

Resolving the spectrum usage along all the dimensions of the spectrum will provide important information that will help in exploiting the spectrum efficiently (Petrin and Steffes, 2004a). In the real time scenario, the knowledge obtained from spectrum surveying can be input to DSA networks in order to help them in identifying potential opportunities for secondary access. In addition, multi-dimensional spectrum data can be used to identify the characteristics of the primary transmitters such as polarization

type and azimuth location (Petrin and Steffes, 2005).

Furthermore, the results of a spectrum survey can also help in interference avoidance. The 6.75 - 7.1 GHz band is primarily used to provide fixed microwave services, while radio astronomy studies are also performed in this band. The interference from the primary users can potentially hinder the astronomy studies (Rogers et al. 2005; Petrin and Steffes, 2004b). In such scenarios, the temporal characteristics of the primary users can be studied in order to identify periodic spectrum users, and methods can be developed that allow the passive services to dynamically use the spectrum when the primary user is absent. Besides collecting the spectrum data, a spectrum study mainly involves processing the data in order to detect the presence of signals and then analyzing the data in order to characterize the spectrum occupancy.

Previous works have used supervised techniques such as Naive Bayesian Classifier (NBC), Decision Trees (DT), Support Vector Machine (SVM), Linear Regression (LR)) and unsupervised algorithm such as Hidden Markov Model (HMM)) have not adequately characterized spectrum occupancy sufficiently. In this work, a novel frequency data grouping was done using power density plot techniques.

METHODOLOGY

The description of the measurement location and the equipment used is presented in the following sub-sections.

Measurement Location

The spectrum occupancy measurement site for this work is Maitama located in the Federal Capital Territory, Abuja, Nigeria. The google map of the site is shown in Fig. 1 while the Geographical Coordinates are shown in Fig. 2.



Fig. 1: Google Map of Measurement Location

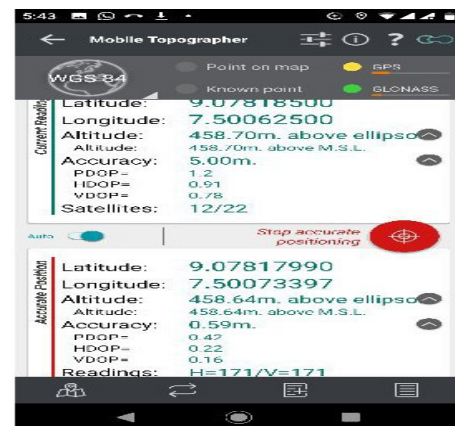


Fig. 2: Geographical Coordinates of the Site

Measurement Equipment

Aaronia Spectran HF-6065 V4 hand held spectrum analyzer was used in collecting PSD data. The spectrum analyzer has a frequency range of 10MHz to 6GHz implying that it has ability to capture data lying within the range when appropriate antennae is used. For this work, an Omni directional antennae having a range of 10MHz to 3GHz and a Dell vPro laptop Core i7 on Windows 10 with 500GB HDD laptop connected via USB cable to the spectrum analyzer with an MCS software designed specifically to run on Aaronia Spectrum Analyzer was used. The entire equipment was connected to a backup system of 850VA inverter and a 200 AH deep cycle battery. The snapshot of the spectrum analyzer used is shown Plate 1.



Plate 1: Aaronia Spectran 6065 V4

Fig. 3 shows the block diagram of the measurement system while Table 2 shows the parameter configuration of the spectrum analyzer.

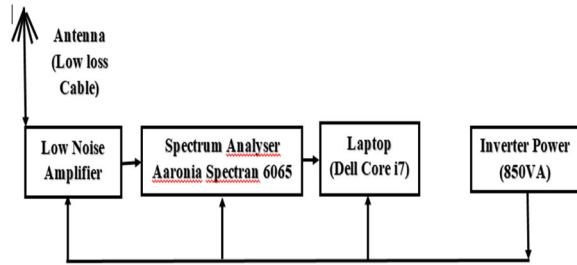


Fig. 3: Block diagram of Measurement System

Table 2: Parameter Configurations of Spectrum Analyzer

Parameter	Value
Frequency Range of the Analyzer	10MHz-6GHz
Frequency Range of the Antennae	10MHz-3GHz
Frequency Range for the Study	30-300MHz
Resolution Bandwidth (RBW)	100KHz
Video Bandwidth (VBW)	100KHz
Sweep Time	15.13sec
Detection Type	RMS
Sample Points	5401
Attenuation Factor	Auto

Data Analysis using Power Density Plots

The research dataset has a huge dimension of features (columns) that will make learning for a model difficult. The dataset has a total of 5712 rows of time slots and 5401 columns of frequency which makes a total of 30,850,512 data elements. To solve the dimensionality challenge, power density plots of each of the frequency was done. A density plot is a smoothed, continuous form of a histogram computed from data that indicates how each frequency and power (measured in decibel milliwatts) are distributed. The x-axis represents the variable power in dBm, while the y-axis represents the density estimate of the probability density function. On the x-axis, the probability density is expressed as probability per unit. The probability density function of a normal distribution is given by Equation 1.

$$f(x) = \frac{1}{\sqrt{\pi\sigma^2}} e^{-\frac{(x-\mu)^2}{2\sigma^2}} \quad (1)$$

Visual observation was used to group the plots by combining plots with similar structures. After the groupings, 12 distinct sub-bands used for modeling and prediction emerged as shown in Table 3.

Table 3: Frequency Groupings based on Power Density Plots

Frequency Sub Band	Frequency Range (MHz)
Band 1	30 – 47
Band 2	47.05 – 68
Band 3	68.05 - 74.80
Band 4	74.85-87.45
Band 5	87.5-108
Band 6	108.05 – 137
Band 7	137.05 – 144
Band 8	144.05 – 174
Band 9	174.05 – 200
Band 10	200.05 – 230
Band 11	230.05 – 267
Band 12	267.05 – 300

Artificial Neural Network Model Design

The ANN is made up of three layers: input, hidden layers, and output. ANN models were used to estimate functions and parameters by training a large proportion of datasets known as the training dataset. Neural Networks have the ability of performing complex nonlinear modeling of relationships without having a prior understanding of the underlying structures. The topology of the ANN consists of fully interconnected processing nodes with no interconnections between the nodes within the same layer.

Model Design of Input Layer

The input layer is the time series of the feature vector for the hourly spectral occupancy. For a new data input A , (A is not part of the ANN training process), the percentage occupancy can be obtained using the following model. The occupancy of the j^{th} frequency point in the data can be obtained from Equation 2.

$$Occupancy(j) = \left[\sum_{k=1}^N w_j(k) \phi_j(k) \right] \times 100 \quad (2)$$

where w_j is the weight vector of the j^{th} frequency point, $k = 1, 2, \dots, N$ and $N = 24$ (24 hours). ϕ_j is the input vector of the j^{th} frequency point obtained from A given as Equation 3.

$$\phi_j = \frac{\sum_{i=1}^I Q(t_i, f_j)}{I} \quad (3)$$

where I is the number of samples obtained from the time series data in an hour, t_i is the index of the time series data. Similarly,

$$Q(t_i, f_j) = \begin{cases} 1, & \text{if } A(t_i, f_j) \geq \lambda \\ 0, & \text{if } A(t_i, f_j) < \lambda \end{cases} \quad (4)$$

Autoregressive Neural Network Model

The Spectrum Occupancy Prediction Model has an autoregressive (AR) model, hence finding the AR model's coefficients is one of the most important tasks. Model selection,

model parameter determination, and model validation are all part of the AR modeling process. The synaptic weights and adaptive coefficients of a feed-forward network's activation function are used to calculate the AR model's coefficients. Several methods have previously been proposed for finding the coefficient of an AR model. These techniques include Kalman filter, Yule-Walker, Expectation-Maximization, Least Square, Burg, Forward-Backward algorithm. The traditional techniques ignores the errors that exist in the coefficient matrix. However, using a NN to estimate AR coefficients has several advantages over the traditional techniques. The coefficients are derived via an approach that simulates the nonlinear relationship between the input vector and the goal output utilizing operations inspired by organic neural systems in the human body. The model order was derived using the feature vector obtained from the acquired data. Thus, the goal is to estimate the model coefficients from the neural network.

The training data and the appropriate actual occupancy (calculated from the raw data) are sent to a NN-based function, together with the number of neurons in the hidden layer, to obtain the AR coefficients. The entire data set was randomly splitted into 70%, 15% and 15% for Training, Validation and Test dataset respectively. The order of the AR model is taken as the number of rows in the training data (dimension of the feature vector). The input layer is the time-series of the feature vector for the hourly spectral occupancy i.e 24 hours.

Based on the training data and the corresponding output data, an NN model trains itself to come up with the best weights which can generally be used by the AR model for unseen data. After computing the weights, the performance is first tested on the entire training data, after which it is tested on the test set. Obtaining the output due to the obtained weights is done by simply multiplying the weights by the target data. ANN was used to model the generated

data by AR model and to predict the future values of the time series as shown in Equation 5 and Fig. 4.

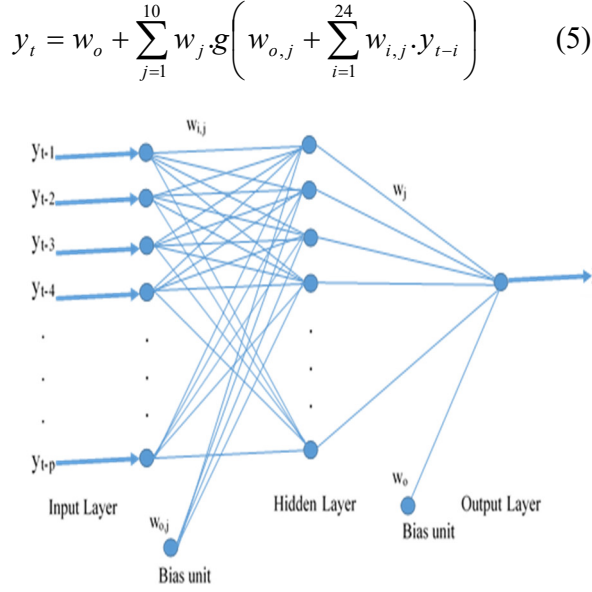


Fig. 4: Autoregressive Neural Network Model Design

RESULTS AND DISCUSSION

Tables 4, 5 and 6 show that the predicted model fits so well to the actual values for both training, testing and validation sets as can be seen in their correlation coefficients (R). The regression plots are also used to validate the network performance. Results show that the fit is reasonably good for all data sets, with regression (R) values of 98.89%, 92.29% and 92.46% for the training, validation and testing dataset respectively.

Table 4 shows a minimum performance prediction for the training dataset of 93.96% in sub band 1 and a maximum prediction of 100% in sub bands 9 and 10.

Table 4: Training Performance for Spectrum Occupancy Prediction

Sub-Bands	Frequency Range (MHz)	%
Band 1	30 – 47	93.96
Band 2	47.05 – 68	99.88
Band 3	68.05 - 74.80	99.97
Band 4	74.85-87.45	99.92
Band 5	87.5-108	99.18
Band 6	108.05 – 137	99.76
Band 7	137.05 – 144	98.60
Band 8	144.05 – 174	99.99
Band 9	174.05 – 200	100.00
Band 10	200.05 – 230	100.00
Band 11	230.05 – 267	99.95
Band 12	267.05 – 300	95.45
Average		98.89

Table 5 shows a minimum performance prediction for the validation dataset of 83.29% in sub band 4 and a maximum prediction of 97.37% in sub bands 7.

Table 5: Validation Performance for Spectrum Occupancy Prediction

Sub-Bands	Frequency Range (MHz)	%
Band 1	30 – 47	91.37
Band 2	47.05 – 68	95.34
Band 3	68.05 - 74.80	80.50
Band 4	74.85-87.45	83.29
Band 5	87.5-108	96.29
Band 6	108.05 – 137	90.00
Band 7	137.05 – 144	97.37
Band 8	144.05 – 174	96.65
Band 9	174.05 – 200	96.62
Band 10	200.05 – 230	90.55
Band 11	230.05 – 267	93.99
Band 12	267.05 – 300	95.45
Average		92.29

Table 6 shows a minimum performance prediction for the test dataset of 80.98% in sub band 10 and a maximum prediction of 97.67% in sub bands 7 and therefore band 7 is the most reliable for decisions on Cognitive Radio deployment.

Table 6: Test Performance for Spectrum Occupancy Prediction

Sub-Bands	Frequency Range (MHz)	%
Band 1	30 – 47	84.27
Band 2	47.05 – 68	95.36
Band 3	68.05 - 74.80	95.75
Band 4	74.85-87.45	97.02
Band 5	87.5-108	94.87
Band 6	108.05 – 137	90.06
Band 7	137.05 – 144	97.67
Band 8	144.05 – 174	96.57
Band 9	174.05 – 200	90.36
Band 10	200.05 – 230	80.98
Band 11	230.05 – 267	96.66
Band 12	267.05 – 300	89.98
	Average	92.46

Table 7: Test Performance for Spectrum Occupancy Prediction

BANDS	FREQUENCY SUB BANDS (MHz)	ACTUAL (%)	PREDICTED (%)	DIFFERENCE (%)	ACCURACY (%)
Band 1	30-47	43.0269	42.9399	0.087	91.3
Band 2	47.05-68	34.4264	34.3203	0.1061	89.39
Band 3	68.05-74.8	34.2628	34.2229	0.0399	96.01
Band 4	74.85-87.45	34.1166	34.1067	0.0099	99.01
Band 5	87.50-108	31.1067	31.0464	0.0603	93.97
Band 6	108.05-137	28.2962	28.2839	0.0123	98.77
Band 7	137.05-144	23.3524	23.3784	0.026	97.4
Band 8	144.05-174	27.7163	27.6858	0.0305	96.95
Band 9	174.05-200	25.7852	25.8057	0.0205	97.95
Band 10	200.05-230	24.5455	24.5668	0.0213	97.87
Band 11	230.05-267	18.6279	18.6586	0.0307	96.93
Band 12	267.05-300	18.1455	18.1909	0.0454	95.46
		343.4084	343.2063	0.4899	
	AVERAGE	28.6174	28.6005	0.0168	98.32

Table 7 shows the actual and NN predicted proportion of spectrum occupancy and also the performance accuracy. Best prediction occurred in sub band 4 with an accuracy of 99.01% while the lowest accuracy of 89.39% occurred in sub band 2. Overall, for the entire band of study (30-300 MHz) performance accuracy is 98.32%.

CONCLUSION

A new hybrid model for spectrum occupancy prediction was developed using ensembles of ANN and AR models comprising of both nonlinear and linear models respectively. This is because real-world problems are complex and no single model can capture patterns equally well. A hybrid model is

more robust with regards to possible structural change in the data.

Clearly, band 1 had the highest actual and predicted spectral occupancy values and therefore should be avoided for Cognitive Radio (CR) deployment while sub band 11 and 12 have the least actual and predicted spectral occupancy and may be considered for CR deployment. The performance of the Neural Network prediction model reveals accuracy of 92.46% to an unseen test dataset, an accuracy of 98.89% on the training dataset and an accuracy 92.29% to the validation dataset.

REFERENCES

- Akyildiz I. F., Lee, W.Y., Vuran, M. C., & Mohanty S. (2006). Next Generation/Dynamic Spectrum Access/Cognitive Radio Wireless Networks: A Survey. *Elsevier Computer Networks Journal*, 50(13), 2127-2159.
- Dame E (2001). The Dutch UMTS Auction in Retrospect. *CESifo Group Technical Report*.
- Doerr C., Grunwald D., & Sicker D. C. (2008). Dynamic Control Channel Management in Presence of Spectrum Heterogeneity. In *IEEE Military Communications Conference, MILCOM*, 1–8.
- Ellingson S. (2005). Spectral Occupancy at VHF: Implications for Frequency-Agile Cognitive Radios. *IEEE Vehicular Technology Conference*, 2(1), Dallas, 1379-1382.
- Gupta A., & Jha R. K. (2015). A survey of 5G Network: Architecture and Emerging Technologies. *IEEE Access*, 3(1), 1206-1232.
- Hoffman J. R., & Matheson R. J. (2005). RSMS Measurement and Analysis of LMR Channel Usage. *International Symposium on Advanced Radio Technologies*, 13-19, Boulder, CO, USA.
- Kyeremateng-Boateng H., Conn M., Josyula D., & Mareboyana M. (2020). Prediction of Radio Frequency Spectrum Occupancy, *2020 IEEE 19th International Conference on Trust, Security and Privacy in Computing and Communications (TrustCom)*, 2020, pp. 2028-2034, doi: 10.1109/TrustCom50675.2020.00278
- Matheson R., & Morris A. C. (2012). The Technical Basis for Spectrum Rights: Policies to enhance Market Efficiency. *Telecommunications Policy*, 36(9), 783-792.
- McHenry M. A., Tenhula P. A., McCloskey D., Roberson D. A., & Hood C. S. (2006). Chicago Spectrum Occupancy Measurements & Analysis, and a Long Term Studies Proposal. *Proceedings of Workshop on Technology and Policy for Accessing Spectrum (TAPAS)*, Boston, USA.
- Mishra A., Varshney G., & Karandik ar, A. (2012). Analysis of the 3G and BWA Auctions in Indian. *Proceedings of ITS India*, 1(1), 1-15.
- Oluwafemi I. B., Bamisaye A. P., & Faluru M.A. (2021). Quantitative Estimation of TV White Space in Southwest Nigeria. *TELKOMNIKA Telecommunication, Computing, Electronics and Control Journal*, 19(1), 36-43.
- Peha J. M. (2009). Sharing Spectrum through Spectrum Policy Reform and Cognitive Radio. *Proceedings of the IEEE*, 97(4), 708-719.
- Petrin A., & Steffes P. G. (2005). Analysis and Comparison of Spectrum Measurements Performed in Urban and Rural Areas to Determine the Total Amount of Spectrum Usage. *International Symposium on Advanced*

Radio Technologies, Boulder, CO, USA, 9-12.

- Petrin A., & Steffes P. G. (2004a). Measurement and Analysis of Urban Spectrum Usage. *Proceedings of International Symposium on Advanced Radio Technologies*, Boulder, CO, USA), 45-48, NTIA Special Publication SP- 04-409.
- Petrin A., & Steffes P. G. (2004b). Study of Spectrum Usage and Potential Interference to Passive Remote Sensing Activities in the 4.5 cm and 21 cm Bands. *IEEE International Geoscience and Remote Sensing Symposium*, 3(1), Anchorage, Alaska, USA, 1679- 1682.
- Re M., & Valentini G. (2012). Ensemble Methods: A Review, *Advances in Machine Learning and Data Mining for Astronomy*. Chapman & Hall, 563-594.
- Rogers A., Salah J., Smythe D., Pratap P., Carter J., & Derome M. (2005). Interference Temperature Measurements from 70 to 1500 MHz in Suburban and Rural Environments of the Northeast. *IEEE International Symposium on New Frontiers in Dynamic Spectrum Access Networks*, Baltimore, MD, USA, 119-123.
- Seflek İ., & Yıldız E. (2019). Evaluation of Spectrum Occupancy and Comparison for Three Different Regions. *Journal of Fundamentals of Applied Science*, 11(1), 40-64.

STRUCTURAL ASSESSMENT OF A LATTICE TOWER IN FEDERAL CAPITAL TERRITORY, ABUJA

Auta S.M., Okunyomi O.O., & Kolo, D.N.

Civil Engineering Department, Federal University of Technology, Minna, Nigeria

E-mail: (oladipupo.okunyomi@yahoo.com)

Abstract

Since the licensing of GSM operators in Nigeria from 2001, there was an astronomical increase in construction and maintenance of telecommunications towers. In a bid to reduce maintenance cost, tower sharing was adopted by some telecommunication providers. The Nigerian Communications Commission guideline for installation of masts and towers stipulates that all lattice towers should be checked for their structural health status every five years. This requirement has promoted this research work. The objective of the study includes selection of a lattice tower with weakest parameters, determine the tower's structural stability and its utilization percentage. A 45m tower, with 3-legs, erected over 8 years and shared by three telecommunication operators in the Federal Capital Territory (FCT) was selected. Audit was conducted on the tower and its foundation. There were no warped member and no visible crack on the tower foundation. The average compressive strengths of the stub columns determined using the digital Schmidt hammer were 25.1, 25.9 and 25.9 N/mm² for legs A, B and C. From the structural analysis using the EPA model, the tower utilization percentage was found to be at 59.4% after optimization. The STAAD pro. V8i analyses showed that the utilization ratio of the tower members is ≤ 1 . Furthermore, design properties for the tower members are less than the properties of the actual tower members used and there was no failed member identified after the structural analysis. In conclusion, the lattice tower can be said to be stable and fit for continuous use.

Keywords: EPA model, lattice tower, stub column, tower audit, tower sharing

INTRODUCTION

In the recent past, the number of telecommunication towers has risen astronomically due to licensing of more network providers like Globacom, MTN, Airtel and Etisalat (Okonji, 2013). This is due to the growing demand for wireless and broadcast communication which has prompted a dramatic increase in communication tower construction and maintenance. Failure of such structures is however a major concern (Sharma *et al*, 2015). Tower sharing which involves sharing one tower by two or more network operators has increased in a bid to reduce maintenance cost. Such towers may need to be strengthened or made taller to support several sets of antennas (GSMA publication, 2012). It is therefore extremely important that towers are effectively maintained to

ensure continued safety and efficient operation throughout their lifetime.

In recent years, a number of tower failures caused by heavy rains and strong windstorms were recorded in Nigeria. These failures resulted in great economic loss and loss of lives. Another problem the telecommunications towers is facing is the upkeep of the aging towers along with staying within a maintenance budget that is decreasing (Sullen, 2015).

The Nigeria Communication Commission (NCC) 2009, specified that major inspections shall be performed at least once in every 5 years for self-supporting towers. The assessment of structural integrity of the selected lattice tower will help determine stability of the selected tower. It will further show the threat posed by poorly maintained towers and their potential danger to life and properties in their host communities.

METHODOLOGY

The materials used for this study includes the following.

- digital Schmidt hammer
- mechanical toolbox
- Microsoft office suite
- STAAD pro V8i software
- measuring tape
- personal protective equipment.

This research work involved tower selection, thorough physical inspection of the selected tower, non-destructive test on tower's stub column using Schmidt hammer and structural analyses of the entire towers using

the effective projected area (EPA) model and STAAD pro. V8i software.

The tower selected has been in service for over eight years and was previously used by one telecoms operator (9mobile). However, it was acquired by an infrastructure provider (IHS), who leased it to two more telecoms operators (Airtel and MTN). This indicates that tower sharing is now taking place on a tower previously erected to be used by a single telecom operator. The tower height is 45m supported on three legs and located in Abuja-FCT as shown in Table 1. Relevant documents (Site approved drawing, Soil test report, Tower drawing) were obtained to aid the tower modelling, design, and analyses.

Table 1: Details of selected tower

Item	Description
Site Identification	B0653 (IHS_ ABJ_0704E)
No. of Operators	3
Site Location	Plot 7, Unity Hill Estate, Behind Sunny-Ville Estate, Dakwo District, FCT, Abuja, FCT
Site Coordinates	Latitude: 8.97312, Longitude: 7.43745
Tower Manufacturer	Mast Projects
Type of Tower	Medium duty Lattice Tower
Tower Design Capacity	12 m ²
Tower Height	45m
Tower Top Rating	1.2m ² /m spread over the upper 10m of tower
Age	8 years
Tower legs	3 legs

FOUNDATION AUDIT USING SCHMIDT HAMMER

A non-destructive test was carried out on the tower stub columns to determine the foundation compressive strength. The test was carried out using a digital Schmidt hammer. The tower legs were labelled alphabetically from A-C in anticlockwise direction for easy referencing.

Member's Audit

The tower audit encompasses a thorough inspection of the tower members and bracings, the bolts and nuts conditions at the connections, the state of other tower accessories like the access ladder, rest platforms, paints, aviation warning lights, earth cables and also records of all the telecom equipment installed on the tower in presented in Table 2.

Table 2: Tower Antenna Audit

Antenna Type	Diameter (mm)	Total Number
GSM 1	2500 x 300 x 200	3
GSM 2	1500 x 170 x 150	8
GSM 3	1300 x 150 x 100	11
RRU	480 x 290 x 180	17
MW 1	300.00	2
MW 2	600.00	7

Structural Analysis using EPA Model

The effective projected area (EPA) model is computed using the Microsoft excel spreadsheet. It is safe to assume that the effect of wind forces on the exposed areas of the antennas gives a quick overview of the present load exerted on the tower since the self-weight of the antennas to the tower is negligible. A typical 0.6m diameter antenna weighs 14 kg compared to tower's maximum uplift force of 890 kN per leg and tower mass of 7582 Kg.

The model is therefore based on calculations of the overall EPA of the antennas against the tower capacity. The dimensions of each antenna and their respective installation heights are recorded.

The result obtained is rated against the tower's design capacity to determine the percentage of tower utilization. The tower loading is optimized using the local basic wind speed as provided by the Nigeria Meteorological Agency.

A tower whose utilization percentage falls below 100% after optimization is termed satisfactory while that whose utilization

exceed 100% is termed overloaded. An overloaded towers is recommended for load shedding according Etisalat Tower Specification (2012).

Structural analysis using STAAD Pro. V8i

The STAAD pro. V8i stands for Structural Analysis and Design computer programme. It is a software that is used for analysing and designing structures like buildings, towers, bridges, industrial, transportation and utility structures. It enables 3D modelling of steel structures and aids structural analyses. The load considered includes tower's self-weight as presented in Table 3, equipment load, wind load on the antennas and wind intensity on the tower members. The tower members are designed to BS 5950-1: 2000 (EN 1993-1-8)

The software has a friendly user interface. The tower model starts with the setting-out of the structure in a grid system. The dimensions are defined, subsequently the nodes are connected with beams. The topmost layer is drawn inside the base grid, elevated. Once the simple model is drawn, the tower members are defined with material specifications using the tower assembly drawing. Finally, the tower is loaded with calculated loads.

STAAD Pro can generate quite a large range of outputs. For this research work, the outputs are limited to the utilization ratio on the tower members and safety of the tower.

Table 3: Equipment loading NA means not applicable

S/N	Description	Numbers	Length (mm)	Width (mm)	Thickness (mm)	Weight (Kg)	Total weight (Kg)	Total weight (KN)
1	GSM 1	3	2500	300	200	25	75	0.75
2	GSM 2	8	1500	170	150	20	160	1.6
3	GSM 3	11	1300	150	100	10	110	1.1
4	RRU	17	480	290	180	15	255	2.55
5	MW 1	2	300	NA	NA	10	20	0.2
6	MW 2	7	600	NA	NA	14	98	0.98

Wind pressure on the tower is calculated based on BS 6399-2 (1997) (EN 1991-1-4). It takes into consideration local basic wind speed (V_b) and three multiplying factors (S_1 , S_2 , S_3) to obtain the design wind speed (V_s). The multiplying factors for topography, height above ground, and structure life represent S_1 , S_2 , and S_3 respectively. The values for the multiplying factors were obtained from the reinforced concrete designer's handbook by Reynolds and Steedman (1998).

Thereafter, the wind pressure per node is calculated using the equation 1.

$$Wk = 0.613V_s^2 \quad (1)$$

as presented in Table 4.

Where W_k = wind pressure.

V_s = design wind speed

The wind pressures obtained are applied vertically on tower member in STAAD pro. V8i.

Table 4: Wind Pressure Calculation

Height (m)	Abuja Basic Wind Speed (v_b) (m/s)	Topography Multiplying Factor (s_1)	Height Above Ground and Wind Braking Multiplying Factor (s_2)	Life of Structure (s_3)	Design Wind Speed (v_s) (m/s)	Wind Pressure (w_k) (n/m ²)	Wind Pressure (w_k) (kn/m ²)
2	35	1	0.78	1	27.3	456.86277	0.46
4	35	1	0.78	1	27.3	456.86277	0.46
6	35	1	0.79	1	27.65	468.6522925	0.47
8	35	1	0.79	1	27.65	468.6522925	0.47
10	35	1	0.9	1	31.5	608.24925	0.61
12	35	1	0.9	1	31.5	608.24925	0.61
14	35	1	0.9	1	31.5	608.24925	0.61
16	35	1	0.94	1	32.9	663.51733	0.66
18	35	1	0.94	1	32.9	663.51733	0.66
20	35	1	0.96	1	33.6	692.05248	0.69
22	35	1	0.96	1	33.6	692.05248	0.69
24	35	1	0.96	1	33.6	692.05248	0.69
26	35	1	0.96	1	33.6	692.05248	0.69
28	35	1	0.96	1	33.6	692.05248	0.69
30	35	1	1	1	35	750.925	0.75
32	35	1	1	1	35	750.925	0.75
34	35	1	1	1	35	750.925	0.75
36	35	1	1	1	35	750.925	0.75
38	35	1	1	1	35	750.925	0.75
40	35	1	1.03	1	36.05	796.6563325	0.80
42	35	1	1.03	1	36.05	796.6563325	0.80
44	35	1	1.03	1	36.05	796.6563325	0.80
46	35	1	1.03	1	36.05	796.6563325	0.80

The wind load on the equipment is generated from the force the wind exerts on the projected surface area of the equipment and it is obtained using the equation 2

$$F = c_f \times W_k \times A \quad (2)$$

Where c_f = force coefficient,

W_k = wind pressure and

A = Area

The force values obtained per equipment are applied perpendicularly to the tower

member where the equipment is installed. The Table 5 shows the forces acting on each type of antenna.

Table 5: Wind Load on Equipment

Description	Length (h) (mm)	Width (b) (mm)	Thickness (a) (mm)	h/b	a/b	Force coefficient (cf)	Area (A) (m ²)	Force (F) (KN)
GSM 1	2500	300	200	8.33	0.67	1.7	0.75	1.02
GSM 2	1500	170	150	8.82	0.88	1.7	0.26	0.35
GSM 3	1300	150	100	8.67	0.67	1.7	0.20	0.26
RRU	480	290	180	1.66	0.62	1.2	0.14	0.13
MW 1	300	NA	150	NA	NA	1.2	0.07	0.07
MW 2	600	NA	300	NA	NA	1.2	0.28	0.27

NA means not applicable

RESULTS AND DISCUSSION

It was observed from the physical inspection that the tower and its accessories are in good condition with the only exception being the

tower paint. The Nigeria Civil Aviation Authority (NCCA) requires red and white paint of the telecommunications tower to be bright for pilots' visibility. Table 6 provides description on the conditions of the tower and its accessories.

Table 6: Tower Audit Result

Item	Description
Structural Members	No warped member detected
Access Ladder	Accessible and railings are in good condition
Rest Platforms	Gratings on platforms are not blocked and do not accumulate water or not corroded
Bolts and Nuts	Bolts and nuts are not loose and no missing bolts
Aviation Warning Light	Aviation warning lights (AWL) are in place and functional
Earthen cables	Copper cables for tower earthen
Antennas	Antennas properly clamped
Tower paint	Faded
Thunder Arrestor	Properly bolted

Tower Foundation Audit

The average compressive strengths of the tower legs are presented in Table 7. The compressive strength of the stub columns met the foundation design specification as

seen on the site drawing approval with mean compressive strengths of 25.1, 25.9 and 25.9 N/mm² for legs A, B and C respectively. The physical conditions of the stubs are in good condition as there was no visible cracks or blisters on them.

Table 7 Compressive Strength of Stub Columns

S/N	Rebound Values (R)		
	Leg A	Leg B	Leg C
1	26	28	42
2	27	30	28
3	35	27	35
4	30	25	27
5	32	33	30
6	33	30	31
7	25	28	28
8	25	30	26
Mean Compressive strength X (R)	28.5	29	29
Mean Compressive strength F (N/mm ²)	25.1	25.9	25.9

Structural analysis using EPA Model

The tower utilization percentage after optimization with local wind speed stands at

59.4% as presented in Table 8 The tower loading can therefore be declared satisfactory.


Table 8 Tower Utilization Percentage

Parameters	Result
Tower Height	45m
Tower Capacity	12m ²
Tower is rated for top	10m
Summation Antennas EPA	8.09m ²
Lever arm	40m
Percentage utilization based on EPA	67.40%
Design Wind Speed	40m/s
Abuja Basic Wind Speed	35m/s
Optimized Tower Utilization	59.4%

Structural analysis using STAAD Pro. V8i

From the report generated using STAAD Pro. V8i, the utilization ratio (actual ratio to allowable ratio) of all the tower members are ≤ 1 (less or equal to one). The average

percentage of tower utilization is 83.52%. Also, the sizes of the tower members generated due to the present load exerted on the tower are less than the actual size of tower members. Finally, there is no failed member identified after the analysis as presented in Fig. 1.

	Job File	Sheet No	16	Rev
	Software licensed to			
	File			
Job File 45m Tower Modelling/Analysis				Rev
By 0.0.0				Date 26-May-21
Client MENG Project Research				End 0.0.0
File 45m Tower Modelling and				Date/Time 09-Jun-2021 12:29

Utilization Ratio Cont...

Beam	Analysis Property	Design Property	Actual Ratio	Allowable Ratio	Ratio (Act./Allow.)	Clause	L/C	Ax (cm ²)	Ix (cm ⁴)	Iy (cm ⁴)	Iz (cm ⁴)
356	ISA70X70X6	ISA60x50x3	0.929	1.000	0.929	BS-4.8.3.3.1	5	2.950	2.891	11.409	0.089
357	ISA70X70X6	ISA60x50x3	0.996	1.000	0.996	BS-4.8.3.3.1	4	6.250	10.081	41.010	0.521
358	ISA70X70X6	ISA60x50x3	0.823	1.000	0.823	BS-4.8.3.3.1	5	2.950	2.891	11.409	0.089
359	ISA70X70X6	ISA65x45x3	0.936	1.000	0.936	BS-4.8.3.3.1	5	2.640	2.072	8.252	0.079
360	ISA70X70X6	ISA65x45x3	0.928	1.000	0.928	BS-4.8.3.3.1	4	6.250	10.081	41.010	0.521
361	ISA70X70X6	ISA65x45x3	0.857	1.000	0.857	BS-4.8.3.3.1	4	6.250	10.081	41.010	0.521
362	ISA70X70X6	ISA65x45x3	0.800	1.000	0.800	BS-4.8.3.3.1	5	2.640	2.072	8.252	0.079
363	ISA70X70X6	ISA60x50x3	0.960	1.000	0.960	BS-4.8.3.3.1	4	5.750	7.871	31.944	0.479
364	ISA70X70X6	ISA65x45x3	0.786	1.000	0.786	BS-4.8.3.3.1	5	2.640	2.072	8.252	0.079
365	ISA70X70X6	ISA60x50x3	0.833	1.000	0.833	BS-4.8.3.3.1	4	5.750	7.871	31.944	0.479
366	ISA70X70X6	ISA60x40x3	0.917	1.000	0.917	BS-4.8.3.3.1	5	2.340	1.435	5.730	0.070
367	ISA70X70X6	ISA60x60x4	0.895	1.000	0.895	BS-4.8.3.3.1	4	4.710	6.558	26.074	0.251
368	ISA70X70X6	ISA65x35x3	0.891	1.000	0.891	BS-4.8.3.3.1	5	2.030	0.939	3.787	0.061
369	ISA70X70X6	ISA60x60x4	0.782	1.000	0.782	BS-4.8.3.3.1	4	4.710	6.558	26.074	0.251
370	ISA70X70X6	ISA65x35x3	0.886	1.000	0.886	BS-4.8.3.3.1	5	2.030	0.939	3.787	0.061
371	ISA60X60X5	ISA65x35x3	0.921	1.000	0.921	BS-4.8.3.3.1	5	2.030	0.939	3.787	0.061
372	ISA60X60X5	ISA60x60x4	0.625	1.000	0.625	BS-4.8.3.3.1	4	4.710	6.558	26.074	0.251
373	ISA60X60X5	ISA60x50x4	0.857	1.000	0.857	BS-4.8.3.3.1	4	3.880	3.742	14.782	0.207
374	ISA60X60X5	ISA65x35x3	0.803	1.000	0.803	BS-4.8.3.3.1	5	2.030	0.939	3.787	0.061
375	ISA60X60X5	ISA65x35x3	0.722	1.000	0.722	BS-4.8.3.3.1	5	2.030	0.939	3.787	0.061
376	ISA60X60X5	ISA60x50x3	0.820	1.000	0.820	BS-4.8.3.3.1	4	2.950	2.891	11.409	0.089
377	ISA60X60X5	ISA60x20x3	0.327	1.000	0.327	BS-4.8.3.3.1	5	1.120	0.159	0.647	0.034
378	ISA60X60X5	ISA60x40x3	0.934	1.000	0.934	BS-4.8.3.3.1	4	2.340	1.435	5.730	0.070
379	ISA60X60X5	ISA60x20x3	0.294	1.000	0.294	BS-4.9	3	1.120	0.159	0.647	0.034
380	ISA60X60X5	ISA60x20x3	0.558	1.000	0.558	BS-4.8.3.3.1	4	1.120	0.159	0.647	0.034
381	ISA60X50X6	ISA60x20x3	0.889	1.000	0.889	BS-4.8.3.3.1	4	1.120	0.159	0.647	0.034
382	ISA60X50X6	ISA60x20x3	0.153	1.000	0.153	BS-4.8.3.3.1	3	1.120	0.159	0.647	0.034
383	ISA60X50X6	ISA60x20x3	0.392	1.000	0.392	BS-4.8.3.3.1	4	1.120	0.159	0.647	0.034

Failed Members

There is no data of this type.

Fig 1: Extract of STAAD Pro computation sheet

CONCLUSION

The structural assessment of a lattice tower was presented. From the study, the following can be deduced:

- The tower's physical condition is satisfactory. No cracks on the foundation and no deformed member seen on the tower. However, the tower coating (paint) was found to have worn out hence would need repainting.
- The structural analysis of the tower shows that members are in stable condition and within permissible specifications.

- In view of paragraphs (i) and (ii) above, the tower can therefore be considered fit for continuous use.

REFERENCES

- British Standard Institute, (1997). BS 6399-2: loading for buildings. Wind loads. Retrieved June 10, 2021
- British Standard Institute, (2000). BS 5950-1: design, fabrication, and erection of structural steelwork. Retrieved June 10, 2021
- Etisalat Tower Specification (2012). Technical specifications for the design and manufacture of telecommunications lattice towers of

- modular sections and monopoles for use in Nigeria. Issue 1 Version 2.0. May 2012.
- GSMA publication (2012). Mobile-Infrastructure-sharing. pp 48. <https://www.gsma.com/publicpolicy/wp-content/uploads/2012/09/Mobile-Infrastructure-sharing.pdf>
- Nigeria Communication Commission (NCC) 2009, Guidelines on Technical specifications for the Installation of telecommunications masts and towers. Issued April 2009.
- Okonji, E. (2013). THISDAY newspaper online publication. Nigeria: Menace of Indiscriminately Mounted Communication Masts. May 23. pp 1.
- Reynolds, C.E. and Steedman, J.C. (1998). Reinforced concrete designer's handbook (10th ed.). London, United Kingdom. E & FN Spon, Taylor & Francis group. 11 New Fetter Lane, London EC4P 4EE.
- Sharma, K.K., Duggal, S.K., Singh, D.K., & Sachan, A.K. (2015), Comparative Analysis of Steel Telecommunication Tower Subjected to Seismic & Wind Loading. *Civil Engineering and Urban Planning: An International Journal* (CiVEJ) Vol.2, No.3. pp 15-33.
- Sullen E.J. (2015). Analysis of radio communication towers subjected to wind, ice and seismic loadings. A Thesis Presented to the Faculty of the Graduate School of the University of Missouri – Columbia.

COMPARATIVE STUDY ON CO₂ CAPTURE USING ACTIVATED CARBON FROM SUGARCANE BAGASSE AND ZEOLITE (ZSM-5)

Abdullahi, A.¹; *Alhassan M.²; Alhassan. B.³; Audu, O. A.²; Ayobamiji C. I.²; Isah, A. G.²; & Kovo, A. S.²

¹Maryam Abacha American University of Niger, Maradi, Niger Republic.

²Chemical Engineering Department, Federal University of Technology Minna, Nigeria¹

³Entrepreneurship Development Centre, Kwara State Polytechnic, P.M.B 1375, Ilorin, Kwara state Nigeria. E-mail: *moh.alhass@futminna.edu.ng

Abstract

Global warming is the main driving force that led to climate change as a result of the release of greenhouse gases such as carbon dioxide (CO₂) into the atmosphere. To prevent this from continuing happening, the amount of CO₂ in the atmosphere must be reduced to at least a level below 1990's. To achieve this, several technology such as adsorption using solid adsorbent like activated carbon from Sugarcane Bagasse (SB) (a tremendous waste from sugarcane which would have ended up littering the environment as experienced in developing countries) and Zeolite (ZSM-5) were proposed and developed. However, there is need to compare the adsorptive capacities of these adsorbents to inform their choice. To achieve that, activated carbon from (SB) was produced; while ZSM-5 was procured, activated using Zinc chloride (ZnCl₂) and used for CO₂ adsorption studies. The properties of the activated carbons were determined using standard techniques and the result shows that the activated carbon produced from SB has a pore volume of $1.632 \times 10^{-1} \text{ cm}^3$, pore size of 14.74 \AA and surface area of $304.027 \text{ m}^2/\text{g}$, while that of the ZSM-5 are: SiO₂/Al₂O₃ mole ratio of 80/20, the nominal cation form is Ammonium, 0.05 % of Na₂O, surface area of $425 \text{ m}^2/\text{g}$ and an estimated pore size of $5.4 - 5.6 \text{ \AA}$. The performance of the adsorbents at 25°C was evaluated and compared using a cylindrical adsorption column and an analytical weighing balance. The result shows that the CO₂ adsorption increases with time till an equilibrium point was reached at 40 min where the adsorption capacity per gram of the activated carbon and ZSM-5 were found to be 35 mg and 30 mg respectively. The adsorption kinetics was found to obeys second-order kinetics with a regression (R^2) above 0.99. These results suggest that the activated carbon from SB is more effective than the ZSM-5 in CO₂ adsorption in this study.

Keywords: Activated carbon, Adsorption, Carbon capture, Kinetics, Sugarcane bagasse, Zeolite.

INTRODUCTION

The most widely acknowledged greenhouse gas generated from the day to day human endeavor is the carbon dioxide (CO₂), its contribution to global warming is well over 60% (Wu *et al.*, 2014). It is also the primary causes of climate change. The naturally generated CO₂ is never a threat to earth on its own but the anthropogenically emitted CO₂ which are entirely produced by the usage of fossil fuel has made it a threat. It has been estimated that if things remain the way

they are between the year 2010 and 2060, 282-701 gigatonnes of CO₂ will be generated through fossil fuel combustion.

The rising level of CO₂ in the atmosphere is now a widespread concern to the entire world. This has led to quite a number of researches in the area of CO₂ capture. These researches are focused toward eliminating or sequestering anthropogenically generated CO₂ (Creamer *et al.*, 2014). In a move towards mitigating global warming, Kyoto protocol stated that "It impels the European

Union and the Industrialized Nations (37 of them) to lower their greenhouse gas emission to at least a level lower than the average emitted in the 90's''(Yu *et al.*, 2012). The international Energy Agency (IEA) has set out to achieve the goal of $\pm 2^{\circ}\text{C}$ i.e. increment in temperature to be contained at 2°C as related to the pre-industrial era. In order to make this goal a realistic one, CO_2 capture and storage technology are needed (Yu *et al.*, 2012). Since the main producers of CO_2 are the energy generation plants that are powered by fossil fuel, this technology will therefore be quite effective in the energy sectors (EIA, 2021).

The developed technologies are mainly absorption (physical and chemical) and adsorption (physisorption and chemisorption). Each one of these technologies has its own shortcomings or weak points but adsorption (especially physisorption i.e. use of solid sorbents) seems to be the most preferred due to the factors like the surface area, regeneration energy etc. Examples of these sorbents are zeolites, activated carbon, metal organic framework etc (Yaumi *et al.*, 2017).

In terms of impurity removal and product recovery from purification processes, activated carbon is preferable due to their large surface area and affinity for the adsorption of heavy metals (Saleem *et al.*, 2012). There are more than enough materials that can be used as precursor for activated carbon production, as far as they are carbonaceous material with high combustion strength (David & Kopac, 2014). Materials commonly used in the production of Activated Carbon are sugarcane bagasse, wood, nut kernels, shells, etc. However activated carbon has been produced from sugarcane bagasse Zeolite has been used in CO_2 adsorption but limited information is available on the comparisons between the adsorptive capacities of the two adsorbent,

which is the focus of this research work. The precursor used in the production of the activated carbon in this work is sugarcane bagasse and the zeolite used is ZSM-5.

MATERIALS AND METHODS

Adsorbents:

The sugarcane Bagasse (SB) was collected from Badegi Sugarcane farm, in Bida, Nigeria and the variety of the sugarcane is S₉ C0959 and S₂₇B C0997. The particle size of the mixtures of these species had earlier been discussed in Alhassan *et al.* (2017). Zinc chloride (ZnCl_2) of analytical grade was obtained from sigma Aldrich, UK. Zeolite Ammonium i.e zeolite Socony Mobile -5 (ZSM-5) powders produced by Zeolite international was obtained through sigma Aldrich, UK. The Zeolite has characteristics white powder, with $\text{SO}_2 / \text{Al}_2\text{O}_3$ mole ration of 80:20, the nominal cation form of the Zeolite is ammonium, Na_2 of 0.05%. The surface area of the ZSM-5 is 425 m^2 and an estimated pore size of between 5.4 – 5.6 Å.

Synthesis of Sugarcane Bagasse Activated Carbon

Prior to carbonization, the Bagasse was thoroughly washed with water to remove any debris which may be present in it. The washed sample was then dried in a Gallenkamp oven operated at 105°C until constant weight was obtained. A sieve stack was arranged and particle size distribution of the SB was determine as described and earlier reported in Alhassan *et al.* (2017) where the bulk of sugarcane particle (87.87%) was found to be retained within the screen size range of 1.18mm to 0.18mm. This particle size of the SB was used in the production of sugarcane Bagasse activated carbon (SBAC).

About 1.6kg of the dried sample of the (SB) with particle size between 1.18-0.18 was placed inside a crucible and placed in a muffle furnace and the door was closed. Nitrogen was then passed through the inlet gas tube to flushed oxygen out of the system so as to create an inert condition for carbonization. The furnace was set to 480°C and heated at the rate of 10°C/min, the nitrogen flow rate of 1mL/second and held at 480°C for 1hr. The furnace was shut down and allowed to cool to room temperature. These carbonization conditions were based on the optimum condition for high yield of char (solid carbon) which were reported in (Alhassan and Andresen, 2013). The Sample was then removed from the furnace and placed in a desiccator. About 579g of SBC was recovered and activated with one molar (1M) solution of zinc chloride (ZnCl₂) by mixing at a reagent to sample mixture ratio of 1:1. The sample was left for 48 hr to allow the penetration of the impregnated ZnCl₂ solution into the pore of the SBC. To remove the excess ZnCl₂, the sample was thoroughly washed with distilled water and filtered. At each wash, the distillate pH was determined. The washing was stopped as soon as the distillate pH is neutral. The washed sample was then oven dried at 110°C to give sugarcane bagasse activated carbon (SBAC) which was used for the adsorption studies.

Characterization of Raw Sugarcane Bagasse and Activated Carbon.

The physical and chemical properties of the raw bagasse and the carbon produced before and after activation were determined using a standard method. The moisture and ash contents were determined using ASTM E871, ASTM E872 and ASTM D1102 respectively while the pH values were determine using ASTM D 3838-05(2011) procedure. Thermogravimetric analysis of

the sample was carried out using a thermal analyzer model: mettler Toledo TGA/STDA 857. Surface area and pore volume were determined using BET NOVA 42 00e Quantavhrome instrument. SEM; JSM-840A, Japan was used to determine the morphology and purity of the sample; SEM test Method (ASTM B487) was used to determine the morphology of the sample. PAN analytical X-ray, Philips analytical machine was used to determine crystallographic structure of the samples of the activated carbon produced at a scan rate of 2-100 °C per min. The spectra were analyzed using PC-APD diffraction software, while the functional groups present in the sample were determine using Fourier Transformed Infrared Spectroscopy (FTIR) model FT-IR-8400S (Shimadzu). These procedures as well as the results obtained were earlier reported in Alhassan *et al.* (2017) where the present report focuses on the comparison between CO₂ Adsorption capacity of SBAC and ZSM-5.

CO₂ Adsorption Experiment (sugarcane bagasse)

The gas adsorption column used in this experiment is cylindrical in nature, the adsorption column was held by a standing wooden support, the hose delivering CO₂ (from the gas cylinder) is connected to the base end of the column, the other end of the column i.e. the upper part has an open end where an exit hose can be fitted, the open end was well corked and an exit hose was connected through the opening at center of the hose (Alhassan *et al.*, 2017).

With the aid of an analytical weighing balance 1g. (5.4 cm bed height) of activated carbon were measured and placed in the column (with a foam support) and the gas cylinder's tap was opened at 1L/min and the

time of adsorption was varied (5, 10, 15...) min till q_e is achieved. This operation was carried out at ambient pressure and temperature. The same operation was repeated for 2g and 3g (10.8 and 16.2 cm bed heights) of activated carbon. The weight of the activated carbon samples were measured at the end of every run (i.e. 5 min) to ascertain the difference in weight of the activated carbon (sample) in order to determine the amount of CO_2 that has been adsorbed and the time of adsorption was equally determined.

CO₂ Adsorption Experiment (Zeolite)

The experiment procedure followed was as described for sugarcane bagasse and the amount of CO_2 adsorbed was determined using equation 1.

$$\text{Amount of CO}_2 \text{ adsorbed} = \frac{M_t(\text{mg}) - M_o(\text{mg})}{M_o(\text{g})} \quad (1)$$

where:

M_o = initial mass before adsorption

M_t = final mass after adsorption

Adsorption Isotherm

This is a way to represent the variations (isothermal) found in adsorption experiment i.e. the variation in the quantity of adsorbate taken up by an adsorbent at a constant temperature and at the equilibrium pressure of the adsorbed gas. Out of the several isothermal models in use for predicting the adsorption equilibrium distribution, the Langmuir and the Freundlich isotherm models (for pressure) are used in the analysis of the experimental data recorded. These models are shown in equations 2 and 3.

Langmuir:

$$\frac{p}{(\frac{x}{m})} = \frac{1}{b}p + \frac{1}{(ab)} \quad (2)$$

Freundlich:

$$\log\left(\frac{x}{m}\right) = \log a + \frac{1}{n} \log p \quad (3)$$

where:

P = pressure (mmHg) of CO_2

X = weight of CO_2 (g)

m = weight of solid adsorbent (g)

a , b and n represent constant values

These constant values depend on the nature and type of adsorbent and temperature. From a plot of $p/(x/m)$ against p and $\log x/m$ against $\log p$, the intercept and slope can be obtained which are in turn used to determine the constants.

Adsorption Kinetics

A lot of kinetic models exist which can be used in the modeling of gas adsorption (using activated carbon), some of which are Lagergren's pseudo-first order, Lagergren's pseudo-second order, Elovich, intra-particle diffusion etc. kinetic modeling is done at a constant temperature. Some factors (in independent processes) could control adsorption kinetics such as diffusion (bulk, film and intra-particle), chemical reaction, temperature, pH (Ifechukwu *et al.*, 2016, Kajjumba *et al.* 2018). The kinetic and equilibrium data generated in this work was fitted using the Lagergren's pseudo-first order, Lagergren's pseudo-second order models and the intra-particle diffusion models (Alhassan *et al.*, 2017).

Regression coefficient (R^2) value is a good accuracy test tool which helps in testing the conformity of the experimental result (Adilla *et al.*, 2013). This tool is used in this work.

Table 1: The Lagergren kinetic equations (Kajjumba *et al*, 2018)

Kinetic Equation	Linear Form	Plot Made
Pseudo-first order	$\log(q_e - q_t) = \ln q_e - k_1 t$	$\log(q_e - q_t)$ vs. <i>Time</i>
Pseudo-second order	$\frac{t}{q_t} = \frac{1}{(k_2^2 q_e^2)} + \frac{t}{q_e}$	t/q_t vs. <i>Time</i>
Intra-particle diffusion	$qt = kt^{\frac{1}{2}} + C$	qt vs $time^{\frac{1}{2}}$

Where:

q_e in mg/g represent the quantity of CO₂ adsorbed at equilibrium and q_t represent the quantity of CO₂ adsorbed at time t , C is the thickness of boundary layer, k_1 in (min⁻¹) and k_2 in (g/mgmin) represent the pseudo-first order and pseudo-second order rate constants, k in (mg/gmin^{1/2}) represent the diffusion rate. The plot of $\log(q_e - q_t)$ vs. *Time* gives k_1 , that of t/q_t vs. *Time* gives k_2 , while that of qt vs. $time^{1/2}$ gives k . slopes and intercepts of all the plots were evaluated.

RESULTS AND DISCUSSION

Carbon dioxide adsorption Capacity

The following bed heights of 5.4, 10.8 and 16.2 cm which represent 1, 2, and 3 grams of adsorbents were loaded into the column and the adsorption experiments were conducted at room temperature of 25° and the average values of the results are presented in Fig. 1. Fig. 1 shows vividly the relationship between the adsorbent loaded into the column and the quantity of CO₂ adsorbed. It was noticed from the graph (Fig. 1) that the quantity of CO₂ adsorbed increases as the time of adsorption increases, this continued till the 40th minute for the activated carbon (Fig. 1a) and 35th minutes for the zeolite (Figure 1b) which then flattens (the flattened portion of the graph could be as a result of adsorption capacity or equilibrium been

reached). Similar observation was reported in Adila *et al*; (2013) for activated carbons.

The effect of the variation in bed height does not pass unnoticed, the bed height is directly proportional to the CO₂ uptake of each gram of the adsorbents. at the bed heights of 5.4, 10.8 and 16.2 cm the CO₂ uptake are 35, 71 and 106mg for the activated carbon and 29, 61, and 90mg for the zeolite respectively. This is as a result of the increment in the number of active sites on the adsorbents (Alhassan *et al.*, 2016).

The adsorption capacity of the activated carbon for each of the masses 1, 2 and 3g are 35mg/g, 35.5mg/g and 35.33mg/g for activated carbon while for zeolite of the same masses (Fig. 1b) the capacities are 29, 30.5, and 30mg/g respectively. The adsorption capacity of the sugarcane bagasse activated carbon used in this work is a bit lesser when compared with that reported in (Alhassan *et al.*, 2017). This could be due to differences in the preparation approach. However, comparing the adsorption capacity of the activated carbon (Fig. 1a) and the zeolite (Fig. 1b), the activated carbon adsorbs more CO₂ than the zeolite when compared through the same time interval. This could be attributed to the large pore size exhibited by activated carbons. Similar observations were made by Abdulsalam and Alhassan (2018) where activated carbons

and zeolite were used to purify biogas generated from cow dung.

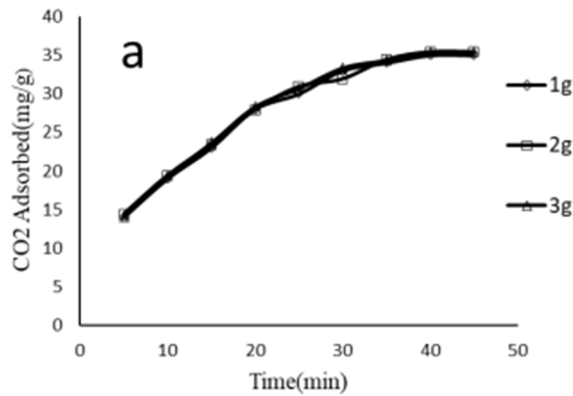


Fig 1: Graph of CO₂ adsorbed against time for (a) activated carbon and (b) Zeolite

Kinetic Analysis

Three kinetic models were used in the modeling of CO₂ adsorption onto activated carbon (synthesized from Sugarcane Bagasse) and zeolite, the kinetic parameter

obtained are presented as shown in Tables 2 and 3.

Pseudo-first-order kinetic model

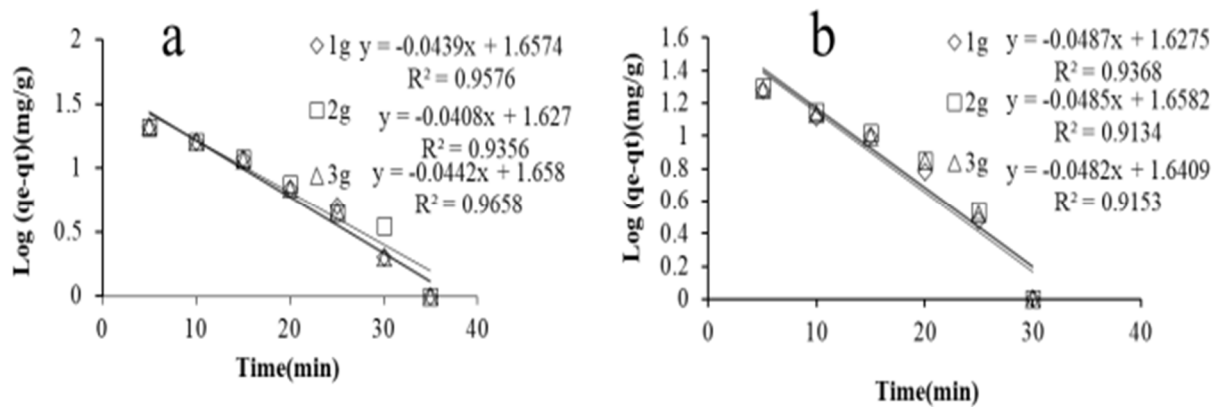
The linear form of the Lagergren kinetic model (pseudo-first-order) as shown in Table 1 was applied in fitting the adsorption behavior, and the result generated was plotted in a graph shown in Fig. 2. The results of the kinetic behavior of each of the masses, the regression coefficients and the adsorption equilibrium are tabulated in Tables 2 and 3. One of the most noticeable relationships in both graphs is that $\text{Log}(q_e - q_t)$ is inversely proportional to time for all masses of activated carbon and zeolite. Critically, considering the graphs and the factors tabulated in Tables 2 and 3, it was observed that the kinetic data fits into the three kinetic models with R^2 values greater than 0.9.

Table 2: kinetic Parameters for Activated Carbon

Kinetic models	Parameters	Masses (g)		
		1	2	3
Pseudo-first-order model	$(q_e)_{\text{actual}}$ (mg/g)	35	35.5	35.33
	K_1 (1/min)	0.101	0.0940	0.102
	$(q_e)_{\text{cal}}$ (mg/g)	45.349	42.364	45.499
	R^2	0.9576	0.9356	0.9658
Pseudo-second-order model	$(q_e)_{\text{cal}}$ (mg/g)	46.083	46.083	46.296
	K_2 (g/mgmin)	1.653×10^{-3}	1.71×10^{-3}	1.682×10^{-3}
	R^2	0.9925	0.9937	0.9943
	h (mg/gmin)	3.51	3.627	3.61
Intra-particle diffusion model	K (mg/gmin ^{1/2})	5.0063	4.9641	5.0397
	C (mg/g)	3.876	4.4117	4.0844
	R^2	0.9668	0.9733	0.964

Table 3: Kinetic Parameters for Zeolite

Kinetic models	Parameters	Masses (g)		
		1	2	3
Pseudo-first-order model	$(q_e)_{\text{actual}}$ (mg/g)	29	30.5	30
	K_1 (1/min)	0.112	0.112	0.111
	$(q_e)_{\text{cal}}$ (mg/g)	42.413	45.520	43.742
	R^2	0.9368	0.9134	0.9153
Pseudo-2econd-order model	$(q_e)_{\text{cal}}$ (mg/g)	42.017	44.444	43.103
	K_2 (g/mgmin)	1.453×10^{-3}	1.332×10^{-3}	1.437×10^{-3}
	R^2	0.9913	0.9907	0.991
	h (mg/gmin)	2.565	2.630	2.669
Intra-particle diffusion model	K (mg/gmin ^{1/2})	4.8734	5.1573	4.9921
	C (mg/g)	0.289	0.0049	0.4566
	R^2	0.9713	0.9765	0.9769

**Fig. 2:** graph of pseudo-first-order kinetic model for (a) activated carbon and (b) for zeolite)

Pseudo-Second-Order Kinetic Model

The pseudo-second-order kinetic model shown in Table 3 was also applied in fitting the adsorption behavior and the result generated was interesting, the plots of these results can be seen in Fig. 3. The results of the kinetic behavior (k_2) of each of the masses, the regression coefficients, the initial adsorption rate and the adsorption capacities are also tabulated in Table 2.

Comparing Fig. 3(a) and (b) with Table 2 and 3 it can be established that the adsorption experiments carried out in this work fits well into this kinetic model, the R^2 s for all masses both for activated carbon and zeolite are in accordance with literature i.e. above 0.90 and the initial adsorption rate is good, which if the experiments were to be carried out in higher temperatures should increase (Alhassan *et al.*, 2017).

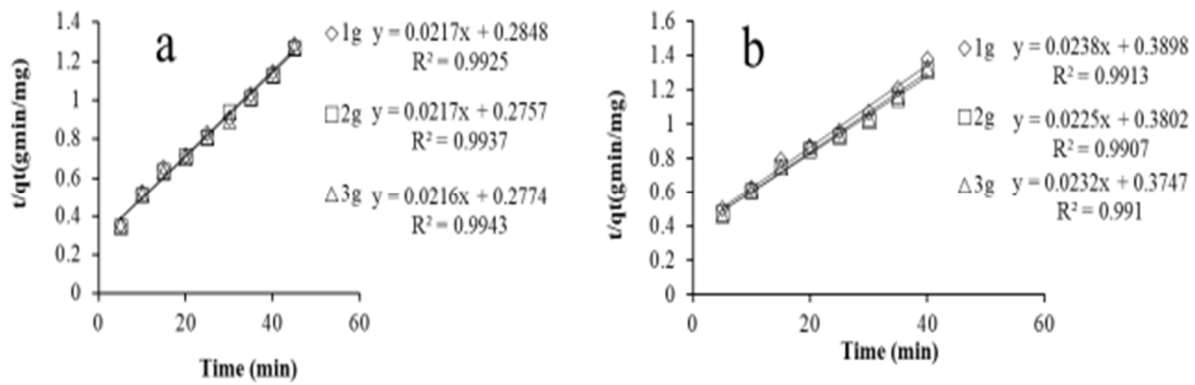


Fig. 3: Graph of pseudo-second-order kinetic model for (a) activated carbon and (b) zeolite

Intra-Particle Diffusion Model

The development of the intra-particle diffusion model was discussed in Adilla *et al.* (2013), this model is quite different from the kinetic models as it presents, the diffusion mechanics of the process. The equation for the model can be seen in Table 1 and the terms in the equation were identified.

The results of the diffusion rate (k) of each of the masses, the regression coefficients and the thickness of the boundary layer are tabulated in Table 2 and 3. Although the fitting of $R^2 \geq 0.9$ is statistically good from

Fig. 4 and can be used to make conclusions about the fitness of the model (Abdulsalam and Alhassan, 2018; Abdulsalam *et al.*, 2018), but based on what can be seen in Fig 4, it can clearly be said that the CO_2 adsorption experiments does not comply with the intra-particle diffusion model because the graph of qt versus $t^{1/2}$ did not pass through the origin, with k as slope and C as the intercept. Therefore it can be conclude that the rate limiting step of this process is not the intra particle diffusion but kinetically controlled adsorption process as suggested by statistical fittings obtained during kinetic model fittings.

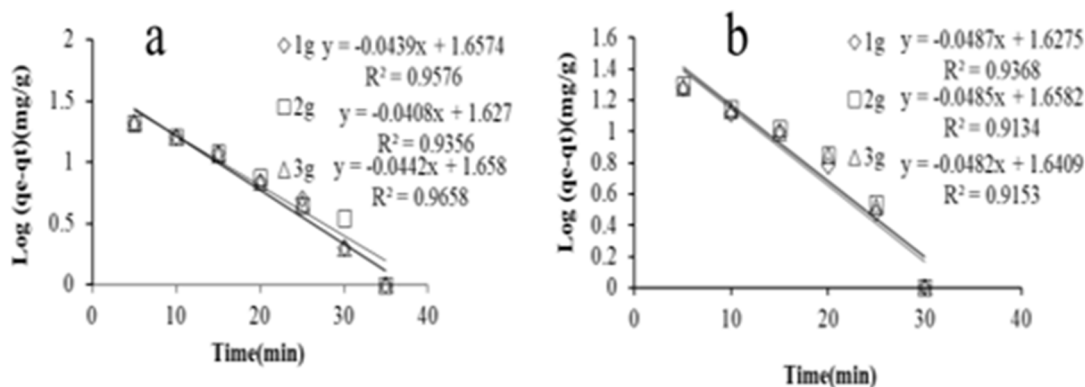


Fig. 4: Graph of intra-particle diffusion model for (a) activated carbon) (b) zeolite

CONCLUSION

CO_2 adsorption using sugarcane bagasse activated carbon and zeolite has been studied, it can be established from the results

that the activated carbon is a better adsorbent compared to zeolite when it comes to CO_2 adsorption. From the results of the characterization it was observed that the activated carbon has a better sorption capacity which makes it a better performer

in CO₂ adsorption. The two adsorbents are good for CO₂ adsorption. The adsorption capacity of each of the masses of adsorbent loaded (1g, 2g and 3g) are; 35, 35.5, and 35.33mg/g at 40min and 298K for the activated carbon and 29, 30.5 and 30mg/g at 40min and 298K for Zeolite, the difference in the amount of CO₂ adsorbed could be attributed to the difference in pore volume and surface area, the surface area of the activated carbon is 328m²/g and that of the zeolite is 425m²/g. The adsorption capacities of each mass of the adsorbent loaded are good. The adsorption experiments carried out in this work fits well into the pseudo-second-order kinetic model with R²s for all masses, both for activated carbon and zeolite well above 0.90. It can be conclude based on this findings that a very good and porous activated carbon with high adsorption capacity which was produced from sugarcane bagasse and used in this work had a better CO₂ adsorption capacity than zeolite and can be employed in CO₂ adsorption.

REFERENCES

- Abdulsalam A., Alhassan, M., Isah, A. G., Kovo, A. S., Olanrewaju, A. O. (1 2018). Comparative studies on the kinetics of biogas purification using activated Carbon and Zeolite, *2nd International Conference on Science and Sustainable Development, IOP Conference Series: Earth and Environmental Science*, 173, 012046. doi :10.1088/1755-1315/173/1/012046
- Abdullahi Abdulsalam and Mohammed Alhassan. (2018). *Studies on biogas purification using activated carbon and zeolite*. 17 Meldrum Street, Beau Bassin 71504, Mauritius: LAP LAMBERT Academic Publishing.
- Adilla, N., Yusup, S., & Hameed, B. H. (2013). Kinetic studies on carbon dioxide capture using lignocellulosic based activated carbon. *Energy*, 1–7. <https://doi.org/10.1016/j.energy.2013.08.050>
- Alhassan, M and Andresen J. (2013) “Effect of Bone during Fixed Bed Pyrolysis of Pistachio nut shell, *International Journal of Science and Engineering Investigations*, volume 2, Issue 12, Pp. 37-48. www.IJSEI.com.
- Alhassan, M., Auta, M., Sabo, J. K., Umaru, M., & Kovo, A. S. (2016). CO₂ capture using amine-impregnated activated carbon from *Jatropha curcas* shell, *14(4)*, 1–11. <https://doi.org/10.9734/BJAST/2016/24253>
- Alhassan, M., Andrew, I., Auta, M., Umaru, M., Garba, M. U., Isah, A. G., Umaru, M. (2017). Comparative studies of CO₂ capture using acid and base modified activated carbon from sugarcane bagasse. *Biofuels*, 1–10. <https://doi.org/10.1080/17597269.2017.1306680>
- Creamer, A. E., Gao, B., & Zhang, M. (2014). Carbon dioxide capture using biochar produced from sugarcane bagasse and hickory wood. *Chemical Engineering Journal*, 249, 174–179. <https://doi.org/10.1016/j.cej.2014.03.105>
- David, E., & Kopac, J. (2014). Activated carbons derived from residual biomass pyrolysis and their CO₂ adsorption capacity. *Journal of Analytical and Applied Pyrolysis*, 110(1), 322–332. <https://doi.org/10.1016/j.jaap.2014.09.021>
- Energy Information Administration (EIA) (2021). Biomass explained, retrieve on 6/24/2021, Last updated: June 8, 2021, <https://www.eia.gov/energyexplained/biomass/>
- Ifechukwu, G. Ezemagu, Mathew C. Menkiti, V. I. U. and M. C. A. (2016). Adsorptive approach on nephelometric study of paint effluent using *Tympanotonos Fuscatus* extract. *Chemical Society of Ethiopia*, 30(3), 377–390. <https://doi.org/http://dx.doi.org/10.4314/bcse.v30i3.6>

- Kajjumba, G. W; Emik, S; Öngen, A; Özcan, H. K; & Aydın, S. (2018). Modelling of adsorption kinetic processes errors, theory and application, advanced sorption process applications, *Serpil Edebalı, IntechOpen*, [https://doi:10.5772/intechopen.80495](https://doi.org/10.5772/intechopen.80495)
- Saleem, J; Bin Shahid, U; Hijab, M. Mackey H. & McKay. G. (2019). Production and applications of activated carbons as adsorbents from olive stones, *Biomass Conversion and Biorefinery*, 9, 775–802. <https://doi.org/10.1007/s13399-019-00473-7>
- Wu, X., Yu, Y., Qin, Z., & Zhang, Z. (2014). The advances of post-combustion CO₂ capture with chemical solvents: Review and guidelines. In *Energy Procedia* (Vol. 63, pp. 1339–1346). Elsevier B.V. <https://doi.org/10.1016/j.egypro.2014.11.143>
- Yaumi, A. L., Bakar, M. Z. A., & Hameed, B. H. (2017). Recent advances in functionalized composite solid materials for carbon dioxide capture. *Energy*, 124, 461–480. <https://doi.org/10.1016/j.energy.2017.02.053>
- Yu, C., Huang, C., & Tan, C. (2012). A Review of CO₂ capture by absorption and adsorption. *Aerosol and Air Quality Research*, 12, 745–769. <https://doi.org/10.4209/aaqr.2012.05.0132>.

HYDRAULIC CONDUCTIVITY CHARACTERISTICS OF LEACHATE - CONTAMINATED LATERITIC SOIL

Asogwa, E. O¹., Adie, D. B²., Ibrahim, F.B²., Amadi, A.A¹ and Agbonselobho, M.O¹

¹Civil Engineering Department, Federal University of Technology Minna, Nigeria.

²Water Resources and Environmental Engineering Department, Ahmadu Bello University Zaria, Nigeria. E-mail: e.asogwa@futminna.edu.ng

Abstract

Lateritic soil contamination due to the Leachate from Municipal Solid Waste is a major environmental problem. Landfill leachate is generated from liquids existing in the waste as it enters a landfill or from rainwater that passes through the waste within the facility. The properties and structure of a compacted liner can change with time due to changes in moisture content, capillary forces, and physico-chemical interactions with the liquid waste resulting in a reduction of the effectiveness of the liner as a barrier to contain solid and liquid waste. The changes in chemical characteristics of soils due to leachate contamination may be detrimental to the compacted soils/liner. To protect the groundwater from landfill contaminants, soil liners are widely used to impede the flow of leachate from municipal solid waste. A comprehensive laboratory analysis was carried out to determine the index properties, compaction characteristics and hydraulic conductivity of natural and contaminated lateritic soil. Contaminated samples were prepared by mixing the lateritic soil with varying percentage of leachate at step concentration of 0%, 25%, 50%, 75% and 100% to vary the degree of contamination. The effects of leachate on the Atterberg limits showed increase in liquid and plasticity index values with the increase in the leachate content, thus: Liquid Limit (wl) and plastic index (Ip) at 0% is 51 and 23.08, at 25% (wl = 52.92, Ip = 26.48, at 50% (wl = 53, Ip = 29.28), at 70% (wl = 53.22, Ip = 32.17) at 100% (wl = 54.2 and Ip = 34.13). The hydraulic conductivity of the natural lateritic soil was recorded as 1.40×10^{-6} cm/s and 1.30×10^{-7} cm/s using British standard light (BSL) and British standard heavy (BSH) compactive efforts respectively at 0 day curing time. There was corresponding increase in the hydraulic conductivity of the lateritic soil with increase in the percentage contamination, thus: 25% (4.75×10^{-6} cm/s and 2.78×10^{-7} cm/s), 50% (6.94×10^{-6} cm/s and 4.52×10^{-6} cm/s), 75% (7.90×10^{-6} cm/s and 6.10×10^{-7} cm/s) and finally 100% (5.44×10^{-6} cm/s and 7.33×10^{-7} cm/s) using BSL and BSH compactive effort respectively. Generally, increase in percentage contamination of lateritic soil by leachate caused increase in the hydraulic conductivity, liquid limit, plasticity index and optimum moisture content while maximum dry density decreased.

Keywords: Compaction, Contamination, Leachate, Lateritic soil, Municipal solid waste.

INTRODUCTION

A landfill is an engineered facility used for disposing solid wastes on land without creating nuisances or hazards to public health or safety, and are provided to accommodate the solid waste generated at specific site and at minimal cost in several parts of the world (Amadi, 2007). Recently, the volume of municipal solid waste (MSW) generation has increased in many countries due to the increasing population, increasing standard of living and urbanization (Chen, 2018; Vaverková *et al.*, 2020). The landfill

is the most common method used for the final disposal of MSWs, as it is the most economical, simplest, and appropriate method available (Adhikari *et al.*, 2014; Vaverková *et al.*, 2020). It is known that 95% of the total MSW collected worldwide is disposed of through landfills (Tamru and Chakma 2016; Luo *et al.*, 2019). Despite these benefits, leachate is a threat to the environment due to the presence of toxic inorganic and organic constituents in the leachate. Leachate from the solid waste dump has a significant effect on the chemical properties as well as the geotechnical properties of the soil. Leachate can modify

the soil properties and significantly alter the behavior of soil. Past studies by Goswami and Choudhury (2013); Khan and Pise (1994); Khan *et al.* (1994); Nayak *et al.* (2009) and Foreman & Daniel (1986) have shown that the index and engineering properties of soil contaminated with leachate lead to changes due to chemical reactions between the soil mineral particles and the contaminant. In connection with any possible applications, knowledge of the behavior of contaminated soil is required and hence the present investigation is carried out. The decrease in porosity and pore size in porous media leads to a decrease in hydraulic conductivity (Vinten *et al.*, 1983; Vangulck & Rowe, 2004; Banihashem & Karrabi, 2020). Suspended solids in the leachate accumulate in the soil pores, causing physical clogging of the soil and a decrease in hydraulic conductivity. Metzger *et al.* (1983) reported that unfiltered wastewater (containing suspended solids) causes about 50% reduction in soil hydraulic conductivity, while filtered wastewater causes a reduction in hydraulic conductivity.

This paper presents the results of a laboratory testing program carried out to determine the effect of leachate contamination for a period of 14 days on the geotechnical characteristics (consistency limits, compaction characteristics and hydraulic conductivity) of lateritic soils.

MATERIALS AND METHODS

Lateritic Soil

The Lateritic soil used for this study was collected from a borrow pit in Lapai-Gwari Road, Lat: 9°31'15" N and 9°32'30" N and Longitude 6°26'15" E and 6°28'00" E Minna, Nigeria. The sample was obtained from a depth not less than 1.5m to avoid organic top soil from mixing up with the sample. The soil is a reddish brown lateritic soil, air dried and passed through sieve 425 µm before carrying out laboratory tests on it.

Municipal Solid Waste Leachate

Municipal Solid Waste (MSW) leachate sample was collected from a selected active non engineered landfill site in Minna. The leachate was scooped from a sump, sieved and stored in a covered container placed in an incubator to avoid further reactions. The waste stream is mainly domestic and some percentage of commercial wastes. The site has no form of cover hence the wastes are exposed to direct sun and rainfall. The waste stream is mainly domestic and some percentage of commercial wastes.

METHODS

Test Programme

Laboratory tests were conducted to determine the index properties, compaction characteristics and hydraulic conductivity of natural and contaminated lateritic soil according to standard procedures in BS 1377 Part 2 and 4 (1990) and Head (1994). Contaminated samples were prepared by mixing the lateritic soil with varying amount of leachate content, at step concentration of 0, 25, 50, 75 and 100% by weight to vary the degree of contamination.

The hydraulic conductivity test was carried out and measured using the falling head permeability test condition as recommended by BS 1377 (1990) together with Head (1994). Two energy levels to simulate compactive effort expected in the field namely British Standard Light (BSL) and British Standard Heavy (BSH) were used. After compaction, specimens were cured from 0 to 56 days, thereafter, they were soaked for at least 24 hours in tap water. The hydraulic conductivity (k) was then calculated using equation 1.

$$k = \frac{aL}{AT} \ln \frac{H_1}{H_2} \quad (1)$$

where a=The area of the stand pipe

L= Height x Thickness= 9.4 cm²

A= Area of the sample

T=The time interval between two heads

H_1 and H_2 = The falling height of water

RESULTS AND DISCUSSION

Compaction Characteristics of Natural and contaminated lateritic soil

Compaction tests were carried out on leachate contaminated soil specimens at a step concentration of 25%, 50%, 75% and 100% leachate by weight. The results for BSL compaction are presented in Fig. 1.

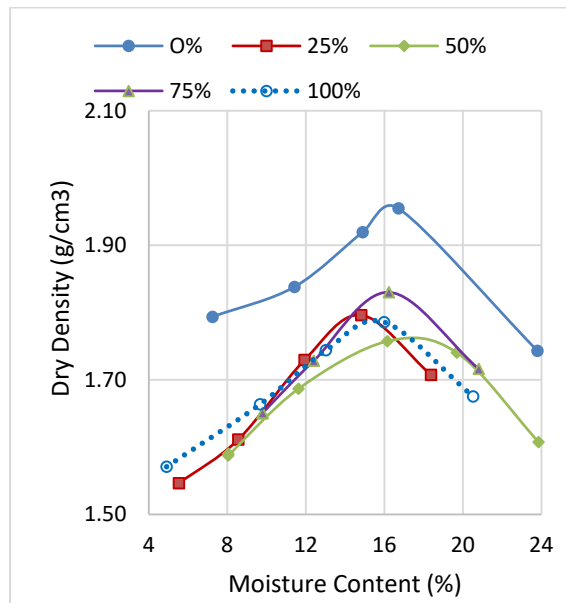


Fig. 1: Effect of Leachate on BSL Compaction Characteristics of lateritic soil.

The maximum dry density for the natural lateritic soil is 2.28 g/cm^3 at the optimum moisture content of 16.4%. With the presence of leachate 25% to 100% the compaction characteristics changed achieving maximum dry density and OMC were 1.79 g/cm^3 and 14.9%, 1.77 g/cm^3 and 18.0%, 1.83 g/cm^3 and 16.3% and finally 1.78 g/cm^3 and 16.3% respectively.

Thus, the maximum dry density of the laterite soil decreased with increasing concentration of leachate while optimum moisture content increases with increasing concentration of leachate. This is mainly due to the chemical reaction between the minerals present in the soil and the compounds present in the leachate. The presence of chemicals in leachate, changes the structure of pore fluid in soil, thereby

affecting the properties of soil. Maximum reaction occurred at a leachate concentration of 75%. The decrease in maximum dry density reflects the effect caused by chemical reaction (due to change in the nature of the pore fluid) between the leachate and the soil. Hence it is anticipated that in the present study the decrease in maximum dry density is due to chemical reaction between the leachate and the soil. From 25% to 100% leachate concentration, significant amount of leachate is already present in soil, which can cause chemical reaction between the leachate and soil particles.

Effect of leachate on Atterberg limits of Lateritic soil

Contaminants alters the properties of their host soils. The variation of liquid limit (wL) of soil with percentage leachate added is demonstrated in Fig. 2. It can be deduced from Fig. 2 that the leachate has notable implication on the liquid limit of the soil. The liquid limit of the lateritic soil increased with increase in percentage leachate added. This can be attributed to leachate characteristics. Mineralogical analyses of lateritic soil revealed the presence of kaolinite mineral in addition to montmorillonite, quartz, and calcite. The liquid limit behaviour of a montmorillonite soil is controlled essentially by diffuse double layer forces and that of kaolinitic soil by shearing resistance at particle level (Osinubi and Nwaiwu, 2005). In the case of lateritic soils, because of its low cation exchange capacity, the effects due to changes in diffuse double layer are negligible. However, the increase in liquid limit (wl) of the lateritic soil are mainly due to increase in clay content of the lateritic soil. As illustrated in Fig. 2, the liquid limit of the soil has increased from 51% to 54.2% (when leachate concentration increased from 0 to 100%) while the plasticity index (Ip) of the lateritic soil increases with the increase in the leachate concentration. The plasticity index of the soil has increased from 23.08% to 34.13%.

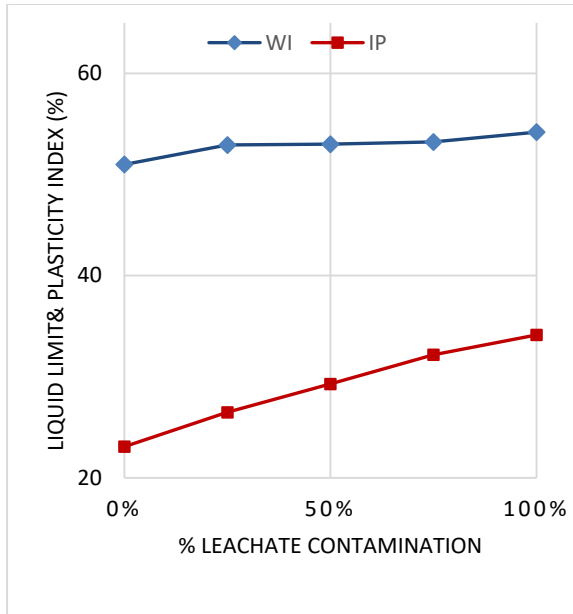


Fig.2: Variation of Liquid Limit and Plasticity index with Percentage contamination.

HYDRAULIC CONDUCTIVITY

Effect of Leachate on the Hydraulic Conductivity of Compacted Lateritic soil

The leachate used in the present study has basic characteristic ($\text{pH}=8.14$). Figs. 3 and 4 shows that the hydraulic conductivity of the soil increased when compared to its base value.

With increase in leachate concentration the hydraulic conductivity of the lateritic soil increases. This increase in hydraulic conductivity of the soil is attributed to chemical reaction between the basic leachate and the clay minerals.

It is reported in literature that strongly acidic and strongly basic liquids can dissolve clay minerals (Uppot and Stephenson, 1989).

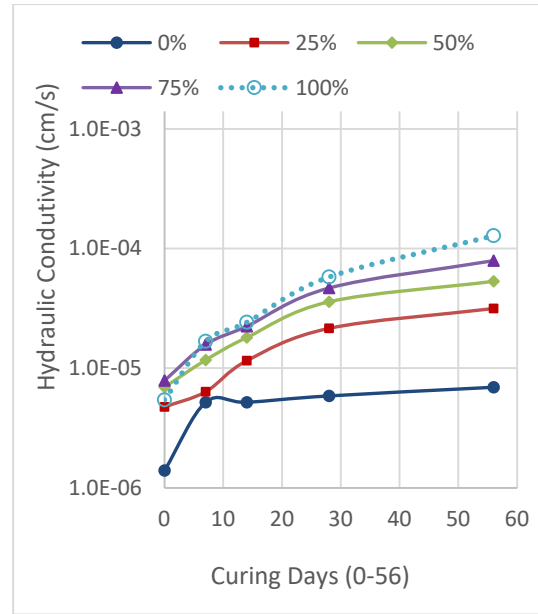


Fig.3: Variation of Hydraulic Conductivity with Percentage contamination at different curing days using BSL Compactive effort.

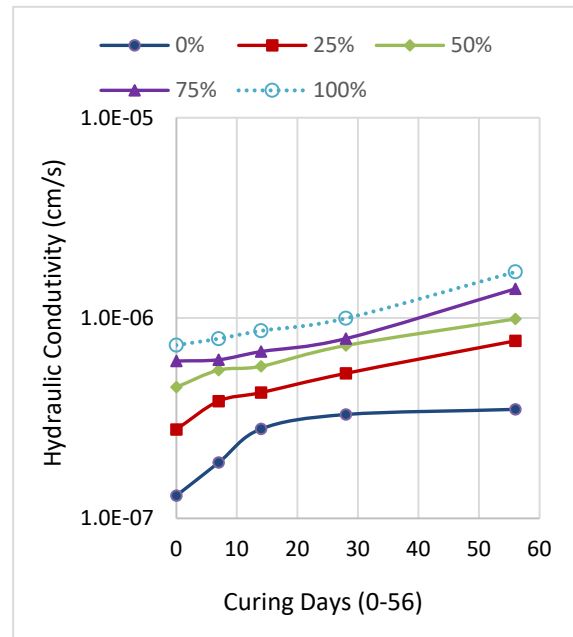


Fig.4: Variation of Hydraulic Conductivity with Percentage contamination at different curing days using BSH Compactive effort

The dissolution of clay mineral particles by basic leachate increases the effective pore space and the hydraulic conductivity increases. It can be concluded that the hydraulic conductivity of the compacted lateritic soil using two compactive efforts (BSH and BSL) at 7 to 56 days curing time increases with increase in the leachate

concentration. Hence the increase in hydraulic conductivity of lateritic soils after contamination with the leachate is attributed mainly to the following reasons:

- a) Chemical reaction between the leachate and the clay minerals;
- b) The structural changes which occurred in a soil after contamination with leachate i.e. when pore water is replaced by leachate, voids ratio increases compared to that with water as pore fluid.

CONCLUSION

The purpose of this research was to investigate the effect of leachate on the properties of lateritic soil. An extensive laboratory testing program was carried out to achieve the objectives. To alter the degree of contamination, the amount of leachate mixed with soil varied up to 100%. The following important conclusions are made based on test results:

- Leachate contamination leads to increase in the hydraulic conductivity of the soil tested. This is attributed to the chemical reactions with the leachate and the soil particles. It was observed that at 25% leachate concentration, the hydraulic conductivity of the lateritic soil increased to 4.75×10^{-6} cm/s and 2.78×10^{-7} cm/s from 1.40×10^{-6} cm/s and 1.30×10^{-7} cm/s of the base soil using BSL and BSH compactive efforts respectively at 0 day curing time. At 50% leachate concentration the hydraulic conductivity of the soil tested increased to 6.94×10^{-6} cm/sec and 4.52×10^{-6} cm/s using BSL and BSH compactive efforts respectively. At 75% leachate concentration the hydraulic conductivity of the tested soil increased to 7.90×10^{-6} cm/s and 6.10×10^{-7} cm/s using BSL and BSH compactive efforts respectively. Similarly, when the soil was mixed with 100% leachate the increase in hydraulic conductivity was 5.44×10^{-6} cm/s and 7.33×10^{-7} cm/s using BSL and BSH compactive efforts respectively.

Highly acidic or basic leachate can have significant effect on the index and engineering properties of the soil.

- Experimental results indicated that with the increase in percentage of leachate, maximum dry density (ρ_d) decreased from an initial value of 15.89 g/m^3 to 14.03 g/m^3 and optimum moisture content increased to 24.8% from an initial value of 20.1%.

REFERENCES

- Adhikari, B., Dahal, K. R. & Khanal, S. N. 2014. A review of factors affecting the composition of municipal solid waste landfill leachate. *International Journal of Engineering Science and Innovative Technology*, 3 (5), 272–281.
- Amadi, A. (2007). Unsafe waste disposal practices in Nigerian cities: Geo environmental perspectives. *NSE Technical Transactions*, Vol. 42, No. 2, 31 – 44.
- Banihashem, S. & Karrabi, M. 2020. Investigation of suspended particle size effects on clogging of soil filters under laminar flow. *European Journal of Environmental and Civil Engineering*. <https://doi.org/10.1080/19648189.2020.1761455>.
- Beena. K.S and Meril George. (2010). Contaminant Transport from MSW Landfill: A Case Study. *Proc. of Indian Geotechnical Conference, Bombay, India*. Vol 1, pp.433-436.
- Chen, Y. C. 2018. Effects of urbanization on municipal solid waste composition. *Waste Management Journal*, 79, 828–836. DOI:10.1016/j.wasman.2018.04.017.
- Chinade, A.U., Umar, S.Y. and Osinubi, K.J. (2017). Effect of Municipal Solid Waste Leachate on the Strength of Compacted Tropical Soil for Landfill Liner. *International Research Journal of Engineering and Technology (IRJET)*. Vol 04 Issue: 06.
- Foreman, D.E., Daniel, D.E., 1986. Permeation of compacted clay with organic chemicals. *Journal of*

- Goswami, D and Choudhury B.N., (2013). Atterberg's Limit and shear strength characteristics of leachate contaminated Lateritic soil. *Indian Journal of Research. PARIPEX* Vol. 3 Issue 4. www.worldwidejournals.com.
- Khan, A.K, Pise, P.J. (1994). Effect of Liquid wastes on the physico-chemical Properties of lateritic soil. *Proceedings of Indian Geotechnical Conference, Warangal*, pp.189-194.
- Luo, H., Zeng, Y., Cheng, Y., He, D. & Pan, X. 2019. Recent advances in municipal landfill leachate: a review focusing on its characteristics, treatment, and toxicity assessment. *Science of the Total Environment* 703, 135468. DOI: 10.1016/j.scitotenv.2019.135468.
- Metzger, L., Yaron, B. & Mingelgrin, U. 1983. Soil hydraulic conductivity as affected by physical and chemical properties of effluents. *Agronomie* 3 (8), pp.771–778. <http://hal.archives-ouvertes.fr/hal-00884570>.
- Osinubi, K.J and Nwaiwu,C.M.O (2005). Hydraulic conductivity of compacted lateritic soil. *Journal of Geotechnical and Geo-environmental Engineering*. 131:1034 – 1041.
- Sunil, B. M., Shrihari. S., and Sitaram, Nayak (2009). Shear strength characteristics and chemical characteristics of leachate-contaminated Lateritic soil. *A Journal of Engineering Geology*, Vol. 106, pp 20–25 (*ELSEVIER*). www.elsevier.com/locate/enggeo.
- Serin Issac, (2019). Experimental Investigation on Leachate-Contaminated Lateritic Soil. *International Journal of Scientific Research in Computer Science, Engineering and Information Technology* © IJSRCSEIT | Volume 4
- Seracettin Arasan, (2010). Effect of Chemicals on Geotechnical Properties of Clay Liners: A Review, *Research Journal of Applied Sciences, Engineering and Technology*. 2(8): 765-775.
- Sitraram Nayak, B.M. Sunil and S. Shrihari. 2007 Hydraulic and Compaction Characteristics of leachate Contaminated Lateritic Soil, *Journal of Engineering Geology, Science Direct, ELSEVIER*, 94 (3) pp.137-144. DOI:10.1016/j.enggeo.2007.05.002.
- Tamru, A. T. & Chakma, S. 2016. Effects of landfilled MSW stabilization stages on composition of landfill leachate: a review. *International Journal of Engineering Research & Technology* 4 (03), 1–4.
- Uppot, J.O. and Stephenson, R.W. (1989). Permeability of clay under organic permeants. *Journal of Geotechnical Engineering*. 115(1), 115-131.
- Vinten, A. J. A., Mingelgrin, U. & Yaron, B. 1983. The effect of suspended solids in wastewater on soil hydraulic conductivity: II. Vertical distribution of suspended solids. *Soil Science Society of America Journal* 47 (3), 408–412.
- Vangulck, J. F. & Rowe, R. K. 2004 Influence of landfill leachate suspended solids on clog (biorock) formation. *Waste Management Journal* 24 (7), 723–738.
- Vaverková, M. D., Elbl, J., Koda, E., Adamcová, D., Bilgin, A., Lukas, V., Podlasek, A., Kintl, A., Wdowska, M., Brtnický, M. & Zloch, J. 2020. Chemical composition and hazardous effects of leachate from the active municipal solid waste landfill surrounded by farmlands. *Sustainability (Switzerland)* 12 (11), 1–20. <https://doi.org/10.3390/su12114531>.

INTEGRATED MODE SELECTION AND BANDWIDTH ALLOCATION SCHEME FOR INTERFERENCE MITIGATION IN D2D NETWORKS

*Ameh, A. I.¹; Usman, A. U.²; Mohammed, A. S.² & Salihu, B. A.²

¹Electrical & Electronic Engineering Department, Federal University of Technology, Minna, Nigeria

²Telecommunication Engineering, Federal University of Technology, Minna, Nigeria

Email : ameh247@gmail.com

Abstract

As the steep growth in mobile data traffic continues to gain lots of attention in recent years, discussions of the next generation of mobile networks - the fifth generation (5G), have gained significant traction both in the academia and industry. In addition to more capacity, stringent requirements for improving energy efficiency, decreasing delays, and increasing reliability have been envisioned in 5G. Many solutions have been put forward, one of them being Device-to-Device (D2D) communications where users in proximity can communicate directly with one another. Interference management between Cellular User Equipment (CUE) and D2D user Equipment (DUE) is one of the most critical issues when D2D is introduced to cellular network because D2D users share the same licensed spectrum with cellular users. This work considers an overlaying network scenario where a Mode Selection and Bandwidth Allocation Scheme (MS-BAS) is developed to mitigate cross-tier interference, while delivering an average data rate of more than 50 Mbps across the network, indicating an over 12% improvement when compared with the existing Selective Overlay Mode Operation (SOMO). The results obtained show the efficacy of the algorithm in significantly mitigating cross tier interference in the network.

Keywords: Interference mitigation, cross-tier, D2D communication, User Equipment.

INTRODUCTION

With an ever-growing number of connected devices using the cellular network, service providers are faced with the challenge of improving spectrum reuse, throughput, energy consumption, coverage, and reduction of end-to-end latency. Network performance would rise if closely located user pairs are allowed direct communication with each other, rather than through the traditional Up-link and Down-link communication channels of the Base Stations (BS) (Safaei *et al.*, 2017). Additionally, the creation of new peer-to-peer services and location-based applications would all be driven by an efficient Device-to-Device (D2D) communication system, which incidentally, is one of the identified enabling technologies for the 5G cellular network. This, of course, comes with its challenges, chief among

which is interference between the User Equipment (UEs). With enabled D2D communication between devices in proximity, there would be an introduction of interference between D2D User Equipment (DUEs) and other D2D Users, known as Co-Tier Interference, as well as interference between D2D users and traditional Cellular User Equipment (CUEs), the Cross-Tier Interference.

There are numerous problems inherent with Macro-D2D Heterogenous Networks which include handover, neighbour discovery, security, interference, mobility management, etc. (Asadi *et al.*, 2014). This research focuses on the mitigation of cross-tier interference in the two-tiered network, by developing schemes towards the optimization of throughput.

In this work, a Mode Selection and Bandwidth Allocation Scheme was

developed to mitigate cross-tier interference in the network, and the performance of the scheme was evaluated through simulations on MATLAB and comparison with related works.

INTERFERENCE MANAGEMENT

Interference is an undesired signal picked by neighbouring receivers. It has a mathematical relationship with signal-to-interference-plus-noise ratio (SINR), throughput and transmit power as expressed below:

- i. $Interference \propto \text{transmit Power}$
- ii. $Interference \propto \frac{1}{\text{throughput}}$
- iii. $Interference \propto \frac{1}{SINR}$
- iv. $Interference \propto \frac{\text{transmit power}}{SINR * \text{throughput}}$

Enabling D2D links within a cellular network pose a big threat of interference to the cellular links in the network. D2D links can cause interference between cellular users and D2D users, resulting in an increase in co-tier interference. Cross-tier interference is also possible with D2D communication underlying cellular communication. Interference can be mitigated through mode selection, optimum resource allocation, and power control. Setting the maximum transmit power limits of the D2D transmitter is an effective technique of limiting the interference between DUEs and CUEs (Noura and Nordin 2016). A general scenario of interference in D2D underlayed cellular networks is depicted in Fig. 1:

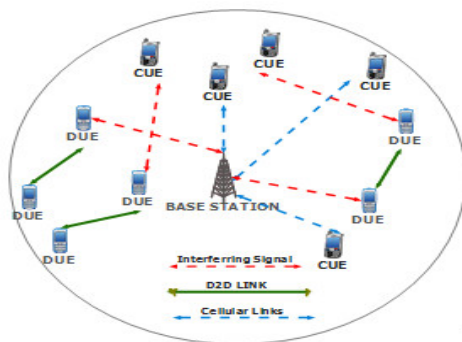


Fig. 1: An interference scenario in D2D underlayed cellular network.

Some interference mitigation techniques are briefly described below:

Bandwidth Allocation

The easiest way to coordinate the cross-tier interference between the cellular and device tier is to use bandwidth allocation, which will simplify the interference between DUEs and CUEs. Cho and Jantti (2013) used bandwidth allocation, where the spectrum band was divided into two parts, as shown in Fig. 2. One part would be dedicated to CUEs and the other part would be assigned to DUEs. However, effective resource allocation in heterogenous networks is required to balance the amount of bandwidth assigned to DUEs and the amount of bandwidth to be allocated to CUEs. A large amount of bandwidth allocated to CUEs will enhance the throughput of CUEs; nevertheless, this improvement is achieved at the expense of DUEs. Similarly, allocating a large amount of bandwidth to DUEs increases the throughput of DUEs but the throughput of CUEs will decrease (Shami *et al.*, 2019).

Investigation shows that the existing interference mitigation techniques are broadly categorized as centralized, distributed and semi-distributed (Barik *et al.*, 2020). Although both centralized and distributed methods have benefits and drawbacks, trade-offs can be made between them. Interference management strategies of this type are referred to as semi-distributed or hybrid. Various levels of participation can be established in the strategies of semi-distributed interference management. Such strategies can be appropriate for relatively massive networks (Alzubaidi *et al.*, 2022).

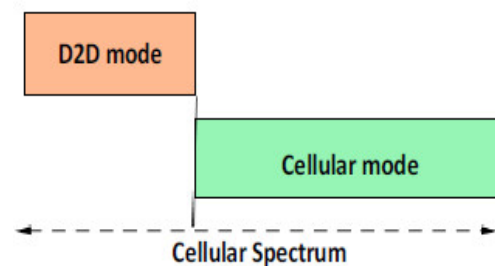


Fig. 2: Spectrum Allocation

Power Control

Although higher transmit power of D2D users can provide wider coverage and better signal quality, it can, at the same time, cause tremendous interference to the cellular network. The power control (PC) mechanism is one approach to deal with cross-tier interference generated from DUEs to the cellular network for both the UL and the DL case, as well as the co-tier interference between DUEs in a two-tiered cellular network with D2D communication. It coordinates the interference imposed by DUEs to the cellular network and the interference from a DUE to a neighbouring DUE by controlling the transmit power levels of DUEs to improve system capacity, coverage, and reduce power consumption (Koushik and Shahedur, 2021). To meet these goals, PC schemes aim at maximizing the transmit power and at the same time limiting the generated interference, but they may lead to increased power utilization or degraded energy efficiency of the system (Nasser *et al.*, 2019).

Mode Selection

Selecting transmission mode (Cellular or D2D mode) is one of the difficult tasks in communication for potential D2D users after discovery. Although they may be in proximity to each other, it might not be optimal for them to operate efficiently and effectively (Alquhali *et al.*, 2020 and Ansari *et al.*, 2018). Therefore, mode selection enables the BS and the D2D users to decide which communication mode to operate in, based on some distinguishing criteria like interference among D2D pairs, distance between D2D pairs, and Cellular users. The quality of the channel condition and Signal-to-interference plus noise ratio (SINR) is one of the most common selection metrics. Predefined SINR threshold is often considered as the mode selection criteria for D2D communication. Therefore, proper mode selection determines the performance of D2D communication (Librino & Quer, 2018).

Each of the communication modes affects the amount of interference between cellular users and D2D users or between multiple DUEs (Chen *et al.*, 2018).

Related Works

Zhai *et al.* (2017) proposed a unified resource management scheme to minimize the total transmit power of all UEs by jointly optimizing mode selection, resource allocation, and power control, to tackle the incidence of interference and power consumption by UEs arising from complicated spectrum sharing pattern. The work achieved an enhancement of energy efficiency and network capacity, although it was not validated through comparison with other schemes.

Yang *et al.* (2017) considered the effects of both the interference caused by the generic D2D transmitter to others, and the interference caused by all others to the generic D2D receiver. The work achieves higher energy efficiency compared with the blind power control scheme, although increasing the energy means increasing the interference and hence decreases the spectrum efficiency.

Swetha and Murthy (2017) proposed the resource management scheme in overlay D2D network where bandwidth is allocated to D2D overlay devices by the base station, based on the bandwidth resource blocks earmarked for D2D mode. The challenge is the maximization of the reserved bandwidth if not optimally utilized. When the resource block assigned for D2D mode is exhausted the base station assigns subsequent UE to CUE mode. Equations (1) and (2) were used to compute both line of sight (LOS) and non-line of sight (NLOS) pathlosses for the transmissions.

$$P_{LOS} = 65 + 21\log_{10}(d) \quad (1)$$

$$P_{NLOS} = 71.1 + 34\log_{10}(d) \quad (2)$$

The static allocation of bandwidth to communication tiers without recourse to the number of UEs per tier was a limitation of this work. This lead to wastage of scarce

spectral resources, leading to degraded data rates.

Li *et al.*, (2018) considered a relay mode for D2D UEs. Additionally, they proposed an evolutionary game-based approach for D2D mode selection in order to address a potentially large population of DUEs. The evolutionary game was formulated with a utility function that takes into account both the achievable throughput of DUEs and the radio resource consumption. The work yielded a higher number of D2D connections than the baseline schemes, although it did not consider other D2D communication modes.

Li (2019) proposed SFR for both the licensed and unlicensed band. Using unlicensed band that considers resource allocation based on SFR gives a good design.

Song *et al.* (2019) adopted an interference limited area control method; this constraint is used to reduce interference between D2D communication and cellular network.

Hassan and Gao (2019) proposed an Active Power Control (APC) technique, which not only reduces cross-tier interference in a Macro User Equipment (MUE), generated from the downlink transmission power of an inadequately deployed femtocell, but also reduces unnecessary power consumption to achieve a green femtocell network. The work, however assumed all UEs were static throughout their simulation. This is very unrealistic in a mobile communication network.

Gao *et al.* (2019) proposed an energy-efficient resource block (RB) assignment and power control strategy for underlay device-to-device (D2D) communication in multi-cell networks, where more than one D2D pair is allowed to share the same RBs with cellular user equipments (CUEs). Although there was significant reduction in energy loss, there was inconsistency in network energy efficiency, as it first increases and then decreases when the transmit power increases.

Adejo *et al.* (2020) employed SFR to adequately model an interference frame considering the overlapping bandwidth allocation. The result obtained allowed BS to be tuned to achieve desired network performance which may be a disadvantage.

Authors in Rana *et al.* (2021) proposed two D2D interference mitigation scheme referred to as power control scheme 1 (PCS1) and power control scheme 2 (PCS2) which both centred on the difference between computed SINR and target SINR to basically mitigate interference caused by number of D2D pairs in a D2D cellular communication network. The difference between the two Power Control Schemes is in the scaling factors used. In PCS1 a scaling factor of 2 dBm was used and that of PCS2 used power scaling factor of 3 dBm. Equation (3) was used in computing the path loss between different communication paths; from D2D Transmitter (D2DT) and macro base station during uplink transmission or from macro base station to D2D Receiver (D2DR) during downlink transmission.

$$PL_{diff_{layer}}(dB) = 128.1 + 37.6 * \log d(KM) \quad (3)$$

where $PL_{diff_{layer}}(dB)$ is path loss either base station to D2DR or from D2DT to CUE, d is the distance between transmitter and receiver in Km . Equation (4) was used to measure the path loss between D2D communication path.

$$PL (dB) = 148 + 40 * \log d(Km) \quad (4)$$

SINR was computed using (5) and compared with the target SINR value:

$$\gamma_B = \frac{P_x G_x}{\sum_1^N w P_y G_y + N_o} \quad (5)$$

where γ_B is receiver's SINR, P_x is desired transmit power of D2DT, G_x is channel gain when considering the desired transmitter and receiver. P_y is the transmit power of aggressor, G_y is the channel gain of aggressor, N_o is noise and w is an SINR factor that is either 0 when D2D and CUE do not use the same resources otherwise it is 1.

When γ_B is greater than target SINR, the next transmit power will be less than the present power by power scaling power within the range of accepted minimum and maximum transmit power. When γ_B is less than the target SINR, the next transmit power will be greater than the present power by same power scaling factor. And when γ_B is equal to the target SINR, the next transmit power will be the same with the present transmit power.

Although the power control schemes were consistent in their output, they, however, utilized very high power for their operation. This lead to increased noise and interference. Energy consumption by the UEs was also high, and the pathloss model used also lead to high losses when compared with other works.

From these reviews, it is evident that a lot of work has been done towards the mitigation of interference in D2D enabled networks, using a wide variety of schemes ranging from mode selection, resource block assignment, soft frequency reuse, etc., to power control, link adaptation, as well as a combination of two or more of the schemes. Some of the works yielded good results, but with complex or cumbersome methodologies. Energy inefficiency, as well as ease of system manipulation (simplicity of system parameters) were partly or wholly lacking in various schemes. Being the primary users of the network, the cellular tier of the Macro-D2D network tended to receive greater priority in bandwidth allocation schemes, which was simply borne of the assumption that more users would be operating in cellular mode, whereas this might not always be the case. This assumption led to spectrum wastage, as well as the partial loss or complete non-realization of such benefits of D2D connections as coverage expansion (more

connections within the network), energy conservation (especially from less pressure on the base station), reduced latency (improved response time), improved data rates (due to spectral efficiency), improved signal quality (due to higher SINR), as well as reduced interference within the network.

RESEARCH SYSTEM MODEL

The research system model as shown in Fig. 3 captures transmission in cellular communication. It gives an illustration of D2D communication between a D2D user equipment (DUEs) and communication between a cellular user equipment (CUE) and its serving base station.

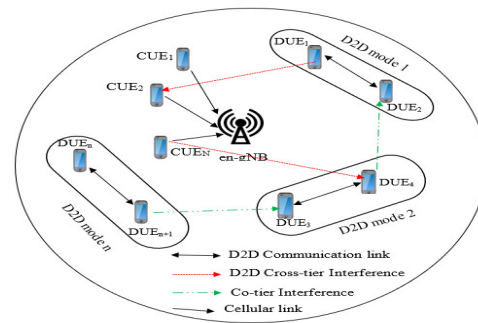


Fig. 3: Research System Model.

The simulation of the D2D communication schemes on MATLAB was guided by the research system parameters in Table 1, where cellular user equipment were represented as $CUE_1, CUE_2 \dots CUE_N$; macrocell base station as $en - gNB$; and D2D user equipment as $DUE_1, DUE_2, DUE_3, DUE_4 \dots CUE_n, CUE_{n+1}$. The system pictured co-tier interference scenario where signal from neighbouring D2D pair is received as interference by nearby D2D pair and cross tier interference as a result of common bandwidth shared among macro – tier and D2D-tier network. Table 1 presents the system parameters sourced from referenced literatures, viz (Swetha and Murthy, 2017), and (Rana *et al.*, 2021).

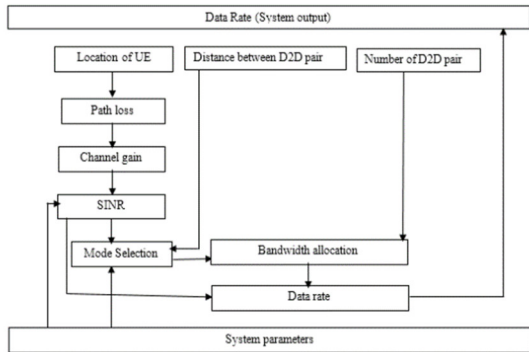
Table 1: System Parameters

No.	Parameter	Value
1.	Minimum transmit power of UE (DUE and CUE)	0 dBm
2.	Maximum transmit power of UE (DUE and CUE)	23 dBm (Rana <i>et al.</i> , 2021)
3.	System bandwidth	60 MHz
4.	Carrier frequency	2.6 GHz (Rehman <i>et al.</i> , 2020)
5.	Thermal noise density	-174 dBm/Hz (Rana <i>et al.</i> , 2021)
6.	Number of macrocells	1
7.	Number of D2D pairs	1 – 10
8.	Initial transmit power of CUE and DUE	20 dBm
9.	Target D2D distance	10m
10.	Target SINR for DUEs	0 dB

Mode Selection and Bandwidth Allocation Scheme (MS-BAS)

The mode selection and bandwidth allocation begins with communication mode selection, which is determined based on receiver's SINR and distance between transmitting UE and receiving UE. While the bandwidth allocation phase of the scheme is centered on the mode of UE communication, and the number of UEs in that mode. Being the primary users of the network, a greater priority is given to CUEs during bandwidth allocation; they receive a higher reserve of the bandwidth at 60%, while 30% is reserved for D2D communication. The number of UEs in D2D mode determines the allocation of the remainder 10% bandwidth.

Fig. 4 is the block diagram of the MS-BAS.

**Fig. 4:** Block Diagram of the MS-BAS.

From Fig. 4, the path loss block works with inputs from location of UE and specified

path loss model to compute the propagation path loss between a transmitter and receiver. The path loss model for D2D communication is presented in equation (6) adopted from Swetha and Murthy (2017); and that of cellular communication is captured in equation (7), Jiale *et al.*, (2018); Zhao *et al.*, (2018); Hassan *et al.*, (2018).

$$L_{D2D} = 65 + 21\log_{10}(d(m)) \quad (6)$$

$$L_{cell} = 15.3 + 3.7\log_{10}(d(Km)) \quad (7)$$

where d is the distance between the transmitter and the receiver.

The channel gain block computes the propagation channel gain based on computed propagation path loss between a transmitter and a receiver, using equation (8) Onu *et al.*, (2018); Zhao *et al.*, (2018); Swetha and Murthy (2017).

$$G = 10^{(-Path\ loss)/10} \quad (8)$$

The SINR block computes the receiver's SINR using specified thermal noise value from system parameters block, channel gain and SINR mathematical model in equation (9) (Junjie *et al.*, 2021; Jiale *et al.*, 2018; Xiaoqin, and Yang 2018).

$$SINR_{rx} = \frac{P_{tx}G_p}{\sum_{c=1}^{co=n} P_{tr}G'_p + \sum_{cx=1}^{cx=n} P_{tr}G'_p + N_o} \quad (9)$$

Where:

$SINR_{rx}$ = receiver's SINR,

P_{tx} = desired transmit power,

G_p = channel gain between transmitter and its receiver,

P'_{tr} = interfering signal transmit power,

G'_p = propagation channel gain of the aggressor and its victim,

N_o = thermal noise,

$\sum_{co=1}^{co=n} P'_{tr} G'_p$ = summation of all co-tier interfering signals in the network, and

$\sum_{cx=1}^{cx=n} P'_{tr} G'_p$ = summation of all cross-tier interfering signals in the network.

The number of D2D pairs determines the D2D co-tier interfering signals in the network. For n^{th} D2D pairs, there would be $(n - 1)$ D2D interfering signals. Likewise, the number of CUEs in the network determines the CUE co-tier interference.

The mode selection algorithm determines the mode of communication of all UEs in the network. The criteria for mode selection are based on the distance between D2D pairs, and computed D2D SINR. When the distance between the D2D pair is less than or equal to a target distance of 10m (Swetha and Murthy, 2017), the UE is assigned to D2D mode subject to reference computed SINR, otherwise it is assigned to cellular mode. When the reference SINR of UE is greater than the set target SINR of 0 (Swetha and Murthy, 2017), the UE is assigned D2D mode, otherwise, it is assigned cellular mode.

Equation (10) explains the mode selection mathematically.

$$\begin{cases} \text{if } d_{D2D} \leq d_{\text{target}} \text{ and } \text{SINR}_{\text{computed}} \geq \text{SINR}_{\text{target}} & \text{assign UE to D2D Mode} \\ \text{otherwise} & \text{assign UE to CUE mode} \end{cases} \quad (10)$$

The bandwidth allocation block assigns bandwidth to both cellular and D2D communication modes. The allocation of bandwidth is centrally done by the base station based on the number of UE in cellular and D2D modes at a particular time. 60% of the network bandwidth is reserved for CUE mode, 30% of network bandwidth is reserved for D2D mode and the remaining 10% is allocated dynamically to either D2D

or cellular mode based on the user traffic. When the number of DUEs is greater than or equal to the number of CUEs, the 10% dynamic network bandwidth is allocated to D2D mode; otherwise, it is allocated to cellular mode. The mathematical expression for bandwidth allocation by nodes to either D2D or cellular mode, within a macrocell is presented in equations (11) and (12).

$$\begin{aligned} \text{if } N_{DUE} \geq N_{CUE} = \\ \begin{cases} BW_{D2D \text{ mode}} = 40\% \text{ of network bandwidth} \\ BW_{CUE \text{ mode}} = 60\% \text{ of network bandwidth} \end{cases} \end{aligned} \quad (11)$$

$$\begin{aligned} \text{if } N_{DUE} < N_{CUE} = \\ \begin{cases} BW_{D2D \text{ mode}} = 30\% \text{ of network bandwidth} \\ BW_{CUE \text{ mode}} = 70\% \text{ of network bandwidth} \end{cases} \end{aligned} \quad (12)$$

where N_{DUE} is the number of DUE, N_{CUE} is the number of CUE, $BW_{D2D \text{ mode}}$ is the bandwidth allocated to D2D mode, and $BW_{CUE \text{ mode}}$ is the bandwidth allocated to cellular mode.

The mode selection and bandwidth allocation scheme allocate spectrum to UEs based on the communication mode of the UEs. When the computed SINR is greater than the target SINR, and their distance apart is not greater than the target distance, the two UEs will proceed into D2D mode of communication and exchange information. Otherwise, the two UEs will communicate in cellular mode.

After mode selection, spectrum is centrally allocated by the base station, based on the distributed traffic density of UEs on the network. UEs periodically update the base station with their current operating mode, so that it maintains an updated number of UEs in a particular mode (D2D or cellular) per time. The base station reserves 60% of the spectrum for CUEs, and 30% for D2D. The remaining 10% is dynamically allocated based on the conditions in equations (11) and (12) to minimize spectrum redundancy in the network. The number of DUE is limited by distance of D2D devices, which often accommodate less UE compared to CUE mode. To avoid large quantity of bandwidth

been redundant; 30% of the system bandwidth was allocated to DUE; being the secondary users, as its fixed operating bandwidth. 60% of the system bandwidth was allocated to CUEs being the primary users, where number of UEs operating in such mode is not restricted by distance between transmitting and receiving user accommodating more UEs. The reserved 10% system bandwidth is to compensate the operating mode with the higher UEs per time. The system output of mode selection and bandwidth allocation scheme displays the data rate of DUE, CUE, both CUE and DUE, and average data rate of both DUE and CUE all computed at data rate block using equations (13), (14), (15) and (16);

$$D_{D2D}^{MSBAS} = BW_{D2D\ mode} \log_2(1 + SINR_{D2D}) \quad (13)$$

$$D_{CUE}^{MSBAS} = BW_{CUE\ mode} \log_2(1 + SINR_{CUE}) \quad (14)$$

$$D_{UE}^{MSBAS} = BW_{D2D\ mode} \log_2(1 + SINR_{D2D}) + BW_{CUE\ mode} \log_2(1 + SINR_{CUE}) \quad (15)$$

$$D_{UES}^{Average} = \frac{\sum_{i=1}^p(D_{D2D}^1) + \sum_{i=1}^n(D_{CUE}^1)}{(p+n)} \quad (16)$$

where:

$$D_{D2D}^{MSBAS} = \text{data rate of D2D}$$

$$D_{CUE}^{MSBAS} = \text{data rate of CUE}$$

$$D_{UES}^{Average} = \text{average data rate when considering both D2D and CUE}$$

$$SINR_{D2D} = \text{signal-to-interference-plus-noise ratio of D2D}$$

$$SINR_{CUE} = \text{signal-to-interference-plus-noise ratio of CUE}$$

$$p, n = \text{maximum number of iterations (D2D, CUE).}$$

Table 2 is the Pseudocode for the Mode Selection and Bandwidth Allocation Scheme (MS-BAS).

Table 2 Pseudocode for the Mode Selection and Bandwidth Allocation Scheme

Pseudocode for MS-BAS	
1.	Initialization: Booting of UEs and base station
2.	Load input parameters into the memory of UEs and base station
3.	Idle State of UEs: <ul style="list-style-type: none"> - Neighbour discovery using broadcast packet - Update neighbour Table
4.	Active state of UEs: <ul style="list-style-type: none"> - Exchange packets with discovered neighbours - Compute: <ul style="list-style-type: none"> • Path loss using (6) and (7) • Channel gain using (8) • SINR using (9) - Decision: <ul style="list-style-type: none"> - if $D_{D2D} \leq D_{target}$ <ul style="list-style-type: none"> { Yes: then $SINR_{D2D} \geq SI$ { No: then assign UE to C if $SINR_{D2D} \leq SINR_{target}$ <ul style="list-style-type: none"> { Yes: then assign UE { No: then assign UE to
5.	Base station updates Active UE Mode Table
6.	Base station Computes Number of Active DUE and CUE
7.	Bandwidth Request by UEs
8.	Decision: <ul style="list-style-type: none"> $N_{DUE} < N_{CUE}$ { Yes: then $B_{DUE} = 30\%$ of Ba $N_{DUE} \geq N_{CUE}$ { Yes: then $B_{CUE} = 70\%$ of Ba $N_{DUE} \geq N_{CUE}$ { Yes: then $B_{DUE} = 40\%$ of Ba $N_{DUE} \geq N_{CUE}$ { Yes: then $B_{CUE} = 60\%$ of Ba
9.	Compute data rate using equations (13) – (16)
10.	Output computed data rate
11.	End

Fig. 5 is the Flowchart of the integrated Mode Selection and Bandwidth Allocation Scheme (MS- BAS). After communication modes have been assigned to UEs based on the design constraints

The performance of the mode selection and bandwidth allocation scheme (MS-BAS) was compared with that of Selective Overlay Mode Operation (SOMO) for D2D communication, as presented in Swetha and Murthy (2017) (Separation distance between UEs, and target SINR), bandwidth is allocated based on the number of UEs per communication tier.

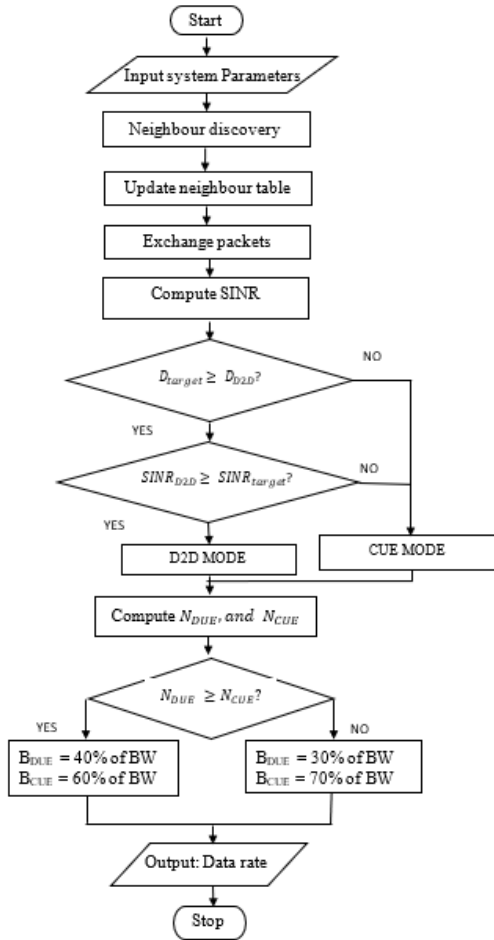


Fig. 5: Flowchart of MS-BAS

RESULTS AND DISCUSSION

The performance of the mode selection and bandwidth allocation scheme (MS-BAS) was analyzed based on varying distance between DUEs, and the number of D2D pairs. The results are presented in Figs. 6-13. At constant number of D2D pair, the distance between DUE was varied and the corresponding MS-BAS data rate was computed. The evaluated performance of MS-BAS is presented in Figs. 6 – 9, which shows data rate variation of DUEs when

N_{DUEs} and N_{CUEs} are 12 and 8 respectively, assuming 20 UEs. The distance between DUEs ranges from 0 – 10 m. The range of distance used was in accordance with the adopted D2D target distance of 10m (Swetha and Murthy, 2017). N_{DUEs} and N_{CUEs} were kept constant and $N_{DUEs} > N_{CUEs}$. Fig. 6 presents the data rate of DUE as DUE distance changed.

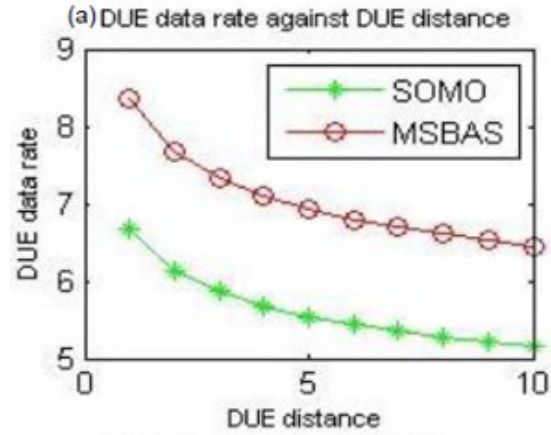


Fig. 6: Data rate of DUE as DUE distance changed.

As the distance between DUE increased, the data rate decreased. The change is attributed to increase in path loss due to increase in distance. As path loss increases, SINR and data rate decreases. The data rate performance of MS-BAS scheme at DUE distances ranging from 0 – 10 m, when compared outperformed that of SOMO.

Fig. 7 presents CUE data rates when DUE distance changed from 0 – 10m.

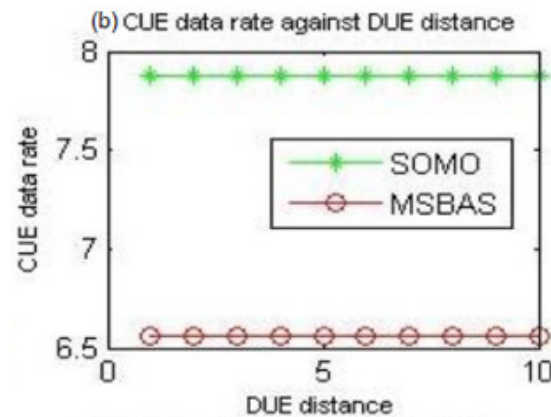


Fig. 7: CUE data rate with varied DUE distance.

The result indicated that SOMO CUE data rate outperformed that of MS-BAS when compared. The higher CUE data rate of SOMO is due to the larger CUE mode operating bandwidth of 70%, compared to that of MS-BAS of 60% when ($N_{DUEs} > N_{CUEs}$).

Fig. 8 is a plot of the entire system performance (all UEs) of the network.

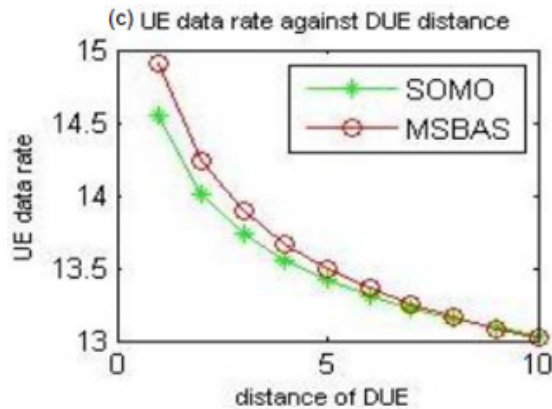


Fig. 8: UE data rate with varied DUE distance.

The result shows that MS-BAS outperformed SOMO.

Fig. 9 is the average data rate representation for both schemes.

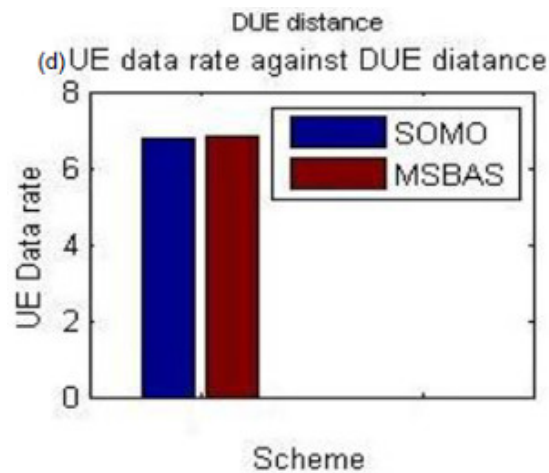


Fig. 9: Average data rates of UEs

The UE average data rates of SOMO and MS-BAS were 7.09 Mbps and 7.26 Mbps respectively. MS-BAS average UE data rate performed better than SOMO by 2.34 %.

From results presented in Figs. 6-9, when N_{DUEs} and N_{CUEs} are 12 and 8 respectively

and DUE distance ranges from 0 – 10 m, MS-BAS tradeoff CUE data rate for DUE data rate. The entire UE average data rate of MS-BAS was slightly higher than that of SOMO.

To analyze the impact of the number of D2D pairs on the communication network with respect to interference, the distance of DUEs was kept constant and the number of D2D pairs were varied. The simulation results show the impact of increased number of D2D pairs on DUE, CUE and UE data rate performance, as presented in Figs. 10 - 13.

Figs. 10-13 presents the data rate of DUE, CUE, entire UE (DUE and CUE), and average UE data rate when the DUE distance was kept constant and number of D2D pairs were altered from 1 – 10 pairs, assuming 20 UEs. The initial N_{CUE} and N_{D2D} were 18 and 2 respectively. As the number of D2D pairs increased by 1; N_{DUE} increase by 2 and N_{CUE} decreased by 2.

Fig. 10 is a plot of the DUE data rates with increasing number of D2D pairs.

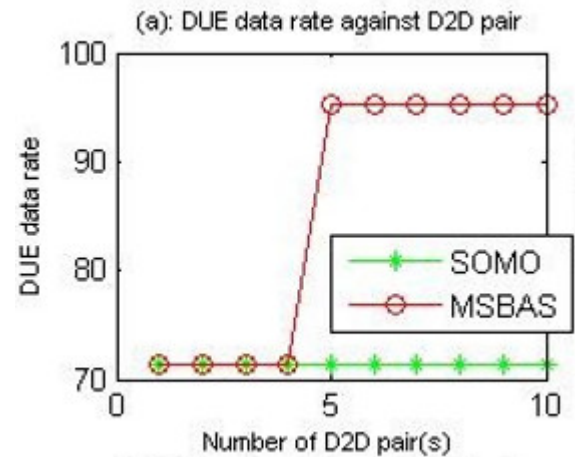


Fig. 10: DUE data rates with increasing DUE pairs

From Fig. 10, when $N_{DUE} < N_{CUE}$ (4 D2D pairs, 8 DUE, 12 CUE), the MS-BAS DUE data rate is equal to that of SOMO. This is so because when $N_{DUE} < N_{CUE}$, MS-BAS bandwidth would be 30% of system bandwidth and likewise SOMO bandwidth; both MS-BAS used the same DUE distance, D2D path loss, SINR, and data rate models.

When the number of D2D pairs increased to 5 (10 DUE and 10 CUE); $N_{DUE} = N_{CUE}$ and MS-BAS bandwidth would change to 40% of system bandwidth, while SOMO bandwidth remains 30% of system bandwidth. Also, when number of D2D pairs increased from 5 – 10 pairs ($N_{DUE} > N_{CUE}$); MS-BAS would use 40% of system bandwidth. The difference in operating bandwidth accounted for the two different data rate levels. MS-BAS operating at 30% of system bandwidth when number of D2D pairs was four and below had same data rate with the SOMO scheme. But when MS-BAS operated at 40% of system bandwidth, from 5 – 10 D2D pairs, the data rate of MS-BAS scheme outperformed that of SOMO by 25%.

Fig. 11 is a plot of CUE data rates with increasing number of D2D pairs.

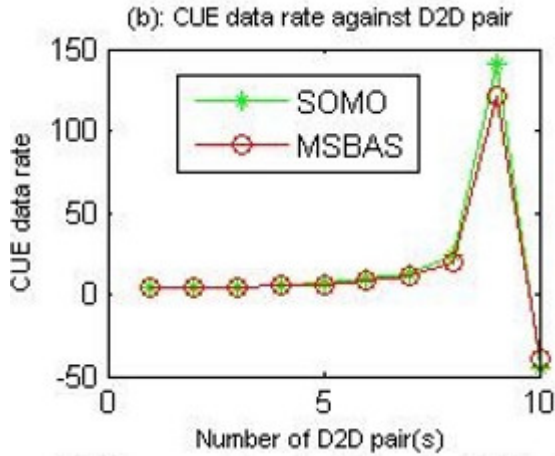


Fig. 11: CUE data rates with increasing D2D pairs.

The plot indicates that the MS-BAS CUE data rate and that of SOMO were the same within the range of 1 – 4 D2D pairs in the D2D network. However, at 5 – 8 D2D pairs, SOMO performed slightly better than the MS-BAS. At 9 D2D pairs, the performance of SOMO CUE data rate was better when compared with that of MS-BAS by 14.28 %, while MS-BAS performed better at 10 D2D pairs when compared to SOMO by 16.68 %.

Fig. 12 is performance of all UEs in the network as the number of D2D pairs increased.

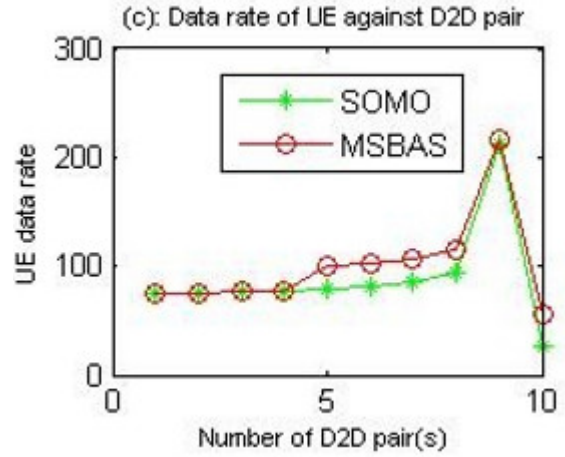


Fig. 12: UE data rate with increasing D2D pairs

The plot presents the data rate performance of all the UEs in the network. At each DUE distance, the data rate of DUEs and CUEs were summed up and plotted. The graphs show that the total UE data rate of SOMO and MS-BAS within range of 1 - 4 D2D pairs, were the same. However, from 5 – 10 D2D pairs MS-BAS data rate outperformed that of SOMO by 22.52 %, 21.82 %, 20.57 %, 17.72 %, 1.67%, and 53.93 % respectively. This outperformance results directly from the additional 10% bandwidth dynamically assigned to DUEs once the condition $N_{D2D} \geq N_{CUE}$ was met, from the formation of 5 D2D pairs upwards.

Fig. 13 is the average UE performance for both schemes

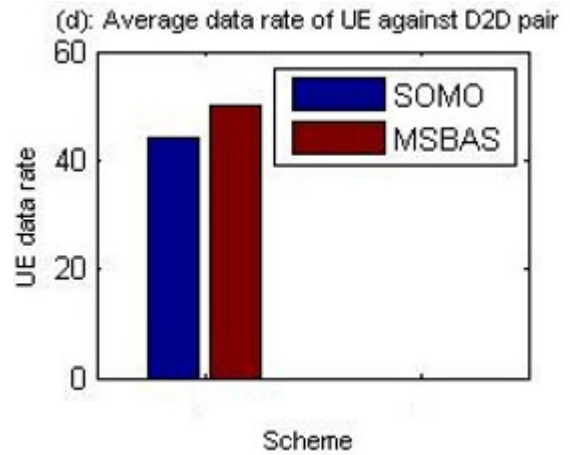


Fig. 13: Average UE data rates with increasing D2D pairs.

The plot shows the average of the entire UE (DUE and CUE) data rate, when number of D2D pairs increased from 1 – 10 and the DUE distance was kept constant. The average data rate of SOMO and MS-BAS stood at 44.08 Mbps and 50.17 Mbps respectively. The MS-BAS average data rate outperformed that of SOMO when compared by 12.14 %.

CONCLUSION

In this work, mode selection and bandwidth allocation techniques were integrated to mitigate cross-tier interference in a macro-D2D network. The mode selection sub-scheme focused on the UE separation distance and the receiver's SINR to assign communication mode to UEs, while the bandwidth allocation sub-scheme allocated a fixed fraction of 60% to CUEs (being the primary users of the network), and 30% for D2D connections, while dynamically allocating the remainder 10% to deserving communication tier based on the number of UEs in that mode, to maximize data rate (throughput), and limit spectrum wastage, which is an inherent problem with overlay architecture.

The integration of the Mode Selection and Bandwidth Allocation Schemes (MS-BAS) lead to the attainment of better system performance against previous works. Therefore, the MS-BAS addresses the problem of cross-tier interference, while improving system throughput and avoiding spectrum redundancy.

REFERENCES

- Adejo, A., Asaka, O., Bello-Salau, H., & Alenoghena, C. (2020). New framework for interference and energy analysis of soft frequency reuse in 5g networks. *Bulletin of Electrical Engineering and Informatics*, 9(5), 1941–1949. <https://doi.org/10.11591/eei.v9i5.2536>.
- Alquhali, A. H., Roslee, M., Alias, M. Y., & Mohamed, K. S. (2020). D2D communication for spectral efficiency improvement and interference reduction: A survey. *Bulletin of Electrical Engineering and Informatics*, 9(3), 1085–1094. <https://doi.org/10.11591/eei.v9i3.2171>
- Alzubaidi, O.T.H.; Hindia, M.N.; Dimiyati, K.; Noordin, K.A.; Wahab, A.N.A.; Qamar, F.; Hassan, R. (2022) Interference Challenges and Management in B5G Network Design: A Comprehensive Review. *Electronics*, 11, 2842. <https://doi.org/10.3390/electronics11182842>.
- Asadi, A, Wang Q, and Mancuso V, (2014). A survey on device-to-device communication in cellular networks, *IEEE Communications Surveys & Tutorials*, vol. 16, no. 4, pp. 1801–1819.
- Barik P.K., Shukla A, Datta R., and Singhal C., (2020). A Resource Sharing Scheme for Intercell D2D Communication in Cellular Networks: A Repeated Game Theoretic Approach. *IEEE Transactions on Vehicular Technology*. Volume: 69, Issue: 7, Page(s): 7806 – 7820. DOI 10.1109/TVT.2020.2991476.
- Chen, H., Deng, X., Gao, M., Yang, L., Guo, L., & Chi, M. (2018). Location Related Communication Mode Selection and Spectrum Sharing for D2D Communications in Cellular Networks. *International Conference on Intelligent Transportation, Big Data & Smart City* pp. 169-173. [doi:10.1109/icitbs.2018.00051](https://doi.org/10.1109/icitbs.2018.00051).
- Cho B, Koufos K, and Jantti J, (2013) Interference control in cognitive wireless networks by tuning the carrier sensing threshold, *IEEE International Conference on Cognitive Radio Oriented Networks*, pp. 282-287.

- Gao, X.; Yang, K.; Yang, N.; Wu, J. (2019) Energy-efficient resource block assignment and power control for underlay Device-to-Device communications in multi-cell networks. *Computer Networks*, 149, 240–251.
- Hassan, T. U., & Gao, F. (2019). An Active Power Control Technique for Downlink Interference Management in a Two-Tier Macro–Femto Network. *Journal of Sensors*, 19(9), 504 - 528.
- Hassan, T. U., Gao, F., Jalal, B., & Arif, S. (2018). Interference Management in Femtocells by the Adaptive Network Sensing Power Control Technique. *Journal of Future Internet*, 10(3), 2015 - 2028.
- Jiale, Z., Shuangzhi, L., Dan, M., & Xiaomin, M. (2018). Research on Joint Mode Selection and Resource Allocation Scheme in D2D Networks. *International Conference on Cyber-Enabled Distributed Computing and Knowledge Discovery*, 429 – 432.
- Junjie Tan, Ying-Chang Liang, & Gang Feng (2021). Deep Reinforcement Learning for Joint Channel Selection and Power Control in D2D Networks. *IEEE Transactions on Wireless Communications*, (20)2, 1363 – 1378.
- Koushik, M. & Shahedur, R. (2021); Multi-cell Interference Management in In-band D2D communication under LTE-A Network. *4th International Conference on Computing, Electronics and Communications Engineering*, pp 16-17 Aug 2021, University of Essex, Southend, UK.
- Li, Y, Song, W. Su, Z, Huang, L, Gao, Z, (2018) A distributed mode selection approach based on evolutionary gam for Device-to-Device communications. *IEEE Access* 2018, 6, 60045–60058.
- Li, M. (2019). Soft Frequency Reuse-Based Resource Allocation for D2D Communications Using Both Licensed and Unlicensed Bands. *International Conference on Ubiquitous and Future Networks*, 384–386. <https://doi.org/10.1109/ICUFN.2019.8806044>.
- Librino, F., & Quer, G. (2018). Distributed Mode and Power Selection for Non-Orthogonal D2D Communications: A Stochastic Approach. *IEEE Transactions on Cognitive Communications and Networking*, 4(2), 232–243. doi:10.1109/tccn.2018.2809721.
- Nasser, A., Muta, O., Elsabrouty, M., & Gacanin, H. (2019). Interference Mitigation and Power Allocation Scheme for Downlink MIMO-NOMA HetNet. *IEEE Transactions on Vehicular Technology*, 1–1. doi:10.1109/tvt.2019.2918336.
- Noura M and Nordin R (2016). A Survey on Interference Management for Device-to-Device (D2D) Communication and its Challenges in 5G Networks, *Journal of Network and Computer Applications*, Volume 71, Pages 130-150. <http://dx.doi.org/10.1016/j.jnca.2016.04.021>
- Onu, C., Bala. S., & Abolarinwa J. (2018). Enhanced Fractional Frequency Reuse in LTE A Heterogeneous OFDMA Network. *ATBU, Journal of Science, Technology & Education (JOSTE)*, 6 (2), 18 – 27.
- Rana, Z.A., Abdul, R.J., Shakir, M., Mohammad, Z.K., Abdulfattah, N. & Muhammad, R. (2021). Interference Mitigation in D2D Communication Underlying Cellular Networks: Towards Green Energy. *Computers*,

- Materials & Continua*, 68(1), 45 – 58.
- Rehman, S. U., Hussain, A., Hussain, F., & Mannan, M.A. (2020). A Comprehensive Study: 5G Wireless Networks and Emerging Technologies. *International Electrical Engineering Conference (IEEC 2020)*, 5, 25-32.
- Safaei, B, Mahdi, A, Monazzahy, H, Milad B and Ejlali, A., (2017). Reliability Side-Effects in Internet of Things Application Layer Protocols. *International Conference on System Reliability and Safety; At: Milan, Italy*.
- Shami T.M, Grace D., Burr I A., and Vardakas J.S. (2019). Load balancing and control with interference mitigation in 5G heterogeneous networks. *EURASIP Journal on Wireless Communications and Networking*:177 <https://doi.org/10.1186/s13638-019-1487-0>.
- Song, X., Han, X., Ni, Y., Dong, L., & Qin, L. (2019). Joint uplink and downlink resource allocation for D2D communications system. *Future Internet*, 11(1), 1–6. <https://doi.org/10.3390/fi11010012>
- Swetha, G.D., & Murthy, G.R. (2017). Selective Overlay Mode Operation for D2D communication in dense 5G cellular networks. *IEEE Symposium on Computers and Communications*. doi:10.1109/iscc.2017.8024610
- Xiaoqin, L., Yang, X. (2018). Mode Selection and Resource Allocation Algorithm Based on Interference Control for D2D Communication. *International Conference on Communications, Circuits and Systems*, 10(1), 286 – 290.
- Yang, C. Li, J, Semasinghe, P, Hossain, E, Perlaza, S.M, Han, Z, (2017) Distributed interference and energy-aware power control for ultra-dense D2D networks: A mean field game. *IEEE Trans. Wireless Communication*.16, 1205–1217.
- Zhai, D Sheng, M. Wang, X. Sun, Z. Xu, C. Li, J. (2017) Energy-saving resource management for D2D and cellular coexisting networks enhanced by hybrid multiple access technologies. *IEEE Trans. Wireless Communication*. 16, 1.
- Zhao, J., Li, S., Dan, M., & Xiaomin, M. (2018). Research on Joint Mode Selection and Resource Allocation Scheme in D2D Networks. *International Conference on Cyber-Enabled Distributed Computing and Knowledge Discovery*. 429 – 432.

PHYSICO-CHEMICAL ANALYSIS OF BIO-OIL PRODUCE FROM CO-PYROLYSIS OF *SIDA RHOMBIFOLIA* WITH LOW AND HIGH DENSITY POLYETHYLENE

*Abdullahi, A. M., Garba, M. U., Eterigho E. J., Alhassan, M., Adeniyi. O. D.

Chemical Engineering Department, Federal University of Technology, Minna. Nigeria.

Corresponding author email: abdulmusavespa@gmail.com

Abstract

Bio-oil was successfully produced from three samples *Sida Rhombifolia* (SR), Low Density Polyethylene (LDPE) and High Density Polyethylene (HDPE). Two step techniques was employed and this include pyrolysis of SR and co-pyrolysis of the samples. The preliminary analysis of the samples shows that the SR has volatile matters of 76.42 wt. %, LDPE 97.89 wt. % and HDPE 92.86 wt. %. These volatiles indicated that higher yield of bio-oil could be produced from the samples. The maximum yield of bio-oil obtained from pyrolysis of SR was 48.10 wt. % at pyrolysis parameters of temperature 500 °C, reaction time 60 minutes and particle size 2-4 mm. However co-pyrolysis increase the yield of the bio-oil from 48. 10 wt. % to 76.20 wt. %. The physio-chemical properties of the bio-oil: calorific value, viscosity, density. pH, moisture content, flash and pour point was carried out to determine the quality of the bio-oil while GC-MS and FTIR analyses were carried out to determine hydrocarbon composition present in the bio-oil. In order to ascertain the quality of the bio-oil produced, the properties were compared with the standard properties of diesel and gasoline. The GC-MS analysis shows that the bio-oil obtained from pyrolysis of SR contains 77.77 % oxygenated organics and 22.23 % aliphatic hydrocarbon. Co-pyrolysis reduces the organics from 77.77 % to 5.32 % and increases the aliphatic from 22.23 % to 88.48 % with the appearance of aromatic hydrocarbon. Therefore the co-pyrolysis shows an effective synergy between SR with LDPE and HDPE as well as the increase of the yield and quality of the bio-oil.

Keywords: SR, LDPE, HDPE, Bio-oil, Pyrolysis, Co-pyrolysis

Introduction

Renewable resources are the natural sources that can be replenished after its consumption. It can be classified into sustainable (those that can be naturally renewable) and renewable with careful planning as lingo-cellulosic biomass. Ligno-cellulosic biomass is a complex bio-polymer which primarily consisting of cellulose, hemicellulose and lignin. It is divided into three feedstock; woody biomass (forestry and wood waste), non-woody biomass (weeds such as *sida rhombifolia*, agriculture residues such as straws, bagasse strover and so on) and organic waste (animal waste and sewage sludge). Therefore, lignocellulosic is a promising renewable resource for sustainable production of various bio-oil (Tumuluru *et al.*, 2011 and Tian *et al.*, 2022). This study utilized the weed *Sida*

rhombifolia (known as arrow leaf) which is a non-woody biomass species found in most parts of the north central, southwest and south-south of Nigeria. The morphology features of the species; is a glabrous, ramous, erect, perennial that grows from 90 to 120 cm high, with a short erect stem, leaf and root. It grows in uncompleted buildings, along roads and river banks. With these characteristics, the SR is yet to have attention for bio-oil production as transport fuel in Nigeria. Furthermore, the proximate and ultimate analysis of non-woody biomass indicated highest energy values, volatile content, higher fixed carbon contents and low ashes (Kumar *et al.*, 2011).

Asadullah *et al.* (2007) was among one of the several researchers who produced bio oil from pyrolysis of biomass. It was confirmed in their research that the bio oil cannot be

used directly as transportation fuel because of adverse characteristics. These characteristics, particularly the instability of bio oil is associated with the high oxygen and water content that is hydrogen deficiency. In-order to increase the amount of hydrogen in the bio oil, plastic material such as Low and High Density Polyethylene (LDPE and HDPE) that are Hydrogen-rich are used to supplement the deficiency (Esso *et al.*, 2022).

In recent times, there has been a rise in environmental concern over plastic waste generation and disposal worldwide, resulting from the rise in population and industrialization. Plastics are materials that are made of wide range of synthetic and natural compounds, and are malleable and can be molded into different shapes and sizes. Plastics have become an indispensable materials used in several countries of the world, due to their durability, lightweight as well as flexibility and are utilized in a range of industrial and domestic areas (Khan *et al.*, 2016).

MATERIALS AND METHOD

Materials

Sida Rhombifolia was collected from road side in shabu along Jos road Lafia. Nasarawa State, Nigeria. LDPE and HDPE were collected from waste plastic dump site in Lafia. Nasarawa State, Nigeria.

METHODS

Preliminary Investigation of SR

Prior to pyrolysis, SR was physically treated by removing any adhering dirt on the surface then sun dried for 48 hour and subsequently dried in oven at 105 °C for one hour to remove moisture content.

The SR was milled to smaller particles sizes range between 1.0 - 8.0 mm. Proximate analysis of SR, LDPE and HDPE were conducted so as to ascertain the moisture content, volatile content, the fixed carbon and the ash content. On the other hand, the

ultimate analysis that provides the composition (wt. %) of carbon, hydrogen, nitrogen, oxygen and sulphur (CHNOS) for the SR, LDPE and HDPE were also conducted.

The thermal behaviour of the three samples (SR, LDPE and HDP) were performed by using a thermogravimetric analyser (Perkin Elmer, TGA 4000 Made in Netherlands model,). The samples were first analysed in a nitrogen atmosphere, pressure of 2.0 bar and heating rate of 20 °C/min. Derivative Thermo- gravimetry (DTG) was also used to evaluate the degree of loss of material's weight when temperature is elevated.

Pyrolysis of Set-Up

A pyrolyser as shown in the schematic diagram in figure 1 was used for experiment. The set-up comprises N₂ gas cylinder, valve, tubes and shells, pressure gauge, reactor, electric cell heater, condenser, ice bath and gas collector couple. The setup was used to investigate the pyrolysis parameters; temperature, reaction time, particle size at the desired heating rate. The condenser attached to the pyrolysis reactor was used to condense the volatile products from the reactor by exchanging with water at temperature below 25°C while the volatile passing through the tube side of the condenser. The temperature was varied from 350 °C to 650 °C, reaction time from 30 to 120 minutes and particle sizes between 1 mm to 8 mm.

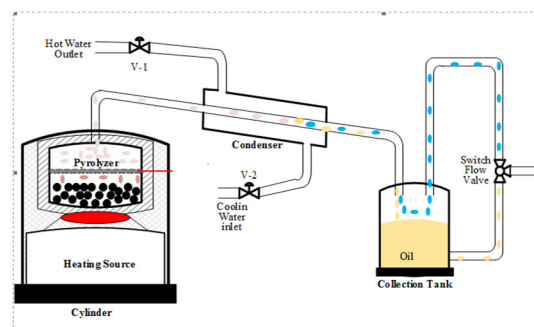


Fig. 1: Pyrolysis process setup

The equation for the calculation of bio-oil yield are given as follows:

$$\% \text{ Yield of Bio-oil} = \frac{\text{Volume of bio oil (ml)}}{\text{Starting weight of SR}} \quad (1)$$

$$\% \text{ Yield of Bio-Char} = \frac{\text{Weight of solid Char (g)}}{\text{Starting weight of SR}} \quad (2)$$

$$\% \text{ Yield of gas} = 100 \% - (\% \text{ oil} + \% \text{ Char}) \quad (3)$$

Characterization of Bio-Oil

The characterization of bio-oil produced from pyrolysis and co-pyrolysis was conducted to ascertain the viscosity, calorific value, density, moisture content, flash point, pour point, cetane, octane number, FTIR and GC-MS.

RESULTS AND DISCUSSION

Preliminary investigation of SR

Lignocellulose analysis of *Sida rhombifolia*

The lignocellulose analysis of *Sida rhombifolia* (SR) are presented in Table 1. The Table 1 shows that the SR has cellulose 52.14 wt. %, hemicellulose 28.35 wt. % and lignin 17.67 wt. % respectively (Tian *et al.*, 2022).

Table 1: Lignocellulose analysis of *Sida rhombifolia*

Parameter	Wt. %
Cellulose	52.14
Hemicellulose	28.35
Lignin	17.67

Proximate and Ultimate analysis of SR

The proximate and ultimate analyses of SR, LDPE and HDPE are presented in Table 2. The Table 2 shows that the proximate analyses of SR has higher volatile matter 76.42 wt. % with low ash content 1.54 wt. % compared with the volatile matter of rice husk (68.20 wt. %) and sweet grass (69.14 wt. %) (Tumuluru *et al.*, 2011). The ultimate analysis of SR shows low hydrogen 5.00 wt. %. These results of SR corroborated with the result of other researchers (Ringer, *et al.*, 2006; Oyeibanji *et al.*, 2022). The proximate and ultimate analyses of LDPE as presented in

the Table 2 shows volatile content 97.39 wt. % with low ash content 0.53 wt. %, hydrogen 15.37 wt. % and no sulphur present. Similarly HDPE has volatile content 92.86 wt. % with ash content 3.68 wt. %, hydrogen 14.37 wt. % and no sulphur present. The ultimate analysis shows LDPE and HDPE have higher hydrogen as presented in the Table 2 which could serve as donor to SR during pyrolysis (Esso *et al.*, 2022).

Table 2: Proximate and ultimate analysis of SR

Composition	SR (wt. %)	LDPE (wt. %)	HDPE (wt. %)
Proximate			
Moisture Content	4.30	1.24	1.32
Volatile Content	76.42	97.39	92.86
Fixed Carbon	17.44	0.84	2.14
Ash Content	1.84	0.53	3.68
Ultimate			
Carbon	60.00	83.63	84.63
Hydrogen	5.00	15.37	14.37
Oxygen	37.00	0.34	0.44
Nitrogen	1.00	0.66	0.56
Sulphur	0.02	0.00	0.00

Thermo-Gravimetric and Differential Thermal Analysis

Thermo-Gravimetric Analysis of SR

The Thermo-Gravimetric Analysis (TGA) are presented in Fig. 2 (a). The curve pattern in the Fig. 2 (a) was divided into three phases; the first phase is evaporation at temperature 49⁰C to 246.57⁰C where the SR content was heated and the moisture elimination occurred. The second phase at temperature 240⁰C to 370⁰C is devolatilization where the volatile matters been removed. Temperature above 370⁰C to 426⁰C, an accelerated decomposition of internal constituent (cellulose and hemicellulose) with an approximate weight loss of about 72 wt. %. At this phase, the

most significant complex organic compounds including partial lignin were breaking down for more removal of volatile substance. The third phase shows continuous removal of volatile component at temperature 500 °C. This explanation corroborated with the research work reported by Dewangan, (2014) where degradation of biomass involves three main stages; moisture removal, decomposition of unstable polymers and continuous slight valorization (Dewangan, 2014).

Differential Thermal Analysis of SR

The Differential Thermal Analysis (DTA) are presented in Fig. 2 (b). The Fig. 2 (b) shows the decomposition of cellulose, hemicelluloses and lignin was assigned to corresponding temperature peaks and reaction time as presented in Fig. 2 (b). At temperature 256.0 °C endothermic reaction occurred where the heat absorbed by the SR caused the decomposition of hemicelluloses and CO₂ and CH₂ been released. At temperature 283.03 °C correspond to the maximum decomposition rates of celluloses while at temperature 380 °C correspond to the maximum decomposition rate of lignin. Above temperature 380 °C correspond to time when volatilisation begins. The volatilisation continue up to temperature 500 °C as presented in Fig. 2(b). The DTA analysis of SR was slightly difference from research work presented by Bu *et al.* (2014).

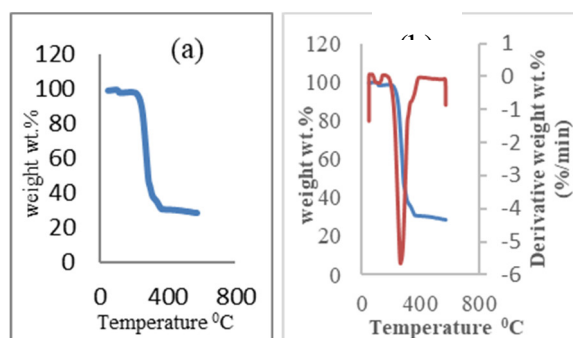


Fig. 2: (a) TGA of SR (b) DTA of SR

Thermo-gravimetric analysis of LDPE and HDPE

The thermal degradation of LDPE and HDPE are presented in Fig. 3 (a). The Fig. 3

(b) shows three stages for decomposition: the first stage at temperature 135 °C - 300 °C the LDPE and HDPE begins to decompose, at second stage, a significant thermal decomposition occurred at 300 °C – 500 °C where short and long chain of hydrocarbon decomposed and at third stage, a steady thermal decomposition continues till end of the decomposition at temperature above 500 °C.

Differential Thermal analysis (DTA) of LDPE and HDPE

The DTA curve of LDPE and HDPE are presented in Fig. 3 (b). The decomposition of short chain hydrocarbon of LDPE and long chain hydrocarbon of HDPE was assigned to corresponding temperature peaks and reaction time as presented in the Fig. 3(b). At temperature 285 °C endothermic reaction occurred that is, LDPE and HDPE begins to absorbed heat which could resulted to the decomposition of hydrocarbon though the decomposition of LDPE started before the HDPE. At temperature 400 °C appears to be the highest peaks in the thermograph which was assigned to the time when the decomposition rates of LDPE and HDPE occurred. The decomposition continuing up to the temperature 500 °C.

It was observed that the complete decomposition of LDPE and HDPE was achieved at final temperature of 500 °C as presented in the Fig. 3. This explanation of thermal decomposition of LDPE and HDPE corroborated with the research work of Garba *et al.*, (2018).

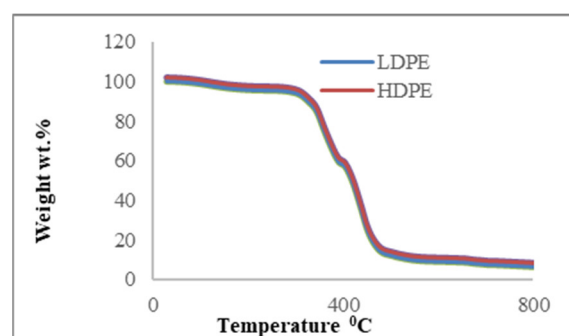


Fig. 3: TGA (a) LDPE

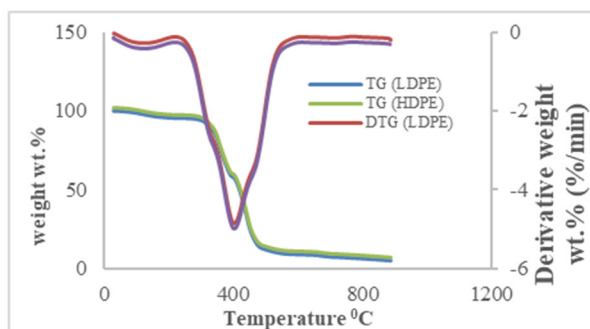


Fig. 3: DTA (b) HDPE

Pyrolysis of SR

The pyrolysis parameters namely; temperature, reaction time and particle size for production of the bio-oil were investigated using set-up in Fig. 1.

Effect of Temperature on pyrolysis of SR

The influence of temperature on pyrolysis of SR in the production of bio-oil was presented in Fig. 4 (a). Fig. 4(a) shows that the yield of bio-oil was 48.1 wt. % at temperature 500 °C with low bio-char 29.5wt. % (Dewangan *et al.*, 2014). A sudden decrease in bio oil yield was observed from 48.1 to 46.9 wt. % as temperature increased from 500 °C to 550 °C and continued to decrease as temperature increases to 600 °C. Ali *et al.* (2016) and other researchers reported that at temperatures between 450 °C and 500 °C, higher yield could be achieved depending on the nature of biomass as either woody or non-woody Dewangan *et.al.* (2014).

Effect of reaction time on pyrolysis of SR

The influence of reaction time was investigated in the production of bio-oil Fig. 4 (b) presents the influence of reaction time on pyrolysis SR. The maximum yield of 48.30 wt. % was obtained at reaction time of 60 minutes which implies that at 60 minutes, there was total degradation of the SR particles. As reaction time increase from 60 to 70 minutes, the yield decreases and bio-char increased as presented in the Fig. 4 (b). The reaction time corroborated with the submission of Dewangan *et.al.* (2014).

Effect of particle size on pyrolysis of SR

Fig. 4 (c) presents the influence of particle size on pyrolysis of SR. The highest yield was 50.55 wt. % at particle sizes between 2.0 mm and 4.0 mm. At these particle sizes, there was higher penetration of heat inside SR which favours the breakdown of the cellulose, hemicellulose and lignin. This explanation corroborated with the research work of Zang *et al.* (2013). As particle size increases from 4.0 to 8.0 mm the char increases linearly as presented in Fig. 4 (c). This implies that, the SR demonstrated inverse relationship between bio oil and bio-char.

It can be inferred from the pyrolysis parameters that, the highest yield of bio-oil was achieved at temperature of 500 °C, reaction time of 60 minute and particle size range of 2-4 mm. The parameters obtained in this study were compared with the research works; Dewangan *et al.* (2014) and Ali *et al.* (2016) for the influence of temperature and reaction time, Dewangan *et al.* (2016) for the influence of particle size.

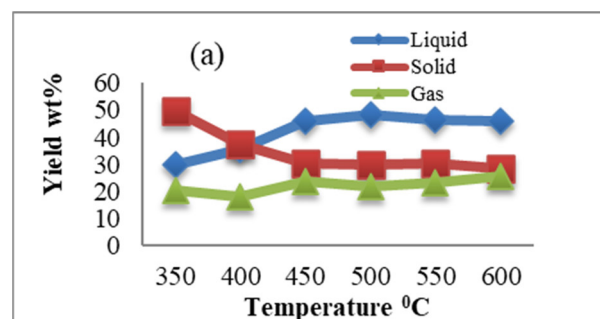


Fig. 4(a) Effect of temperature

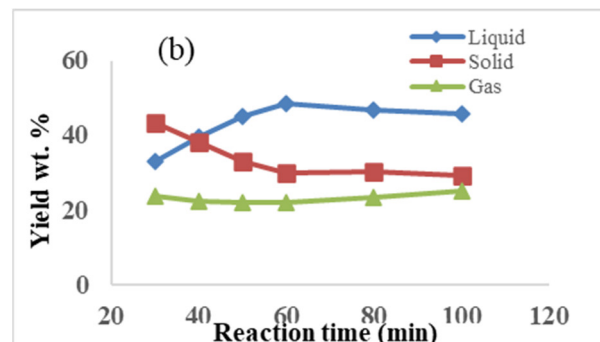


Fig. 4: (b) Effect reaction time

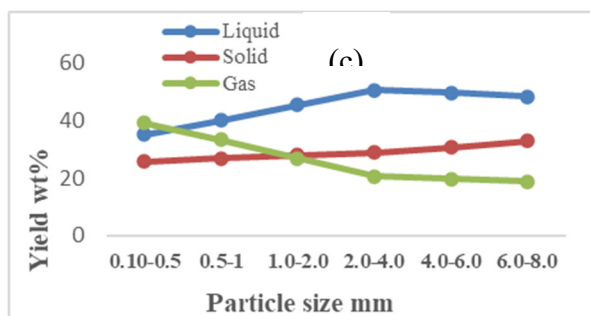


Fig. 4: (c) Effect particle sizes

Pyrolysis of LDPE and HDPE

The pyrolysis of LDPE is presented in Fig. 5 (a). Fig. 5 (a) shows that the yield of oil from pyrolysis of LDPE was 78.6 wt. %. Similarly, the pyrolysis of HDPE is presented in Fig. 5 (b). The Fig. 5 (b) also shows that the yield of oil from pyrolysis of HDPE was 75.20 wt. %. Though, it was observed that the yield of the oil from LDPE was slightly higher than the yield of oil from HDPE. These results of pyrolysis of LDPE and HDPE corroborated with explanation of Sogancioglu *et al.* (2017). However, the yield of the oil from both pyrolysis of LDPE and HDPE are higher than the yield of bio-oil from pyrolysis of SR.

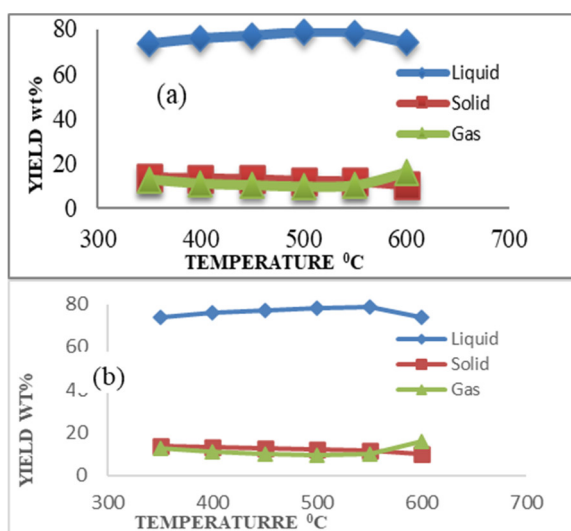


Fig. 5: Pyrolysis (a) LDPE (b) HDPE

Co-Pyrolysis of SR with LDPE

The co-pyrolysis of SR with LDPE are presented in Fig. 6 (a). It was observed from Fig. 6 (a) that co-pyrolysis produced higher bio-oil yield of 68.4 wt. % with low solid

char than the bio-oil yield of 50.55 wt. % from pyrolysis of SR alone. The highest yield of bio-oil occurred as a result of the synergistic effect between SR and LDPE (Abnisa *et al.*, 2014; Hassan *et al.*, 2016). Also the co-pyrolysis of SR with HDPE was presented in Fig. 6 (b). It can be seen from the Fig. 6 (b) that the yield of bio-oil from co-pyrolysis was 64.5 wt. %. The yield of bio-oil from co-pyrolysis of SR with HDPE was little lower than the yield of bio-oil from co-pyrolysis of SR with LDPE. Though the co-pyrolysis of SR with LDPE and HDPE showed effective synergy. This synergy was due to free radicals generated from linear molecule of long and short branch chain of LDPE and HDPE (Sun *et al.*, 2013) and (Dewangan *et al.*, 2016).

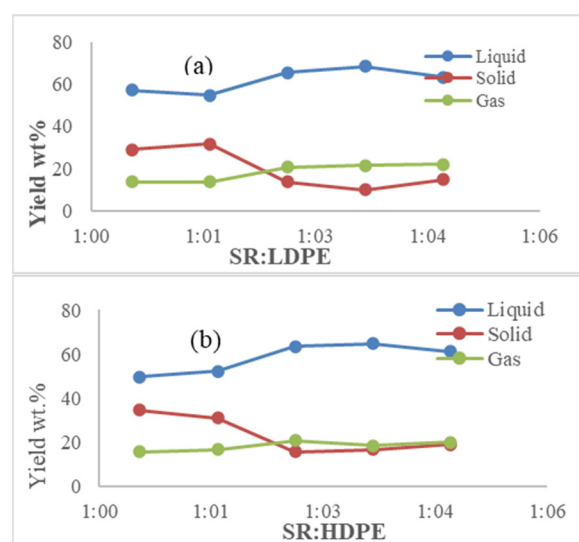


Fig. 6: Co-Pyrolysis (a) SR with LDPE (b) SR with HDPE

Physical Properties of Bio-Oil

The physical properties of the oil from pyrolysis of SR, LDPE, HDPE and co-pyrolysis of SR with LDPE and HDPE are presented in Table 3. The Table 3 shows that the calorific value of bio-oil from pyrolysis of SR was 17.01 MJ/kg which is lower than the acceptable standard limits of the calorific values of diesel and gasoline as 42.60 and 43.71 MJ/kg as presented in Table 3.

Table 3. Physical properties of the bio-oil

Sample description	pH Value	Viscosity (cst)	Density (kg/m ³)	Moisture Content (wt. %)	Caloric Value (MJ/Kg)	Flash Point (°C)	Pour Point (°C)
SR	5.97	13.23	1.0460	4.30	17.01	36	-32
LDPE	6.96	5.06	0.7801	2.01	35.04	54	-21
HDPE	6.89	5.73	0.7806	2.14	34.02	53	-21
SR LDPE	6.75	6.01	0.7887	2.70	27.90	51	-35
SR:HDPE	6.41	6.94	0.7893	2.75	26.17	50	-34
Diesel fuel	-	2- 4.5	0.8450	0	42.60	60	-40
Gasoline	-	0.006	0.7197	-	43.71	-43	-57

This low calorific value was due to the presence of oxygen in significant amount and thereby reducing the enthalpy of the bio-oil (Mohanty *et al.*, 2011) hence, this bio-oil cannot be used directly as transport fuel unless it undergoes further treatment by co-pyrolysis with LDPE and HDPE to remove oxygen in significant amount.

The calorific value of oil from pyrolysis of LDPE and HDPE are 35.04 MJ/kg and 34.02 MJ/kg respectively (Demetra *et al.*, 2016) and (Dongxue *et al.*, 2019). The calorific value from co-pyrolysis SR with LDPE and HDPE are 27.90 and 26.17 MJ/Kg. The increase could be attributed to effective interaction between free radicals of SR with LDPE and HDPE. Onal *et al.* (2014) and Martinez *et al.* (2014) explained that the oil from co-pyrolysis with plastic has higher calorific value than pyrolysis of individual biomass.

The viscosity of the oil from pyrolysis of SR was 13.23 cst while LDPE and HDPE are 5.06 and 5.73 cst respectively. This clearly reveal that the viscosity of LDPE and HDPE was much closer to the viscosity of diesel 2- 4.5 cst as presented in the Table 3. However, the bio-oil from co-pyrolysis of LDPE and HDPE are 6.01 and 6.94 cst. The decrease in the viscosity was due to the influence of hydrogen donor from LDPE and HDPE during co-pyrolysis as well as rapid condensation (Bardalai, 2015). The moisture content from the pyrolysis of SR was 4.20 % while LDPE and HDPE are

2.01 and 2.14 % respectively. The moisture content of the bio-oil from co-pyrolysis are 2.70 and 2.75 % respectively. The co-pyrolysis shows significant reduction in the moisture content. This reduction is corroborated by other researchers such as Abnisa *et al.* (2014) where co-pyrolysis biomass with plastic reduced the moisture content in the bio-oil.

The density of the oil from pyrolysis of SR was 1.0460 kg/m³ while LDPE and HDPE are 0.7801 and 0.7806 kg/m³ respectively. It was observed that the density of the oil from LDPE and HDPE was very close to the density of gasoline but the density of the oil from SR alone was higher than the density of both diesel and gasoline as presented in the Table 3. The density of the bio-oil reduced from 1.0460 to 0.7887 and 0.7893 kg/m³ respectively. This implies that there was effective synergy between SR with LDPE and HDPE. This assertion was similarly reported by other researchers (Bardalai 2015). The pH of the oil from pyrolysis was 5.97 while LDPE and HDPE are 6.96 and 6.89 respectively. Though the major contributory factor for high pH in the bio-oil from pyrolysis of SR was due to the presence of organic acids such as carboxylic acid (Bardalai, 2015). The pH of bio-oil from the co-pyrolysis was 6.01 and 6.95 respectively. The pH does not apply as measurable properties in gasoline.

The flash point of the oil from pyrolysis of SR was 36 °C while LDPE and HDPE are 54

$^{\circ}\text{C}$ and 53°C respectively. The flash point of the bio-oil from the co-pyrolysis was 48°C and 51°C respectively. It was observed that the flash point of the blend was close to flash point of diesel 60°C but not close to flash point of gasoline as -43°C (George *et al.*, 2015). The pour point of bio-oil from pyrolysis of SR was -32°C while LDPE and HDPE are -23°C and -21°C respectively. The pour point of the oil from the co-pyrolysis are -35°C and -34°C respectively. It was observed that the co-pyrolysis does not improve the pour point of the bio-oil significantly as is to the pour point of gasoline.

Chemical Properties of Bio-Oil

This study focused on producing higher quality bio-oil that can be used as a transport fuel. The bio-oil produced from pyrolysis of SR and co-pyrolysis with LDPE and HDPE were analysed using Gas Chromatography and Mass Spectroscopy (GC-MS) and Fourier Transform Infra-Red (FTIR).

GC-MS analysis of the bio-oil pyrolysis

The GC-MS analysis of bio-oil from pyrolysis of SR are presented in Fig. 7 (a). The hydrocarbon compounds exist in the bio-oil obtained from pyrolysis of SR contains carbon number ranging $\text{C}_9\text{-C}_{24}$ with high concentration of $\text{C}_9\text{-C}_{18}$. The analysis corroborated by the research work of Hassan *et al.* (2009) where the bio oil also contains higher molecular weight. The analysis as presented in the Fig. 7 (a) shows the highest peak was assigned to Phenol compound in peak nine. The first peak at retention time of 3.443 minutes was assigned to Propanoic acid ($\text{C}_3\text{H}_7\text{O}_2$), retention time of 4.842 compound is Oxirane ($\text{C}_3\text{H}_6\text{O}$), retention time of 5.37 minutes compound is Acetamide (CH_3CONH_2), retention time of 7.508 compound is Butane (C_4H_{10}), retention time of 8.551 minutes compound is 1,2-Ethanediol ($\text{C}_2\text{H}_6\text{O}_2$), retention time of 9.553 minutes compound is Phenol ($\text{C}_6\text{H}_5\text{OH}$), retention time of 9.767 minutes compound is 3-Penten-2-one ($\text{C}_5\text{H}_8\text{O}$), retention time of 9.917 minutes compound is

Propanoic acid, retention time of 12.633 minutes compound is 2-Propanol ($\text{C}_3\text{H}_8\text{O}$), retention time of 14.473 minutes compound is Decane. It can be deduced that the GC-MS analysis of bio-oil obtained from SR contains 77.77 % oxygenated organics while 22.23 % are aliphatic hydrocarbon (Wang *et al.*, 2021).

The GC-MS analysis of oil from pyrolysis of LDPE is presented in Fig. 7 (b). The analysis shows that the majority of hydrocarbon compounds are light and heavy aliphatic compound with carbon number ranging from $\text{C}_6\text{-C}_{24}$ though with high concentration from carbon number ranging $\text{C}_6\text{-C}_{15}$. The first compound identified from the analysis was 1-hexene, (C_6H_{12}) at retention time of 1.91 minutes and last compound identified was Tetracosane ($\text{C}_{24}\text{H}_{50}$) at retention time of 2.26 minutes. It also shows that the hydrocarbon compounds are straight chain as well as branch chain hydrocarbon compounds, this is because long chains hydrocarbon were breakdown to form shorter ones thus generating a new substance during thermal degradation of LDPE. Therefore, the list of hydrocarbon compounds identified from GC-MS analysis of the oil from pyrolysis of LDPE are alkane and alkene compounds (Yang *et al.*, 2016).

The GC- MS analysis of oil from pyrolysis of HDPE are presented in Fig. 7 (c). The analysis shows that the majority of hydrocarbon compounds are also light and heavy aliphatic compounds with carbon number ranging from $\text{C}_6\text{-C}_{28}$ though with majority $\text{C}_9\text{-C}_{15}$. The first compound identified from the analysis was Nonene (C_9H_{18}) at retention time of 3.062 minutes and last compound identified as Tetracosane ($\text{C}_{28}\text{H}_{58}$) at retention time 28.45 minutes. Similarly, the Fig. 7 (c) shows that the majority of hydrocarbon compounds are straight chain as well as some branch chain. This long chain hydrocarbon compounds were breakdown to form smaller ones during pyrolysis (Al-Salem 2019).

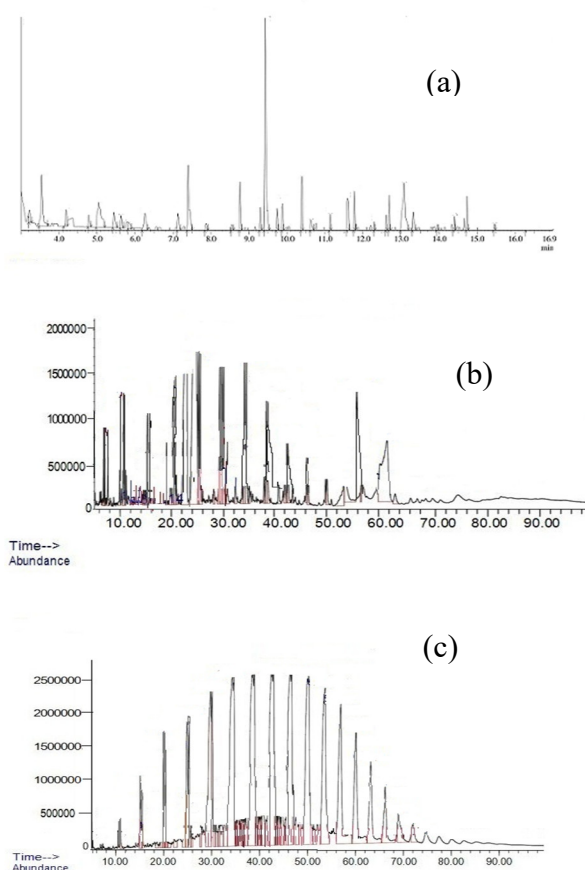


Fig 7: GC-MS analysis of the bio-oil obtained from (a) SR (b) LDPE (c) HDPE

GC-MS Analysis of the Bio-Oil obtained from Co-Pyrolysis

The GC-MS analysis of bio-oil from co-pyrolysis of SR with LDPE are presented in Fig. 8 (a). The co-pyrolysis lead to appearance of aromatic with more of aliphatic hydrocarbon and little oxygenated organic compounds. The oxygenated which emanated from SR begins to disappear as indicated by retention time of the peaks as presented in the Fig. 8 (a). This disappearing could be attributed to the effect of LDPE which donated hydrogen during co-pyrolysis consequently, oxygenated compounds such as esters, ethers, aldehyde and ketones began to reduce. It was observed that the influence of LDPE shows that the 77.77 % of oxygenated organic in the bio-oil from pyrolysis of SR reduces to 5.32 % while the 22.23 % of aliphatic in the bio-oil increases to 88.48 % with appearances of aromatic hydrocarbon of 6. 20 %.

The GC-MS analysis of bio-oil from co-pyrolysis of SR with HDPE was presented in Fig. 8 (b). It also shows that the co-pyrolysis reduced significantly the oxygenated organics that emanated from SR as indicated by retention time of the peaks as presented in Fig. 8 (b). It was observed that the influence of HDPE shows that the 77.77 % of oxygenated organic in the bio-oil from pyrolysis of SR reduces to 21.05 % while the 22.23 % of aliphatic in the bio-oil increases to 73.53 % with appearances of aromatic hydrocarbon of 5.42 %.

Therefore, it can be deduced that the co-pyrolysis shows an effective synergy between SR and LDPE and HDPE as well as the increase in the yield and quality of the bio-oil (Thuan *et al.*, 2022).

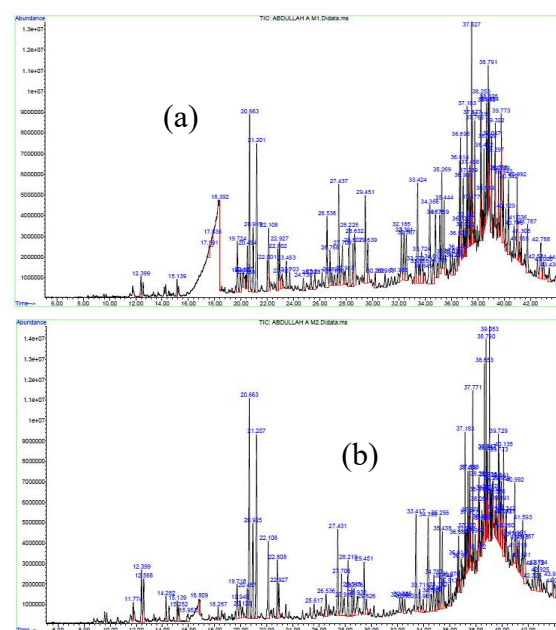


Fig. 8: GC-MS analysis of co-pyrolysis (a) SR with LDPE (b) SR with HDPE

FTIR Analysis

The result of FTIR analysis of bio-oil from SR is presented in Fig. 9 (a). The absorption bands of 725.25, 923.86, 1103.32, 1282, 1410.80, 1603.82, 1705.12, 3063.061, 3456.55, and 3842.04 cm^{-1} correspond to functional groups; C-H, CH-CH₂, C=O, C-O-C, C=O, C=C, COO, CH-CH, OH, N-H, O-H and O-H respectively. The absorption

bands as presented correspond to light compounds; alkane, ketones, esters, ethers, aromatic, alcohol and carboxylic acid. This result of the FTIR analysis corroborated with the FTIR analysis of bio-oil described by Zhang *et al.* (2016). It was observed that the FTIR confirmed the presented of oxygenated organic compound as presented in the Fig. 9 (a).

The FTIR of the oil from pyrolysis of LDPE was presented in Fig. 9 (b). The absorption bands of 725.25, 964.44, 902.72, 1473.44, 1604.20, 2731.29, 2729.30 and 2939.61 cm^{-1} correspond to functional group $\text{CH}=\text{CH}$, $-\text{CH}=\text{CH}$ (trans), $-\text{CH}_3$, $-\text{C}-\text{CH}_3$, $-\text{C}-\text{CH}_3$, and $-\text{C}-\text{CH}_3$ respectively. The bands as presented correspond to alkane and alkene (Sachin *et al.*, 2011).

The FTIR of the oil from pyrolysis of HDPE is presented in Fig. 9 (c). The absorption bands 887.28, 991.23, 1226.77, 1465.94, 1604.26, 2731.29, 2729.30 and 3616.58 cm^{-1} correspond to functional group $\text{CH}=\text{CH}$, $-\text{CH}=\text{CH}$ (trans), $-\text{CH}_3$, $-\text{C}-\text{CH}_3$, $-\text{C}-\text{CH}_3$, and $-\text{C}-\text{CH}_3$ respectively. The bands as presented correspond to alkane and alkene (Sachin *et al.*, 2011).

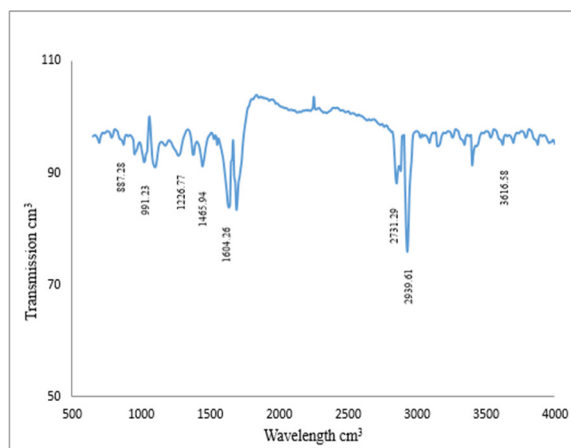
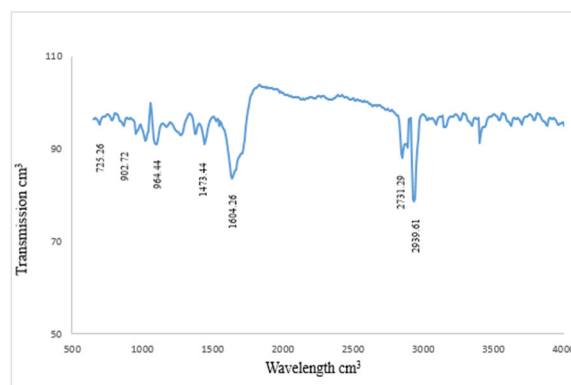
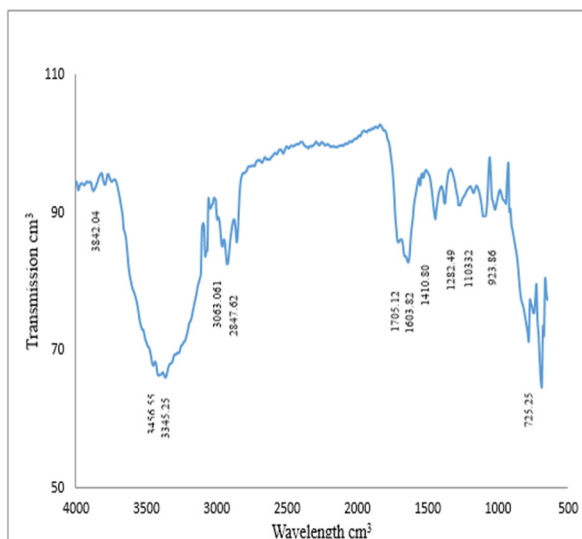


Fig. 9: FTIR of the oil from (a) SR (b) LDPE (c) HDPE

CONCLUSION

This study investigated the production of high quality bio-oil from co-pyrolysis of SR with LDPE and HDPE. From preliminary study, the proximate analysis shows that the SR has volatile matters of 76.42 wt. %, LDPE of 97.89 wt. % and HDPE of 92.86 wt. % which indicated the potentials for producing high yield of oil. The highest yield of bio-oil from pyrolysis of SR was 48.10 wt. % at temperature 500 °C, in reaction time of 60 minutes and particle size of 2-4 mm. However, the co-pyrolysis increased the yield of bio-oil from 48.10 wt. % to 76.20 wt. %. The physio-chemical properties of the bio-oil shows that the calorific value, viscosity, density, flash point and pour point increases significantly. The GC-MS analysis of bio-oil shows that the influence of co-pyrolysis reduced the oxygenated organic contained in the bio-oil from 77.77 % to 5.32 % while aliphatic increased from 22.23 % to

88.48 % with appearances of aromatic hydrocarbon of 6.20 %. Therefore, it can be deduced that the co-pyrolysis shows an effective synergy between SR with LDPE and HDPE as well as the increase of the yield and quality of the bio-oil.

REFERENCES

- Abnisa, F., Daud, W. M. A.W., & Saliu, J.N. (2014). Pyrolysis of Mixtures of Palm Shell and Polystyrene: an Optional Method to Produce a High Grade Pyrolysis Oil. *Environmental Progress and Sustainable Energy*, 33, 1026-33.
- Ali, N., Saleem, M., Shahzad, K., Hussain, S., Chughta, A. (2016). Effect of operating parameters on production of bio-oil from fast pyrolysis of maize stalk in bubbling fluidized bed reactor. *Journal of Chemical Technology*. 18, 3, 88—96, 10.1515
- Al-Salem, S., M. (2019). Thermal pyrolysis of high density polyethylene (HDPE) in a novel fixed bed reactor system for the production of high value gasoline range hydrocarbons (HC). *Process Safety and Environmental Protection*, 127, P171-179.
- Asadullah, M., Rahman, M., A., Ali, M., M., Rahman, M., S., Motin, M., A. (2007). Production of bio-oil from fixed bed pyrolysis of bagasse. *Fuel*. 86 (16): 2514-2520.
- Bardalai, M. (2015). A review of physical properties of biomass pyrolysis oil. *International Journal of Renewable Energy Research (IJRER)*, 5(1): 277-286.
- Bu, Q., Lei, H., Wang, L., Wei, Y., Zhu, L., Zhang, X., Liu, Y., Yadavalli, G., Tang, J. (2014). Bio-based phenols and fuel production from catalytic microwave pyrolysis of lignin by activated carbons. *Bioresour. Technol.*, 162, 142-147.
- Dewangan, A., K. (2014). Co-pyrolysis of Lignocellulosic Biomass and Synthetic Polymer. *Biomass and Synthetic Polymer*. T-R 110CH0464
- Dewangan, A., Pradhan, D., & Singh, R. K. (2016). Co-pyrolysis of Sugarcane Bagasse and Low-Density-Polyethylene: Influence of Plastic on Pyrolysis Product Yield. *Fuel*, 185, 508-516.
- Dongxue, Y., Helong, H., Songgeng, L. (2019). Two-step catalytic co-pyrolysis of walnut shell and LDPE for aromatic-rich oil. *Energy Conversion and Management*. 198 111816
- Esso, S., B., E., Xiong, Z., Chaiwat, W. Kamara, F., M. (2022). Review on synergistic effects during co-pyrolysis of biomass and plastic waste: Significance of operating conditions and interaction mechanism. *Biomass and Bioenergy*. 159, 106415.
- Garba, M.U., Inalegwu A, Musa U., Aboje A.A., Kovo A.S. and Adeniyi O.D. (2018), Thermogravimetric characteristic and kinetic of catalytic co-pyrolysis of biomass with low- and high-density polyethylenes, *Biomass Conversion and Biorefinery*, Springer-Verlag Berlin, Germany, (1),143-150
- Hassan, E., M., Yu, F., Ingram, L., Steele, P. (2009). The Potential Use of Whole-tree Biomass for Bio-oil Fuels. *Energy Source*. 31:20, 1829-1839, DOI: 10.1080/15567030802463364.
- Khan, M., H., M. Sultana, M. R. Al-Mamun, and M. R. Hasan, (2016). Pyrolytic Waste Plastic Oil and Its Diesel Blend: Fuel Characterization. *Journal of Environmental and Public Health* Volume, Article ID 61-67
- Kumar, M., Patel, S., K., Hamid, P., F. (2011). Characteristics of some forestry nonwoody biomass species and estimation of their power generation potentials. *Energy sources*, part a: recovery, utilization, and environmental effects. 132.1650-1654
- Martinez, J. D., Vesses, A., Mastral, A. M.,

- Murillo, R., Navarro, M. V., & Puy, N. (2014). Co-pyrolysis of Biomass with Waste Tyres: Upgrading of Liquid Biofuel. *Fuel Process Technology*, 119, 263-71.
- Mohanty, P., Pant, K., K., Naik, S., N., Das, L., M., Vasudevan P. (2011). Fuel production from biomass. *Indian perspective for pyrolysis oil*, 6 11-34.
- Onal, E., Uzun, B. B., & Putin, A., E. (2014). Bio-oil Production via Co-pyrolysis of Almond Shell as Biomass and High-Density Polyethylene. *Energy Conversion and Management*, 78, 704-710
- Oyebanji, J., A., Fayomi, O., I., S., Oyeniyi, P., G., Akor, & Ajayi, S., T. (2022). Physico-Chemical analysis of pyrolyzed bio-oil from *Lophira alata* (Iron wood) wood. Volume 4. 4-9
- Ringer, M., Putsche, V., Scatell, J. (2006). Large-scale pyrolysis oil production and economic analysis; technical report; National renewable energy laboratory: Cole Boulevard, Co, USA. NREL/TP -510-37779.
- Sachin, K., Singh, R., K. (2011). Recovery of hydrocarbon liquid from waste high density polyethylene by thermal pyrolysis. *Brazilian Journal of Chemical Engineering*. Vol. 28,665-666.
- Sogancioglu, M., Yel, E., Ahmetli, G. (2017). Pyrolysis of waste high density polyethylene (HDPE) and low density polyethylene (LDPE) plastics and production of epoxy composites with their pyrolysis chars. *Journal of Cleaner Production*. 165: 369e381.
- Sun, X., Y., L., Xiang, J., Hu, S., Su, S. (2013). Pyrolysis and dehalogenation of plastics from Waste Electrical and Electronic Equipment (WEEE): A review. *West Management*. 33. 462-473
- Tian, D., Shen, F., Hu, F., Huang, M., Zhao, L., He, J., Li, Q., Zhang, S., Shen, F. (2022). Complete conversion of lignocellulosic biomass into three high-value nanomaterials through a versatile integrated technical platform.
- Thuan, A., V., Khanh, Q., VuLy, T., H., Kwon, B., Hyun Hwang, T., Kim, J., Kim, J. (2022). Co-pyrolysis of lignocellulosic biomass and plastics: A comprehensive study on pyrolysis kinetics and characteristics. *Journal of Analytical and Applied Pyrolysis*. Vol. 163, 105464
- Tumuluru, J. S., Wright, C. T., Hess, J. R., & Kenney, K. L. (2011). A review of biomass densification systems to develop uniform feedstock commodities for bioenergy application. *Biofuels, Bioproducts and Biorefining*, 5(6), 683–707
- Wang, X., Zhai, M., Guo, H., Panahi, A., Dong, P. (2021). High-temperature pyrolysis of biomass pellets: The effect of ash melting on the structure of the char residue. *Fuel*, 285, 1-2 119084
- Yang, J., Rizkiana, J., Widayatno W., B., Karnjanakom, S., Kaewpanha M., Hao X., Abudula, A., Guan, G. (2016). Fast co-pyrolysis of low density polyethylene and biomass residue for oilProduction. *Energy Conversion and Management* 120 422–429
- Zhang, X., Wang, T., Ma, L., Zhang, Q., Jiang, T. (2013). Hydrotreatment of bio-oil over Ni-based catalyst. *Bioresource Technology*. 127 306-311.
- Zhang, H. L., Lei Z., Xiaolu Z. (2016). Thermal behavior and kinetic study for catalytic co-pyrolysis of biomass with Plastics.

A COMPARATIVE ANALYSIS OF GRILLAGE METHOD AND BEAM LINE ANALYSIS OF A REINFORCED CONCRETE WAFFLE BRIDGE DECK

Adamu, H. N.; Abbas B.A.; Abubakar, M.; Yusuf, A.; Kolo, D.N. & Shehu, M.

Department Of Civil Engineering, Federal University of Technology, Minna

Corresponding email: h.adamu@futminna.edu.ng

Abstract

The analysis of a reinforced concrete waffle bridge deck using Chanchaga Bridge as a case study was carried out with the aid of computer programme written in MATLAB. The bridge deck which is a beam bridge was idealized to be a waffle slab. A mathematical model of the bridge was developed using the method of grillages because very complex shapes of problem domain with prescribed conditions can be handled easily using the method. The bridge deck was modelled as interconnection of grid elements. The analysis was carried out using direct stiffness matrix method. The nodal displacements and the resulting static internal forces; shear forces, bending moments and twisting moments of each grid element were determined using the matrix. The results obtained using the method of grillages were then compared with beam line analysis and the former method gave a 10% decrease in forces which will result in the reduction of overall design and materials by 10%.

Keywords: Beam line analysis Computer-aided, Grillage analysis, MATLAB, waffle bridge deck.

INTRODUCTION

Waffle slabs are structural elements with a combination of top slab and a system of spaced longitudinal and transverse beams (Nithyambigai *et al.*, 2021). They are efficient in resisting lateral loads than flat slabs, and are suitable for large spans. They can withstand heavier load and cover large span as they exhibit higher stiffness and smaller deflections. The waffle slab system is an evolution of the solid slab that results from the elimination of concrete below the neutral axis that allows an economic increase in the total thickness of the slab with the inclusion of voids in a rhythmic arrangement. Waffle slabs are more advantageous as compared to other slabs such as flat slabs and RCC slabs, in terms of loading, large spans and aesthetic appearance (Khot *et al.*, 2016).

In recent years, there has been a sudden increase in the use of waffle slabs. That, however, makes it necessary to examine new ways in which it can be used in construction. Principally, static analysis of waffle slabs determines the amount and distribution of

shear forces, bending moment and torsional moments acting on the structure (Chowdhury & Singh, 2012).

Over the years, researchers have analyzed waffle slabs substantially based on conventional methods; both analytical and numerical methods available in literature such as plate analogy by Timoshenko (1987), Rankine Grashoff theory (Hasan *et al.*, 2021), Finite Element Analysis and grillage analogy (Mallick and Bhushan 1983). However, it was clearly stated by Mallick and Bhushan, (1983) that when using grillage analysis, it should be substantiated by a detailed computer analysis. The direct stiffness gives more accurate results as concluded by Halkude and Mahamuni, (2014). However, research on the use of grillage analysis for waffle bridge decks has been rarely carried out.

Up until now, waffle slabs are found more in number in building construction than in bridge construction. An argument against this is that loads are distributed in two orthogonal directions in waffle slabs as against the one-way loading system in bridges. As a result, engineers deem it

incompatible with bridges as loads are transferred in one way only in bridges. However, technical reasoning has shown that when loads are transferred to bridges in one way only, large twisting moments are produced, the orthogonal rib system in a waffle slab provides an efficient means of resisting these twisting moments by incorporating large bending moments in the two orthogonal directions (Kennedy and Bahkt, 1983).

The use of voided slab for a bridge deck was analysed by Rampariya and Choudhury, 2020 and concluded that they are more economical for greater spans of more than 15m. Also stated by Vaignan and Prashad, (2014), rectangular shaped cellular decks withstand more load than voided slabs when they analysed voided and cellular deck slab using MIDAS CIVIL.

For this purpose, serious attention needs to be given to the analysis of waffle slabs as bridge decks. Several methods have been used in the analysis of bridges. Each of the three dimensional structure is simplified based on assumptions on geometry, materials and relationship between components. The accuracy of analysis is dependent on the method used.

Bridge decks have been analyzed using several methods such as finite element (Halkude and Mahamuni, 2014), finite strip grillage analogy (Mallick and Bhushan, 1983) and orthotropic plate (Khot *et al.*, 2016).

Therefore, this research aims to analyse a solid slab bridge deck which is idealized as a waffle slab grillage analogy and then compare with conventional static beam line analysis of a bridge. The analysis of the waffle bridge deck using method of grillages was performed using direct stiffness method. MATLAB was used for writing the code as well as the analysis while excel program was used for beam line analysis.

Grillage method of analysis involves representing the bridge deck as a 2 by 2 system of interconnected beams intersecting

each other. It is a numerical approach in analyzing bridge decks and also easy to use and comprehend (Shreedar and Kharde, 2013).

As structures become complex and large, several methods of simplifying their analysis have been developed among which use of computer aid. Computer aided analysis is a way of solving continuous system problems by dividing them into discrete elements thus simplifying analysis taking into consideration compatibility and boundary conditions. In the grillage analysis, the structure is represented by a plane grillage of discrete but interconnected beams. Almost any arrangement in plan is possible, so skew, curved, tapering or irregular decks can be analyzed. But the usual layout is sets of parallel beams in two directions by assuming the plane of the grillage to be horizontal whereas beam line analysis uses the moment distribution method in the analysis of loads; both static and moving to obtain the internal forces and settlements at the support.

METHODOLOGY

In a simple form of grillage analysis, each beam is assigned a torsional stiffness and flexural stiffness in the vertical plane. Vertical loads are applied only at the intersections of the beams. The matrix stiffness method of analysis is used by the existing software, to find the rotations about two horizontal axes and the vertical displacement at these nodes, and hence the bending and torsional moments and vertical shear forces in the beams at each intersection. Warping stresses and shear lag are neglected in the analysis.

Problem Formulation

A 125 m span simply supported right bridge deck of width 7.3m simply supported ends on two opposite sides and fixed ends on the other two sides. The thickness of the slab is assumed as 0.075m and the overall depth of the grid beam is assumed as 0.375m. The width of the grid beam is assumed as 0.15m. The grade of concrete M30 and steel of grade

Fe 460 are assumed. The cracked moment of inertia is used to determine the rigidities of the deck. The dead loading considered is the self-weight and wearing course. The live load on the floor is HA loading as given in BS 5400-part 2 (1987) Clause 6.2.1. Load combination 1 of the BS 5400 part 2 is used. In this, eleven transverse members and five longitudinal members have been modeled with centre to centre spacing of ribs at 1.2m in both ways having same flexural and torsional rigidities.

Table I: Properties of Bridge Deck

Dimension	Actual Measurement
Width	11.8m
Length	123m
No of spans	10
Width of footpath	2m
Width of Notional Lanes	3.8m
Thickness of Slab Topping	0.075m
Depth of Bridge Deck	0.37m
Width of Grid Beam	0.15mm
Depth of Asphalt Overlay	0.05m
Grade of Concrete	C30
Grade of Steel	E460

Location of Grid Lines

- Grid lines should be adopted along line of strength.
- The longitudinal gridlines run in parallel direction to the edge of the deck that is free. For longitudinal direction, it may be along the longitudinal webs, centre line of girders or edge beams etc.
- Where isolated bearings are present, the grid line may be along the line joining center of bearing.

- For transverse direction, it should be considered as one of each end connecting the center of bearing and along the center line of transverse beam (Surana and Agrawal, 1998).

Number and Spacing of Grid Lines.

- Where possible, odd numbers of gridlines should be chosen in both longitudinal and transverse directions.
- The ratio of spacing of transverse grid line to those of longitudinal grids may be taken as 1 to 2.
- As regards to the depth of slab, the minimum distance between longitudinal grid lines is limited to two to three times of the slab depth and the maximum separation of longitudinal members should not be more than one fourth of the effective span (Pandey and Maru, 2015).

A typical output gives the external reactions at each support. The bending and torsional moments will, in general, show a discontinuity at each joint. For an orthogonal grillage, each change in bending moment is equal to the change in torsional moment at that joint in the member at right angles to the one considered. Similarly, the change in torsional moment equals the change in bending moment in the perpendicular member.

Approximately one half of the local load can be distributed over the eight nodes of the vicinity to get correct results, even near the loaded point. An appropriate idealization for a continuous structure is carefully selected. Each T-section of the longitudinal and transverse sides of a waffle slab is represented by a grillage beam. The transverse grillage members should extend to the edge of the real slab and their ends should be attached to longitudinal grillage beams, even if the real slab has no significant edge stiffening.

2.3 Grillage Modeling

The slab is supported on orthogonal beam arrangement for the reason that each grillage member will represent a rib, and therefore the internal forces in the members can be taken directly for calculating load distribution. The spacing of ribs is the centre-to-centre spacing of 1.525 m. As a general rule, the spacing in either directions should be very similar. The explanations for this involves the application of load and distribution, and to keep almost the same mesh size, and therefore accuracy both ways. A spacing of 1.525 m for transverse grillage is chosen. Fig. 1 shows the modeling of the bridge deck.

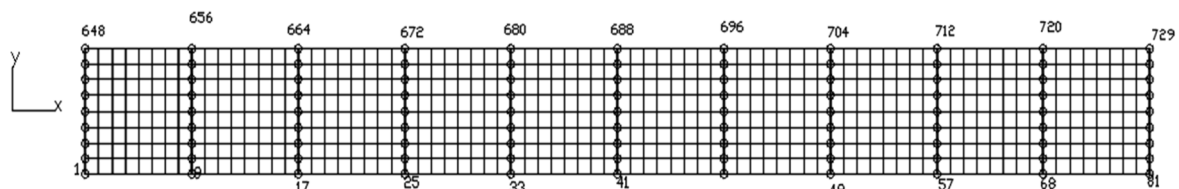


Fig. 1: Grillage Model of the Bridge Deck

The Analysis Model

Figure 1 shows a plan view of the analysis model of the idealized grillage. Full bending and torsion continuity is assumed at the nodes.

When establishing the data for idealization, it is most vital to ensure that the major axis of the elements is correctly oriented. In the case of the grillage shown in Fig. 1 the I_y values mentioned in Table 1 are the values of major axes.

They correspond to the local y axes of the members, which are in the global xy plane for the main beams and the transverse grillage members. These edge structures induce additional loading. These elements have an effect on the load distributions and exterior girder behaviour and were accounted for in modelling the bridge deck. Although the transverse grillages in this model were fairly basic, for some bridges and certain loading cases the transverse grillage members will become very important and will need modelling adjustments. For instance, when diaphragms

are present in a bridge, the transverse grillage members model these elements.

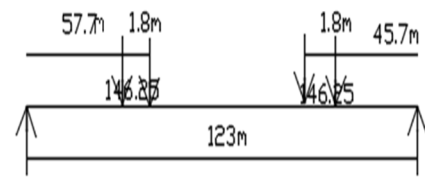


Fig. 2: Statical Diagram for Maximum Moment and Shear.

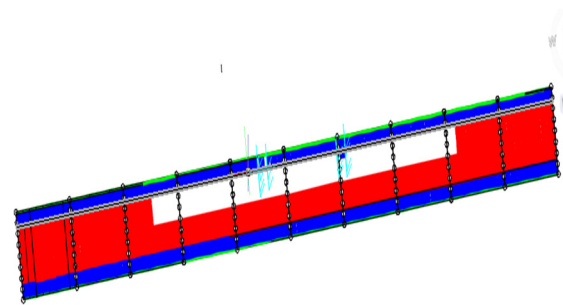
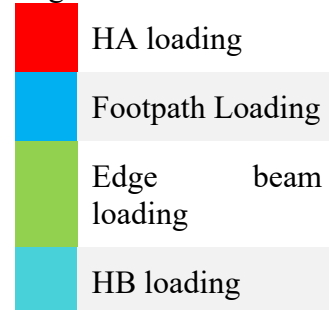


Fig. 3: Schematic Representation of Load Distribution

Legend



Dead load only

Analysis

1. Defining the nodal coordinates.
2. Numbering of numbers.

3. establishing the connectivity of elements
4. The length and angle of orientation
5. Material properties are modulus of elasticity and rigidities are defined.
6. For each element, the stiffness matrix computed the software.
7. The stiffness matrix for a grid member is a 6 by 6 matrix.
8. First the degrees of freedom at each node are identified and numbered; two perpendicular rotational displacement and one translational displacements $\Delta_1, \theta_2, \theta_3$.
9. The structures stiffness matrix for two nodes (one element) becomes;
The global stiffness matrix is obtained by combining all the element stiffness matrices.
10. Assignments of boundary conditions.

Formulation of Stiffness Matrix

Governing differential equation

$$EI \frac{d^4 v}{dx^4} = q \quad (1)$$

$$EI \frac{d^2 v}{dx^2} = M \quad (2)$$

$$EI \frac{d^3 v}{dx^3} = F \quad (3)$$

$$EI \frac{d^4 v}{dx^4} = 0 \quad (4)$$

Integrating

$$Elv = a_0 + a_1 x + a_2 x^2 + a_3 x^3 \quad (5)$$

The rotational degree of freedom

$$\frac{dv}{dx} = 0; \quad (6)$$

Applying boundary conditions

Solving for coefficients,

$$x = 0: \frac{dv}{dx} = 0; v = 1; \Rightarrow a_0 = 0 \text{ and } a_1 = 1 \quad (7)$$

$$x = L: \frac{dv}{dx} = 0; v = 0 \quad (8)$$

$$\frac{dv}{dx} = 0; \Rightarrow 2a_2 + 3a_3 l \quad (9)$$

$$v = 1 + a_2 l + a_3 l^3$$

$$\Rightarrow a_2 = \frac{3}{l^2} \text{ and } a_3 = \frac{2}{l^3} \quad (11)$$

Equation 5 becomes

$$v = 1 - \frac{3x^2}{l^2} + \frac{2x^3}{l^3} \quad (12)$$

$$-EI \frac{d^3 v}{dx^3} = F \Rightarrow -EI \left(\frac{12}{l^3} \right) = \frac{12}{l^3} EI \quad (13)$$

$$EI \frac{d^2 v}{dx^2} = M \Rightarrow M_{x=0} = - \left(\frac{6}{l^2} \right) \quad (14)$$

$$k_{11} = -F_{x=0} = EI \left(\frac{12}{l^3} \right) \quad (15)$$

$$k_{21} = -M_{x=0} = EI \left(\frac{6}{l^2} \right) \quad (16)$$

By imposing a twisting moment at node 1, gives a rotation θ and applying boundary conditions the constant of integration becomes;

$$T = \frac{GJ}{L} \theta \quad (17)$$

Therefore,

$$k_{33} = \frac{GJ}{L} \quad (18)$$

The remaining forces acting on the grid beam can be determined by applying unit displacement corresponding to translation and rotation at the two nodes of the beam.

$$\begin{bmatrix} k_{11} & k_{12} & k_{13} & k_{14} & k_{15} & k_{16} \\ k_{21} & k_{22} & k_{23} & k_{24} & k_{25} & k_{26} \\ k_{31} & k_{32} & k_{33} & k_{34} & k_{35} & k_{36} \\ k_{41} & k_{42} & k_{43} & k_{44} & k_{45} & k_{46} \\ k_{51} & k_{52} & k_{53} & k_{54} & k_{55} & k_{56} \\ k_{61} & k_{62} & k_{63} & k_{64} & k_{65} & k_{66} \end{bmatrix} = \begin{bmatrix} \frac{12EI}{L^3} & \frac{6EI}{L^2} & 0 & \frac{-12EI}{L^3} & \frac{6EI}{L^2} & 0 \\ \frac{6EI}{L^2} & \frac{4EI}{L} & 0 & \frac{-6EI}{L^2} & \frac{2EI}{L} & 0 \\ 0 & 0 & \frac{GJ}{L} & 0 & 0 & \frac{-GJ}{L} \\ \frac{-12EI}{L^3} & \frac{-6EI}{L^2} & 0 & \frac{12EI}{L^3} & \frac{-6EI}{L^2} & 0 \\ \frac{6EI}{L^2} & \frac{2EI}{L} & 0 & \frac{-6EI}{L^2} & \frac{4EI}{L} & 0 \\ 0 & 0 & \frac{-GJ}{L} & 0 & 0 & \frac{GJ}{L} \end{bmatrix}$$

Code formulation procedure in MATLAB (2015a) software

i. Formation of global stiffness matrix:

function stiffness=formStiffnessGrid(GDof,...


```

numberElements,elementNodes,elementNodes1,elementNodes2,elementNodes3,elementNodes4,elementNodes5,xx,yy,E,I,G,J)

% function to form global stiffness for grid element
% script file
E = 3.01e7;
I = 2.5e-5;
G = 1.31e7;
J = 5e-5;
%for edge beam
E1 = 3.01e7;
I1 = 0.0054;
G1 = 1.31e7;
J1 = 0.0108;
%for footpath
E2 = 3.01e7;
I2 = 0.009 ;
G2 = 1.31e7;
J2 = 0.018;
stiffness=zeros(GDof);
ii. Determination of forces in elements
% forces in elements
EF=zeros(6,numberElements);
iii. Determination of displacements
% displacements
disp('Displacements')
%displacements=displacements1;
jj=1:GDof; format
[jj' displacements]
% function to find solution in terms of global displacements
activeDof=setdiff([1:GDof]',[prescribedDof])
;
U=stiffness(activeDof,activeDof)\force(activeDof);
displacements=zeros(GDof,1);
displacements(activeDof)=U;
end
function outputDisplacementsReactions...
(displacements,stiffness,GDof,prescribedDof)
force=zeros(GDof,1);
force(1)=-10;
stiffness=formStiffnessGrid(GDof,numberElements,...
elementNodes,xx,yy,E,I,G,J);

```

```

prescribedDof=[]';
displacements=solution(GDof,prescribedDof,
stiffness,force);
outputDisplacementsReactions(displacements,
stiffness,...
GDof,prescribedDof)
disp('forces in elements ')
EF=forcesInElementGrid(numberElements,elementNodes,...
xx,yy,E,I,G,J,displacements)
function
displacements=solution(GDof,prescribedDof,
stiffness,...
iv. Determination of reactions
F=stiffness*displacements;
reactions=F(prescribedDof);
disp('reactions')
[prescribedDof reactions]
End

```

RESULTS AND DISCUSSIONS

Analysis of a waffle bridge deck was carried by using grillage analogy method by simulating full HA and HB loading. The displacements and bending moments are shown. The bending moments are estimated from the summation forces in members of adjacent to each other. The results obtained in the grillage analogy method were then compared with beam line analysis method. The results are shown in Figs. 4-6.

Comparison of Bending Moments

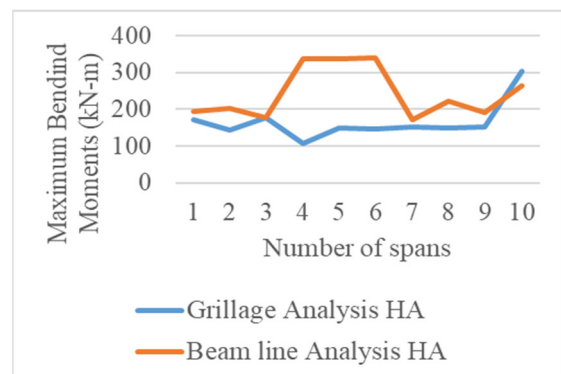


Fig. 4a: Bending Moments for Maximum Span Moments for HA loading.

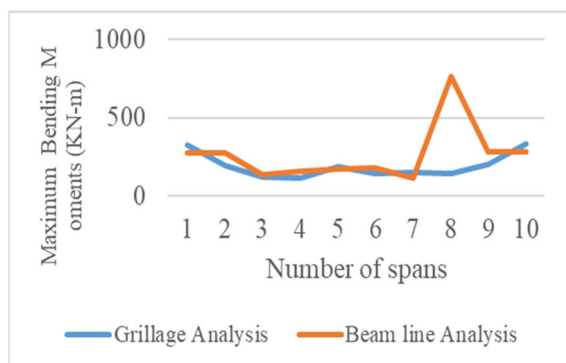


Fig. 4b: Bending Moments comparison for Maximum Span Moments for HB loading

From the graphical representations, the span moments obtained for span in the continuous beam analysed using the method of grillage gave lower bending moment values. The highest span moment occurred as a result of wheel loading on the span which was evenly distributed in grillage analysis to the nodes.

Comparison of Maximum Span Shear Forces

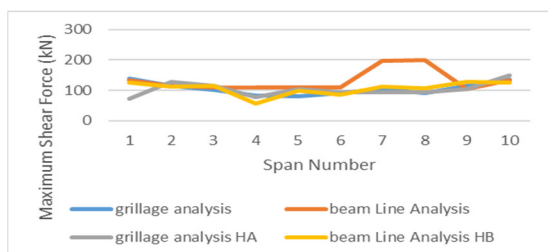


Fig. 5: Maximum Shear Force Comparison for HA and HB loading

The bending moment and shear forces obtained from grillage analysis in the spans showed very similar results to that of the beam line analysis models. Due to the close correlation of the results and the fact that two different methods will never give exactly the same results and that the values obtained from beam line analysis were slightly higher than that of grillage method, it is presumed that the grillage techniques and assumptions used in the moment modelling are appropriate.

Comparison of Deflections

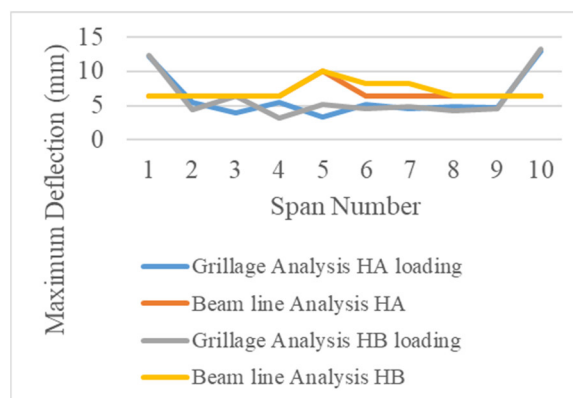


Fig. 6: Deflection Comparison for HA and HB Loading

The deflection results were investigated for critical points for two different sections with different loading conditions. The comparison was made to ensure that the variability in their results as compared to the manual method is not excessive. It was found that the deflection results from the grillage analysis are within 10% of the manual method and the highest deflection occurred at the point of application of wheel load. This shows that the grillage method gives lower deflection values as compared to the other method.

CONCLUSION

The ten span reinforced concrete waffle slab bridge deck (a case study of the Chanchaga Bridge, Minna, Niger State, Nigeria) was modeled using grillage analogy approach. The HA and HB loading of the BS 5400-2 (2000) was applied to the deck. Nodal displacements, reactions and member forces were obtained from the analysis. The values obtained from the grillage analysis were compared with manual calculations (beam line analysis). The following conclusions were arrived at:

The beam line method of analysis used for comparison yielded higher values of bending moments and shear forces, because the models results in a higher stiffness values compared to the manual method.

The maximum moment occurred as a result of HB loading and this could be used for design purposes.

This research work has developed a method (code) for the structural analysis of a waffle bridge deck based on grillage analogy using the stiffness matrix approach and a written code in MATLAB thereby rendering the approach computer amenable

REFERENCES

- British Standard Institution (1987). BS 5400 Part 2. *Code of practice for the design of steel, concrete and composite bridges*. British Standard Institution
- Chowdhury, I. & Singh, J.P. (2012). Analysis and Design of Waffle Slab with different Boundary Conditions. *The Indian concrete journal*, Vol. 2, No.1, 1-10.
- Halkude S. A. & Mahamuni S.V. (2014). Comparison of various methods of analysis of grid floor frame. *International Journal of Engineering Science Invention*, 3(2), Vol. 2, No.1, 01-07.
- Hasan, K., Fayadh, O. & Hasan, Q.F. (2021). Design and analysis of flat and grid slab system with conventional slab comparative approach. *Design Engineering*, Vol. 1, No. 7, 1628-169.
- Kennedy J.B & Bakht B. (1983). *Feasibility of waffle slabs for bridges*. Edmonton, Alberta: Paper presented at The Annual Conference of the Canadian Society for Civil Engineering.
- Khot, S.R., Mahajan, H.V., Purval, D.S., Jadhav, V.V., Siddhartha V.T. & Bharekar, K.T. (2016). Comparative Study of Waffle Slabs with Flat Slabs and Conventional RCC Slabs. *International Journal of Engineering Research & Technology (IJERT)*, Vol. 5(04) Vol 2, No.1, 1-10.
- Mallick, S. K. & Bhushan. N. (1983). Methods of Analysis for Reinforced Concrete Grid Roofs and Floors. *Indian Concrete Journal*, 57(3), Vol. 57, No.3, 76-81.
- MATLAB. (2015). (R2015a). Natick, Massachusetts: The MathWorks Inc.
- Nithyambigi, G, Rameshwaran, P.M & Stella M.F. (2021). Behaviour of waffle slab. Article in press. *Engineering Materials Today: Proceeding*. doi: 10.1016/j.matpr.2021.02.016.
- Pandey, K. K & Maru, S. (2015) Modelling of Skew Bridge Deck Slab by Grillage. *International Journal of Engineering Research and General Science*, Vol. 3, No.4, 1-5.
- Rampariya, R.P & Choudhary, R.K. (2020). Use of voided slab for bridge deck. *AE GA EUM journal*. Vol. 8, No.7, 1-10.
- Shreedar, R. & Kharde, R. (2013). Comparative analysis of grillage method and finite element method of RCC bridge deck. *International Journal of Science and Engineering*, Vol. 4, No.2, 1-7.
- Surana, C.S. & Agrawal, R. (1998) *Grillage Analogy in Bridge Deck Analysis*. India: Narosa Publishing House 16-17.
- Timoshenko, S. (1987). *Theory of plates and Shells*. McGraw Hill, New York.
- Vaignan, B. & Prasad, S.R.K. (2014). Analysis of voided slab deck using MIDAS CIVIL. *International journal of engineering research and technology*, Vol.3, No 9, 1277-1288.

EFFECT OF BINDERS ON THE PROPERTIES OF CONCRETE – A REVIEW

***Oritola, S. F., Olojede, R. O, Kolo, J. L, Ukog, A. S. and Ekpenyong, D. E**
Civil Engineering Department, Federal University of Technology, Minna, Nigeria
E-mail: sfaoritola@futminna.edu.ng

Abstract

There is a need for alternative materials which will partially or fully replace cement used in concretes and mortars without affecting the quality and other desired properties. The blending of cement with supplementary cementitious or non-conventional material is vital in low-cost construction; these materials are referred to as binders or pozzolanas. The binders discussed in this study are; Ordinary Portland cement, Fly ash, ground granulated blast furnace slag, silica fume, metakaoline and Cassava peel ash. The properties considered in the study were grouped into fresh properties, mechanical properties and durability properties. Findings from this study reveals that cassava peel ash, metakaoline, ground granulated blast furnace slag, fly ash and silica fume enhance the workability of fresh concrete when added as blended material. These binders also enhance the compressive, tensile and flexural strength of concrete when administered optimally. Ordinary Portland cement has poor acidic attack resistance and weak resistance to extreme temperature thereby putting its durability in doubt. Cassava peel ash, metakaoline, ground granulated blast furnace slag, and Fly ash tend to exhibit reasonable durability properties even at adverse conditions such as acidic attack. This study reveals that these binders which are waste products can be used to enhance durability and mechanical properties of concrete. Rather than being discarded, these materials can be used in concrete production thereby promoting the sustainability of the environment.

Keywords: Binders, concrete, durability, mechanical properties, waste material.

INTRODUCTION

Concrete is one of the most commonly used construction materials in civil engineering practice and construction works around the world, there's great dependency on concrete (Olafusi *et al.*, 2015). It is the world's most widely used construction materials because of its durability properties, it is a multipurpose construction material (Serdar *et al.*, 2019). Concrete is readily available, relatively cheap, flexible to handle and can be formed into any desired shape and any desired form (Anejo & Damen, 2014). In a broad sense, concrete is made from the combinations of cementitious material (cement, lime, pozolanas), aggregates (fine and/or coarse) and water. However it can also accommodates some additives and/or admixtures added to the basic constituents to vary the properties of the concrete when it is green or hardened (Anejo & Damen, 2014) .

Concrete exhibits quite acceptable properties that are required of a construction material and due to its flexibility, it can be mixed with other constituent elements which makes it more adaptable (Mamoon & Mondal, 2019). Properties of concrete can be grouped into fresh or green properties which are properties exhibited by concrete from its mixing state to the time it start solidifying, this behavior is generally termed as workability which is used to describe its cohesiveness and consistency (Suryawanshi *et al.*, 2015).

The materials used in concreting tend to alter the properties of concrete, be it coarse, fine or the binders. That is to say, properties of the concrete are dependent on the type of constituent used in the concrete mix (Wallevik, 2009). Binders play one of the key roles in a concrete mix, it's the material that holds other constituents together. A binder is any material either liquid or solid

that holds or draws other materials together to form a cohesive whole mechanically; chemically, by adhesion or cohesion. In a clearer sense, binders are liquid matter that harden by a chemical or physical process and bind fibres, filler powder and other particles added into it (Strijov, 2020).

The new trend that have emerged in construction materials research area is to find out the material with a good concession between the usage performances on one hand, and the durability and sustainability on the other hand (Aubert *et al.*, 2019). It is against this backdrop that this review was embarked upon, the study covers mainly, literatures written within the last ten years, the study also considered the most commonly used binders based on findings from previous researches. These commonly used binders are fly ash, ground granulated blast furnace slag, metakaoline, cassava peel ash and silica fume. They are all regarded as industrial waste product.

Chemical Composition of Binders

The chemical composition of materials is commonly determined using the X-ray fluorescence (XRF) method. This approach involves the emission of characteristic "secondary" (or fluorescent) X-rays from a material that has been excited by bombarding with high-energy X-rays or gamma rays. The elemental chemical analysis results which gives the oxides composition of ordinary Portland cement, ground granulated blast furnace slag, fly ash, silica fume and rice husk ash as reported in previous work is depicted in Table 1.

Table 1: Chemical composition of binders

Oxides	OPC	GGBS	Fly ash	Silica fume	RHA
CaO	67.2	34.0	3.5	0.1	0.8
SiO ₂	22.3	35.5	53.7	96.0	93.4
Al ₂ O ₃	4.4	15.4	28.1	0.1	0.2
MgO	1.0	9.4	0.8	0.2	0.4
TiO ₂	0.2	1.2	-	-	-
Fe ₂ O ₃	3.4	1.0	11.6	0.6	0.2
MnO	0.1	0.9	-	0.2	-
K ₂ O	0.6	0.9	-	0.4	2.0
Na ₂ O	0.2	0.2	0.8	0.1	0.1
SO ₃	0.6	2.5	0.4	-	0.2

Effect of Binders on the Properties of Concrete

Workability

From the results of the compacting factor test conducted on samples of cement-Cassava peel ash blended concrete at various percentage replacements with 0.6 water binder ratio. It was observed that the slump and compacting factor values reduces as the CPA was increased. This shows that more water is needed to achieve better workable mix. It is observed that the percentage replacement level of cement with CPA did not have any appreciable influence on the densities of the test specimens of the blended concrete. This may be attributed to the lower specific gravity of the CPA which was much lower than that of cement (Olatokunbo *et al.*, 2018).

The standard values of slump required for the different working conditions shows that the concrete remains stable in the range of very low to low workability (Oladipo *et al.*, 2013). This means they can be applied on road vibrated by mechanical power operated machine and hand operated machine in accordance with the provision of the -BS 4550 method of testing cement British Standard Institute London (Neville and Brooks, 1987). In other words, the concrete embedded with CPA up to 50 percent constituent is still stable and could be

acceptable in most concrete works in the building industry.

Quareshi *et al.* (2014), carried out research on the effect of fineness of ordinary Portland cement (OPC) (ASTM type 1) on the workability of high strength concrete. Six OPC samples of fineness ranging from 1525 to 3741 cm^2/g each weighing 15kg were prepared. Slump and compacting factor tests were carried out to determine the workability. The slump test according to Fig. 1 shows that the slump increases with increase in fineness up to 2500 cm^2/g and remains constant up to 3400 cm^2/g and afterward, it then increases with increasing fineness. The compacting factor test also shows an increase in workability with increase fineness according to Fig. 2.

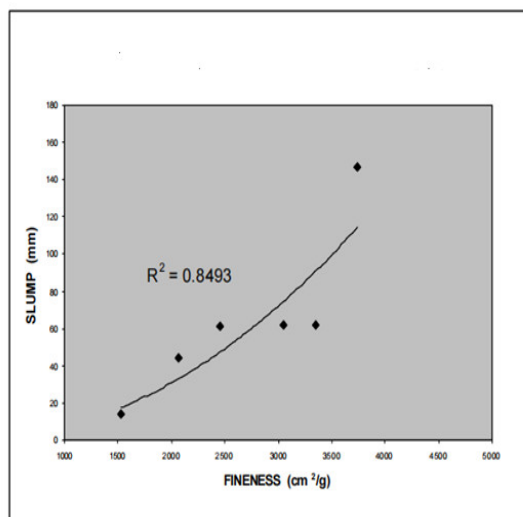


Fig. 1: Fineness of cement on slump

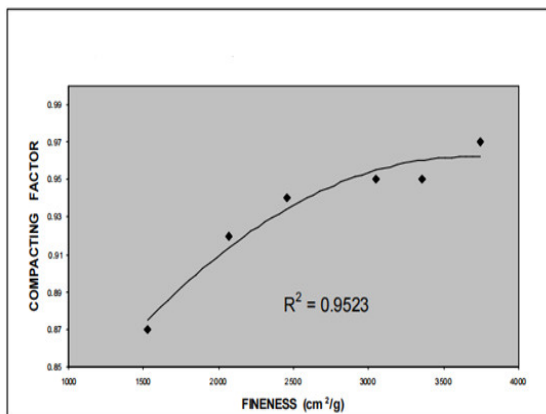


Fig. 2: Fineness of cement on Compacting factor

Adam (2021) carried out a research on the effect of blending Ordinary Portland Cement (OPC) type class 42.5N with fly ash (ASTM Class F) on the workability of self-consolidating concrete (SCC). Three different total binder content levels of 400, 460, and 520 kg/m^3 were adopted. For each total binder content level, one Powder-Type SCC mix (SCC-P), one Admixture-Type SCC mix (SCC-A), and one Combined-Type SCC mix (SCC-C) were prepared. In addition to the three SCC mixes, one NVC mix was made for the sake of comparison. Two different chemical admixture types were utilized in the study. Naphthalene Sulphonate superplasticizer (SP) was incorporated to improve workability and flowability, while modified polycarboxylate viscosity modifying admixture (VMA) was used to control bleeding and limit segregation of fresh concrete. It was observed that all investigated SCC mixes achieved the required flowability, viscosity, passing ability, and segregation resistance, additionally; it was observed that there were no signs of neither bleeding nor segregation during slump flow testing of all SCC mixes. Table 2 shows the results of the slump flow test, L-Box test and sieve segregation test.

Table 2: Properties of Fresh Concrete

	Slump Flow		L-Box	Sieve Segregation
	D, cm	T ₅₀ , s	Passing ability	Segregation ratio, %
NVC-1	7.0*	---	---	---
SCC-A-1	65.0	1.20	0.80	15
SCC-C-1	64.0	1.25	0.79	12
SCC-P-1	67.0	1.15	0.80	16
NVC-2	6.0*	---	---	---
SCC-A-2	65.0	1.10	0.82	17
SCC-C-2	66.5	1.16	0.82	18
SCC-P-2	67.0	1.30	0.79	18
NVC-3	7.5*	---	---	---
SCC-A-3	64.0	1.35	0.79	17
SCC-C-3	65.0	1.15	0.80	18
SCC-P-3	64.0	1.10	0.81	15

Compressive Strength

From the outcome of several studies carried out, compressive strength seems to be the

most popular evaluating parameter for concretes. This is due to the fact that it is the quality that access the load carrying capacity of a concrete mix. Despite the fact that a lot of binders are being considered overtime, to produce cheaper concrete, the compressive strength of concrete cannot be compromised.

Table 3 presents the outcome of two different researches with similar mix design. Amudhavalli & Mathew (2012) investigated the effect of silica fume on strength and durability parameters of concrete by partial replacement of cement with silica fume at 0, 5, 10, 15 and 20% levels.

Table 3: Compressive Strength of Concrete using Silica fume and Fly ash as binder.

Mix	Binder	Compressive Strength (N/mm ²)	
		28 Days Strength of Silica Fume	28 Days Strength of Fly Ash
M1	0	38.30	39.53
M2	5	41.29	40.95
M3	10	46.76	42.50
M4	15	47.3	39.36
M5	20	44.27	38.15

(Amudhavalli & Mathew, 2012; Kiran & Ratnam, 2014)

The compressive strength test was carried out conforming to IS 516-1959 to obtain compressive strength of concrete at the age of 28 days. The result indicated significant improvement in the compressive strength of concrete because of the high pozzolanic nature of the silica fume and its void filling ability. Similarly Kiran & Ratnam, (2014) performed similar experiment although with Fly ash and the result shows increase in strength gain too with the increase in Fly ash content, although with different optimum replacement levels, Silica fume had 15% optimum replacement while fly ash was 10% optimum replacement.

Slag mixes is also found to have better strength performance than the plain CEM I

42.5R mix at all ages, contrary to other studies at 20°C (Ogirigbo and Black, 2015) where early age strength development was found to be retarded with composite cements. The high temperatures here speed up the strength development. The reason is because hydration of slag in the presence of PC depends on the breakdown and dissolution of the glass slag structure by hydroxyl ions released during the hydration of PC (Ogirigbo & Inerhunwa, 2017), and this process is known to be accelerated at high temperatures (Escalante *et al.*, 2001).

Furthermore; Suryawanshi *et al.* (2015) investigates the effects of Metakaolin & Super plasticizer on strength properties of M-35 grade concrete. The experimental program was designed to find the compressive strength of concrete by partially replacing the cement in concrete production. The replacement levels of cement by metakaolin are selected as 4%, 8%, 12%, 16% and 20% for constant water-cementitious material ratio of 0.43. For all mixes compressive strength is determined at 3, 7, 28 days for 150 X 150 X 150 mm size cubes. The experimental study shows that 12% replacement of cement by metakaolin gives higher strength.

Similarly, Sharbaf *et al.* (2017) investigated on the effects of water to binder (w/b) ratio and binder content on mechanical and durability properties of High Performance Concrete (HPC). Twelve combinations with w/b ratios of 0.3, 0.34, 0.38, and 0.42 and binder contents of 330, 440, and 550 kg/m³ were made. The result of compressive strength tests after 7 and 28 days of curing indicated an increase with increase in binder content. Patel *et al.* (2015) researched on effect of binder volume on fresh and hardened properties of Self Compacting Concrete (SCC) and the study showed contrary outcome, this time around the compressive strength decreased as binder quantity increased. This may be due to decreased in aggregate volume in mix proportion. On increasing the binder, compressive strength was increased.

Increase in compressive strength for higher binder volume may be due to very strong bond between aggregate and cement. For higher volume of binder quantity and lower water binder ratio, the strength of concrete cube was increased.

In the same manner Olatokunbo *et al.* (2018) investigated the effect of partial replacement of cassava peel ash with ordinary Portland cement at 5, 10, 15, 20 and 25%. The cassava peel ash was obtained by calcinations of cassava peel to 7000 °C temperature. Cube samples of size 150 x 150 x150 were prepared for concrete grade 30 and cured in water for 7, 14, 28, 90, 120 and 180 days after which they were subjected to compressive strength, tensile strength, durability, porosity, water absorption, slump, compact factor and shrinkage tests. The results showed that partial replacement of 10 and 15% gave compressive strength comparable to the control with 0% replacement and optimum replacement of 10%. Osuide *et al.* (2021) embarked on similar studies and found that the strength of cement-CPA concrete is similar to those of normal concrete, especially at later age (56 days and above), when not more than 15% CPA is used and from the values of the compressive strength obtained, concrete made with unreplaced cement (control) at 28 days strength was not up to two times the value of the strength of concrete made with CPA replacing cement by 50% at 28 days which makes the strength acceptable, the findings also correlates with Oladipo *et al.* (2013).

Suzuki *et al.* (2020) carried out the compressive strength tests on the concrete incorporated with fly ash possessing various chemical composition, which are high and low calcium and the result shows that compressive strength of concrete with high calcium fly ash indicates a strong correlation with calcium content fly ashes, also in the case of 10% and 20% replacement levels, the compressive strength exceeds that of concrete without fly ash even as early as on the 3rd day. Sabarish (2019), also worked on

partial replacement of cement with fly ash in concrete elements. The cement was replaced by fly ash accordingly in the range of 0% (without fly ash), 10%, 20%, 30% & 40% by weight of cement for M-25 and M-40 mix. These tests were carried out to evaluate the compressive strength after 28 days and split tensile strength after 56 days. The result indicated that compressive strength reduces when cement replaced fly ash. As fly ash percentage increases compressive strength and split strength decreases. Andreola *et al.*, (2019) worked on the partial replacement of cement with fly ash and metakaolin with the purpose of reaching compressive strength closer to a bio- concrete containing only cement. Mixtures with partial substitution of 0, 40, 50, 60 and 70% of cement by mass were produced with a volumetric fraction of bamboo set as 40%. The compressive behavior of the bio-concretes was analyzed at 7, 28, 60 and 90 days. The results revealed that it was possible to reach between 60% and 90% of the reference strength, producing workable bio- concretes using binders with low CO₂-emission.

Awodiji & Onwuka (2016) re-investigated the compressive strength of ordinary Portland cement (OPC) concrete and lime concrete (LC) using five selected mix ratios. Materials used in concrete production were ordinary Portland cement, hydrated lime, granite chippings as coarse aggregates and river sand for fine aggregate. Optimum values of compressive strength recorded for OPC concrete at 7 days and 28 days of curing were 11.55N/mm² and 26.96N/mm² respectively. The results obtained showed that the compressive strengths at 90 days curing for LC are approximately half of the compressive strength values of OPC concrete at 28 days. Compressive strength values at 90 days for the LC were close to that of the 7 days strength values for OPC concrete. The compressive strength values of LC increased with increasing curing age which informs non-deterioration of concrete. Compressive strengths at 7 days curing of LC showed no results of strength gain.

Split Tensile Strength

Adam (2021) researched on the effect of Binder Content on Properties of Different Self- Consolidating Concrete Types, the study used three different binder content levels of 400, 460, and 520 kg/m³. From the findings it was observed that with increase in the binder content, the concrete also exhibited higher splitting tensile strength. However in a contrasting outcome Olatokunbo *et al.* (2018) on the effect of cassava peel ash on the tensile splitting strength, it was observed that in each case generally the tensile splitting strength decreases as the percentage of the CPA increased. The result in Table 4 shows the increase in split tensile strength for the mix M3 to be 4.10N/ N/mm² and 4.95 N/mm² at 7 and 28 days respectively. The maximum increase in split tensile strength was observed at 10% replacement of silica fume. The optimum silica fume replacement percentage for tensile strengths was found to be a function of w/c ratio of the mix. The optimum 28-day split tensile strength was obtained in the range of 5–10% silica fume replacement level.

Table 4: Split Tensile strength of concrete with Silica fume.

Mix	% Silica Fume	Split Tensile Strength (N/mm ²)	
		7 days	28days
M1	0	3.11	4.67
M2	5	3.65	4.80
M3	10	4.1.	4.95
M4	15	3.83	4.63
M5	20	3.65	3.98

(Amudhavalli & Mathew, 2012)

Durability

Acid Attack Resistance

The reaction of acids with concrete is as a result of conversion of calcium compounds into calcium salts of the attacking acid. The action of acids on cement paste is majorly on

the components of the hardened cement paste. It is assumed that this action leads to a conversion of all the calcium compounds, un-reacted residue of C₃S and C₂S in cement grains, calcium hydroxide, calcium silicate hydrate, and calcium aluminate hydrate to the calcium salt of the attacking acid (Bakharev *et al.*, 2003). This reaction makes concrete structure to deteriorate. The percentage of loss in compressive strength was 11.91%, 8.18%, respectively according to Bakhrev *et al.*, (2003). Thus, replacement of silica fume was found to have increased the durability against acid attack. This is due to the silica present in silica fume which combines with calcium hydroxide and reduces the amount susceptible to acid attack.

OPC concrete is more vulnerable than slag concrete to acid attack due to the differences in chemical and phase composition. The cement paste in OPC concrete is rich in calcium due to presence of residues of C₂S and C₃S, portlandite [Ca(OH)₂], and C-S-H with average Ca/Si ratio of 1.7. However, the calcium-containing compounds in the cement paste react with the acetic acid, producing gel- like white cover, that contains calcium acetate, which is the product of chemical reaction of OPC paste with the acetic acid solution. Since calcium acetate is soluble, it leaves the cement paste. Decalcified C-S-H and silica gel, another reaction product, have no structural properties. This results in OPC concrete surface becoming softer and could be removed, thus, exposing the interior concrete layers to deterioration (Bakharev *et al.*, 2003).

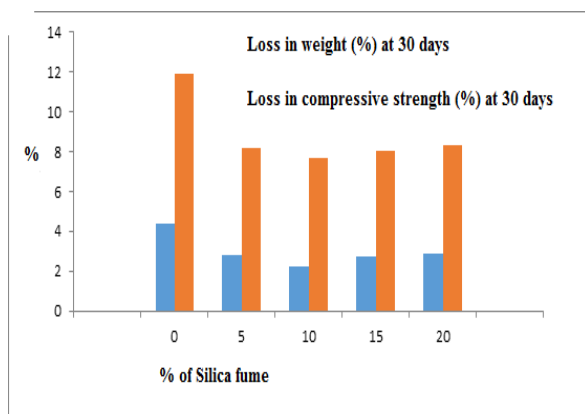


Fig. 3: Effect of acid attack on weight and compressive strength of cubes (Amudhavalli & Mathew, 2012)

Khajuria & Siddique (2014) investigated the effect of iron slag replacement of sand on the durability of concrete to sulphate attack. Magnesium sulphate (MgSO_4) solution of 50g/l was used to assess sulphate resistance of concrete. Although iron slag was replacing sand, however it is possible that it could still retain some certain desirable properties when replacing cement too. The result indicated that iron slag was having better resistance to sulphate attack.

Kirubajiny *et al.* (2017) reported the durability aspects of fly-ash-based-geo-polymer concrete (FBGPC). A concrete culvert was cast and exposed to coastal environment for 6 years. FBGPC culvert was carbonated in the top slab 135 mm and leg 90 mm while OPC culvert reported maximum value of 10 mm and 20 mm respectively. Chloride resistance in the FBGPC was higher (2.5 times) compared to OPC in the coastal environment. Micro-structure test results affirmed the dissolutions of carbonation in FBGPC when exposed to the actual conditions, whereas leaching was detected in the normal concrete. Also, SEM/EDX images showed that the chloride was precipitated as a layer on the FBGPC. Micro-structure images shows higher sulfate penetration and no development of calcium silicate hydrate in the FBGPC. Based on the porosity test, the geo-polymer concrete recorded fine pores stuck between 1.25 and 25 nm diameter, while the pores in ordinary concrete ranges

from 25 nm to 50,000 nm (Kirubajiny *et al.*, 2017). Zhang *et al.* (2016); Ye *et al.* (2019) and Awoyera *et al.* (2019) reported similar findings.

Kirubajiny *et al.* (2017), also reported that slag mixes exhibited better resistance to chloride ion penetration than the normal concrete mix, especially at 90 days of exposure. This can be attributed to two factors. The first, being the pore structure, which was seen from the results of the penetration tests to be more compact for the slag mixes than the normal concrete mix. The second, being the chloride binding abilities of the mixes. Several studies (Cheng *et al.*, 2005; Thomas *et al.*, 2012 & Ogirigbo & Inerhunwa, 2017) have shown that slag blended concrete are denser than normal concrete mix. The test results for the rapid chloride penetration into cassava peel ash concrete specimens at 7, 28 and 90 days were 4400, 3650 and 2464 coulombs, respectively while that of normal concrete are 6650, 5608, and 2750 coulombs, respectively (Kirubajiny *et al.*, 2017). Olatokunbo *et al.* (2018) also reported that, cassava peel ash concrete mixes produced lower permeability results at 7, 28, 90 days. It was observed that 15% had the highest resistance to acid attack which shows that it can serve as a suitable replacement if the right percentage is used. Durability and sulphuric acid resistance improved considerably at 10% replacement of cement with cassava peel ash (Olatokunbo *et al.*, 2018).

Water Absorption

Zabihi-samani *et al.* (2018) in their study observed that concrete with water absorption value less than 5% was recognized as a high quality concrete. From the study; water absorption of concrete incorporating FA ranged from 4.4-7.3%, 4.5-7.0%, 5.7-8.1% to 7.4-9.9% at the 20 °C, 400°C, 600°C and 800 °C, respectively. Concretes containing 0%, 30%, 50%, 70% FA resulted in less than 5% water absorption at the 20 °C. Similarly, the water absorption results of less than 5%

were achieved for the concretes containing 0%, 30% fly ash at the 400°C. According to these results, increase in temperature up to 800 °C leads to increase in water absorption value for all FA concretes. The values of the absorbed water indicated that 5% CPA cement replacement had the least amount of absorbed water while 25% had the most water absorption (Zabihi-samani *et al.*, 2018).

Porosity

Zabihi-samani *et al.* (2018) mentioned that concretes incorporating high volume fly ash were exposed to 400°C, 600°C and 800 °C high temperatures. The highest value of porosity was recorded by concrete containing 90% FA at all temperatures while the lowest value of porosity was recorded by concrete containing 30% FA. Olatokunbo *et al.* (2018) mentioned that, for cassava peel ash, porosity for the mixes, increases in values with increased cement replacement.

Drying Shrinkage

Olatokunbo *et al.* (2018) reported that the CPA average particle size had a significant effect on the drying shrinkage of concrete. 20 % CPA addition in concrete mixture exhibited higher shrinkage value than the control. 15% CPA addition in concrete was comparable, while the shrinkage for 25% was lower compared to the control. The high fineness of CPA particle size increased the pozzolanic activity and contributed to the pore refinement of the CPA concrete paste matrix. Thus, it can be mentioned that the addition of micro-fine particles to concrete would reduce the drying shrinkage.

CONCLUSION AND RECOMMENDATIONS

Based on several literature reviews considered in this study, the following can be deduced:

Cassava peel ash, metakaoline, ground granulated blast furnace slag, fly ash and silica fume enhance the workability of a

fresh concrete. The fineness of cement also helps to improve the workability of concretes in terms of flow ability.

Cassava peel ash, metakaoline, ground granulated blast furnace slag, fly ash and silica fume contributed to the compressive, tensile and flexural strength of concrete when administered optimally.

Ordinary Portland cement has poor acidic attack resistance along with minimal resistance to extreme conditions such as temperature thereby putting its durability in doubt.

Cassava peel ash, metakaoline, ground granulated blast furnace slag, Fly ash tend to exhibit a reasonable durability properties even at adverse conditions such as acidic attack.

Waste products such as Cassava peel ash, metakaoline, ground granulated blast furnace slag, fly ash and silica fume, rather than being discarded, can be used to enhance some properties of concrete.

Over reliance on Portland cement can be minimized if these binders that are by products are fully utilized for construction purposes.

Environmental pollution can be reduced drastically if the waste materials are used for construction purposes thereby enhancing the sustainability of the Engineering industry.

In fact, cement manufacturing firms should consider incorporating some of these waste at the point of production to minimize the cost of production.

REFERENCES

- Adam, I. (2021). Effect of binder content on Properties of different types of self-consolidating Concrete. *Engineering Research Journal* 131, 131(June), 19–37.
- Alexander, M., Jaufeerally, H., & J, M. (2003). Structural and Durability Properties of Concrete made with slag. *Journal of Civil Engineering*

- dept. University of Cape Town. 6, 1–30.
- Amudhavalli, N. K., & Mathew, J. (2012). Effect of silica fume on Strength and durability parameters of concrete. *International Journal of Engineering Sciences & Emerging Technologies*, 3(1), 28–35.
- Andreola, V. M., Gloria, M. Y. R., Santos, D. O. J., & Filho, R. D. T. (2019). Partial Replacement of cement by combination of Fly ash and Metakaolin in Bamboo Bio-Concretes. *3rd Int.l Conference on Bio-Based Building Materials*, 37(2), 102–106.
- Anejo, J. A., & Damen, R. M. (2014). Rate Of Strength Development Of Concrete Made Using Selected Nigerian Cement Brands. *International journal of technology enhancements and emerging engineering research*, 2(12), 48–51.
- Aubert, J. E., Tribout, C., & Escadeillas, G. (2019). Potential organic binders to stabilize earth construction materials. *3rd International Conference on Bio-Based Building Materials*, 37(2), 170–175.
- Awodiji, C. T. G., & Onwuka, D. O. (2016). Re-Investigation of the Compressive Strength of ordinary Portland cement concrete and Lime concrete. *International Journal of Geology, Agriculture and Environmental Sciences* Vol. 4(1), 12–16.
- Awoyera P, & Adesina A (2019): A critical review on application of alkali activated slag as a sustainable composite binder. Case Study Constr Materials
- Bakharev, T., Sanjayan, J. G., & Cheng, Y. (2003). Resistance of alkali-activated slag concrete to acid attack. *Cement and Concrete Research*, Vol. 33, (1607–1611).
- Eme, O., Chukwuma, J. N., & Ezeibe, C. (2016). Cement Classification in Nigeria: The Prospects for the new Standardization. *Specialty Journal of Politics and Law*, 1(1), 1–13.
- Ghosh, S., Mohanty, I., & Saha, P. (2018). Contribution of Steel Slags on the Fresh and Harden Properties of Concrete – A Review. *International Journal of Emerging Technology and Advanced Engineering* Vol. (2), 1–11.
- Jackson, D., Moon, J., & Gotti, E. (2013) Material and elastic properties of Al-tobermorite in ancient Roman seawater concrete. *American Ceramic Society* 96(8): 2598–2606
- Khajuria, C., & Siddique, R. (2014). Durability of Iron Slag Concrete to Sulphate Attack. *International Journal of Advanced Scientific and Technical Research*, 2(4), 795–801.
- Kiran, T. G. S., & Ratnam, M. K. M. V. (2014). Fly Ash as a Partial Replacement of Cement in Concrete and Durability study of Fly Ash in acidic Environment. *International Journal of Engineering Research and Development*, 10(12), 1–13.
- Ma, J., Wang, D., Zhao, S., Duan, P., & Yang, S. (2021). Influence of Particle Morphology of Ground Fly Ash on the Fluidity and Strength of Cement Paste. *Materials*, 14(283), 1–18.
- Mamoon, M. Z. S., & Mondal, A. U. (2019). Analysis of water absorption Properties by using Polystyrene sanded concrete. *International Journal of Civil Engineering, Construction and Estate Management* 7(3), 1–11.
- Mataalkah, F., Soroushian, P., Weerasiri, R. R., & Peyvandi, A. (2017). Development of indigenous binders as construction materials. *Construction Materials* 16(65), (1–11).
- Neville, A.M. and Brooks J. J. (1987).

- Concrete Technology, London: Prentice Hall.
- Ogirigbo, O. R., & Inerhunwa, I. (2017). Strength and Durability Performance of Slag Blended Cements in High Temperature Environments. *Nigerian Journal of Environmental Sciences and Technology*, 1(2), 265–272.
- Olafusi, O. S., Adewuyi, A. P., Otunla, A. I., & Babalola, A. O. (2015). Evaluation of Fresh and Hardened Properties of self-Compacting Concrete. *Journal of Civil Engineering*, 5, 1–7.
- Olatokunbo, O., Anthony, E., Rotimi, O., & Solomon, O. (2018). Assessment of Strength Properties of Cassava Peel Ash-Concrete. *International Journal of Civil Engineering and Technology*, 9(1), 965–974.
- Osuide, E., Ukeme, U., & Osuide, M. (2021). An Assessment Of The Compressive Strength Of Concrete Made With Cement Partially Replaced With Cassava Peel Ash. *A Journal Publication of Samuel Adegboyega University*, 6(1), 64–73.
- Patel, B. G., Desai, A. K., & Shah, S. G. (2015). Effect of Binder Volume on Fresh and Harden Properties of Self Compacting Concrete. *International Journal of Engineering Research & Technology (IJERT)*, 4(09), 599–605.
- Qureshi, L. A., Jawad, A., Bukhari, I. A., Munir, M. J. and Zakrya, B. (2014). Variation in fineness of Portland cement and its effect on properties of high strength concrete. *Journal of University of Engg and Technology, Taxila, Pakistan*.
- Rodríguez-Navarro, C. (2012). *Binders in historical buildings: Traditional lime in conservation* (pp. 91–112).
- Sabarish, K. (2019). Experimental studies on partial replacement of cement with fly ash in concrete elements. *International Journal of Civil Engineering and Technology*, 8(9), 293–298.
- Sandhu, R. K., & Siddique, R. (2017). Influence of rice husk ash (RHA) on the properties of self-compacting concrete: A review. *Construction and Building Materials*, 153, (751–764).
- Serdar, M., Bjegović, D., Štirmer, N., & Peču, I. B. (2019). Alternative binders for concrete: opportunities and challenges 10. (1–21).
- Sharbaf, M., Najafabadi, N. S., & Eftekhari, M. (2017). Effects of w / b ratio and binder content on Mechanical and Durability Properties of High Performance Concrete. *International Journal of Engineering Inventions*, 6(1), 40–48.
- Sheen, Y., Huang, L., Wang, H., & D, L. (2014). Experimental study and strength formulation of soil-based controlled low-strength material containing stainless steel reducing slag. *Construction and Building Materials*, 54(2014), 1–9.
- Sheen, Y., Le, D., & T, S. (2015). Innovative usages of stainless-steel slags in developing self-compacting concrete. *Construction and Building Materials*, 101(2015), 268–276.
- Srivastava, V., Agarwal, V. C., & Kumar, R. (2012). Effect of Silica fume on mechanical properties of Concrete. *J. Acad. Indus. Res*, 1(4), 176–179.
- Strijov, M. (2020). New Binder Systems and Concrete Concepts for Low-Emission Construction Challenges Regarding Workability of Fresh Concrete. *Journal university of Berlin*, <https://doi.org/10.13140/RG.2.2.31470.02883>
- Suryawanshi, Y. R., Kadam, A. G., Ghogare, S. S., Ingale, R. G., & Priyanka, L. (2015). Experimental Study on

- Compressive Strength of Concrete by Using Metakaolin. *International Research Journal of Engineering and Technology*, 2(2), 235–239.
- Suzuki, A., Pushpalal, D., & Kashima, H. (2020). An appraisal of compressive strength of concrete incorporated with chemically different fly ash. *The Open Civil Engineering Journal*, 14, 188–199.
- Wallevik, J. E. (2009). Rheological properties of cement paste: Thixotropic behavior and structural breakdown. *Cement and Concrete Research*, 39(1), 14–29
- Xiaolu, G., Huishenh, S., & Kai, W. (2014). Effects of steel slag powder on workability and durability of concrete. *Journal of Wuhan University of Technology*.
- Ye H., Chen Z., and Huang, L (2019). Mechanism of sulfate attack on alkali-activated slag: the role of activator composition. *Cem Concr Res* 125 (32-41).
- Yunfeng, L., Yan, Y., & Ling, W. (2009). Recycling of industrial waste and performance of steel slag green concrete. *J. Cent. South Univ. Technol*, 16, 0768–0773.
- Zabihi-samani, M., Mokhtari, S. P., & Raji, F. (2018). Effects of Fly ash on Mechanical Properties of Concrete. *Journal of Applied Engineering Sciences*, 8(2), 35–40.
- Zhang Z, H., Zhu H,J., Zhou C,H., & Wang H, (2016): Geopolymer from kaolin in China: An overview. *Journal of Appl. Clay Sci.* 119, 31–410.

APPLICATION AREAS OF OPTICAL WIRELESS COMMUNICATION TECHNOLOGIES IN 5G, 6G AND INTERNET OF THINGS: EXPECTATIONS, DIRECTIONS, AND THREATS

Abdullahi, B B., Michael, D., Suleiman, Z. and Abraham,. U. U.

Department of Telecommunication Engineering, Federal University of Technology, Minna, Niger State. Email: babadoko.pg915977@st.futminna.edu.ng,

Abstract

Optical Wireless Communication (OWC) systems are indispensable in the actualization of the expected 5G and 6G wireless communication systems. The significant issues concerning the quality of service of 5G and 6G communication systems are high capacity, high security, high quality of experience, low-energy consumption, low latency, massive connectivity, reliable and effective connectivity. 6G in comparison to 5G communication will offer better performance in regards to the stated performance metrics. It is very important to emphasize that the Internet of Things (IoT) based on internet data is an integral part of 5G and beyond. This review is a presentation of how OWC technologies, such as free-space optics communication(FSO), infrared light communication(IRC), light fidelity(LiFi), optical camera communication(OCC), and visible light communication(VLC) will be an effective solution for the successful deployment of 5G, 6G, and IoT systems with inherent challenges of supporting the extensive varieties of heterogeneous traffic and in satisfying the mentioned quality of service-related performance metrics

Keywords: Diffused Spots Communication Links, Hybrid RF-Visible Light Communication, IoT, LiFi, Line of Sight Communication Links Optical Small Cell.

INTRODUCTION

In the past few years, the request for high data rate services has increased dramatically. The congestion in the radio frequency (RF) spectrum (3 kHz ~ 300 GHz) is projected to limit the exponential growth of future wireless systems until and unless new segments of the spectrum are opened. Even with the use of advanced engineering, for example; signal processing and advanced modulation schemes, there are still threats to meet the demands of the users in the fifth generation (5G)/and sixth generation (6G) technologies of a wireless network using the existing carrier frequencies as only radio frequency-based wireless communication technologies are not adequate in meeting the requirements of Fifth Generation and beyond and also Internet of Things networks that is according to (Jatau, *et al.*, 2020).

Hence, the need for more research work to determine the usage of the new spectrum that would fulfill the high data rate needs(Masroor *et al.*, 2021; Wei *et al.*, 2021)

through hybridized RF/optical or optical/optical wireless systems that can provide an optimal solution for recovering the shortcomings of individual systems as well as ensuring better performance indicators of each of the technologies.

The potential band of spectrum available can give tens of Gigabit per second to Terabit per second(Gbps-Tbps) for users shortly (Chow *et al.*, 2020). Optical wireless communication (OWC) systems are also key to effective solutions to bandwidth problems, power/interference management issues, strict regulation, and low-speed problems in radio frequency systems. This paper gives a tutorial survey of the most important setbacks in OWC systems that operate at short ranges such as indoor systems which can support future technologies and also talked a little about free-space optics (FSO) technology that can transmit over a long distance (that is an open space optical technology) for future wireless signal transmission and reception. We also considered the challenging issues facing the

implementation of 5GB (i.e 5G and Beyond) and designed of embedded small optical wireless cells (attocell) to support RF signal within a definite size of building geometrics using different optimization algorithms such as illustrated by (Coelho *et al.*, 2021). The Internet of Things (IoT) network is extremely important since higher data rates (speed of download/upload) demand by end-users are expected in the nearest future as a large number of end-user devices or sensors would be connected in IoT. Tactile internet will be a critical feature of the upcoming Internet of Things (IoT) which of course required ultra-high frequency and low latency for efficiency, It will allow for real-time communication systems within society, industry, and business use cases, since IoT would generate a large volume of data optical wireless systems will also play important role. The optical wireless communication technologies have applications in monitoring, resource sharing, and sensing in rapid device connections of IoT system networks (Saeed, *et al.*, 2019; Pathak *et al.*, 2015; Katz & Ahmed, 2020; Menaka *et al.*, 2021)

In addition, optical wireless communication can achieve the low-power requirements and ultra-high security requirements of the Internet of Things (Lai *et al.*, 2020; Masroor *et al.*, 2021; Rahman *et al.*, 2016). The 5G communication system specification is already completed, and 5G was expected to be fully deployed by 2020 is according to (Chowdhury *et al.*, 2019). The novel 5G communication which has already been launched in some American, European, and Asia countries and was also approved for use in Nigeria by FGN on Wednesday, September 8, 2021, 5G will provide a very good grade of service (QoS). This review aims to present the areas of application of OWC technologies that complement RF technologies to solve the problems that are associated with deployment of 5G/6G and IoT systems. This review provide herein possible detailed 5G/6G and IoT solutions using different optical wireless

communication systems. The outline of this paper can be summarized as below:

- i. A brief discussion of types of OWC technologies.
- ii. Explanation of the main features of 5G and IoT system networks. 6G requirements are also briefly presented.
- iii. The scope of diffused spots links as a solution for mobility problems in indoor optical wireless communication systems and different optimizations techniques employed in recent works on small optical cells as a means of densifying the network were surveyed.
- iv. Some projects recently carried on the optical wireless communication technologies that improve system support for the 5GB and IoT solutions are captured, and the research trends are discussed.
- v. Threaten issues in Optical Wireless Communication as it affects the deployment for the 5G,6G, and IoT solutions are also captured.

The remaining parts of this paper are programmed as follows: Section 2 describes different OWC technologies; Section 3 provides a brief overview of the 5G, 6G, and IoT requirements; and Section 4 describes the potential of the OWC technologies to meet the demands of the 5G, 6G, and IoT systems. Section 5 presents a few key challenging issues of optical wireless communication in the implementation of 5G/6G and IoT and solutions. Section 6 concludes this paper.

2. BRIEF OVERVIEW OF THE OWC TECHNOLOGIES

The optical broadband includes the infra-red (IR) spectrum, the visible light spectrum, and the ultraviolet spectrum benefits from an almost unlimited 800 THz bandwidth when compared to the 300 GHz RF spectrum (Gautam *et al.*, 2021). Infrared light spectrum (1 mm – 750 nm for infrared)

usage was discovered, considered, and tested over time, the usage of the visible light spectrum (380 – 780 nm) is still undergoing laboratory testing because the spectrum almost new to both industries and researchers.

Light Visible Communication technology was introduced in the early 2000s with performing experimental prototypes being presented several years after (Chowdhury *et al.*, 2020; Masroor *et al.*, 2021). Starting from the 2010s, the technology became more popular and the laboratory experiment sh1Gb/s data rate was reached and exceeded soon after (Eltokhey *et al.*, 2019). The technology has been further developed and today's papers report experimented data rates that exceed 10 Gb/s though, mobility of the system caused blockage of signal (total signal loss) due to the LoS nature of light Khalid *et al.*, 2021) presented that, the proper (field of view) FOV adjustment is very important for achieving good lighting efficiency and higher data rate in a VLC link, with envisioned data rates of few hundreds of Gb/s (Rahman *et al.*, 2018). In parallel with the improvement of the data rates, as the VLC technology was developing, new applications were identified and VLC has become a worldwide business (Pathak *et al.*, 2015). The intensive research efforts have also led to the standardization of optical communications using visible light by IEEE (Wei *et al.*, 2021). Lifi is the modernization of VLC which implements bi-directionality, multiuser access, and handover capabilities.

Light Fidelity (LiFi) OWC system was first introduced by Professor Harald Haas at TEDGlobal 2011, LiFi is similar to wireless fidelity (WiFi) technology.

Optical Camera Communication (OCC), and free-space optics (FSO) Optical communication systems-

They are not expensive to imbed into routine use, manufacture of dedicated infrastructure is not required, instead they both (i.e FSO & OCC) relied on the innovation/modifications of existing ones. Despite the pros of optical

wireless communication systems, it also has some demerits. For example; Optical wireless communication system is mostly dependent on line-of-sight (LOS), effective in a small coverage area because it is sensitivity to sudden blockage of a connection as the device orientation affects the channel gain significantly, other light sources caused interference, outdoor atmospheric conditions cause performance degradation and transmitted power is limited due to eye/ skin safety regulations.

To surpass the aforementioned demerits, seamless OWC usage is a threatening issue. OWC Technologies are all designed to complement RF communication technology, with high security, enormous and unregulated bandwidth, and not to replace it (RF), but there are indications that optical wireless technologies are good for usage in the future 5G and beyond (Haas *et al.*, 2020). The transmitter, receiver types differ depending on the technology used and also depend on the communication media as in Wang *et al.* (2021) shown in Table 1.

Transmitter used in OWC system (photodiodes)- LED and LD are the commonest transmitters often used in optical wireless communication systems, they are based on either white light generation, or quantum techniques, and related color conversion techniques to achieve higher conversion efficiency.

According to Haas (2011) improvements in the use of optical transmitters are based on the following; i. The multichip-based white light generation ii. The Resonant Cavity LEDs (RCLED) iii. The Super Luminescent Diode (SLD) iv. Narrowing down the LED diameter, v. The quantum dots methods and lastly, Tx characteristics in an indoor scenario with the characteristics such as; the room size and model, the reflection characteristics of the environment, the placement of windows and doors, the layout of optical transmitters, and their parameters. Hence, optimizing the above parameters can improve the performance metrics of OWC systems. There are lots of efforts on how to

achieve higher capacity and reliable OWC channels through modulation schemes because the device orientation affects the channel gain significantly Katz (2020).

- a. Receiver (photo-detectors) there are two types of receivers namely; APD photo-detectors and PIN Photo-detectors. APD PDs are good for high-speed, long-haul communications but it is not cost-effective. While PIN PDs are known for their high reliability for all categories of communication and are cost-effective solutions for OWC. The higher sensitivity of the APD is due to the choice of a higher number of layers and a smaller depletion region, this makes it a long-distance communication receiver.

The PIN PD is more applicable for indoor short-distance scenarios because of the high ambient brightness available in indoor environments.

- b. Transmission Media- Visible Light Communication uses visible light (VL) only as of the communication medium, Optical Camera Communication employs either Infrared Light or Visible Light as a communication medium, Free Space Optics use any of the three media namely; Ultraviolet Light, Visible Light, and Infrared Light as media and Light Fidelity used VL for downlink while at the uplink it employed either of UL, VL or IR.

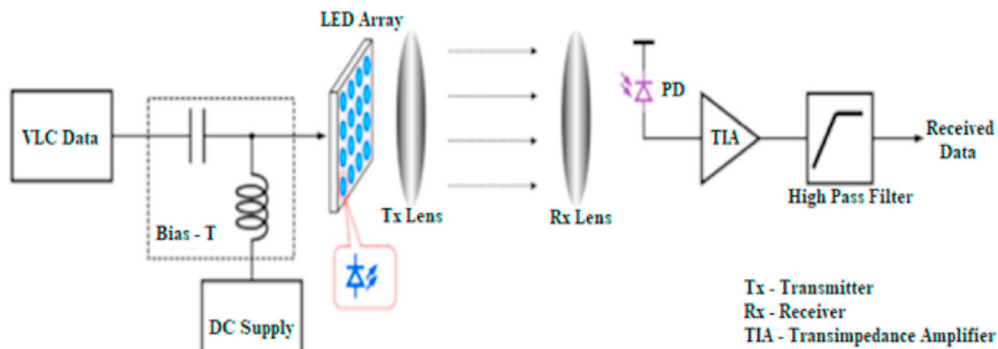


Fig.1. Structure of a Typical VLC System Masroor, (2021)

Table 1: OWC Technologies for the Future Heterogeneous Networks

Transmitter	Diffused Laser Diode /Light Emitting Diode	Light Emitting Diode spread Light	Laser Diode or Light Emitting Diode	Laser Diode
Media	Downlink: VL Uplink: UV/ IR/VL	Infrared/Visible Light	Visible Light	Ultraviolet/ Visible Light/ Infrared
Receiver	Light Detector	Camera	Light Detector	Light Detector
OWC Technologies	Light Fidelity	Optical Camera Communication	Visible Light Communication	Free Space Optics

2.1 Data Transmission Techniques / Modulation Techniques

Traditional Radio Frequency Communication links differ from Optical

Frequency Communication links as such different methods of modulation are used. Modulation schemes that worked perfectly in RF links may not necessarily do well in the optical domain. Therefore, four (4)

criteria that determine the choice of a particular modulation technique for OWC systems of specific interest are-: (1) The average power used (power efficiency) of a given modulation format, this is considered because of eye hazards and power consumption in mobile terminals. (2) The complexity of the modulation format (and power consumption in portable devices). (3) The third factor is the available channel bandwidth and receiver bandwidth requirements. (4) The criteria relating to the physical limitations in the transmitter (i.e. LD or LED) which the modulation format may have to take into account.

Modulation in OWC systems is comprised of two stages: (i) the information is coded as a waveform(s) (ii) The waveforms are modulated onto the continuous high sinewave power of the (carrier frequency) Intensity modulation (IM) and direct detection (DD) is the preferred transmission technique in OWC systems according to Chow *et al.* (2020).

Intensity Modulation can be obtained by changing the bias current of either Laser Diode or Light Emitting Diode. For Optical Wireless Communication systems, the transmitted signal had always been positive in intensity. Direct detection (DD) is also the simplest method that is used to detect an intensity-modulated signal. The light detector generates a current which is proportional to the incident of optical power intensity. Below is the expression of the IM/DD channel as given by Haas *et al* , (2020)

$$z(t) = R(x) t \otimes h(t) Rn(t) \quad (1)$$

where R is the light detector responsivity, $z(t)$ is the instantaneous photocurrent received, t is the absolute time, \otimes denotes convolution, $h(t)$ is the channel impulse response, $x(t)$ is the instantaneous transmitted power and $n(t)$ is the background noise (BN), which is modeled as white Gaussian noise and is independent of the received signal.

Delay Spread is an important parameter in wireless communication (i.e Spread of time in which signal energy arrived at the receiver due to the temporal dispersion of the incoming

Signals). The delay spread of an impulse response is given by (Abdelrahman, 2019):

$$DS = \sqrt{\frac{\int (t - \mu)^2 (h(t; T_f; R_f))^2 dt}{\int (h(t; T_f; R_f))^2 dt}} \quad (2)$$

And μ is the mean delay, which is given by:

$$\mu = \frac{\int t (h(t; T_f; R_f))^2 dt}{\int (h(t; T_f; R_f))^2 dt} \quad (3)$$

Note: $h(t; T_f; R_f)$ is the channel impulse response LOS while at diffuse spot or a Lambertian surface r th reflection order impulse response of $h_r(t; T_f; R_f)$.

The SNR was given by

$$SNR = \frac{(RP_r)^2}{\sigma_{total}^2} \quad (4)$$

Where P_r is the average optical receiver power and σ_{total}^2 is the total variance of the noise which was given by:

$$\sigma_{total}^2 = \sigma_{PA}^2 + \sigma_{BN}^2 \quad (5)$$

Where σ_{PA}^2 is the noise variance of the pre-amplified signal and σ_{BN}^2 is the ambient lights noise variance. Three broad types of modulation schemes can be applied in OWC (a) baseband modulation, (b) multicarrier modulation, and (c) multicolor modulation Ghassemlooy *et al.* (2017)

a. Baseband Modulation

The main baseband modulation techniques considered in OWC include (i) pulse amplitude modulation (PAM), (ii) pulse position modulation (PPM), (iii) pulse

interval (PIM) modulation, and (iv) carrier less amplitude phase (CAP) modulation.

b. Multicolor Modulations

Multicolor modulation has recently been considered to provide high data rates or multiple access for users by (Z. Wang, et al, (2018). White light can be generated from blue, green, and red (BGR) kinds of LEDs which means data can be transferred through each color or wavelength. The multiplexing used here is wavelength division multiplexing (WDM). In addition to the above, this author, Huang et al.,(2018) achieved white light from four-color LDs which provide a better result compared to three colors LEDs in terms of multiple access and higher data rates due to the improved modulation capabilities of LDs. However, the slow response of phosphor, which reduced the modulation bandwidth of white LEDs to a few MHz is a challenging task, these effects can be improved upon but, it requires complex signal processing and advanced modulation formats.

c. Multicarrier Modulation

Subcarrier modulation (SCM) is another advanced modulation technique that can be used in OWC systems to transmit multiple carriers. This can provide multiple access for concurrent users at high speed (data rate). SCM is not power-efficient, unlike the single carrier technique. For example, one quadrature phase-shift keying (QPSK) or binary PSK subcarrier requires about 1.5 dB more power than OOK.

According to Rahman *et al.* (2016) reducing the average power requirements in SCM modulation gives a high data rate in orthogonal frequency division multiplexing (OFDM) when applied in indoor OWC systems to achieve high data rates over a noisy channel and to reduce Inter Symbol Interference, but according to Wei et al., (2021) did not achieve a high SNR. OFDM's because of challenges due to frequency sensitivity and offset and phase noise as well as the high peak to average power ratio

(PAR) while Performance improvement of the OWC systems depends on the use of complex modulation schemes to mitigate the effect of ISI and increase the data rates. But these modulation techniques require a complex transmitter-receiver (transceiver) on the need for more optimization techniques. Abdelrahman *et al.* (2019).

2.2 Medium Access Control Protocols

The concurrent support of many mobile terminals from just one access point in OWC wireless networks is very important. The mobile terminals may have different service requirements. In the case of production plants, the transmission delay may be more important than the peak data rate. Developing optimum multiuser access techniques which avoid multiuser interference and achieve high-frequency efficiency must be first considered. Fundamentally, the total data rate of an access point is greater when supporting many users as compared to a single-user scenario. A promising access technology in OWC that can achieve this is non orthogonal multiuser access (Chowdhury *et al.*, 2020). The uses of OWC are shown in the following articles are related to multiuser access in OWC networks (Chowdhury *et al.*, 2018; Dehghani Soltani, 2019; Wang *et al.*, 2021; Pathak *et al.*, 2015; Masroor *et al.*, 2021).

2.3 Interference Mitigation and Mobility Support

Many access points which are spatially distributed is one of the characteristics of the wireless network. A certain area is covered by one access point when a user equipment or mobile device enters the coverage zone of an access point, the system performs a seamless handover from the access point to which the UE device was previously connected to the new access point. The main merit of optical wireless networking is that atto-cells (very small cells) can be generated where a cell is defined by the coverage area of an access point. The same transmission

resource can be reused many more times because of the small size of the coverage area, it is a very important opportunity for frequency reuse if compared to large area cells in RF systems. This principle of cell shrinkage is the main reason why Radio Frequency communication needed improvements (more interference due to large cell size) which could affect data rates (speed) significantly. But interference is kept at minimal levels even as the size of the cell gets smaller in OWC.

2.4 Network Topology is the arrangement of the elements (links, nodes,

etc.) of an OWC network. It is used to define or describe the arrangement of various types of wireless communication networks, including command and control of optical networks. Topology is the physical or logical depiction of the structure of the network.

2.5 Communication Distance is the distance between OWC Tx and Rx that, allows for effective communication. Performance metrics e.g SNR, SNIR, interference level, signal strength, latency rate, and data rate etc can be used to determine the effective distance in the communication system.

Table 2. Comparison of the Performance Metrics in Various OWC Technologies

Challenges	VLC	LiFi	OCC	FSO
Information Security	High	High	High	High
Communication Topology	Unidirectional or bidirectional	Must be bidirectional	Unidirectional	Unidirectional or bidirectional
Communication Distance	20m	10m	60m	Greater than 10,000km
Mobility support	Optional	Must	Optional	No
Environmental effect	Indoors: No Outdoors: Yes	Indoors: No Outdoors: Yes	No	Yes
Interference level	Low	Low	No	Low
Data rate	10 Gbps using LED and 100 Gbps using LD	10 Gbps using LED and 100 Gbps using LD	55 Mbps	40.665 Gbps

3. IMPORTANT CHARACTERISTICS OF THE 5G AND IOT NETWORKS AND THE POSSIBILITY OF 6G REQUIREMENTS :

5G networks will deliver an extensive variety of services comprising ultra-reliable and low-latency communications (uRLLC), massive machine-type communications (mMTC), and enhanced mobile broadband (eMBB) as presented in Fig. 2. In order to

achieve all of the aforementioned characteristics of 5th generation networks (i.e existing cellular towers), must be complemented by a modern system called small cells with multi-inputs/ multi outputs MIMO antennas technology. For more information on the requirements, core properties, and vision of 5G wireless cellular mobile communication networks, we refer the reader to Gohar *et al.* (2021). However, wireless data traffic volume and the

momentousness of connected devices are expected to surge to hundred times of equipment in a given shape's meter. Moreover, data-thirsty applications such as sending heliographic videos require a special frequency band that is currently not available in the mm-wave spectrum. The above situation would be task-oriented and a challenging one in the area space or frequency efficiency as such, higher frequency spectrum bands are required for

connectivity. Hence, a broader radio frequency spectrum bandwidth has become a necessity and can only be found at the sub-terahertz bands (terahertz –terahertz) frequency bands systems. Moreover, the recent upturn of assorted mobile applications, specifically those supported by programable smart systems and Artificial Intelligence (AI) technology, is challenging / exciting deliberations on the future expansion of wireless communications.

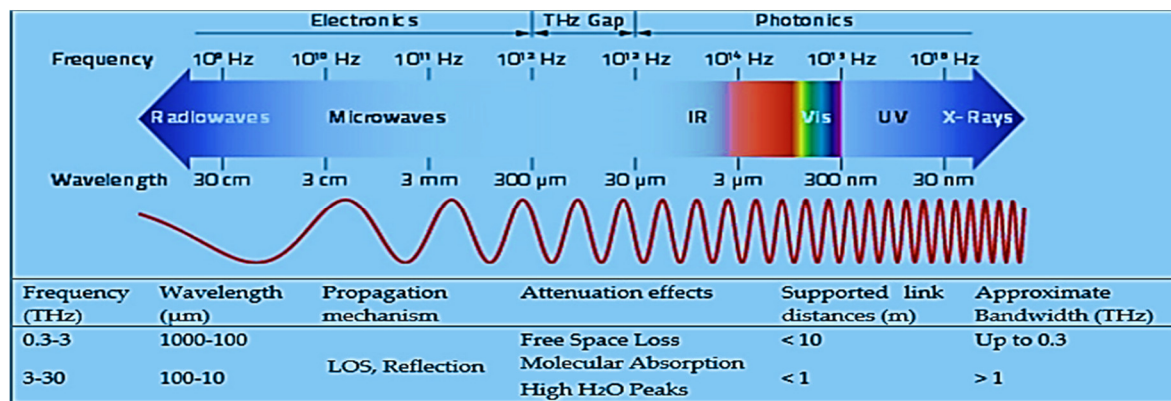


Fig. 2. Electromagnetic Spectrum and Wavelength of Terahertz and Millimeter Waves (Alsharif *et al.*, 2020)

The followings are among the expected expansions of hybrid of RF and optical wireless communications to support the implementation of 5GB multi-layer heterogeneous networks such as; basic vehicular communications which covered vehicle-to-vehicle (V2V), vehicle-to-road/infrastructure (V2R/V2I) communications and was extended to models and services in V2X umbrella, for example, vehicle-to-power grid (V2G), vehicle-to-pedestrian (V2P) - direct communication, vehicle-to-vulnerable road user (VRU), vehicle-to-network (V2N) - including cellular networks and Internet, Vehicle to sensors (V2S), and vehicle-to-home (V2H). V2X allows vehicles to directly communicate with each other, also to other road users and roadside infrastructures, for the purpose of actualizing smart mobility, environmental sustainability, traffic efficiency, driver

convenience, and better road safety. For the aforementioned provisions, V2X contributes to fully autonomous driving development through its unique non-line-of-sight sensing capability which allows vehicles to detect potential hazards, traffic, and road conditions from longer distances.

IoV has advantages of extending from the normal vehicle driving and precaution safety to novel target domains for example enhanced traffic management, road infrastructure construction and repair, vehicle insurance, automobile production, logistics, repair, and transportation.

Note that IoV involves the Internet and includes heterogeneous access networks, therefore IoV is a typical use case of the Internet of Things (IoT); however, IoV contains intelligent “terminals” such as vehicles (it could be - autonomous). The complexity of the V2X/IoV claims for strong support infrastructure.

The 5G slicing technology is considered to be an appropriate candidate. The fifth-generation, sixth-generation mobile network technologies offer compelling ingredients, in terms of capacity, flexibility, services, and speed to respond to the increasing need and threat addressed to communication systems and Internet (Ji *et al.*, 2021). 5G can render robust kinds of services to concurrently satisfy different customer/tenant needs in a multi-x fashion (the notation -x stands for the tenant, domain, operator, and provider).

The 5G network slicing concept (based on virtualization and software) enables programmability and modularity for

network resources provisioning, adapted to different vertical service requirements (in terms of bandwidth, latency, mobility, etc.) (Soldani, 2021). In a general view, a Network Slice (NSL) is a managed logical group of subsets of resources, organized as virtual dedicated networks, isolated from each other (with respect to performance and security), but sharing the same infrastructure. The NSLs functionalities are implemented by Physical/Virtual network functions (PNFs/VNFs), chained in graphs, to compose services dedicated to different sets of users. The slices are programmable and have the ability to expose their capabilities to the users.

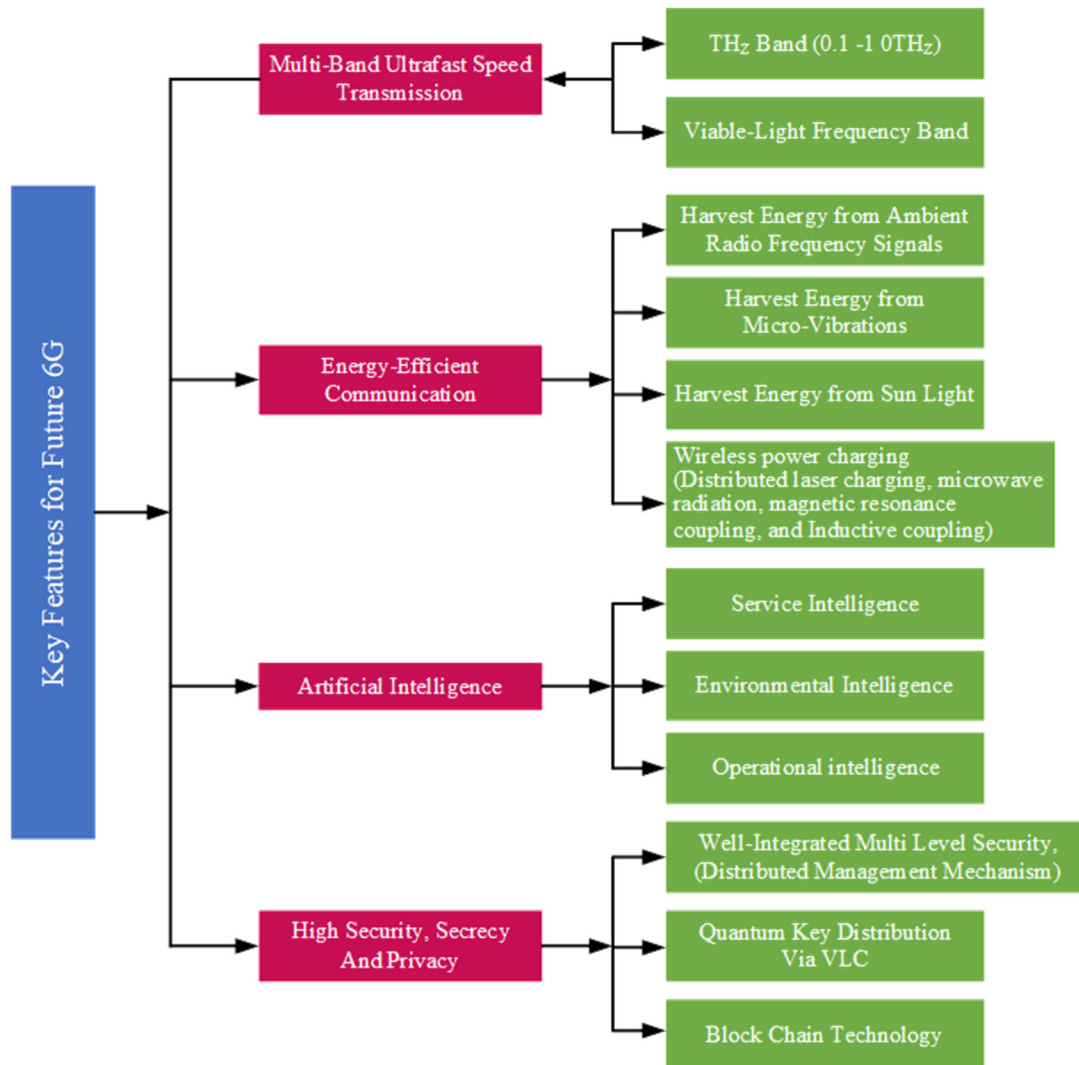


Fig. 3: Main Characteristics For Future 6G (Letaief *et al.*, 2019; Zakrzewski & Łąga, 2020; Alsharif *et al.*, 2020; Soldani, 2021)

According to Soldani (2021) Fig. 3 illustrates future wireless communication characteristics which include: massive machine type communication (mMTC); Ultra reliability low latency communication (URLLC); Enhanced mobile broadband (eMBB) According to Obreja *et al.* (2021) the authors also presented two-hop hybrid active-and-passive relaying scheme are to provide concurrent wireless information and power transfer (SWIPT) by considering both time-switching (TS) and power-splitting (PS) receiver architectures. Dynamic modeling that involves dual-hop time-period (TP) metrics was also proposed by Ottersten *et al.* (2021) for energy efficiency in 5G/6G and IoT systems.

4. THE POTENTIAL IN THE OPTICAL WIRELESS COMMUNICATION SYSTEMS TO MEET DEMANDS OF THE FUTURE OF SYSTEMS

Reports have shown that platforms such as cellular connectivity are supported by OWC according to Alsulami *et al.* (2020), OWC systems also support electronic health (eHealth) that is according to (Eltokhey *et al.*, 2019), space communication, and smart shopping according to Ghassemlooy *et al.* (2017), and smart home presented by Nencioni *et al.* (2021). underwater communications, V2X communications can be supported by OWC networks according to Zhang, Zhao *et al.* (2020). Very encouraging concepts for which OWC system can be used in the identified 6G verticals, which opens new areas of research for 6G such as VLC, Light-based IoT, Living surfaces, and optical communications through bio-tissues (BAN) RF radiations exposure affects the cells and tissues that, may have effects in human health which is an existing challenging problems, OWC also gives importance to environmentally sustainable safety, this is so, because human bodies are transparent to radio and microwaves frequencies, while they are not transparent to visible light. The above feature makes

optical wireless transmission via visible light safe for human health.

4.1 Optical Wireless Communication Systems as a Successor for 5G and 6G Technologies

Network slicing presented a virtualization technology for 5G which could allow OWC to play an important role in a short distance scenario such as V2V, M2M, Hybrid RF, and other OWC indoor scenarios (Arai, *et al.* 2021).

4.2 5G Use Scenarios and Suitability of Optical Wireless Communication

In the year 2014, a 5G research was initiated at the workshop entitled “Research views on IMT Beyond 2020” at Working Party 5D, by International Telecommunications Union Radio Communication Sector. This review focused on the connection of a random number of mobile terminals to an infrastructure that is composed of multiple fixed optical access points, which covers a small area defined by wireless networking with light. The communication channels are expected to be non-line of sight or hybrid (Arfaoui *et al.*, 2020).

Furthermore, the connection is supposed to be smoothly maintained as the mobile terminals roam between optical access points and RF access points. Wireless connectivity employing light requires a set of basic technologies, which were mentioned (Chowdhury *et al.*, 2020). The main technologies at the outer boundaries, starting with channel models, are the same as in RF networks hence integration with an optical signal is possible since the optical radiation does not interfere with radio waves. The areas of application of OWC can be further extended because it does not use radio waves (Chowdhury *et al.*, 2020) and the license-free communication band. Any technology can be used to complements radio waves for user needs. Thus, acceptance of OWC need not be constrained to only post 5G and 6G technologies. However, specific solutions

are needed for each category due to the characteristics of light. New solutions are functions of the actual channel models, the optical front-end systems, and the devices types. The optical devices and their components determine the key system parameters such as peak data rates, link distance (Hakeem *et al.*, 2020), etc. The optical front-end system has a very significant impact on the actual link budget, which is limited by the maximum optical output power and the receiver sensitivity. The link budget is logically fed into the channel models, which vary largely with the actual deployment scenario (Zakrzewski & Łaga, 2020).

In complementing RF with light wave using principles such as software-defined networking (SDN) are used to integrate the optical wireless networks into existing RF wireless networks, (Zadobrischi *et al.*, 2019). However, the initial application area will be terrestrial indoors since about 80–90% of all Internet traffic originates and terminates indoors (Jenila & Jeyachitra, 2021; Molinaro *et al.*, 2020; Storck & Duarte-Figueiredo, 2020). This would also provide a medium for harnessing the lighting infrastructure to build the optical wireless networks on top of the downlink direction, this could be based on white light (standardization as required by existing VLC). The uplink uses the infrared spectrum or RF as a medium for the downlink, this permits for full-duplex operation, which is advantageous for delay-sensitive applications. Arai *et al.* (2021) reported the applicability of OWC to the following use scenarios as follows:

4.2.1 EMBB: Enhanced Mobile Broadband- It is also quite possible to envision, for example, the use of OWC in a limited indoor space; this is the scenario for which Li-Fi, VLC which are consider as post 5G and 6G and they are expected to use higher frequency bands than are currently in use. However, assuming the use of frequencies above 300 GHz, the wavelength

would be 1mm or less, making communications more susceptible to absorption in matter and air. Thus, the characteristics of the transmitting radiation would become closer to those of visible light. Because a sufficiently large frequency band is available for the OWC, it may prove to be an excellent solution for implementing the ultrafast communications expected in post 5G and 6G. Therefore, one may consider that OWC is a viable candidate for post 5G and 6G and IoT networks (Chowdhury *et al.*, 2020).

Moreover, high-speed network connectivity is required to support massive IoT connectivity. Hence, the optical spectrum has the potential to serve the large volume of data traffic generated by high-data-rate heterogeneous multimedia applications in the 5G, 6G, and IoT networks (Chowdhury *et al.*, 2019).

4.2.2 URLLC: Ultra-Reliable, Low-Latency Communication- This scenario assumes wireless operation in the manufacturing industry, telemedicine surgery, smart grids, vehicle automation, etc., and requires precision from the viewpoints of throughput, delay, and reliability. Adoption of OWC is unlikely in this scenario because of the difficulty in ensuring ubiquity as previously described in Section. 4.2.1 except for the use of Hybrid RF and OWC (Diffused Spots/NLOS Links). However, it may be adopted as an alternative measure in places where radio waves are not used, such as at medical sites. Hence, even though RF and optical signals both propagate at the speed of light, the communication using the optical band is faster than that using RF bands because the propagation is rapid in the optical communication systems. Additionally, the processing time in an optical system is short. Therefore, these OWC-based network technologies can offer services with negligible latency in the communication systems (Chowdhury *et al.*, 2018).

4.2.3 MMTC: Massive – Machine - Type Communication- OWC is expected to only find limited use in this scenario. Since this scenario involves low-speed or immobile objects, line-of-sight communication is easily secured. In such an environment, OWC can play a significant role. In particular, VLC and Li-Fi use visible light as a transmission source so that communication paths can be visually determined, which would greatly facilitate designing the communication path. Conversely, the use of OWC would be limited because IoT devices installed outside the line of sight, for example, behind shelves, would be inaccessible according to Haas *et al.* (2020); Katz & Ahmed (2020); Chow *et al.* (2020).

4.2.4 Ultra-Low-Energy Consumption- Among a few important criteria, energy efficiency is one of the most important requirements for all 5G, 6G, and IoT systems. Most OWC system infrastructures are based on LEDs. Currently deployed LEDs consume a very small power. Moreover, huge studies are currently ongoing around the world to reduce the power consumption by LEDs. LEDs can also be used for illumination and communication. Therefore, no additional energy is consumed by an LED transmitter, therefore the OWC-based communication technologies can provide energy-efficient communication systems that are an important requirement for the 5GB and IoT deployments.

4.2.5 Reliable connectivity and Ultra-High Security- As it is expected of 5G, 6G, and IoT networks OWC signal has a high signal to interference noise ratio and cannot pass through an object (e. g wall) so without entering into the building, therefore, security is assured (Silva & Guerreiro, 2020) since the exchange of information would be highly secured and will be free of jamming of data, used especially for health purposes (e.g Body Area Network).

4.3 Achieving Network and Infrastructural Qualities- is another area

where OWC, specifically visible light systems play important roles. Since 5GB (5G and beyond) systems are to be used together with 3G applications it will require 3D base stations, hence research into measurement and data-driven modeling of propagation entity is essential which in turn required planning to utilize 3D broad bands. The aforementioned may be complicated at optical wireless frequency band because of the line of sight nature of the system. Obviously, the Poisson point process (PPP) and other mathematical model would be employed Future communication would network demand.

4.3.1 Network restriction using highly restricted heterogeneous networks- That is constrict stationing of atto-cells and the boost of frequency usage. The small cell sites are placed in capacity-starved areas to increase capacity and speed up traffic offload from the neighboring sites stated in this paper (Akhtar *et al.*, 2020).

Fig. 4. Shows multi-tier networks using RF/OWC (Tomkos *et al.*, 2020)

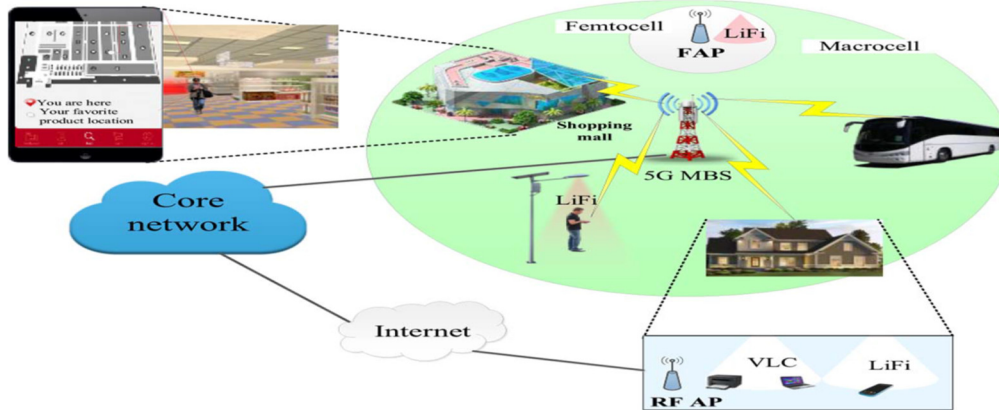
To increase network capacity these are the 3 main sources require below.

- i. Restricting the network
 - ii. The spectrum should be made more efficient, and
 - iii. A more frequency band should be used.
- Hence, all of the above three sources can give high data rate, provision of hybrid network connectivity, and massive device connectivity for 5G, 6G, and IoT communication systems can be achieved (Zhang *et al.*, 2020) This is the main focus of our research work. Below are some reviewed work on OWC small cells.

4.3.2 Multi-tier Architecture and Convergence of Heterogeneous Networks:

Future communication would demand a high data rate, low latency for the system to achieve, the network will exploit a multi-tier

technologies of VLC and LiFi build a tier under RF small cells short distance scenario while multi-tier design can consist of larger coverage RF base station, RF small cells, or optical small cells.



architecture of macro cell networks and underlying small cells containing optical VLC, LiFi, and RF small cells as illustrated in Fig. 4 in section 4 above. The optical

Table 3: Review of other reviewed Papers

S/No	Authors (year)	Title	Methodology	Results
1	Tomkos <i>et al.</i> , 2020)	Toward the 6G Network Era: Opportunities and Challenges	Reviews the opportunities and challenges of 5G network.	
2	(Tariq <i>et al.</i> , 2020)	A Speculative Study on 6G	Reviewed possible technologies for the future 6G network. Also, The limitations of 5G network that form the basis of our 6G vision were discussed. The 5G and 6G were compare in terms of use cases.	Identify that 5G is very week in areas such as true AI, time buffer, ultra-sensitive application, satellite integration e.t.c.
3	Wang <i>et al.</i> , (2020)	An Overview of Key Technologies and Challenges of 6G	Presented the key characteritics for comparing 5G and 6G networks. Also, investigated the vision of 5G soon and contemplates. about the ambitious technologies which will lead to the implementation of 6G networks.	The suggested key performance indicators for 6G network against 5G was highlighted. Also, likely challenges of 6G networks and technology area of the 6G was pointed out. These technologies are artificial intelligence, THz communication along with Radio Stripes and quantum networks.

4	(Chowdhury <i>et al.</i> , 2019)	The Role of Optical Wireless Communication Technologies in 5G/6G and IoT Solutions: Prospects, Directions, and Challenges	Presents how optical wireless communication technologies, such as visible light communication, light fidelity, optical camera communication, and free space optics communication, will be an effective solution for successful deployment of 5G/6G and IoT systems.	The results of the reviews shows the 5G, 6G and IoT requirements such as ultra-high bit rates per device, ultra-long-range communication with ultra-low-power consumption and ultra-low latency of less than 1 ms for 6G. also, predicted that the 6G network will hit the market between 2027-2030. The challenges of the service quality of 5G and 6G communication systems are high capacity, massive connectivity, low latency, high security, low-energy consumption, high quality of experience, and reliable connectivity.
5	(Arai <i>et al.</i> , 2021)	Optical Wireless Communication: A Candidate 6G Technology?	Reviews trends in Mobile Radio Communications and Optical Wireless Communication and the possibility of using OWC for 5G network and beyond.	The results shows that the possibility of using OWC is limited
6	(Alsharif <i>et al.</i> , 2020)	Sixth Generation (6G) Wireless Networks: Vision, Research Activities, Challenges and Potential Solutions		
7	(Zakrzewski & Łaga, 2020)	Potential use of fiber-optic and Li-Fi systems in private 5G/6G networks dedicated to the industrial IoT	Reviews the potential of using fiber-optic and Li-Fi system for private 5G/6G Networks dedicated to the industrial IoT.	The results of the review suggested that the combination. of private and public network resources will significantly increase the potential of IoT solutions, as this will enable the

				<p>Combination of production, analytical and logistics processes. Also, that fast decision-making systems, efficient transmission of Massive data can be realized by fiber-optic networks.</p> <p>The result also, proposes the Li-fi interface for tunneling of optical fiber path for digitized radio signal in the baseband.</p>
8	(Wang <i>et al.</i> , 2020)	Wireless Channel Measurements and Models: Trends and Challenges	Presented the vision of the application scenarios, performance metrics, and potential key technologies of 6G wireless communication networks. And then conducted a comprehensive review of 6G wireless channel based on their measurements, characteristics, and models for all frequency bands and all scenarios, with special attention on millimeter-wave (mm-wave), terahertz, and optical wireless communication channels	

Table 4. Summary of Related Reviewed OWC Systems (LOS / Diffused Spots Links)

<i>Reference(s)</i>	<i>Improvements</i>	<i>Limitations</i>	<i>Link/Techniques</i>	<i>Comments</i>
(Zhang <i>et al.</i> , 2020)	channel quality is increased by 0.32% and 6.08%	the advantages are not very prominent	NLoS/ Q parameter	No delay spread.
(Tivig & Borcoci, 2020)	secured network	Only bandwidth 75MHz was considered	ETSI and 3GPP functional architectures for slicing support Genetic algorithm for controlling the optical wireless channel	Low Speed & high latency
(Wang <i>et al.</i> , 2021)	Simultaneous wireless communication with 4-PAM format and positioning achieved.	No Mobility	LOS Link/ Filter enhance RSS indoor OWC	2.5Gb/s achieved
(Eltokhey <i>et al.</i> , 2019)	Bit Rate: 50 Mbps Bandwidth: 70MHz (Average SNR, & Average Delay Spread respectively) Scenario 1: 17.9881dB 1.0270×10 ⁻⁹ s Scenario 2: 19.4327dB 0.9528×10 ⁻⁹ s.	The authors developed optimization based on the impulse response, not, considering that the eye safety regulations must be considered. in real practical systems. Need improvement in bit rate.	Diffuse NLOS/ PSO Algorithm.	Shows up to 42% and 23% improvement achieved in the average delay spread and the average SNR, respectively. Also shown was the improvement in the standard deviation of SNR by up to 65% in the presence of the noises & losses.
(Alsulami <i>et al.</i> , 2020)	The Image Receiver (ImR) provides better results compared to the ADR in terms of the supported data	Increases system complexity, there is an effect of shadowing.	LOS Link/ using RYGB LDs as a transmitter. The proposed data Centre contains 30 racks that are divided into three rows.	A data rate of 8.5 Gbps can be achieved for downlink comm. by using the ImR, while the ADR provides varied data rates between 1.5Gbps and 7 Gbps.
(Aljohani <i>et al.</i> , 2020)	The use of ADR has improved Data Rate by an average of 35%	To provide an efficient and low complexity power allocation approach, robust Optimization Techniques would be required	NLOS/NOMA (non-orthogonal multiple access (NOMA) visible light communication (VLC) system is investigated)	The outcome shows that ADRs improve the data rate by an average of 35% compared to a system using wide FOV receivers.

5. OPEN AREAS OF RESEARCH AND IMPORTANT CHALLENGING ISSUES IN OWC-BASED 5G, 6G, AND IoT REMEDIES

There are threatening issues that must be adequately addressed to use the optical wireless communication systems for unfolding 5G, 6G, and IoT. Some threatening problems are concisely discussed below:

Frequent Handover: Wireless communication systems in the future as pointed out earlier will comprise of heterogeneous small restricted networks that will cause a very frequent changing of cells by UEs (handovers). The frequent changing from one cell to the other (handover) will be between optical and RF networks and also between optical networks. Due to the very small size of optical cells, they may trigger many unnecessary handovers. Therefore, unnecessary handover and the ping-pong effect avoidance are also important issues.

The inter-cell optical interference: This is an open research issue often caused by the properties of the data-link layer and physical layer differ in the optical and RF-based wireless networks, thereby bringing about a huge setback for the mobility support in RF/optical hybrid systems. Inter-cell interference: Managing inter-cell optical interference is a serious issue in the deployment of optical VLC and LiFi networks. The restricted use of LEDs for the OWC technologies may create high interference in the 5G/6G and IoT networks. Inter-cell interference of optical hybrid system is a threatening problem.

Natural Atmospheric loss: This includes scattering, air absorption, free space loss, refraction, and scintillation of the weather conditions all affect the performance of the OWC technologies. In the open space environment, dust and fog affect the light

signal from the transmitter (LED or LD) to the receiver (Light Detector).

The communication channel nature in the FSO is greatly affected (free space loss) because of bad weather conditions. The mitigation techniques for weather condition losses in OWC systems are threatening the use of the technologies concerning reaching the goal of the 5GB networks, especially in the outdoor conditions.

Inadequate Uplink Communication using OWC technologies: The user equipment is modeled with a low-power LED to suppress the excessive use of power. Due to the low-power LEDs, most optical systems example; visible light communication and Light Fidelity cannot perform well in uplink communication. Most of the user equipment employed LEDs that produce diffused lights with low power that are easily affected by downlink high-power lights. It, therefore, limit uplink communication. In addition, a little deflection or movement of the receiver of a mobile device can easily affect the uplink communication link. Hence, this is an important problem to be solved in the nearest future to efficiently support uplink communication using optical wireless communication systems (VLC and LiFi).

The Low Data Rate: OCC system and the Visible light Uplinks have very low data rate that require improvement according to Chowdhury, (2019), low data rate is a great setback of the existing OCC system, to provide a high data rate is a highly challenging issue due to its low-frame rate and medium of cameras communication. In this reviewed paper, the most recent data rate obtained in the OCC system is only 55 Mbps (Arai *et al.*, 2021; Saeed *et al.*, 2019). There is need to increase the speed of downloads to fulfill the demands of service quality in the 5G/6G and IoT networks.

Eye and skin safety regulation: Light energy due to the fluctuations in the brightness of a light can be noticed by humans. This is an important issue in the OWC systems as it

affects performance. Different modulation schemes on the OWC systems may cause flickering that harms human health. The modulation of LEDs should be done in such a manner that flickering is avoided, this is a challenging issue.

Data rate improvement of the FSO backhaul system: The backhaul systems in the 5G/6G systems have to handle an enormous volume of data traffic to support high-data-rate services at the user level; otherwise, a bottleneck problem will arise. Hence, increasing the FSO backhaul capacity considering the growth of traffic volume is a challenging task according to Lee *et al.*, (2019).

Machine Learning for OWC: Learning-based networking system will be the key requirement in future 6G communication networks. The ever-increasing complex network structure and requirements demand artificial controlling and decision-making in challenging environments. Integrating machine learning in 6G OWC networks enables intelligent network assignment, auto error correction, efficient decision making, and network re-assignment, among others. Moreover, the machine learning approach is a core demand in indoor mobile wireless communication systems, robot-based dense OWC (i.e small owc or hybrid OWC/RF networks) to perform fast and efficient tasks (Soldani, 2021).

5.1 The threats of OWC: the recent development of OWC devices and the strategies for performance enhancement and indoor applications have been discussed in previous sections section 5.1 talked on solutions to the challenging issues earlier mentioned.

In order to achieve the ubiquitous usage of high-performance metrics (High data rate and low latency of OWC systems) for an indoor environment, this is discuss in sub-section 5.1.

5.1.1 Monolithic and solid-state structural arrays of organic semiconductors: This makes the devices flexible with energy-saving low-temperature processes, fabricated from organic thin-film materials known as Organic semiconductors. Since spectrally tunable laser sources can implement the Color Shift Keying (CSK) efficiently, so also an adaptive wavelength allocation can improve the spectral efficiency of the OWC system, therefore, implementation of tunable laser sources in the OWC system should be studied, so that the corresponding limitations should be rectified.

5.1.2 The uplink establishment on the battery-driven user devices: A demodulation of the downlink beams can be used to resolve this threat. To achieve a Gbps data rate, an enhanced modulation scheme must be utilized. Furthermore, the fully networked link installation will enable the green OWC system as an important improvement to future intelligent internet applications.

5.1.3 Safety of Both Eye and Skin: This is a prerequisite requirement and should always be considered while striving to achieve high-performance metrics in OW communication.

5.1.4 Three Security Levels Out of Eight Security Levels: Defined by Lai (2020) denote complete security, namely, encryption and Message Integrity Code (MIC), coupled with this, the non-encrypted MAC header fields may heighten the danger of confidentiality and integrity. Hence the technology made encryption and integrity optional, a sufficient MAC level protection against danger on the physical level must be included in practical applications.

6. CONCLUSION:

The novel 5G communication technologies were launched by 2020 and commercially available in a few cities of the U.S.A, Europe, some Asia countries, and South Africa. The 5G network usage was approved for use in Nigeria by FGN in 2021. The

shortcomings of the 5G network such as high interference, existing tower mm-wave of 5G inform the development of a 6G communication network which is expected to be launched in between 2027 and 2030. The advantages of 5G/6G and IoT are challenged by tactile internet. The most important and most challenging issues are the provision of high capacity, massive connectivity, low latency, high security, low-energy consumption, high QoE, and highly reliable connectivity for 5GB communication systems. Only RF-based systems are unable to meet the high demands of future 5G/6G and IoT networks. OWC technologies are the best complimentary solution for RF networks. The coexistence of RF and optical wireless systems can achieve the goals of such networks. This review has presented a detailed observation of how OWC technologies will provide an effective solution for the successful deployment of future 5G/6G and IoT networks. The characteristics of 5G, 6G, and IoT systems and features of OWC technologies were presented alongside their specifications. Therefore, this review presented the understanding of the research contributions in different optical wireless systems for future networks.

REFERENCES

- Abdelrahman, Shereen Eltayib. (2019). Enhancing of SNR and Optical Power Distribution in Indoor Visible Light Communications Systems. *Journal of Telecommunication, Electronic and Computer Engineering (JTEC)*, 11(3), 23-26.
- Akhtar, Muhammad Waseem, Hassan, Syed Ali, Ghaffar, Rizwan, Jung, Haejoon, Garg, Sahil, & Hossain, M Shamim. (2020). The shift to 6G communications: vision and requirements. *Human-centric Computing and Information Sciences*, 10(1), 1-27.
- Al Ridhawi, Ismaeel, Otoum, Safa, Aloqaily, Moayad, & Boukerche, Azzedine. (2020). Generalizing AI: challenges and opportunities for plug and play AI solutions. *IEEE Network*, 35(1), 372-379.
- Aljohani, Mansourah K, Alsulami, Osama Zwaïd, Alazwary, Khulood D, Musa, Mohamed OI, El-Gorashi, Taisir EH, Alresheedi, Mohammed T, & Elmirghani, Jaafar MH. (2020). *NOMA visible light communication system with angle diversity receivers*. Paper presented at the 2020 22nd International Conference on Transparent Optical Networks (ICTON).
- Alsharif, Mohammed H, Kelechi, Anabi Hilary, Albream, Mahmoud A, Chaudhry, Shehzad Ashraf, Zia, M Sultan, & Kim, Sunghwan. (2020). Sixth generation (6G) wireless networks: Vision, research activities, challenges and potential solutions. *Symmetry*, 12(4), 676.
- Alsulami, Osama, Hussein, Ahmed Taha, Alresheedi, Mohammed T, & Elmirghani, Jaafar MH. (2018). Optical wireless communication systems, a survey. *arXiv preprint arXiv:1812.11544*.
- Alsulami, Osama Zwaïd, Saeed, Sarah OM, Mohamed, Sanaa Hamid, El-Gorashi, Taisir EH, Alresheedi, Mohammed T, & Elmirghani, Jaafar MH. (2020). *Data centre optical wireless downlink with WDM and multi-access point support*. Paper presented at the 2020 22nd International Conference on Transparent Optical Networks (ICTON).
- Amine Arfaoui, Mohamed, Dehghani Soltani, Mohammad, Tavakkolnia, Iman, Ghrayeb, Ali, Assi, Chadi, Safari, Majid, & Haas, Harald. (2020). Measurements-Based Channel Models for Indoor LiFi Systems. *arXiv e-prints*, arXiv: 2001.09596.

- Arai, Shintaro, Kinoshita, Masayuki, & Yamazato, Takaya. (2021). Optical wireless communication: A candidate 6G technology? *IEICE Transactions on Fundamentals of Electronics, Communications and Computer Sciences*, 104(1), 227-234.
- Ashraf, Shehzad Ali, Blasco, Ricardo, Do, Hieu, Fodor, Gabor, Zhang, Congchi, & Sun, Wanlu. (2020). Supporting vehicle-to-everything services by 5G new radio release-16 systems. *IEEE Communications Standards Magazine*, 4(1), 26-32.
- Borcoci, Eugen, Vochin, Marius, & Obreja, Serban Georgica. On Business Models for Vehicle-to-Everything Systems Based on 5G Slicing.
- Borcoci, Eugen, Vochin, Marius, & Obreja, Serban Georgica. On Systematic Identification of Requirements for Vehicle-to-Everything 5G Slices.
- Celik, Abdulkadir, Saeed, Nasir, Shihada, Basem, Al-Naffouri, Tareq Y, & Alouini, Mohamed-Slim. (2019). End-to-end performance analysis of underwater optical wireless relaying and routing techniques under location uncertainty. *IEEE Transactions on Wireless Communications*, 19(2), 1167-1181.
- Chow, Chi-Wai, Yeh, Chien-Hung, Liu, Yang, Lai, Yinchieh, Wei, Liang-Yu, Hsu, Chin-Wei, . . . Lin, Kun-Hsien. (2020). *Enabling techniques for optical wireless communication systems*. Paper presented at the Optical Fiber Communication Conference.
- Chowdhury, Mostafa Zaman, Hasan, Moh Khalid, Shahjalal, Md, Hossan, Md Tanvir, & Jang, Yeong Min. (2020). Optical wireless hybrid networks: Trends, opportunities, challenges, and research directions. *IEEE Communications Surveys & Tutorials*, 22(2), 930-966.
- Chowdhury, Mostafa Zaman, Hossan, Md Tanvir, Islam, Amirul, & Jang, Yeong Min. (2018). A comparative survey of optical wireless technologies: Architectures and applications. *IEEE Access*, 6, 9819-9840.
- Chowdhury, Mostafa Zaman, Shahjalal, Md, Hasan, Moh, & Jang, Yeong Min. (2019). The role of optical wireless communication technologies in 5G/6G and IoT solutions: Prospects, directions, and challenges. *Applied Sciences*, 9(20), 4367.
- Coelho, Leandro dos S, Mariani, Viviana C, Goudos, Sotirios K, Boursianis, Achilles D, Kokkinidis, Konstantinos, & Kantartzis, Nikolaos V. (2021). *Chaotic Jaya approaches to solving electromagnetic optimization benchmark problems*. Paper presented at the Telecom.
- Dehghani Soltani, Mohammad. (2019). Analysis of random orientation and user mobility in LiFi networks.
- Eid, Mahmoud MA, Seliem, Ashraf S, Rashed, AN Zaki, Mohammed, Abd El-Naser A, Ali, M Yassin, & Abaza, Shaimaa S. (2021). High modulated soliton power propagation interaction with optical fiber and optical wireless communication channels. *Indones J Electr Eng Comput Sci*, 21, 1575-1583.
- Eltokhey, Mahmoud W, Mahmoud, Korany R, Ghassemlooy, Zabih, & Obayya, Salah SA. (2019). Optimization of intensities and locations of diffuse spots in indoor optical wireless communications. *Optical Switching and Networking*, 33, 177-183.
- Gautam, S., Solanki, S., Sharma, S. K., Chatzinotas, S., & Ottersten, B. (2021). <sensors-21-06013-v2 (1).pdf>. *Sensors (Basel)*, 21(18). doi: 10.3390/s21186013
- Gautam, Sumit, Solanki, Sourabh, Sharma, Shree Krishna, Chatzinotas, Symeon, & Ottersten, Björn. (2021). Hybrid

- Active-and-Passive Relaying Model for 6G-IoT Greencom Networks with SWIPT. *Sensors*, 21(18), 6013.
- Ghassemlooy, Zabih, Alves, Luis Nero, Zvanovec, Stanislav, & Khalighi, Mohammad-Ali. (2017). *Visible light communications: theory and applications*: CRC press.
- Gohar, Ali, & Nencioni, Gianfranco. (2021). The Role of 5G Technologies in a Smart City: The Case for Intelligent Transportation System. *Sustainability*, 13(9), 5188.
- Haas, Harald. (2011). Wireless data from every light bulb.
- Haas, Harald, Elmirghani, Jaafar, & White, Ian. (2020). Optical wireless communication: The Royal Society Publishing.
- Hakeem, Shima A Abdel, Hady, Anar A, & Kim, HyungWon. (2020). Current and future developments to improve 5G-NewRadio performance in vehicle-to-everything communications. *Telecommunication Systems*, 75(3), 331-353.
- Huang, Yu-Fang, Chi, Yu-Chieh, Chen, Mu-Ku, Tsai, Din-Ping, Huang, Ding-Wei, & Lin, Gong-Ru. (2018). Red/green/blue LD mixed white-light communication at 6500K with divergent diffuser optimization. *Optics express*, 26(18), 23397-23410.
- Jatau, Melchi, David, Michael, & Zubair, Suleiman. (2020). *LiFi: The Solution to Radio Frequency Saturation*. Paper presented at the 2020 International Conference in Mathematics, Computer Engineering and Computer Science (ICMCECS).
- Jenila, C, & Jeyachitra, RK. (2021). Green indoor optical wireless communication systems: Pathway towards pervasive deployment. *Digital Communications and Networks*, 7(3), 410-444.
- Ji, Baofeng, Wang, Yanan, Song, Kang, Li, Chunguo, Wen, Hong, Menon, Varun G, & Mumtaz, Shahid. (2021). A survey of computational intelligence for 6G: Key technologies, applications and trends. *IEEE Transactions on Industrial Informatics*.
- Katz, Marcos, & Ahmed, Iqrar. (2020). *Opportunities and challenges for visible light communications in 6G*. Paper presented at the 2020 2nd 6G wireless summit (6G SUMMIT).
- Khalid, Waqas, Yu, Heejung, Ali, Rashid, & Ullah, Rehmat. (2021). Advanced Physical-Layer Technologies for Beyond 5G Wireless Communication Networks: Multidisciplinary Digital Publishing Institute.
- Kousaridas, Apostolos, Fallgren, Mikael, Fischer, Edwin, Moscatelli, Francesca, Vilalta, Ricard, Mühleisen, Maciej, . . . Tossou, Bruno. (2021). 5G Vehicle-to-Everything Services in Cross-Border Environments: Standardization and Challenges. *IEEE Communications Standards Magazine*, 5(1), 22-30.
- Lai, Chengzhe, Lu, Rongxing, Zheng, Dong, & Shen, Xuemin. (2020). Security and privacy challenges in 5G-enabled vehicular networks. *IEEE Network*, 34(2), 37-45.
- Lee, In-Ho, Kim, Jung-Bin, Jung, Haejoon, Kwon, Seok-Chul Sean, & Kurniawan, Ernest. (2019). Advanced Wireless Technology for Ultrahigh Data Rate Communication: Hindawi.
- Letaief, Khaled B, Chen, Wei, Shi, Yuanming, Zhang, Jun, & Zhang, Ying-Jun Angela. (2019). The roadmap to 6G: AI empowered wireless networks. *IEEE Communications Magazine*, 57(8), 84-90.
- Liu, Baojing, Han, Chenye, Liu, Xinxin, & Li, Wei. (2021). Vehicle Artificial Intelligence System Based on Intelligent Image Analysis and 5G

- Network. *International Journal of Wireless Information Networks*, 1-17.
- Liu, Qingling, Sarfraz, Shahid, & Wang, Shubin. (2020). *An Overview of Key Technologies and Challenges of 6G*. Paper presented at the International Conference on Machine Learning for Cyber Security.
- Masroor, Komal, Jeoti, Varun, Driberg, Micheal, Cheab, Sovuthy, & Rajbhandari, Sujun. (2021). A Heuristic Approach for Optical Transceiver Placement to Optimize SNR and Illuminance Uniformities of an Optical Body Area Network. *Sensors*, 21(9), 2943.
- Menaka, D, Gauni, Sabitha, Manimegalai, CT, & Kalimuthu, K. (2021). Vision of IoUT: advances and future trends in optical wireless communication. *Journal of Optics*, 1-14.
- Mizmizi, Marouan, Brambilla, Mattia, Tagliaferri, Dario, Mazzucco, Christian, Debbah, Merouane, Mach, Tomasz, . . . Lombardi, Renato. (2021). 6G V2X Technologies and Orchestrated Sensing for Autonomous Driving. *arXiv preprint arXiv:2106.16146*.
- Molinaro, Antonella, Campolo, Claudia, Härri, Jérôme, Esteve Rothenberg, Christian, & Vinel, Alexey. (2020). 5g-v2x communications and networking for connected and autonomous vehicles: Multidisciplinary Digital Publishing Institute.
- Pathak, Parth H, Feng, Xiaotao, Hu, Pengfei, & Mohapatra, Prasant. (2015). Visible light communication, networking, and sensing: A survey, potential and challenges. *IEEE communications surveys & tutorials*, 17(4), 2047-2077.
- Rahman, MT, Bakaul, Masuduzzaman, & Parthiban, Rajendran. (2018). *Analysis of the effects of multiple reflection paths on high speed VLC system performance*. Paper presented at the 2018 28th International Telecommunication Networks and Applications Conference (ITNAC).
- Rahman, Talha, Rafique, Danish, Spinnler, Bernhard, Napoli, Antonio, Bohn, Marc, Koonen, AMJ, . . . De Waardt, Huug. (2016). *Digital subcarrier multiplexed hybrid QAM for data-rate flexibility and ROADM filtering tolerance*. Paper presented at the Optical Fiber Communication Conference.
- Saeed, Nasir, Guo, Shuaishuai, Park, Ki-Hong, Al-Naffouri, Tareq Y, & Alouini, Mohamed-Slim. (2019). Optical camera communications: Survey, use cases, challenges, and future trends. *Physical Communication*, 37, 100900.
- Silva, Mário Marques da, & Guerreiro, João. (2020). On the 5G and Beyond. *Applied Sciences*, 10(20), 7091.
- Soldani, David. (2021). 6G Fundamentals: Vision and Enabling Technologies. *Journal of Telecommunications and the Digital Economy*, 9(3), 58-86.
- Storck, Carlos Renato, & Duarte-Figueiredo, Fátima. (2020). A survey of 5G technology evolution, standards, and infrastructure associated with vehicle-to-everything communications by internet of vehicles. *IEEE Access*, 8, 117593-117614.
- Tariq, Faisal, Khandaker, Muhammad RA, Wong, Kai-Kit, Imran, Muhammad A, Bennis, Mehdi, & Debbah, Merouane. (2020). A speculative study on 6G. *IEEE Wireless Communications*, 27(4), 118-125.
- Tivig, Pantelimon-Teodor, & Borcoci, Eugen. (2020). *Critical Analysis of Multi-Controller Placement Problem in Large SDN Networks*. Paper presented at the 2020 13th International Conference on Communications (COMM).

- Tomkos, Ioannis, Klonidis, Dimitrios, Pikasis, Evangelos, & Theodoridis, Sergios. (2020). Toward the 6G network era: Opportunities and challenges. *IT Professional*, 22(1), 34-38.
- Turner, Jamie SC, Ramli, Mohd Fitri, Kamarudin, LM, Zakaria, Ammar, Shakaff, Ali Yeon Md, Ndzi, David Lorater, . . . Mamduh, Syed M. (2013). *The study of human movement effect on Signal Strength for indoor WSN deployment*. Paper presented at the 2013 IEEE Conference on Wireless Sensor (ICWISE).
- Wang, Cheng-Xiang, Huang, Jie, Wang, Haiming, Gao, Xiqi, You, Xiaohu, & Hao, Yang. (2020). 6G wireless channel measurements and models: Trends and challenges. *IEEE Vehicular Technology Magazine*, 15(4), 22-32.
- Wang, Ke, Song, Tingting, Kandeepan, Sithamparanathan, Li, Hongtao, & Alameh, Kamal. (2021). Indoor optical wireless communication system with continuous and simultaneous positioning. *Optics Express*, 29(3), 4582-4595.
- Wang, Zhaocheng, Wang, Qi, Huang, Wei, & Xu, Zhengyuan. (2017). *Visible light communications: modulation and signal processing*: John Wiley & Sons.
- Wang, Zhaocheng, Wang, Qi, Huang, Wei, & Xu, Zhengyuan. (2018). Multicolor Modulation.
- Wei, Zixian, Zhang, Shi, Mao, Simei, Wang, Lei, Zhang, Li, Chen, Chien-Ju, . . . Luo, Yi. (2021). Full-duplex high-speed indoor optical wireless communication system based on a micro-LED and VCSEL array. *Optics Express*, 29(3), 3891-3903.
- Zadobrischi, Eduard, Cosovanu, Lucian-Mihai, Avătămăniței, Sebastian-Andrei, & Căilean, Alin-Mihai. (2019). *Complementary radiofrequency and visible light systems for indoor and vehicular communications*. Paper presented at the 2019 23rd International Conference on System Theory, Control and Computing (ICSTCC).
- Zakrzewski, Zbigniew, & Łaga, Bogdan. (2020). *Potential use of fiber-optic and Li-Fi systems in private 5G/6G networks dedicated to the industrial IoT*. Paper presented at the Optical Fibers and Their Applications 2020.
- Zhang, Lei, Zhao, Guodong, & Imran, Muhammad Ali. (2020). *Internet of Things and Sensors Networks in 5G Wireless Communications*: MDPI.
- Zhang, Xiangyang, Zhao, Nan, Al-Turjman, Fadi, Khan, Muhammad Bilal, & Yang, Xiaodong. (2020). An Optimization of the Signal-to-Noise Ratio Distribution of an Indoor Visible Light Communication System Based on the Conventional Layout Model. *Sustainability*, 12(21), 9006.
- Zhou, Yuan, Kim, Minseok, Momose, Hideaki, & Yasukawa, Satoru. (2021). *Device-Free Indoor Location Estimation System Using Commodity Wireless LANs*. Paper presented at the Telecom.

COMPARATIVE STUDY OF TAMARINDUS INDICA AND ADANSONIA DIGITATA AS COAGULANTS AND DISINFECTANTS FOR WATER TREATMENT

*Uthman, H.

Chemical Engineering Department, Federal University of Technology, Minna, Nigeria
E-mail: (habibuuthman@futminna.edu.ng)

Abstract

Water is an indispensable resource for humans. The coagulant and disinfectant qualities of Tamarind (*Tamarindus indica*) and Baobab (*Adansonia digitata*) were investigated on various water samples obtained from Kubeba Village well, Abuja, Nigeria and Usuma dam, Abuja, Nigeria. Seeds extract of Tamarind and Baobab were used. Water samples were treated with the extract and the treatment time was varied for 2 hours and 20 hours. From the results obtained, it was found out that the turbidity of the Kubeba water sample increased from 3.15 to 9.24 Nephelometric Turbidity Unit (NTU) indicating 60% increment in the turbidity. While that of the Usuma dam water reduced from 20.7 to 16.01 NTU indicating a decrement by 22.7%. Also, as the treatment time increases, the number of total Coliforms and *Escherichia coli* reduced but not to the limit set by the Nigeria Standard Drinking Water Quality (NSDWQ) for total Coliforms count. The combination of *Tamarindus indica* and *Adansonia digitata* did not bring the physico-chemical and bacteriological parameters to the required set limit or standard of both World Health Organization (WHO) and NSDWQ. Hence, the treated water using *Tamarindus indica*, *Adansonia digitata* and their mixture (*Tamarindus indica* and *Adansonia digitata*) is considered suitable for drinking.

Keywords: *Tamarindus indica*, *Adansonia digitata*, water treatment, coagulation, disinfection, turbidity.

INTRODUCTION

Water is necessary for the sustenance of life; its consumption by humans is a vital ingredient for their welfare and a healthy life. It is a very necessary, irreplaceable and indispensable requirement for man's survival (Ighalo and Adeniyi, 2020; Adeniyi and Oni, 2016). Furthermore, water is important for human, plant, animal and other living things. It is vital to life and development all over the globe. Moreover, water supply in adequate terms of both quality and quantity is very essential to human (Uthman and Nyakuma, 2018; Mao *et al.*, 2014). Water is necessary for the sustenance of life. Availability of water in potable form is drastically reducing due to pollution (Raju *et al.*, 2018). Water pollution from municipal, industrial and medical waste is a cause of the outbreak of diseases in Nigeria (Ighalo and Adeniyi, 2020; Ugwu *et al.*, 2017; Adeniyi and Oni, 2016; Nansubuga *et al.*, 2013).

Water in its natural form is not chemically pure. Water quality is poor in developing countries like Nigeria and when being polluted is a vector of diseases like typhoid, yellow fever, diarrhea and the host of other water borne diseases (Ali *et al.*, 2020; Raju *et al.*, 2018; Uthman and Nyakuma, 2018). Water quality standard around the world depend on the country's choice. According to Rajagopal (2016), World Health Organization (WHO) guidelines and drinking water standard are used in China and in some African countries, European Union drinking water standard (EU) is used in Europe, in the United States of America the drinking water standard are set by the safe drinking Water Act (US EPA 2002). In Nigeria, the Nigeria Standard for Drinking Water Quality (NSDWQ) is set by Nigeria Industrial standard (NIS) and Federal Environmental Protection Agency (FEPA).

Turbidity removal is essential in potable water production (Arukia *et al.*, 2022; Tsie

et al., 2020; Uthman and Nyakuma, 2018; Mao *et al.*, 2014). Coagulation is a well-known process used for the removal of different organic substances from water for human consumption (Tsie *et al.*, 2020; Uthman and Nyakuma, 2018; Ugwu *et al.*, 2017). The use of natural coagulant in water purification is attracting a growing interest due to their advantages over chemical coagulants, such as low toxicity, low cost and elimination of the toxic risk to the human being. Aluminum sulphides intake affects the liver, heart and brain and is related to Alzheimer's degeneration (Buenaño *et al.*, 2019). Also its utilization reduces pH of water; this affects the natural alkalinity, reduces coagulation efficiency and deposition of sludge during water purification (Uthman and Nyakuma, 2018; Choy *et al.*, 2015; Sahu and Chaudhari, 2013). Natural coagulants have various categories ranging from starch container plants, legumes, Moringa oleifera, Baobab seed and Tamarind seeds (Amran *et al.*, 2018; Uthman and Nyakuma, 2018; Choy *et al.*, 2015; Khandelwal *et al.*, 2021).

Chlorine is the most commonly used disinfectant in water treatment. However, it causes disinfection by-products and researches have shown that it can result in the formation of trihalomethane (THM's) and other Halogen hydrocarbon which are cancerous, non-eco-friendly and non-biodegradable (Raju *et al.*, 2018; Edogbanya *et al.*, 2016; Idris, 2014). Baobab (*Adansonia digitata* L) is a fruit producing tree that is widespread all over Tropical Africa and is prevalent throughout the northern part of South Africa (Chisoro *et al.*, 2017; Razafimamonjison *et al.*, 2017; Aluko *et al.*, 2016; Edogbanya *et al.*, 2016; Kamatou *et al.*, 2011).



Fig. 1: Baobab (a) tree and (b) fruit (Source: Rajul *et al.*, 2018; Rahul *et al.*, 2015)

Tamarind is a monotypic genus with botanical name '*Tamarindus indica*' and belongs to Leguminosae (fabaceae) family and Caesalpinoideae sub-family. It is a multipurpose tropical fruit tree. It grows in the savanna regions of Nigeria. It has anti-viral properties and it possesses fungicidal and bactericidal activity agents against *Aspergillus Niger*, *Escherichia Coli*, *Bacillus subtilis* and other harmful microbes (Arukia *et al.*, 2022; Bello *et al.*, 2022; Raju *et al.*, 2018; Razafimamonjison *et al.*, 2017; Rabikul-Islam *et al.*, 2017; Aluko *et al.*, 2016; Rahul *et al.*, 2015; Abiodun and Ogugua, 2013).



Fig. 2: Tamarind Seed (Source: Rajul *et al.*, 2018; Rahul *et al.*, 2015)

This research work is primarily aimed at investigating water treatment and its quality

using Baobab (*Adansonia digitata*) seed and Tamarind (*Tamarindus indica*) seed.

METHODOLOGY

2.1. Collection of Materials

Two samples of water were collected on the same day within 8:00–9:00am to ensure the parameters of interest of the water is not altered according to methods and procedures reported by (Uthman and Nyakuma, 2018). The containers for samples were first washed and emptied and rinsed with specific water sample to be collected. Samples were obtained from lower Usuma dam Abuja, Nigeria and well water in Kubuwa, Abuja, Nigeria.

2.2 Preparation of *Adansonia Digitata* Coagulant

Dried fruits of *Adansonia digitata* (Baobab) seeds (Fig. 1) were collected from local market in Minna, Nigeria as fresh fruits do not possess any coagulation activity (Uthman and Nyakuma, 2018). The fruits were opened and seeds were removed, washed with distilled water and oven dried at 105°C for thirty minutes. They were pulverized using mortar and pestle and then sieved with a sieve of about 1mm size. The residue cake after the extraction of oil and drying was used to prepare 100 mg/L concentration of coagulant reagent, by suspending 30 g of powdered seed in 1 Litre of distilled water which was then stirred for 15 minutes using a magnetic stirrer in order to extract the active components. The suspension was then filtered using a whatman filter paper number 1 to obtain the coagulant solution for the water treatment in accordance with the methods and procedures reported by Edogbanya *et al.* (2016).

2.3 Preparation of *Tamarindus indica* Coagulant

High qualities of dried Tamarind fruits were selected from the pulp purchase from the local market in Minna, Nigeria. The seeds (Fig. 2) were collected, sun-dried for five

days and oven dried at a 105°C for 30 minutes. Then it was ground to powder with a mortar and pestle but to obtain water soluble size of seeds with active ingredients, it was further reduced using a blender. The seed extract was prepared by adding 10 g to 1 liter of tap water.

2.4 Characterization of *Tamarindus Indica* Coagulant

The following equipment was used for analysis and characterization of *Tamarindus indica*: volumetric flask, pipette, tall test tube, turbidimeter, water bath, Spectrophotometer (LABATEC, L-10), conical flask, burette, conductivity meter, thermometer incubator (Meanert, Germany) and pH meter (HACH Senso 3).

2.5 Measurement of Physicochemical parameters

Measurement of pH

The pH of the water samples was measured, i.e., both the sample water and treated water using Electric pH meter (HACH Senso 3).

Measurement of Turbidity

The turbidity of sample(s) was determined using a turbidity meter. Each sample was poured in to the turbidity meter and readings were taken after it stabilized.

Measurement of Temperature

Temperatures of the samples were taken before and after treatment using a thermometer.

Electrical Conductivity (EC)

Thirty cm³ of sample was transferred to a rinsed beaker and cleaned electrode of the conductivity meter was used to measure the electrical conductivity of samples.

Alkalinity

This is the measure of the content of hydroxide and carbonate in water. It was determined by titrating samples with standard hydrochloric acid (HCl) as an indicator.

Total Dissolved Solid (TDS)

Thirty cm³ of sample was transferred to a rinsed beaker and cleaned electrode was inserted in the beaker. The total dissolved solid value was taken from the Jenway 4510 conductivity meter.

2.6 Disinfection Studies

Preparation of *Escherichia coli* Culture

Thirteen grams of Nutrient broth was dissolved in 1000 cm³ of distilled water by heating. This mixture was sterilized for 15 minutes in an autoclave at temperature of 130°C, then cooled and used to prepare *Escherichia coli* culture. The culture was standardized to 1:5000 using normal saline and used to the disinfection experiment.

Disinfection Experiment

One hundred and fifty mg/l of the extract was added to different tubes containing 10 cm³ of *Escherichia coli* suspension and incubated without agitation for 24 hours. Cell survives was assessed by making dilution series of bacteria suspension on Muller Hinton agar dishes and incubated for 24 hours at 37°C.

Triplicates were made for both assay and colonies were counted dishes and the cell survival ratio was estimated by comparing it to a control sample (no added extract). The bio-coagulation and disinfection studies were performed in lower Usama dam water treatment plant laboratory in Bwari, Abuja, Nigeria. Fig. 3 presents the preparation of coagulant from *Tamarindus indica* and *Adansonia digitata* and application to water treatment.

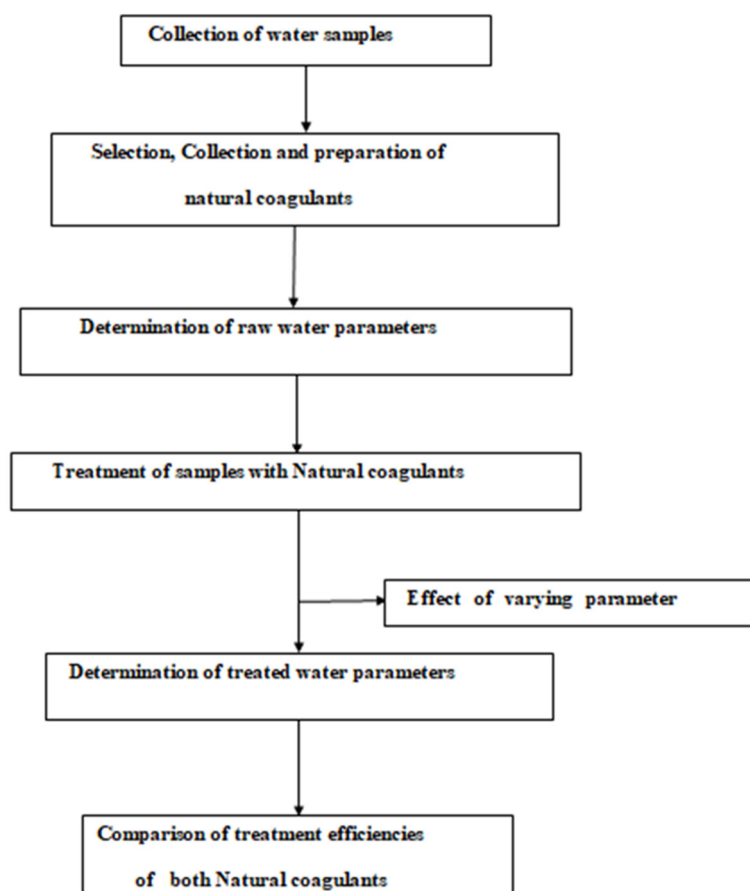


Fig. 3: Preparation of coagulant from *Tamarindus indica* and *Adansonia digitata* and application to water treatment (Rajul *et al.*, 2018).

RESULTS AND DISCUSSION

The effectiveness of *Tamarindus indica* and *Adansonia digitata* as coagulants and disinfectants for water was examined as

presented in Tables 1–5. The results of the analysis of raw water samples collected from two different sources are presented in Table 1.

Table 1: Results obtained from the analysis of raw water samples

Parameter	Kubwa village well water	Usuma Dam Water
Appearance	Clear	Less Cloudy
Turbidity, NTU	3.15	20.7
Conductivity, $\mu\text{s}/\text{cm}$	70	170
pH	7.03	7.02
Temperature, K	302	302
Dissolved oxygen, mg/l	5.00	3.00
Total dissolved substances, mg/l	35	110
Alkalinity, mg/l	30	10
Colour	Colourless	Coloured
Total hardness, mg/l	130	30
Chloride, mg/l	70	10
Total <i>Coliform</i> , viable count/ml	19	85
<i>E. coli</i> , viable count/ml	7	5

The results from the two raw water sources indicated that only the turbidity of Kubwa village well water sample conform to the set limit of WHO, FEPA and NSDWQ which is equal to 5 NTU. This variation in turbidity can be attributed to difference in the water source and content.

The pH of samples is within the standard range of 6.5–8.5 set by FEPA and NSDWQ. Temperature of raw water did not conform to NSDWQ standard, since it was above the set limit. Other physico-chemical parameters investigated were total dissolved substance, Alkalinity, conductivity, colour and water appearance. The pH of samples range of 6.5–

8.5 obtained were in close agreement with values reported by Olanrewaju *et al.* (2018); Rajul *et al.* (2018); Uthman and Nyakuma (2018); Muhammad *et al.* (2016); Rahul *et al.* (2015); Idris (2014).

Both samples failed the total coliform test as set by the Nigeria industrial standard for drinking water, which indicated the present of bacteria or water contamination. This can be as a result of the exposure of the water to the atmosphere. After sample has been analyzed, the results obtained indicated that the water samples are not accepted for drinking according to World Health Organization Standard for potable water.

Treatment of Raw Water Samples with Coagulants

Results obtained from the treatment of water samples with 150 milligram per liter (mg/l) of coagulants at several time intervals are presented in Tables 2–5.

Table 2 presents the results obtained when samples were treated with *Tamarindus indica* for a treatment period of 2 hours. It was observed that the water samples turbidity did not meet the NSDWQ and WHO set limit of 5 NTU and <NTU respectively. The turbidity increased, confirming the theory that Bio-coagulants are not very effective in treating less turbid

water as reported by Uthman and Nyakuma, (2018).

There was also an increase in the faecal contamination of the samples. The pH of the samples: 7.03 for Kubwa well water, Abuja, Nigeria and 7.02 for Usuma dam water Abuja, Nigeria was within the acceptable range of Federal environment protection Agency. This indicates the advantage of bio-coagulants over synthetic as it has no decrease in the pH over set limit. These results agreed strongly with similar results reported by Olanrewaju *et al.* (2018); Rajul *et al.* (2018); Uthman and Nyakuma (2018); Muhammad *et al.* (2016); Rahul *et al.* (2015); Idris (2014).

Table 2: Results of Samples + *Tamarindus indica* 2 hours

Parameter	Kubuwa Village Well Water	Usuma Dam Water
Appearance	Less clear	Cloudy
Turbidity, NTU	10	25
pH	7.03	7.02
Temperature, K	305	300
Dissolved oxygen, mg/l	5.00	4.00
Total dissolved substances, mg/l	43	135
Total hardness, mg/l	150	40
Alkalinity, mg/L	45	18
Chloride, mg/l	120	175
Conductivity, μ s/cm	70	170
Colour	Colourless	Less Coloured
Total Coliform, viable count/ml	30	92
E. coli, viable count/ml	9	11

Table 3 present results obtained from the treatment of samples with *Tamarindus indica* and *Adansonia digitata* for two-hour treatment time. It was observed that the temperature and pH reduced. The water samples turbidity and other physiochemical parameter increased. The increase in electric conductivity of the sample is as a result of the total dissolved substance. The results show a little reduction in the E. coli present

in the treated samples, from 7 to 5 per ml and 5 to 4 per ml for the Kubuwa village well water and Usuma dam water respectively. This reduction in bacteria confirms the antimicrobial ability of *Adansonia* as bio-coagulants. These results compared favourably with similar results reported by Olanrewaju *et al.* (2018); Rajul *et al.* (2018); Uthman and Nyakuma (2018); Muhammad

et al. (2016); Rahul *et al.* (2015); Idris (2014).

Table 3: Results of Samples + *Tamarindus indica* and *Adansonia digitata* after 2 hours

Parameter	Kubwa Village Well Water	Usuma Dam Water
Appearance	Cloudy	Cloudy
Dissolved oxygen, mg/l	3.00	3.00
Colour	Colourless	Less Coloured
Turbidity, NTU	13	28
pH	7.01	7.02
Temperature, K	302	301
Total dissolved substances, mg/l	48	140
Total hardness, mg/l	170	60
Alkalinity, mg/l	48	20
Chloride, mg/l	110	125
Conductivity, $\mu\text{S}/\text{cm}$	82	180
Total <i>Coliform</i> , viable count/ml	33	80
<i>E. coli</i> , viable count/ml	5	4

Table 4 presents the results obtained from raw water samples treated with *Tamarindus* after twenty hours. It was observed that the temperature of the samples were within NSDWQ range. The pH of the Kubuwa well water reduced from 7.03 to 6.90 and from 7.02 to 7.00 for Kubuwa and Usuma water samples. The turbidity of Kubuwa water sample was reduced by 19% and that of Usuma dam water by 26%. The total dissolved solid and alkalinity of both samples reduced. Also, the total *Coliform*

count was reduced by 10 counts per ml while the *Escherichia coli* were reduced to 2 counts per ml. It can be inferred that the coagulation and disinfection effectiveness of *Tamarindus indica* for treatment over period of twenty hours gave a better efficiency. These results agree well with similar results reported by Olanrewaju *et al.* (2018); Rajul *et al.* (2018); Uthman and Nyakuma (2018); Muhammad *et al.* (2016); Rahul *et al.* (2015); Idris (2014).

Table 4: Results of Samples + *Tamarindus indica* after 20 hours

Parameter	Kubuwa Village Well Water	Usuma Dam Water
Appearance	Clear	Clear
Colour	Colourless	Colourless
Turbidity, NTU	8.00	19.00
pH	6.90	7.00
Temperature, K	298	298
Dissolved oxygen, mg/l	3.00	2.00
Total dissolved substances, mg/l	30.9	130.5
Total hardness, mg/l	270	110
Alkalinity, mg/l	19	11
Chloride, mg/l	120	80
Conductivity, $\mu\text{s}/\text{cm}$	50	103
Total <i>Coliform</i> , viable count/ml	20	30
<i>E. coli</i> , viable count/ml	2	1

Table 5 shows the results obtained after samples treatment for 20 hours with the combination of both coagulants (*Tamarindus indica* and *Adansonia digitata*). The turbidity of Kubwa water decreased from 12.8 to 9.14 and that of Usuma dam water decreased from 27.5 to 16.01. There was also a significant decrease in the pH of both samples compare to results of samples treatment with only *Tamarindus indica*. This reduction in pH value indicated the effect of pH on coagulation. Microbial analysis results indicated the reduction in the total Coliform count per ml and completion elimination of the number of *Escherichia coli* present in the Kubwa sample and the *Escherichia coli* of Usuma water decreased from 4 to 2 counts per ml. More so, water

treatment time affects these coagulants and total *Coliforms* and *Escherichia coli* reduce with increase in time. Also, they contributed significantly to improving the colour and appearance of the treated water. The results obtained after samples treatment for over twenty-hours with both coagulants (*Tamarindus indica* and *Adansonia digitata*) was close to the set limits of NSDWQ compared to the results obtained from samples treatment with only *Tamarindus* for both two and twenty-hour time intervals. The results obtained is in a very close agreement with results reported by Olanrewaju *et al.* (2018); Rajul *et al.* (2018); Uthman and Nyakuma (2018); Muhammad *et al.* (2016); Rahul *et al.* (2015); Idris (2014).

Table 5: Result of Samples + *Tamarindus indica* and *Adansonia digitata* after 20 hours

Parameter	Kubwa Village Well Water	Usuma Dam Water
Appearance	Clear	Clear
Colour	Colourless	Colourless
Turbidity, NTU	9.15	16.00
pH	7.00	7.00
Temperature, K	298	298
Dissolved oxygen, mg/l	4.00	6.00
Total dissolved substances, mg/l	35	121
Total hardness, mg/l	190	140
Alkalinity, mg/l	40	15
Chloride, mg/l	75	95
Conductivity, μ s/cm	60	91
Total <i>Coliform</i> , viable count/ml	15	20
<i>E. coli</i> , viable count/ml	0	2

CONCLUSION

Water treatment is an essential process for producing potable water. After water samples were treated with *Tamarindus indica* and *Adansonia digitata* within twenty-hour's period. The turbidity of the Kubwa water sample increased from 3.15 to 9.24 NTU indicating 60% increment in the turbidity and that of the Usuma dam water reduced from 20.7 to 16.01 NTU indicating a decrement by about 22.7%. Also, the bacteria (*Coliforms* and *Escherichia coli*) content of the water was reduced but not to NSDWQ set limit for total *Coliforms* count. The combination of *Tamarindus indica* and *Adansonia digitata* did not bring the physiochemical and bacteriological parameters to the required set limit or standard of both WHO and NSDWQ. Hence, the treated water using both *Tamarindus indica*, *Adansonia digitata* and the mixture of *Tamarindus indica* and *Adansonia digitata* is considered to be suitable for drinking.

It can be inferred from results obtained after analyses in this study that *Tamarindus indica* and *Adansonia digitata* possess coagulation

properties for application as coagulants in water treatment. Therefore, they can be used as alternatives to commercial coagulants and disinfectants used in water treatment. Furthermore, *Tamarindus indica* and *Adansonia digitata* can be employed as coagulants and disinfectants specifically for treatment of water with high turbidity and low contamination.

REFERENCES

- Abiodun, A. A., and Ogugua, C. A., (2013). Physico-chemical and Nutritional Properties of Nigerian Tamarind (*Tamarindus indica* L.) University of Ibadan, Nigeria department of Food Technology.
- Adeniyi, M.J., and Oni, T.J., (2016). Water Contamination in Nigeria and Body Defense Issues. Research Chronicler International Multidisciplinary Journal, 3(3), 11–22.
- Ali, E.M., Falts, S.R., Ramsey, and A.-H.M, (2020). Quality assessment of water along Suez Freshwater Canal and drinking water in Suez Governorate,

- Egypt, *Egyptian Journal of Aquatic Biology & Fisheries*, 24(1), 65–81.
- Aluko, A. E., Kinyuru, J., Chove, L. M., Kahenya, P., and Owino, W. (2016). Nutritional quality and functional properties of baobab (*Adansonia digitata*) pulp from Tanzania. *Journal of Food Research*, 5(5), 23–31.
- Amran, A. H., Zaidi, N. S., Muda, K., and Loan, L. W., (2018). Effectiveness of natural coagulant in coagulation process: a review. *International Journal of Engineering & Technology*, 7(3.9), 34–37.
- An Overview of the Safe Drinking Water Act. United States Environmental Protection Agency (USEPA) (2002).
- Arukia, N., Khan, O., Wanaskar, P., Panchabhai, P., Julme, P., & Ingle, P. A., (2022). Review: Study of Surface Water and Its Treat-ment Using Biocoagulants. *International Journal for Research in Applied Science & Engineering Technology (IJRASET)*. 10(IV), 11–22.
- Bello, T. S., Adebola, M. O., and Asemoloye, M. D., (2022). Modified filters with *Penicillium chrysogenum* culture enhance removal of copper and iron contaminants in water. *Environmental Technology*, Volume 43 (23), 3591–3599.
- Buenaño, B., Vera, E., and Aldás, M.B., (2019). Study of coagulating/flocculating characteristics of organic polymers extracted from biowaste for water treatment. *INGENIERÍA E INVESTIGACIÓN*. 39(1), 24–35.
- Chisoro, P., Kaguru, T., and Assan, N., (2017). Baobab seeds as an alternative protein source in poultry feed. *Scientific Journal of Review*, 6(1), 509–518.
- Choy, S.Y., Prasad, K.M.N., Wu, T.Y., and Ramanan, R.N., (2015). A review on common vegetables and legumes as promising plant-based natural coagulants in water clarification. *International Journal of Environmental Science and Technology*. 12(1), 367–390.
- Edogbanya O. P., Abolude, D.S., Adelanwa, M.A., and Ocholi, O.J., (2016). The Efficacy of the Seeds of *Adansonia digitata* L. as a Biocoagulant and Disinfectant in Water Purification. *Journal of Earth, Environment and Health Sciences*. 2(3) 122–128.
- Ighalo, J.O., and Adeniyi, A.G., (2020). A Comprehensive Review of Water Quality Monitoring and Assessment in Nigeria, *Chemosphere*, 1(2), 127569–127648.
- Idris, M.A., (2015). *Moringa oleifera* seed as disinfectant in water treatment: Optimization and modelling, Ph.D Dissertation, Kulliyah of Engineering, International Islamic University, Malaysia.
- Kamatou, G. P. P., Vermaak, I., and Viljoen, A. M., (2011). An updated review of *Adansonia digitata*: A commercially important African tree. *South African Journal of Botany*, 77(4), 908–919.
- Khandelwal, A., Anand, A., Raghuvanshi, S., and Gupta, S., (2021). Integrated approach for microbial carbon dioxide (CO₂) fixation process and wastewater treatment for the production of hydrocarbons: Experimental studies. *Journal of Environmental Chemical Engineering*, 9(3), 105116–105130.
- Mao, M., Beyene, A., Argaw, A. and Bizuneh, W., (2014). The use of indigenous plant species for drinking water treatment in developing countries. *Journal of Biodiversity and Environmental Science*. 5(3), 269–281.
- Muhammad, J.A., Abraham, T., and Aderemi, B.O., (2016). Synergetic effects of *Moringa oleifera* seed cake extract and *Cactus mucilage* in surface

- water treatment. Research Journal of Engineering and Environmental Science. 1(1), 190–201.
- Nansubuga, I., Banadda, N., Babu, M., Verstraete, W., and Van de Wiele, T., (2013). Effect of polyaluminum chloride water treatment sludge on effluent quality of domestic wastewater treatment. African Journal of Environmental Science and Technology. 7(4), 145–152.
- Olanrewaju, O.O., Jegede, O.J., and Adeoye, A., (2018). Comparison of the Coagulating Efficiency of Moringa Oleifera (Linnaeus) on Wastewater at Lower and Higher Concentration Levels. International Journal of Engineering Science and Application. 2(3), 98–106.
- Rakibul-Islam, Sk., Samin Ishraq, S.M., Kumar Sarker, P., and Kaiser, S., (2017). Ground Moringa Seeds as Bio-coagulant compared with Synthetic coagulant on the basis of Turbidity and colour. International journal of Research in Engineering and Technology. 4(5), 206–211.
- Rajagopal, R., Edwin B. and Michael W., (2016). Drinking Water, The international Encyclopedia of geography. Karina Cardoso Valverde, Edenia Aparecida.
- Rahul, J., Jain, M.K., Singh, S.P., Kamal, R.K., Anuradha, Naz, A., Gupta, A.K., and Mrityunjay, S.K., (2015). *Adansonia digitata* L. (baobab): a review of traditional information and taxonomic description. Asian Pacific Journal of Tropical Biomedicine. 5(1), 79–84.
- Raju, T. D., Ahana K. R., Naji R., Sruthi, S., Veena, V., Shimil, C. P., Sneha K. M., (2018). Role of Moringa oleifera and Tamarind Seed in Water Treatment. International Journal of Engineering Research and Technology 7(4), 454–463.
- Razafimamonjison, G., Leong Pock Tsy, J. M., Randriamiarinarivo, M., Ramanoelina, P., Rasoarahona, J., Fawbush, F., and Danthu, P. (2017). Fatty acid composition of baobab seed and its relationship with the genus *Adansonia* taxonomy. Chemistry & Biodiversity, 14(8), 1600441–1600465.
- Sahu, O. P., and Chaudhari, P. K., (2013). Review on chemical treatment of industrial waste water. Journal of Applied Sciences and Environmental Management. 17(2), 241–257.
- Tsie, M.E., Freeman Ntuli, F., and Lekgoba, T. (2020). Effectiveness of Using Milled Moringa Oleifera Seeds as a Disinfectant in Waste Water Treatment. TEST Engineering & Management, 82(1), 5682–5685.
- Ugwu, S.N., Umuokoro, A.F., Echiegu, E.A., Ugwuishwu, B.O., and Enweremadu, C.C., (2017). Comparative study of the use of natural and artificial coagulants for the treatment of sullage (domestic waste water). Cogent Engineering. 4(1), 1365676–1365690.
- Uthman, H. and Nyakuma, B., (2018). Comparative study of Moringa oleifera and Citrus paradisi as disinfectants and coagulants for water treatment. Chemistry and Chemical Technology. 12(4), 492–499.

PREDICTING THE FLOW CHARACTERISTICS OF RIVER NIGER USING ARTIFICIAL INTELLIGENCE MODELS

¹Gbadebo, O.A., ¹Busari, A. O., ^{1,2}Sadiku, S. and ¹Saidu M.

¹Civil Engineering Department, Federal University of Technology Minna, Nigeria.

^{1,2}Confluence University of Science and Technology, Osara, Kogi State, Nigeria.

*Corresponding author email: g.olukemi@futminna.edu.ng

Abstract

Artificial intelligence (AI), as a branch of computer science, is capable of analysing long-series and large-scale hydrological data. In recent years, AI technology has been applied to the hydrological forecasting modelling. It is essential to determine the hydrological system of River Niger, which is the major water sources of the annual flood in Lokoja, Kogi State, Nigeria. This paper investigates and compares the forecasting capability of three algorithms namely Artificial Neural Network (ANN), Support Vector Machine Regression (SVM Reg.) and Random Forest (RF) to determine the optimal model for forecasting downstream river flow. Daily discharges data from 2001 to 2019 were obtained from National Inland Waterways Authority at Lokoja, Kogi State, Nigeria and applied in the forecasting analysis. Discharge data were divided into 65:35 percent for training and testing respectively. The results of evaluation criteria based on Root Mean Square Error (RMSE), Nash-Sutcliffe Efficiency Coefficient (NSEC), Coefficient of correlation (CC) and Accuracy (ACC) showed that all the models applied gave perfect results except the value obtained for uncertainty analysis in ANN model which was 1.4445 and 0.6219, was slightly high when compare with the values of RF 0.1634 and 0.0134 and SVM Regression models 0.1634 and 0.1210 in testing and training phases respectively. This is caused by the failure of ANN model to carry out pre-processing of discharge data, to remove all the error present in the data unlike the SVM Regression and RF models. Therefore, the RF and SVM Regression algorithms are considerably more adaptive in optimizing the forecasting problem for the river flow prediction.

Keywords: Artificial Neural Network, Machine Learning Models, Random Forest, River Prediction, Support Vector Machine regression.

INTRODUCTION

River flow prediction is a requirement for various uses of water resources like design of reservoir and flood warning systems. The process of hydrology of river flow is very complicated in which a simple data driven model cannot expound its characteristics. It is very essential to investigate the suitable models to a high degree for estimating uncertainties in stream-flow, the nonlinearity and seasonal flow of river. In this study, Artificial Intelligence models which consists of Artificial Neural Network - ANN, Support Vector Machine Regression – SVM Regression and Random Forest – RF were used to predict the streamflow of River Niger, Lokoja, Kogi State, Nigeria.

The SVM technique depends on the principle of statistical learning (Vapnik 1998). The SVM is one type of neural networks that has gain increasing attention in the classification of pattern and in the estimation of nonlinear regression because of its generalization performance (Cao and Tay Francis, 2003). SVM is a type of supervised machine learning algorithm which belongs to kernel-based learning techniques and it uses a linear high dimensional hypothesis space called feature space and thus, the SVM has gained a wide popularity. The basic principle of the SVM is that it uses kernel functions implicitly, mapping the data to a higher dimensional space (Bhagwat and Maity, 2012). Random Forests (RF) are supervised machine learning algorithms that have of recent

gained popularity in water resource applications. It has been used in a various water resource research domain, which include simulation of discharge and water level. Random forest is an alternate approach to physical and conceptual hydrological models for large-scale hazard assessment in various catchments due to its inexpensive setup and operation costs (Jibril et al., 2022). Ighile et al. (2022) applied Machine learning and GIS to predict flood prone areas in Nigeria from 1985 – 2020. They used Receiver operating characteristic curve and Area under Curve to evaluate the ANN and Logistic Regression models and found that both models can predict flood prone areas well.

Miller et al., (2018) applied RF to quantify monthly flow of river from 1950 to 2015 and obtained very high coefficient of NSEC of 0.85. The actual/predicted ratio of 94% implied a better consistency between predicted and actual river flow at almost 2000 gaging station. Sha et al., (2017) compared daily discharge using five various algorithms, given as: Basic extreme learning machine, extreme learning machine with kernels, random forest, back-propagation neural network, and support vector machine. The results indicated that the extreme learning machine with kernels algorithm have the best performance when compared with the other four algorithms, and the basic extreme learning machine algorithm has the least performance. The RF algorithm has good performance in peak flow prediction, while the extreme learning machine with kernels algorithm performed best in low flow prediction. Tongal et al., (2018) Predict and Simulate discharge data with the use of Support Vector Machine Regression (SVM Reg.), Artificial Neural Networks (ANNs), and Random Forest (RF) using precipitation (P), temperature (T), and Potential EvapoTranspiration (PET) as its function. Mohammad et al., (2016), Modelled River discharge time series using support vector machine and artificial neural networks and compared the performance with

conventional method of rating curve and Multi linear regression. The result obtained indicated that the SVM and ANN has a better performance than that of Rating Curve and MLR, which are convectional method. Qiu et al., (1998) combined the use of fuzzy pattern recognition activation function with an ANN model for prediction of runoff. Activation function is a mathematical equation which determines the output of a neural network. This function grouped the runoff into monsoon and non monsoon periods, which pointed nonlinear and periodic behaviour of the river system (Chen et al, 2015). Liong and Chandrasekaran, (2007) applied a machine learning algorithm of SVM and ANN for flood prediction at Dhaka, Bangladesh, and discovered that the predictive ability of SVM is better than that of ANN.

River Niger in Lokoja, Kogi State is always flooded during the peak of the raining season of every year. Thereby leading to the destruction of lives, infrastructures and properties in the area (Jimoh & Salami, 2020). Abdulkadir et al., (2012) applied ANN model to the management of hydropower Reservoir along River Niger in Nigeria. They used ANN to predict reservoir storage capacity along River Niger in Nigeria. The results obtained yield a better prediction both in training and testing phases for Jebba (0.95 and 0.97) and Kanji Reservoir (0.69 and 0.75). They failed to study the predictive power of flow of River Niger as a result, little work has been done on River Niger flow prediction with the use of combination of ANN and Machine learning models. Hence the need to study the flow prediction of the River Niger using the combination of three AI models (ANN, SVM Regression and RF). In view of this, the aim of this paper is to compare the forecasting performance of the three (3) models used for river Niger flow prediction and to find the uncertainties associated with each of the model.

METHODOLOGY

A. Collection of Data

All the relevant discharges (daily discharges data) from Lokoja gauging station at National Inland Waterways Authority which were available from the past were collected from 2001 to 2019. The collected information formed the sample space for the random variable under consideration.

B. Artificial Intelligence and Machine Learning Models

Artificial Neural Network (ANN) model

Artificial neural network (ANN) is a computer programs that is biologically inspired and designed to simulate the way in which the human brain processes information. ANNs gather their knowledge by detecting the patterns and relationships in data and learn through experience, not from programming. The use of ANN models has contributed to an increase of interest within hydrology and hydraulic community. A number of ANN models have been used in hydrological modelling (Renaud & Robert, 2022; Kumar et al., 2016; Tanty, R., & Desmukh, 2015 and Gunathilake et al., 2021). The Artificial Neural Network (ANN)-based machine learning methods have made great progress than ever before,

such as the deep learning and reinforcement learning (Kan et al., 2020). It consists of a three layer feed forward ANN, the input layer consist of nodes, which are joined or linked with an activation function to the hidden layer and it also consists of nodes in the output layer. An objective function is obtained by comparing the differences in the actual and predicted output. ANN model has three layers called input, hidden and output layers. A concept of ANN is introduced from input to hidden layer and is defined as follows:

$$Q_i = \sum_{j=1}^n w_{ij} q_j + b \quad (1)$$

Where Q_i are nodes in the hidden layer ($i= 1, 2, \dots, n$) and q_j^{in} connotes nodes in the input layer ($j= 1, 2, \dots, k$). The connecting factor w_{ij} denotes the weight parameters from the input to the output layers and b is the bias.

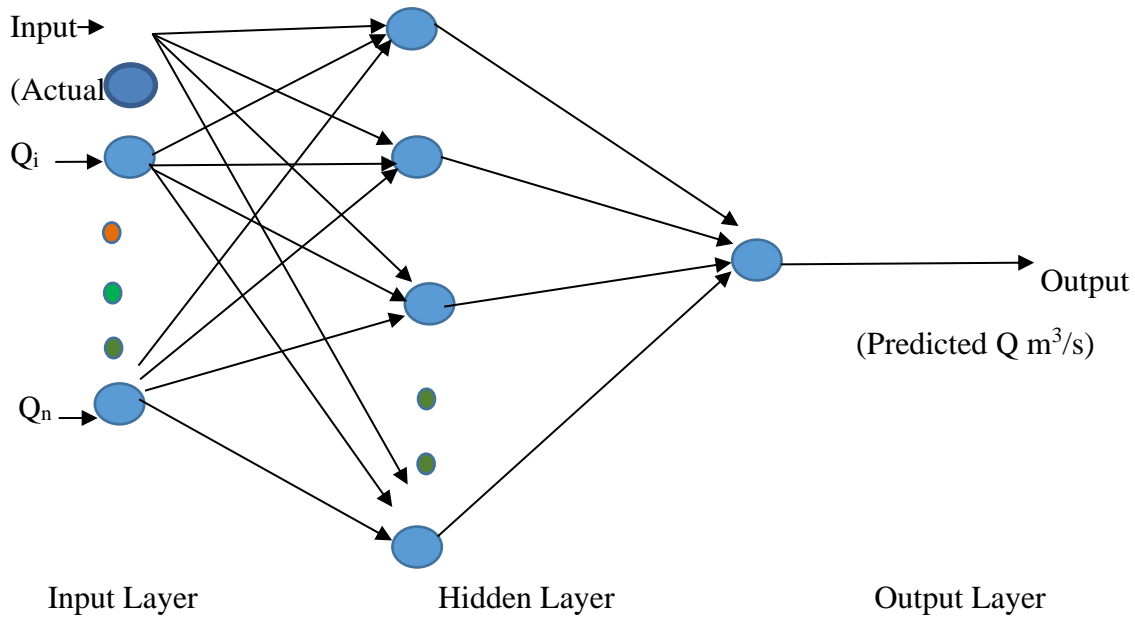


Figure 1 shows a basic overview of ANN topology.

Support Vector Machine Regression (SVM Regression) Model

SVM is a powerful supervised machine learning algorithm which employs various classifications and regression problems. It is based on Structural Risk Minimization as opposing the principle of Empirical Risk Minimization selected by conventional regression methods. It is one of the robust technique for flood prediction. It (SVM Reg.) is a probabilistic approach whereas Support Vector Machine is based on statistical approaches (Anshul, 2021). It uses a hyper-plane that divides and segments the data and classes. SVM find the maximum margin between the hyper-planes that means maximum distances between the two classes. The equation of hyper-plane for a linearly separable data is obtained from straight line equation and given by:

$$y = ax + b \quad (2)$$

By replacing x with x_1 and y with x_2 , and substitute into equation (ii) the equation becomes:

$$ax_1 - x_2 + b = 0 \quad (3)$$

If x is defined by (x_1, x_2) and ω is given by $(a, -1)$, which is a vector normal to hyperplane and b is the offset. Then the equation of the hyper-plane is given as:

$$\omega x + b = 0 \quad (4)$$

The result of the hyper-plane was used to make the river prediction for the stream-flow with the following hypothesis function:

$$Q(x_i) = \begin{cases} +1 & \text{if } \omega \cdot x + b \geq 0 \\ -1 & \text{if } \omega \cdot x + b < 0 \end{cases} \quad (5)$$

The point above the hyper-plane is classified as +1 and below is -1. The aim of this algorithm is to find the hyper-plane that could separate the dataset successfully.

Random Forest (RF) Model

Random Forest is a tree-based computer algorithms, and a supervised machine learning methods which employs the principle of ensemble learning methods, that is widely used in classification and regression problems (Sruthi, 2021). It is a predictive model with high accuracy, stability and ease of interpretation (Li et al, 2016). RF performs better in regression and classification work. Hyper-parameters are employed in random forest to improve the performance and predictive power of models. The ensemble learning technique is a combination of multiple models. It uses bagging and boosting method. Bagging creates many training subset from the training data set with replacement and the output depends on

majority voting. Boosting makes weaker learner to be stronger ones by making a sequential models in a way that the final model will have the highest accuracy. It is calculated as the decrease in node impurity weighted by the probability of reaching that node. The node probability can be calculated by the number of samples that reach the node, divided by the total number of samples. *For classification Gini impurity formula was applied. For regression, variance reduction using mean square error was adopted. Variance reduction can also be estimated using mean absolute error as well in Scikit learn. The equation used for classification is given by Gini impurity as:*

$$\sum_{i=1}^n f_i(1-f_i) \quad (6)$$

Regression equation for variance or mean square error is given as:

$$\frac{1}{n} \sum_{i=1}^n (Q_i - \bar{Q}_i)^2 \quad (7)$$

Regression equation for variance or mean absolute error is given as:

$$\frac{1}{n} \sum_{i=1}^n (Q_i - \bar{Q}_i) \quad (8)$$

Where f_i is the frequency of label i at a node and n is the number of instances or observation, Q_i is the actual discharge and \bar{Q}_i is the mean of actual discharge.

C. Evaluation criteria for Model Performance

The evaluation and comparison of three models is carried out to determine the model with the best performance. The model employed are ANN, Random forest (RF) and Support Vector Machine regression (SVM Regression) models. Four (4) evaluation

criteria were used to determine the best model performance, which are the root mean square error (RMSE) in m^3/s , Nash Sutcliffe efficiency coefficient, correlation coefficient (CC), and the accuracy (ACC). The following evaluation criteria equations were applied in the study as shown:

$$RMSE = \sqrt{\frac{1}{n} \sum_{i=1}^n (Q_i - \hat{Q}_i)^2} \quad (9)$$

$$NSEC = 1 - \sum_{i=1}^n \frac{(Q_i - \hat{Q}_i)^2}{(Q_i - \bar{Q})^2} \quad (10)$$

$$CC = \frac{\sum_{i=1}^n (Q_i - \bar{Q})(\hat{Q}_i - \bar{\hat{Q}})}{\sqrt{\sum_{i=1}^n (Q_i - \bar{Q})^2 (\hat{Q}_i - \bar{\hat{Q}})^2}} \quad (11)$$

$$ACC = 1 - \sum_{i=1}^n \frac{(Q_i - \hat{Q}_i)}{(Q_i)} \quad (12)$$

where Q_i , \hat{Q}_i , \bar{Q} and n represented the actual discharge, predicted discharge, mean discharge and number of instances respectively. RMSE which is the evaluation criteria is a measure of an absolute error. The smaller value of mean square error indicate that the model performance is better. RMSE values ranges from 0 – infinity, while NSEC, CC and ACC values ranges from zero to one (0 - 1), which implies no fit for a value of zero and a perfect or flawless fit for 1.

RESULTS AND DISCUSSION

Evaluation for Model Performance.

The evaluation criteria were done for the ANN, SVM Regression and RF in training and testing but due to the bulkiness of the data, smaller portion of evaluation measures for ANN were presented.

Table 1: Evaluation Criteria for ANN Model in Training phase.

ANN Model		RMSE		NSEC		ACC
Time	Actual (Q)	Predicted	$(Q_i - \hat{Q}^i)^2$		$(Q_i - \hat{Q})^2$	$(Q_i - \hat{Q}/Q_i)$
01-Feb-01	2902	2894.912	50.239	-7.088	11075337.930	0.002
02-Feb-01	2941	2929.425	133.980	-11.575	10817277.810	0.003
03-Feb-01	2949	2963.988	224.640	14.988	10764718.410	-0.005
04-Feb-01	2949	2971.083	487.658	22.083	10764718.410	-0.007
05-Feb-01	2902	2971.083	4772.460	69.083	11075337.930	-0.023
06-Feb-01	2889	2929.425	1634.180	40.425	11162033.970	-0.013
07-Feb-01	2811	2917.915	11430.817	106.915	11689308.200	-0.038
08-Feb-01	2760	2848.972	7916.016	88.972	12040643.430	-0.032
09-Feb-01	2760	2804.001	1936.088	44.001	12040643.430	-0.015
10-Feb-01	2760	2804.001	1936.088	44.001	12040643.430	-0.015
11-Feb-01	2760	2804.001	1936.088	44.001	12040643.430	-0.015
12-Feb-01	2915	2804.001	12320.778	-110.999	10988979.890	0.038
13-Feb-01	2712	2940.94	52413.523	228.940	12376063.880	-0.084
14-Feb-01	2688	2761.753	5439.505	73.753	12545502.110	-0.027
15-Feb-01	2640	2740.657	10131.831	100.657	12887834.560	-0.038
16-Feb-01	2628	2698.523	4973.493	70.523	12974137.670	-0.026
17-Feb-01	2640	2688.001	2304.096	48.001	12887834.560	-0.018
18-Feb-01	2664	2698.523	1191.837	34.523	12716092.330	-0.012
19-Feb-01	2664	2719.580	3089.136	55.580	12716092.330	-0.020
20-Feb-01	2664	2719.580	3089.136	55.580	12716092.330	-0.020
21-Feb-01	2671	2719.580	2360.016	48.580	12666217.850	-0.018
22-Feb-01	2676	2725.726	2472.675	49.726	12630653.220	-0.018
23-Feb-01	2664	2730.116	4371.325	66.116	12716092.330	-0.024
24-Feb-01	2628	2719.580	8386.896	91.580	12974137.670	-0.034
25-Feb-01	2640	2688.001	2304.096	48.001	12887834.560	-0.018
26-Feb-01	2346	2698.523	124272.465	352.523	15085168.820	-0.150
27-Feb-01	2301	2442.110	19912.032	141.110	15436750.490	-0.061
28-Feb-01	2301	2403.117	10427.881	102.117	15436750.490	-0.044
29/02/2001	2251	2403.117	23139.581	152.117	15832146.800	-0.067
30/02/2001	2168	2359.870	36814.096	191.870	16499543.660	-0.088
01-Mar-01	2616	2288.265	107410.230	-327.735	13060728.780	0.125
02-Mar-01	2616	2677.484	3780.282	61.484	13060728.780	-0.023
03-Mar-01	2616	2677.484	3780.282	61.484	13060728.780	-0.023
04-Mar-01	2616	2677.484	3780.282	61.484	13060728.780	-0.023
05-Mar-01	2616	2677.484	3780.282	61.484	13060728.780	-0.023
06-Mar-01	2616	2677.484	3780.282	61.484	13060728.780	-0.023
07-Mar-01	2616	2677.484	3780.282	61.484	13060728.780	-0.023
08-Mar-01	2616	2677.484	3780.282	61.484	13060728.780	-0.023
09-Mar-01	2616	2677.484	3780.282	61.484	13060728.780	-0.023
SUM	30838317		3480735048	445465.217	1.56784E+11	
RMSE			838.5575696	0.1202		
MEAN	6229.963					
NSEC					0.9777	
Uncertainty	0.0144					
Analysis	1.4445					

Comparison of AI Model Performance.

Table 2: Summary of the Model Performances for ANN, RF and SVM Reg.

Algorithm	Training	Testing						
	RMSE	NSEC	CC	ACC	RMSE	NSEC	CC	ACC
ANN	0.1202	0.9778	0.9879	1.0033	6.4284	0.9820	0.9910	1.0020
Random F.	0.0116	0.9961	0.9983	1.0010	3.2955	0.9922	0.9956	1.0016
SVM reg.	0.0348	0.9887	0.9982	1.0010	3.2955	0.9922	0.9914	1.0016

Figure 2 shows the scattered plot of actual and predicted discharges by the three algorithms applied (SVM Regression RF and ANN) in testing phases.

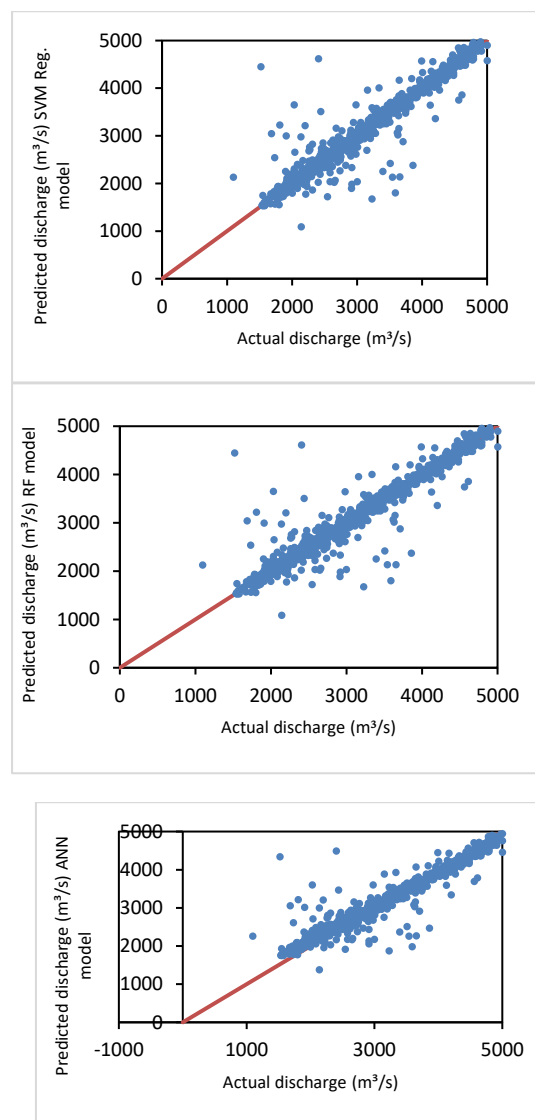
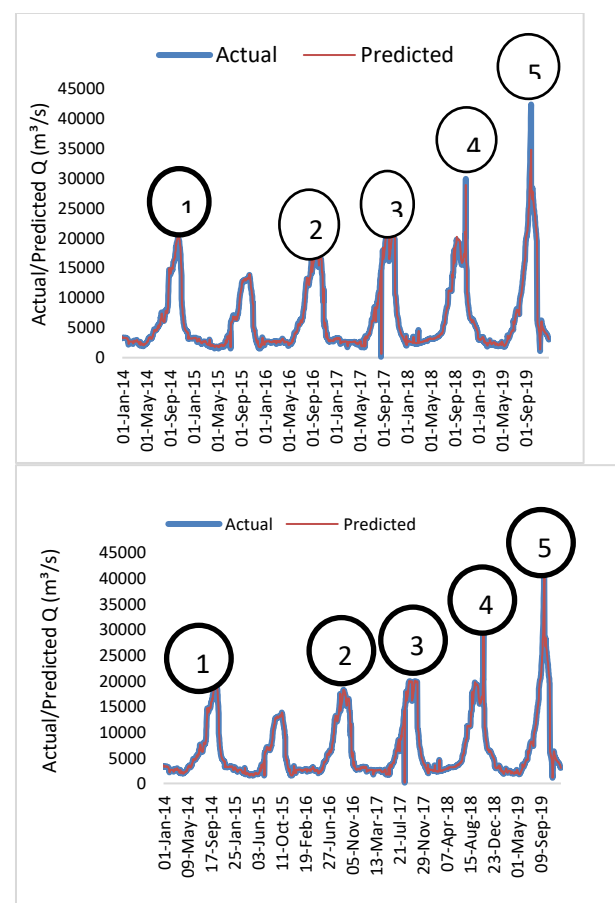


Figure 2: Actual and Predicted discharges of different algorithms in the testing stages.

The SVM Regression and RF models portray good agreement between the actual and predicted discharges in testing stages. The

plot of the intensively distributed dots along the ideal line from 1500 - 2000m³/s implies that the low river flow are mostly well predicted. The reason been that the regular occurrence of low values allows an improved or good generalization of the trained model. The performance of ANN model is not good as compared with that of RF and SVM Reg. in the low flow during the testing phase from 1500 – 2000m³/s. Figure 3 (a – c) depicts the time series of actual and predicted discharges by the ANN, SVM and RF algorithms and starred five actual extreme values. The values are provided in Table 3 together with the algorithms employed.



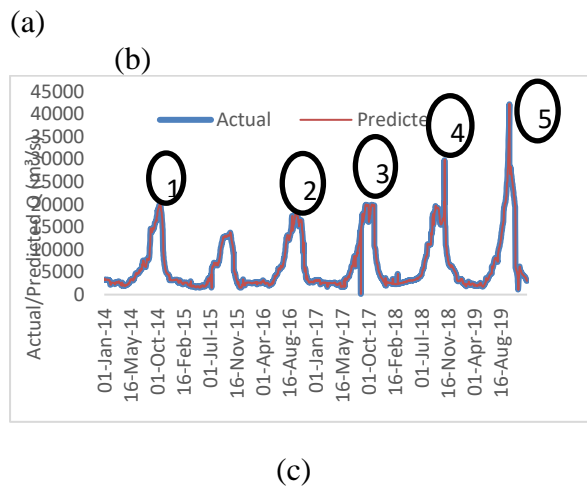


Figure 3: Testing from 2014-2019 (a) ANN; (b) Support Vector Machine Regression (c) Random Forest

It was observed that all the three algorithms employed captured all the extreme values. It started the extreme values for the actual discharges. The peak value was obtained at extreme point 5 for all the models. The peak value was under predicted by the ANN model and have a good prediction for both RF and SVM Regression due to the relative closeness algorithms result. Extreme values 2, 3 and 4 over-predicted the actual discharges, while SVM Regression predicts

well the actual discharge in extreme value 1. RF slightly under predict and ANN slightly over predict the actual extreme value at point 1. The relative mean error between the actual and predicted discharges are the same for both RF and SVM Regression which was 0.0090, while ANN has a slightly higher relative mean error of 0.0100 when compare with that of RF and SVM Regression respectively. In addition, the values of uncertainty analysis 1.4445 and 0.6219 for ANN is very high in training and testing respectively, while RF has the uncertainty values of 0.0134 and 0.1634 in training and testing respectively. SVM Reg. has the uncertainty analysis values of 0.1210 and 0.1634 in training and testing.

Table 3 presented the summary of the values of the extreme points and relative mean error for the three models employed in this study. The values for the extreme points were displayed and the least relative mean error was obtained by SVM Reg. and RF, while the ANN has a slightly high relative mean error when compare with that of SVM Reg. and RF.

Table 3: Extreme and Relative Mean Error values obtained for the algorithm

Algorithm	Extreme Value 1 (m ³ /s)	Extreme Value 2 (m ³ /s)	Extreme Value 3 (m ³ /s)	Extreme Value 4 (m ³ /s)	Extreme Value 5 (m ³ /s)	Relative Mean Error
Actual Q	19695	17280	10855	19640	42248	
ANN	19965.22	17914.08	20299.73	28822.85	33963.24	0.0100
SVM Reg.	19633.11	17495.93	19660.19	29937.88	42361.77	0.0090
RF	19408.46	17495.93	19854.75	29937.88	42361.77	0.0090

Confidence Interval (CI)

Confidence Interval is the range in which the true mean value will lie with a high probability. In order to calculate CI, the distribution function of the mean values or variables in the observation is essential. Assume that the distribution is normally distributed, the CI for the mean value is given in equation (13) as:

$$CI = \bar{Q} \pm z * \frac{\sigma}{\sqrt{n}} \quad (13)$$

where CI is the confidence interval, \bar{Q} is the mean discharge, z is the value for the confidence interval for 95% and 99% CI which is given by 1.96 and 2.57 respectively, σ is the standard deviation and n is the number of instances or observation (DATAtab, 2023). The mean, variance, 95% and 99% CI of the three algorithms employed in this study are provided in Table 4.

Table 4: Statistical Analysis of different algorithm used for testing period.

Algorithm	Mean (m ³ /s)	Variance (m ⁶ /s ²)	Mean of 95% CI (m ³ /s)	Mean of 99% CI (m ³ /s)
Actual Q	6645.01	36398877	6.8994	6.9786
ANN	6686.34	36585845	6.9414	7.0208
SVM Reg.	6655.87	36608461	6.9110	6.9905
RF	6655.87	36608461	6.7125	6.9905

The statistical analysis is essential in order to examine the significance or importance of the differences. The mean value obtained from SVM Regression and RF are closer to the actual mean value as compare with that of ANN that is a slightly above the actual mean. The three models obtained variances that is slightly above the actual variance, this implies that the predicted results are widely distributed. The closest value to the actual is achieved by RF algorithm for the mean with 95% CI, but there is a slight differences in the actual value when compared with the other algorithm employed. As a result, the predicting performances by these three algorithms are comparable.

CONCLUSION

In conclusion, the performances of the three models employed are compared. The purpose is basically to consider a relatively reliable model for river prediction at the downstream part of the river. The input variables employed were the discharges of River Niger from 2001 to 2019. The capability to capture extreme values and four statistical evaluation (RMSE, NSEC, CC and ACC) were employed to estimate the predicting performances. The results

indicated that the three algorithm perform well on generalization and forecasting of daily discharge data used. In addition, Random Forest performs excellently with high efficiency due to its ability to handle binary, continuous and categorical data. It also has the ability to reduce the risk of over-fitting, reduction in training time, fixing of the missing data and the stability is very high. ANN displayed high rate of uncertainty analysis **1.4445** in this study when compared with the RF and SVM Regression. Therefore, the best model with the least error in the stream flow data set is RF followed by SVM regression. The models adopted in this study can be used to solve the nonlinear and non differential problems in multidimensional space.

REFERENCES

- Liong S. & Chandrasekaran S. (2007) Flood Stage Forecasting With Support Vector Machines JAWRA Journal of the American Water Resources Association 38(1):173 – 186. DOI: 10.1111/j.17521688.2002.tb01544.x
- Miller, M. P., Carlisle, D. M., Wolock, D. M. and Wiczorek, M. (2018) A Database of Natural Monthly

- Streamflow Estimates from 1950 to 2015 for the Conterminous United States,” J. Am. Water Resour. Assoc., vol. 54(6),1258–1269, doi: 10.1111/1752-1688.12685.
- Mohammad A. G., Rahman K., Arun G., Mohammad H. F., Atefeh A. (2016). Modelling River discharge time series using support vector machine and artificial neural Networks. *Environ Earth Sci.* 75:685 DOI 10.1007/s12665-016-5435-6
- Qiu L., Chen, S. Y., Nie, X. T., (1998) A forecast model of Fuzzy recognition neural network and its application. *Advances in water science* 9 (3), 258 – 264.
- Renaud J., & Robert L., (2022). Short-Term Hydrological Forecast Using Artificial Neural Network Models with Different Combinations and Spatial Representations of Hydrometeorological Inputs, *Water*, 14(4), 552.
<https://doi.org/10.3390/w14040552>
- Sha, J., Li, X. and Wang, Z. L. (2019). Comparison of daily streamflow forecasts using extreme Learning machines and the random forest method. *Hydrol. Sci. J.*, 64(15), 1857–1866,
Doi 10.1080/02626667.2019.1680846.
- Srthi E. R. (2021) Random Forest Algorithms comprehensive guide with examples. Analythic Vidhya. www.analyticsvidhya.com
- Tanty, R., & Desmukh T. S. (2015) Application of Artificial Neural Network in Hydrology- A Review *International Journal of Engineering Research & Technology (IJERT)*, 4(6). ISSN:2278-0181
- Tongal, H. and Booij, M. J. (2018) Simulation and forecasting of stream flows using machine Learning models coupled with base flow separation, *J. Hydrol.*, 564, 266–282. doi: 10.1016/j.jhydrol.2018.07.004.
- Vapnik VN (1998) Statistical learning theory. Wiley, New York.

ISSN 2465-7425



9 772465 742009



ACADEMIC PUBLISHING CENTRE
FEDERAL UNIVERSITY OF TECHNOLOGY, MINNA